Conference Proceedings of the Society for Experimental Mechanics Series

Hae Young Noh
Matthew Whelan
P. Scott Harvey *Editors*

Dynamics of Civil Structures, Volume 2

Proceedings of the 40th IMAC, A Conference and Exposition on Structural Dynamics 2022

Springer

Conference Proceedings of the Society for Experimental Mechanics Series

Series Editor

Kristin B. Zimmerman
Society for Experimental Mechanics, Inc.,
Bethel, CT, USA

The Conference Proceedings of the Society for Experimental Mechanics Series presents early findings and case studies from a wide range of fundamental and applied work across the broad range of fields that comprise Experimental Mechanics. Series volumes follow the principle tracks or focus topics featured in each of the Society's two annual conferences: IMAC, A Conference and Exposition on Structural Dynamics, and the Society's Annual Conference & Exposition and will address critical areas of interest to researchers and design engineers working in all areas of Structural Dynamics, Solid Mechanics and Materials Research.

Hae Young Noh • Matthew Whelan • P. Scott Harvey
Editors

Dynamics of Civil Structures, Volume 2

Proceedings of the 40th IMAC, A Conference and Exposition on Structural Dynamics 2022

Springer

Editors
Hae Young Noh
Stanford University
Stanford, CA, USA

P. Scott Harvey
University of Oklahoma
Norman, OK, USA

Matthew Whelan
University of North Carolina at Charlott
Charlotte, NC, USA

ISSN 2191-5644 ISSN 2191-5652 (electronic)
Conference Proceedings of the Society for Experimental Mechanics Series
ISBN 978-3-031-05448-8 ISBN 978-3-031-05449-5 (eBook)
https://doi.org/10.1007/978-3-031-05449-5

This Springer imprint is published by the registered company Springer Nature Switzerland AG
The registered company address is: Gewerbestrasse 11, 6330 Cham, Switzerland

Preface

Dynamics of Civil Structures represents one of nine volumes of technical papers presented at the 40th IMAC, a conference and exposition on structural dynamics, organized by the Society for Experimental Mechanics, and held February 7–10, 2022. The full proceedings also include volumes on nonlinear structures and Systems; model validation and uncertainty quantification; dynamic substructures; special topics in structural dynamics and experimental techniques; rotating machinery, optical methods and scanning LDV methods; sensors and instrumentation, aircraft/aerospace, and dynamic environments testing; topics in modal analysis and parameter identification; and data science in engineering.

Each collection presents early findings from analytical, experimental, and computational investigations on an important area within structural dynamics. Dynamics of civil structures is one of these areas which cover topics of interest of several disciplines in engineering and science.

The dynamics of civil structures technical division serves as a primary focal point within the SEM umbrella for technical activities devoted to civil structures analysis, testing, monitoring, and assessment. This volume covers a variety of topics including structural vibrations, damage identification, human-structure interaction, vibration control, model updating, modal analysis of in-service structures, innovative measurement techniques and mobile sensing, and bridge dynamics among many other topics.

Papers cover testing and analysis of different kinds of civil engineering structures such as buildings, bridges, stadiums, dams, and others.

The organizers would like to thank the authors, presenters, session organizers, and session chairs for their participation in this track.

Stanford, CA, USA — Hae Young Noh
Charlotte, NC, USA — Matthew Whelan
Norman, OK, USA — P. Scott Harvey

Contents

Chapter 1
Smart Active Vibration Control System of a Wind Turbine Blade Using Piezoelectric Material

Ali Hashemi and Jinwoo Jang

Abstract Vibration suppression has become one of the major issues in sensitive structures. The active vibration control (AVC) has been widely used in the field of vibration damping in rotary structures. In this article, deriving analytical solution of lateral vibration and active vibration control of a wind turbine (WT) blade are investigated. First, a new semi-analytical solution is developed to obtain the lateral deflection of a wind turbine blade under external loadings. We propose a method to map a wind turbine blade to an Euler-Bernoulli beam with the same conditions, in order to find vibration and dynamic responses of the blade by solving analytical vibration solutions of the Euler-Bernoulli beam. Piezoelectric (PZT) material is used in this research as an actuator-sensor to excite the structures and sense the responses. The governing equations of the beam with piezoelectric patches are derived based on the integration of the piezoelectric transducer vibration equations into the vibration equations of the Euler-Bernoulli beam structure. Finite element model of the wind turbine blade with piezoelectric patches is developed. A unique transfer function matrix is derived. The beam structure is projected to the blade by using a unique transfer function matrix which is derived by exciting the structures and achieving responses. The results obtained from the mapping method are compared with the results achieved from the FE model of the blade. A satisfying agreement has been observed between the results. Next, in order to suppress the transverse vibration of the wind turbine blade, piezoelectric ceramic patches are used as an actuator in combination with linear quadratic regulator (LQR) control system. The obtained results show that the proposed smart control system contains PZT patches and LQR control system is able to efficiently suppress lateral vibration.

Keywords Active vibration control · Smart structure · Structural dynamic · Analytical vibration analysis · Transfer function matrix · Piezoelectric actuator and sensor

1.1 Introduction

The control of unwanted vibration of wind turbine blades plays a key role in ensuring wind turbines' (WT) high efficiency and cost-effectiveness and also, increasing the structure's lifetime. Blade vibrations cause extreme operation instability of wind turbines and even catastrophic failure of the whole turbine which must be prevented from. Many investigations have been conducted to control vibration of sensitive rotary structures by utilizing passive, active, and semi-active control systems. In order to damp the undesired vibration of structures, proper actuators are needed to apply controlling forces. Due to the changing blade dynamics and excitation conditions, passive control methods have been less utilized for rotating structures. Active control typically provides large vibration reduction which can be tremendously helpful in damping unwanted vibration of sensitive structures. This control process needs to employ smart materials. Among different smart materials, piezoelectrics have three unique advantages, being lightweight, low cost, and convenient usage, as well as provide sensing and actuating features which can make them an appropriate material for vibration control. Piezoelectric (PZT) transducers have been widely used in active vibration control systems owing to their special properties as sensor and actuator. PZT transducers have been utilized in various shapes and forms such as perfect layer along surfaces of structures or patches in different sizes. Piezoelectric-based vibration alleviation can reduce the unwanted vibration levels of rotating structures consequently abating the risk of high cycle fatigue while lowering blade weight and drag. In this research, we propose an active vibration control system with PZT patches as sensor and actuator. To simulate the implementation of active control rules on structures, we

A. Hashemi · J. Jang (✉)
Department of Civil, Environmental and Geomatics, Florida Atlantic University, Boca Raton, FL, USA
e-mail: jangj@fau.edu

H. Y. Noh (eds.), *Dynamics of Civil Structures, Volume 2*, Conference Proceedings of the Society for Experimental Mechanics Series, https://doi.org/10.1007/978-3-031-05449-5_1

propose an innovative semi-analytical method to project an actual shape of a wind turbine blade to the same scale of an Euler-Bernoulli beam in order to derive an analytical solution for the wind turbine blade's dynamic response and then use the method to apply controlling rules to a wind turbine blade. Implementation of controlling rule on the wind turbine blade is not feasible by using finite element commercial software like ANSYS due to high computational cost. Hence, the proposed transfer function method is used as a surrogate to obtain the controlled deflections of a wind turbine blade in this research. Therefore, in the first step, we focus on developing a new semi-analytical solution to obtain lateral deflection of a wind turbine blade under different external loadings, and next, a suitable control system is designed in order to suppress unwanted transverse deflection of a wind turbine blade.

Derivation of analytical solutions for vibration and elasticity analysis of structures has always been noticed as an important field of research in structure analysis and design. Due to the low computational cost especially for large-scale structures, analytical solutions of dynamic responses have attracted considerable attention. However, deriving analytical solution for many structures could be very challenging due to their complicated geometry. Moreover, during recent years, a considerable increase of global warming caused sustainable energies, such as wind energy, to have absorbed wide attention as great alternative energy resources. Various types of wind turbines, such as off-shore and on-shore wind turbines with different sizes and power outputs, have been investigated in recent years as a result of this fact. Normally, large and complex wind turbines have been more concentrated due to their efficient power generation capacity. Large-scale wind turbines can suffer from significant vibrational deflection, particularly on the edges of their blades. These unwanted vibrations can cause severe structural damage and failure of the power generation systems. Due to their complex shapes and continuous interaction between wind flows and their blades, analyzing dynamical and vibrational responses of wind turbine blades is tremendously complicated. A new understanding of analytical solutions for analyzing dynamic behaviors of these kinds of structures, can contribute to the analytical analyzing of different mechanical and structural systems including twisters and heavy solid structures. In comparison to analytical methods, the vibration of these twister structures has primarily been investigated using finite element (FM) simulation and other numeric methods such as finite difference (FD) and differential quadrate (DQ). To control vibration of structures, three controlling systems including passive, active, and semi-active have been considered. These systems use various controlling rules such as proportional pulse derivative (PD), fuzzy logic control, and sliding mode control. Active control outperforms other methods for wind turbine blades due to various environmental excitation conditions and it provides large vibration reduction.

At the first step, this research aims to propose a unique semi-analytical solution for a wind turbine blade, which can describe lateral blade movements under specific external forces. In general, a semi-analytical solution technique is proposed to solve linear partial differential equations. The semi-analytical method depends on analytically solving the equations derived by discretizing the spatial coordinates of partial differential equations. Semi-analytical approaches have a substantial advantage over numerical methods in terms of solution time. This study demonstrates how to project the real form of a wind turbine blade to the same size as an Euler-Bernoulli beam to derive an analytical solution for the wind turbine blade's dynamic and vibration response. The blade of the GE 1.5 megawatt model, which has 45 meter blades on a 9 meter tower, is considered in this work. The blade's material is assumed steel in order to simplify deriving equations. Plumbum-titania-zirconia is considered as piezoelectric sensor-actuator patches to sense and actuate structures. At the second step, for the purpose of alleviation of vibrations and transverse deflection of the wind turbine blade with piezoelectric patches, a linear quadratic regulator (LQR) control method is designed in this research. Due to decreasing computational cost, the proposed semi-analytical method is used to project controlled transverse vibration of the actual shape of the wind turbine blade to the Euler-Bernoulli beam instead of utilizing finite element model of the blade in order to implement control rules.

1.1.1 Background

Rotating structures, which have significance in many practical applications such as turbine blade, airplane propellers, and robot manipulators, have been investigated for a long time. The vibrations of twister beams have been widely studied with different types of beam models, e.g., Euler-Bernoulli and Timoshenko, using analytical or semi-analytical solutions and numerical or finite element methods (FEMs). The majority of previous research considered Euler-Bernoulli and Timoshenko models to describe twister and under-loading beams without considering shear deformations. The normal frequencies, mode shapes, and maximum vertical displacements of rotary beams have all been studied in order to better understand their dynamic behaviors. However, it is challenging to obtain dynamic behaviors of rotary beams due to various environmental elements including different wind flows and gravity loads. Huang et al. [1] obtained the natural frequencies of an Euler-Bernoulli beam during high-speed rotation using an exponential series solution. Arvin [2] investigates the nonlinear free vibrations of a rotating beam. He utilizes the von Kármán-strain displacement relations and derived nonlinear motion equations by

Hamilton's principle. Da Silva [3] presents a systematic and versatile research of a helicopter rotor blade's responses. At the first step, he developed full nonlinear partial differential equations governing the motion of the blade, which take into account geometric nonlinearities caused by deformation, and then the system's equilibrium solution was described by the system. Yigit et al. [4] studied the flexural movement of a radially rotating beam connected to a rigid body. Fully connected nonlinear motion equations were derived utilizing the extended Hamilton's principle. Hanagud [5], Baruh [6], and Choura et al. [7] studied dynamical models of rotating Euler-Bernoulli beams without considering centripetal forces on beams. Most of previous studies about dynamical models of structures did not investigate the interaction between fluids and structures [8]. Song et al. [8] established an elaborate model in understanding the fluid-structure interaction between a structure and air flow. The arbitrary mesh interface (AMI) framework was used in conjunction with the open-source OpenFOAM tools. Wang et al. [9] provided numerical simulations of wind turbine blade-tower interaction. The vibration analysis of wind turbine blades or other rotating beam form structures may be broken down into two sections. The first is edge-wise vibration that occurs outside of the rotating circle of the beam, and the second is flap-wise vibration that occurs in the rotation plate. Lee et al. [10] studied flap-wise vibration of a composite rotational Euler-Bernoulli beam and the relationship between rotational speed and natural frequencies. Asr et al. [11] suggested prestressing in the blade structure of the H-Darrieus wind turbine in the context of axial compression stress that their research presented a structural comparison in terms of their dynamic vibrational response among reference and prestressed turbine rotor configurations. Jokar et al. [12] obtained the dynamic modeling and free vibration analysis of horizontal axis wind turbine blades in the flap-wise direction by evaluating blade kinetic and potential energies and using Hamilton's principle. Farsadi et al. [13] perform a semi-analytical solution for the free vibration analysis of uniform and symmetric pre-twisted rotating TW which adopts the Green-Lagrange strain tensor to derive the strain field of the system and Hamilton's principle to derive the governing equations of the dynamic system. Afzali et al. [14] derive a vibration model for a H-rotor/Giromill blade that the authors assume the blade under transverse bending and twisting deformation was treated as a uniform straight elastic Euler-Bernoulli beam. Derivation of the energy equations and simplified aerodynamic models for bending and twisting blades have been distributed, and the equations of Lagrange have been extended to assumed modal coordinates to derive nonlinear motion equations for bending and twisting blades [15–19]. Meksi et al. [20] derived the equations of motion of functionally graded sandwich plates from Hamilton's principle based on a new shear deformation plate theory. Alsabagh et al. [21] implemented the Rayleigh-Ritz method for a typical 5-MW wind turbine blade and developed MATLAB codes and then obtained natural frequencies for both flap-wise and edge-wise vibrational behavior. Chen et al. [22] derive a dynamic model of curved beams by using the absolute nodal coordinate formulation based on the radial point interpolation method (RPIM). Chen et al. [23] examined the free vibration of rotating tapered Timoshenko beams by using the technique of variational iteration. Mokhtar et al. [24] investigate the rotor-stator interaction phenomenon in the finite element (FE) framework by using Lagrange multiplier based on contact mechanics. Tang et al. [25] present a developed approach that is used to identify the operational blade vibration modes by measuring the vibrational displacements with a non-contact single point laser sensor during the wear process. Liu et al. [26] study structural vibrations by establishing a dynamic equilibrium equation of a coupled system. They develop a blade's excitation force model consisting of transverse and vertical excitation forces using a quasi-steady method. Hamilton's principle and the finite element (FE) method with a rotating pre-twisted and leaned cantilever beam model (RPICBM) with the flap-wise-chordwise-axial-torsional coupling are set up by Zheng et al. [27] who validate the efficacy of the model through comparisons with the literature and the FE models in ANSYS. Warminski et al. [28] study dynamics of a rotor composed of a flexible beam linked to a slewing rigid hub based on extended Euler-Bernoulli theory for a slender beam model, which considers a nonlinear curvature, synchronized transverse and longitudinal oscillations, and the hub's non-constant angular velocity. In different engineering structures, rotating composite beams and blades have a wide variety of applications [29]. Rafiee et al. [29] present a comprehensive analysis of scientific papers on rotating composite beams as presented in the past decades that for the flexural study of a sandwich beam combined with a piezoelectric layer. Wang [30] proposes a fundamental mechanics model uses the Maxwell equation in the formulation in order to extract the distribution of the piezoelectric potential. Chen et al. [31] develop a semi-analytical solution of the dynamic features of the AG-WEC by the frequency and time domain analysis based on the potential flow principle. Huang et al. [32] present a high-order finite element model and sliding model control method for a rotating flexible structure with the piezoelectric layers in order to effectively reduce the vibration. Lin [33] uses proportional and derivative controls to damp the vibration of a rotating beam by using a pair of PZT sensor and actuator layers. Bendine et al. [34] investigate on the active vibration control of a composite plate using discrete piezoelectric patches. A finite element model with PZT patches was derived based on first-order shear deformation theory, and a damping effect on composite plate was provided by using PZT actuators and applying linear quadratic regulator (LQR) control algorithm. Larbi and Deu [35] presented an efficient electromechanical finite element formulation to analyze the dynamic analysis of a cantilever beam with piezoelectric patches. Ma et al. [36] investigated on an active vibration control of a moving cantilever beam with piezoelectric ceramics as actuator by using pulse derivative closed-loop feedback system. Sivrioglu et al. [37] successfully tried to attenuate the vibration of a blade with a piezoelectric actuator patch implementing

robust multi-objective control. The controlled response of a fuzzy logic controller was measured for various piezoelectric materials in active vibration control by Sharma et al. [37] and then compared them with each other. A smart active vibration control system was proposed with a new robust controlled by Cui et al. [38]. In their investigation, the system comprised PZT materials, signal conditioning, and the embedded sensor system. Pu et al. [39] applied an adaptive vibration control system contains a filtered-U least mean square algorithm and a surface bonded piezoelectric actuator to a smart structure. An active control system was designed by Brahem et al. [40] based on a full-state linear quadratic regulator controller which was applied to a rotary beam in order to alleviate the vibration. Shakir and Saber [41] developed a linear coupled finite element model by ANSYS for the piezoelectric actuation of a cantilever beam to study smart beam behavior in open- and closed-loop cases. Qiu et al. [42] developed a sliding mode control strategy to damp the vibration of a piezoelectric flexible cantilever plate. The finite element modeling was utilized to simulate the controller on bending and torsional vibration in their research. Ghaderi and Ghatei [43] presented an integrated virtual synchronization/linear quadratic regulator method to identify the system's unknown physical parameter and vibration control of structures based on estimated parameters.

1.2 Theory and Modeling

To obtain analytical solutions for dynamic and vibration responses to any external forces and excitations and applying control rules, unlike complex structures such as wind turbine blades, the Euler-Bernoulli beam has been widely investigated. Since the Euler-Bernoulli beam theory is based on a few key assumptions and the beam has a simple geometric form, analytical study of the Euler-Bernoulli beam is achievable. The Euler-Bernoulli beam theory assumes that "plane sections remain plane" and that deformed beam angles (slopes) are small; thus, shear deformations may be ignored. The novelty of this research work includes the projection of a wind turbine blade's deformations and lateral deflections to the same scale of Euler-Bernoulli beam and then using this mapping system for applying controlling rules on the wind turbine blade and obtained controlled vibration movements of the blade. We proposed a unique transfer function matrix to undertake the projection of a wind turbine blade to an Euler-Bernoulli beam. Lateral deflections of the Euler-Bernoulli beam are transferred to the wind turbine blade by utilizing the proposed transfer function matrix. This projection will permit us to simply obtain the dynamic and vibration responses of a wind turbine using the Euler-Bernoulli beam. Next, to damp the unwanted lateral deflection of the wind turbine blade, linear quadratic regulator (LQR) is considered in this study. An active vibration control is proposed in this study combining piezoelectric material as actuator and a designed linear quadratic regulator control method. The transfer function method is used to implement the control system on the structure in order to decrease computational costs.

To develop the transfer function matrix, both the wind turbine blade and the Euler-Bernoulli beam need to be excited with the same external excitation. At the next step, the lateral movements of selective specific nodes on their surfaces are obtained. Furthermore, in the proposed method, the Euler-Bernoulli beam should have the same length with the wind turbine blade which is 45 meters in this study. We obtain the lateral deflection of the Euler-Bernoulli analytically in this research. FE models are used to calculate the counterpart of the wind turbine blade. Piezoelectric patches are utilized to apply external excitations and sense the dynamic responses of both the wind turbine blade and the Euler-Bernoulli beam. Due to the electromechanical properties, piezoelectric materials are effective sensors and actuators. The piezoelectric sensors/actuators are patched on the surfaces of both structures. The external excitations and the dynamic responses of the structures are measured by the piezoelectric patches. To derive two initial function matrices related to the Euler-Bernoulli beam with PZT patches and the wind turbine blade with PZT patches, same external loadings are applied to the structures, and corresponding responses are obtained. Next, two initial function matrices are used to achieve a total transfer function for the whole system. At the final step, to damp unwanted lateral vibration of the blade, an active vibration control system is designed. To obtain controlled transverse movements of the blade, first, the controlling rules are applied to the to the governing dynamic equations of the beam with PZT patches under an external loading. Then, controlled lateral movements of the blade are obtained using the proposed mapping system. ion of the wind turbine blade.

1.2.1 The Euler-Bernoulli Beam Includes Piezoelectric Patches

An anticipated shape of the beam with patches is depicted in Fig. 1.1.

The beam under discussion here is considered as an Euler-Bernoulli beam with length (L), width (b), and height (h) which are divided into n equal sections. The boundary conditions of the beam are considered to be a cantilever beam, similar to a blade in a wind turbine, attached at one end to a support, in order to achieve the best results. Edgewise vibrations are

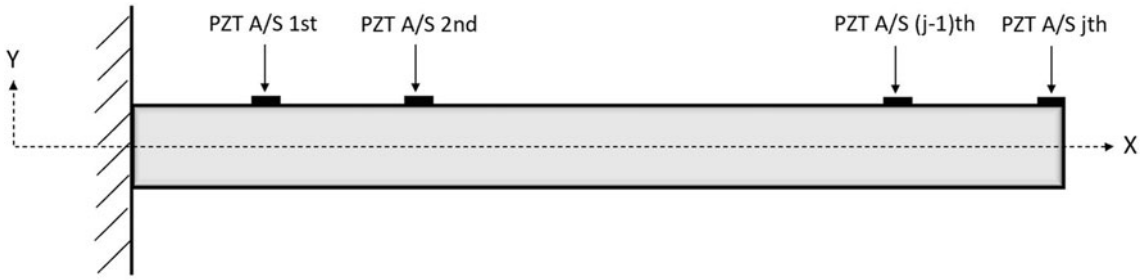

Fig. 1.1 Anticipated figure of the beam with piezoelectric patches

discarded in this research. Moreover, the piezoelectric patches are assumed to be set along the transversal direction of the structure. The length of each piezoelectric patch L_p became the following:

$$L_p = x_{2bj} - x_{1bj} \tag{1.1}$$

where j shows the number of sensors, b indicates the beam, and 2 and 1 are the beginning and the end of the patch, respectively. x_{2bj} and x_{1bj} show the distance of the end tip and the beginning of the n^{th} sensor-actuator from the base, respectively. In this research, L_p is considered as 10 cm for each sensor. Furthermore, the width of each piezoelectric patch is the same as the width of the beam b, and it is located at the end of each section on the beam.

1.2.2 Analytical Modeling of the Euler-Bernoulli Beam Includes PZT Patches

Shearing deformations are neglected in the Euler-Bernoulli theory; therefore, shearing tension and strain are not included. In this theory, the shear force is derived by this equation:

$$V = \frac{dM}{dx} \tag{1.2}$$

The energy method and Lagrange equations are used to obtain the governing equation for the Euler-Bernoulli beam with PZT patches. Then the assumed mode method is employed to solve acquired obtained equation. The total strain energy of the Euler-Bernoulli beam is provided as the following:

$$U = \frac{1}{2}\int_0^L \int_A (\sigma_{xx}\varepsilon_x)\, dA dx \tag{1.3}$$

By inserting the associated equations for stress and strain of the Euler-Bernoulli beam, Eq. 1.3 can be represented as:

$$U = \frac{1}{2}\int_0^L D_{xx}\left(\frac{\partial u_z(x,t)}{\partial x}\right)^2 dx \tag{1.4}$$

where D_{xx} is defined as:

$$D_{xx} = EI(x) \tag{1.5}$$

σ_{xx} and ε_x are the normal stress and normal strain in x direction, respectively. E is the Young modulus, and $I(x)$ is the second moment of area in x direction. To derive the related strain energy equation for the beam, Eq. 1.5 needs to be substituted into Eq. 1.4, as the following:

$$U = \frac{1}{2}\int_0^L \left(EI(x)\left(\frac{\partial u_z(x.t)}{\partial x}\right)^2\right) dx \tag{1.6}$$

where $u_z(x)$ describes the transverse deflection of the beam at some position x.

The total formulation of the Euler-Bernoulli beam's kinetic energy is provided as:

$$T = \frac{1}{2}\int_0^L \int_A \left(\rho v_z^2\right) dA dx dx \tag{1.7}$$

where v_z is velocity and it can be presented as:

$$v_z = \frac{\partial u_z(x.t)}{\partial t} \tag{1.8}$$

To formulate the Euler-Bernoulli beam's cumulative kinetic energy and simplify it, Eq. 1.8 could be replaced into Eq. 1.7, as:

$$T = \frac{1}{2}\int_0^L \left(\rho A(x)\left(\frac{\partial u_z(x.t)}{\partial t}\right)^2\right) dx \tag{1.9}$$

By assuming the linear PZT constitutive relations and obtaining the governing equation of the vibration of the PZT patches, the stress and strain of these patches can be derived as:

$$\sigma_{xx}^p = c_{11}^E S_1 - e_{31} E_3 \tag{1.10}$$

$$\varepsilon_{xx}^p = S_1 = -y\frac{\partial^2 u_z(x,t)}{\partial x^2} \tag{1.11}$$

where *1*, *2*, and *3* show the *X*, *Y*, and *Z* directions, respectively. c_{11}^E, e_{31}, and E_3 are modules of elasticity of the PZT in constant electric field, piezoelectric stress constant, and the electric field across the electrodes of the PZT, respectively. The following is the relation between the electrical field and the voltage applied to the piezoelectric patch electrodes:

$$E_3 = \frac{V(t)}{h_a} \tag{1.12}$$

$V(t)$ is applied harmonic voltage. The correlation between the piezoelectric stress constant and the associated strain constant, d_{31}, is provided as:

$$e_{31} = c_{11}^E d_{31} \tag{1.13}$$

Thus, the equations of the strain energy and kinetic energy of a piezoelectric patch are formulated as:

$$U_j^p = \frac{1}{2}\int_{x_{1a}}^{x_{2a}} \left(c_{11}^E I_p\left(\frac{\partial^2 u_z(x.t)}{\partial x^2}\right)^2 + J_p V(t)\left(\frac{\partial^2 u_z(x.t)}{\partial x^2}\right)^2\right) dx \tag{1.14}$$

$$T_j^p = \frac{1}{2}\int_{x_{1a}}^{x_{2a}} \rho_a h_a b\left(\frac{1}{2}\frac{\partial u_z(x.t)}{\partial x}\right)^2 dx \tag{1.15}$$

To obtain the overall strain of the Euler-Bernoulli beam with the piezoelectric sensor and actuator, the strain energy of the piezoelectric patches must be contributed to the strain energy of the Euler-Bernoulli beam. The above process must

be applied for the kinetic energy of the piezoelectric patches and the Euler-Bernoulli beam, respectively. As a result, the cumulative strain energy and kinetic energy of the beam including PZT patches are obtained as follows:

$$U = \frac{1}{2}\int_0^L \left(EI(x)\left(\frac{\partial u_z(x.t)}{\partial x}\right)^2\right)dx + \frac{1}{2}\int_{x_{1a}.j}^{x_{2a}.j} \left(c_{11}^E I_p\left(\frac{\partial^2 u_z(x.t)}{\partial x^2}\right)^2 + J_p V(t)\left(\frac{\partial^2 u_z(x.t)}{\partial x^2}\right)^2\right)dx_{j=1:n,} \tag{1.16}$$

$$T = \frac{1}{2}\int_0^L \left(\rho A(x)\left(\frac{\partial u_z(x.t)}{\partial t}\right)^2\right)dx + \int_{x_{1a}.j}^{x_{2a}.j} \rho_a h_a b\left(\frac{1}{2}\frac{\partial u_z(x.t)}{\partial x}\right)^2 dx_{j=1:n} \tag{1.17}$$

where j indicates the number of piezoelectric patches.

1.2.3 Assumed Mode Method

To solve the governing equations of the beam and the piezoelectric patch, the assumed mode approximation is used. The transverse deflection under actuation of a surface-bonded PZT patch may be represented as:

$$u_z(x.t) = \sum_{k=1}^{b} \pi_k(x) q_k(x) \tag{1.18}$$

where n_k shows the admissible function which satisfies geometrical boundaries and q_k describes the corresponding unknown. By replacing Eq. 1.18, into Eqs. 1.16 and 1.17, these equations can be represented as:

$$U = \frac{1}{2}\int_0^L EI\sum_{k=1}^{b}\sum_{l=1}^{b}(q_k\pi_k')(q_l\pi_l')dx + \left(\frac{1}{2}\int_{x_{1a}.j}^{x_{2a}.j} c_{11}^E I_p \sum_{k=1}^{b}\sum_{l=1}^{b} q_k q_l \pi_k'' \pi_l'' dx + \frac{1}{2}\int_{x_{1a}.j}^{x_{2a}.j} J_p V(t)\sum_{k=1}^{b} q_k \pi_k'' dx\right)_{j=1:n} \tag{1.19}$$

$$T = \frac{1}{2}\int_0^L \rho A\sum_{k=1}^{b}\sum_{l=1}^{b}\dot{q}_k\dot{q}_l\pi_k\,\pi_l\,dx + \left(\frac{1}{2}\int_{x_{1a}.j}^{x_{2a}.j} \rho_a h_a b\sum_{k=1}^{b}\sum_{l=1}^{b}\dot{q}_k\dot{q}_l\pi_k\,\pi_l\,dx\right)_{j=1:n} \tag{1.20}$$

The Lagrange equation is presented as:

$$\frac{\mathrm{d}}{\mathrm{d}t}\left(\frac{\partial T}{\partial \dot{q}_j}\right) - \frac{\partial T}{\partial q_j} + \frac{\partial U}{\partial q_j} = 0 \tag{1.21}$$

The simple matrix form of the governing equation of the Euler-Bernoulli beam with the PZT patch is derived by substituting Eqs. 1.19 and 1.20 into the Lagrange Eq. 1.21 as:

$$M\{\ddot{q}\} + K\{q\} = -V(t)\eta \tag{1.22}$$

where M, K, and η are presented as:

$$M = \left[\frac{1}{2}\int_0^L \rho A\pi_k\pi_l\,dx + \left(\frac{1}{2}\int_{x_{1a}.j}^{x_{2a}.j} \rho_a h_a b\pi_k\pi_l\,dx\right)_{j=1:n}\right] \tag{1.23}$$

$$K = \left[\frac{1}{2}\int_{-\frac{L}{2}}^{\frac{L}{2}} \rho A\pi_k'\pi_l'\,dx + \left(\frac{1}{2}\int_{x_{1a}.j}^{x_{2a}.j} c_{11}^E I_p \pi_k''\pi_l''\,dx\right)_{j=1:n}\right] \tag{1.24}$$

$$\eta = \left(\frac{1}{2}\int_{x_{1a}.j}^{x_{2a}.j} J_p \pi_i''\,dx\right)_{j=1:n} \tag{1.25}$$

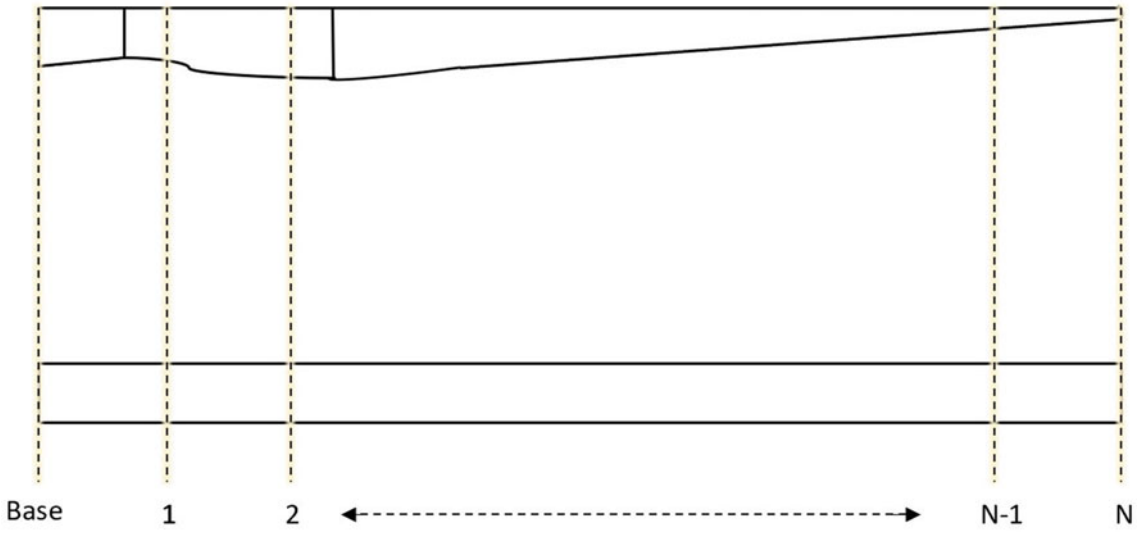

Fig. 1.2 Section's estimated diagram from the blade to the beam

1.2.4 Finite Element Modeling

The FE modeling of the GE 1.5 MW wind turbine's blade including PZT patches is constructed in ANSYS code. The length of the blade is 45 meters. The piezoelectric patches are attached to the blade in the same way as the Euler-Bernoulli beam is, as shown in Fig. 1.2. The connection between the PZT patches and the beam is considered to be perfect. The blade is modeled using the same beam geometry as in the analytical modeling, and the simulation is carried out three-dimensionally. In the combined field of transient structural dynamics and the electric field, the simulation of the model is performed. Defining the blade's structural damping in FEM has a high influence on obtaining a precise approximation of the real blade's behavior. The Rayleigh damping is considered as the structural damping model of the blade. The coefficients are obtained as $\alpha = 0.0027$ and $\beta = 0.0000017$ which are the mass corresponding coefficient and stiffness corresponding coefficient, respectively.

1.2.5 The Wind Turbine Blade Projection on the Euler-Bernoulli Beam

Due to the fact that the velocity of wave propagation in solid media is only related to the frequency ranges of actuation, not the time when excitations are applied to a structure, both systems (the wind turbine blade and the Euler-Bernoulli beam) could be considered as time-invariant. The linear properties may be utilized to determine vibrational features applied to any external force since both systems are linear time-invariant (LTI). As a result of developing a semi-analytical solution for the wind turbine blade to derive the blade's lateral deflections under various external forces, the linear time-invariant feature of the system is employed to depict an efficient, feasible, and accurate model. The proposed method leverages the linear time-invariant characteristics. As a result, only LTI systems may employ the proposed transfer projection function. The transmitted pulse signal is considered as an impulse function to obtain the frequency responses of both the FE model of the blade and the analytical model of the Euler-Bernoulli beam. A pulse signal is applied to every actuator's location of the Euler-Bernoulli beam with piezoelectric patches. Then, the n outcomes of pulse signals are reached using the analytical equations of the beam by each applying the pulse signal to an actuator. Instead of sending the transmitted pulse signal, the unit step function can be utilized in LTI systems to identify structural frequency responses. Herein, in order to solve the equations in the time domain, the unit step function is used. To obtain the system's responses to the transmitted pulse signal, the achieved amplitude responses from n points are differentiated for each actuation. The frequency domain is considered to extract exact responses since many noises were present among the reached responses. Noises show small frequencies and are recognizable in the frequency domain. Furthermore, in the frequency domain, high frequencies generated by the resonance phenomena can be removed. To increase the ratio of signals to noises, overvoltage is required. A step function

output is defined as $y_u(t)$. The outcomes need to be differentiated with respect to time in order to obtain the impulse function responses. The response of the impact function $y_\delta(t)$ equaled as the following:

$$y_\delta(t) = \frac{dy_u(t)}{dt} \tag{1.26}$$

Then, the frequency response is as the following:

$$Y_\delta(\omega) = FFT\left(y_\delta(t)\right) \tag{1.27}$$

By applying the unit step function to each PZT actuator, n outputs from each n sensors are obtained in every actuation (n is 45 in this research). Each element of the function matrix of the beam and the blade is achieved as the following:

$$g_{ij} = FFT\ \ (j\text{th output})\,/FFT\ \ (i\text{th input}) \tag{1.28}$$

where j indicates the number of sensor (output) and i shows the number of actuator (input). Finally, the $[N \times N]$ matrix of function G is derived by repeating this procedure for every section:

$$G(i, j) = g_{ij}\ \ i, j = 1, 2, \ldots, n \tag{1.29}$$

Using these external excitations and associated responses, the $n \times n$ initial function matrix is derived for the Euler-Bernoulli beam with piezoelectric patches. A $n \times n$ initial function matrix is derived for the wind turbine blade with patches by applying the same external excitations and deriving lateral movements in the same way. In order to obtain amplitude responses of the blade, the FE model of the wind turbine blade with patches is constructed in ANSYS code.

By performing the mentioned method on the beam and the blade, two initial function matrices are achieved, G_b and G_w for the beam with PZT patches and the blade with PZT patches, respectively. At this step, the total transfer function matrix is derived by applying any same external dynamic load (U_s) to both systems and concerning the linear feature of the whole system as:

$$Y_b = G_b.U_s \tag{1.30}$$

$$Y_w = G_w.U_s \tag{1.31}$$

By utilizing linear feature of the whole system,

$$Y_w = \left(G_w \Big/ G_b\right).Y_b \tag{1.32}$$

Finally, the total transfer function matrix is obtained using two initial matrices that were achieved in the previous step as:

$$G_T = \left(G_w \Big/ G_b\right) \tag{1.33}$$

Under the same external loading, the total transfer function G_T can project vibrational and tensional outcomes of the analytical solution of the Euler-Bernoulli beam with PZT patches to the wind turbine blade with PZT patches (Eqs. 1.31, 1.32, and 1.33). As shown in Fig. 1.3, the suggested approach may be organized as a semi-analytical solution to determine lateral deflection of the blade to external forces. The steps for determining lateral movements of the wind turbine blade using a semi-analytical method are as follows:

Step 1. Obtain governing equations of the Euler-Bernoulli beam with the attached piezoelectric actuator and sensor using energy method.
Step 2. Solve derived governing equations using the assumed mode method.
Step 3. Develop finite element model of the wind turbine blade with PZT patched.
Step 4. Obtain frequency responses of both systems, the FE model of the blade and the analytical model of the Euler-Bernoulli beam, by applying the transmitted pulse signal.

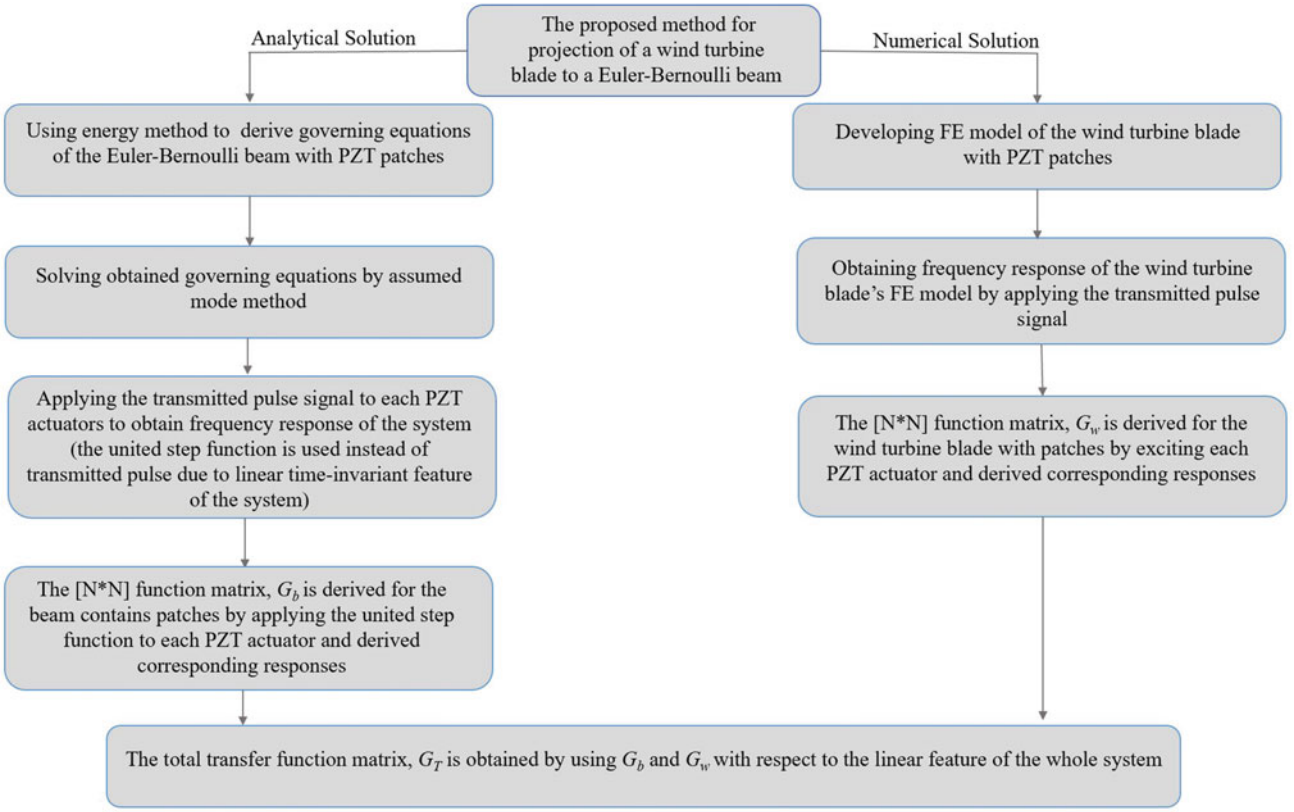

Fig. 1.3 Flowchart of the total transfer function deriving process

Step 5. Derive initial function matrices for the Euler-Bernoulli beam and the wind turbine blade.
Step 6. Obtain the total transfer function using two achieved initial function matrices with respect to linear properties of the systems.

1.2.6 The Implementation of Control System

As one of the aims of this study is to implement a control rule on the wind turbine blade in order to damp the unwanted lateral vibration, linear quadratic regulator (LQR) is considered. The controlling rules of the control system are applied on the wind turbine blade by using piezoelectric patches and the transfer function method. The 45 PZT patches are used to apply the designed linear quadratic regulator rules on the Euler-Bernoulli beam. The linear quadratic regulator is a common design technique which provides practical feedback gains. The purpose of linear quadratic regulator controlling method is trying to determine a state-feedback optimal control force which can minimize the definite quadratic cost function Eq. 1.35. The weighted matrices of the control performance index which are used to design optimal state-feedback gains are usually determined by trial and error via simulation. Authors mainly randomly select Q and R to determine whether they meet simulation requirements. In this research, we continue to adjust Q and R until they meet the requirements which include damping flap-wise deflection and using minimum energy as needed voltage for PZT patches as much as possible. The purpose of this section is to obtain two weighted matrices in LQR controller in order to design an optimal active vibration control system. To derive LQR, the generic form of the system can be written in a state-space form

$$\dot{X} = Ax(t) + Bu(t) \tag{1.34}$$

And which all of the n states x are available for the controller. The optimal state-feedback controller or LQR minimizes the infinite quadratic cost function Eq. 1.35, including the state variables (x) and control action (u). Here, $\{Q, R\}$ are the

symmetric positive semi-defined weighting matrix and the positive weighting factor, respectively, that tune the penalty on the excursion of state variables and control action. To minimize the integral performance index Eq. 1.35, the continuous time algebraic Riccati equation Eq. 1.36 can be used.

$$J = \int_0^\infty \left[x^T(t) Q x(t) + u^T R u(t) \right] dt \tag{1.35}$$

$$A^T P + PA - PBR^{-1} B^T P + Q = 0 \tag{1.36}$$

The state-feedback optimal control force $u(t)$ is [44]:

$$u(t) = Kx(t) \tag{1.37}$$

where:

$$K = -R^{-1} B^T P \tag{1.38}$$

K is unknown as an optimal controller gain and P is the unique, symmetric, positive semi-definite solution to the algebraic Riccati equation (ARE) Eq. 1.36.

The term $x^T(t)Qx(t)$ is a measure of control precision, and the term $u^T Ru(t)$ is a measure of control effort. Here, $X = \{q_1, q_2, \ldots, q_n\}^T$ is the lateral displacement vector obtained from n sensors on the structural system. $u(t)$ is the control input, i.e., controlling force. The state-space representation of Eq. 1.22 is provided as Eq. 1.34; then:

$$x = \begin{pmatrix} x_1 \\ x_2 \end{pmatrix} = \begin{pmatrix} q \\ \dot{q} \end{pmatrix} \tag{1.39}$$

$$A = \begin{bmatrix} 0 & I \\ M^{-1}K & M^{-1}C \end{bmatrix}; B = \begin{bmatrix} 0 \\ M^{-1}U \end{bmatrix} \tag{1.40}$$

where M, K, and C are the system mass, the system stiffness, and the damping matrices, respectively, and U is the control force vector. Figure 1.4 shows the block diagram for the control loop simulation.

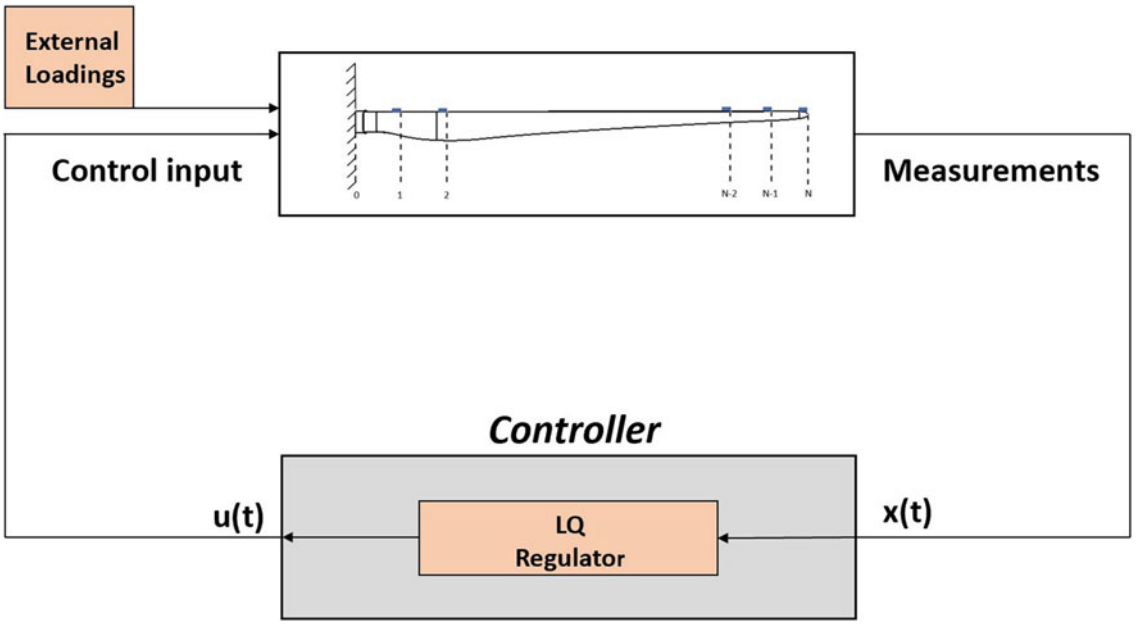

Fig. 1.4 Block diagram for control

1.3 Results and Discussion

The Euler-Bernoulli beam and the FEM model of the wind turbine blade are loaded separately with three external different loadings to validate the proposed semi-analytical solution. A sine distributed load with an amplitude of 20 kg/m^3 and attack angles of 15, 30, and 45 degrees are applied, respectively. The Reilly-Ritz method is employed to discretize a continuous force generated by applied external loadings to the number of divided pieces (number of actuators-sensors) on the Euler-Bernoulli beam. The comparison of analytical and FEM outcomes of the 35th sensors is shown in Fig. 1.5.

Figure 1.5 shows an acceptable compliance between analytical and FEM results. Furthermore, the error between the outcomes of the analytical solution and FEM for each sensor by applying the loading number 2 (30-degree attack angle) are shown in Fig. 1.6. Based on the achieved results, there are no clear and precise patterns in the error rates dependent on sensor locations, as seen in Fig. 1.6. The results demonstrate that as the sensors' distance from the base of the wind turbine increases, the method's accuracy diminishes; nevertheless, there are certain outliers to the patterns, as shown in Fig. 1.6. The vibration domain of the structure naturally grows with augmentation of the distance from support, which is one cause for obtaining escalating rate of errors by raising the sensors' interval from the base. Therefore, the span from the base can be considered as a determining factor for the method's precision.

The control system is implemented on the blade using the transfer function method and the Euler-Bernoulli beam in this research as using the finite element modeling directly to apply controlling rules on structures is tremendously time-consuming. A linear quadratic regulator was designed which is a proper control system as the considered structural system in this study is time-invariant. The 45 piezoelectric patches are used to apply the designed linear quadratic regulator rules on the Euler-Bernoulli beam, and then the controlled lateral deflections of the beam are mapped to the wind turbine blade with the proposed transfer function method to obtain the suppressed transverse vibration of the blade. In the design process of the linear quadratic regulator control method, the R and Q matrices are assumed unity matrix and γI, respectively, in which Gamma is a scalar. The calculation for transient response is performed with a time step of 0.01 sec. Figure 1.7 shows the results of applying controlling rule on the tip of the blade, sensor number 45, which has the maximum lateral deflection. The outcomes of damping vibration of the 45th sensor on the blade under loading number 2 (30-degree attack angel) are provided as below:

The task of the proposed active vibration control system is to suppress the vibration magnitude of the nodes. According to the achieved results, satisfactory performance of the LQR control system with PZT patches, is demonstrated for the wind turbine blade. The results indicate that the performance of the control system outperforms by decreasing the amount of Gamma as it can be seen in Fig. 1.7.

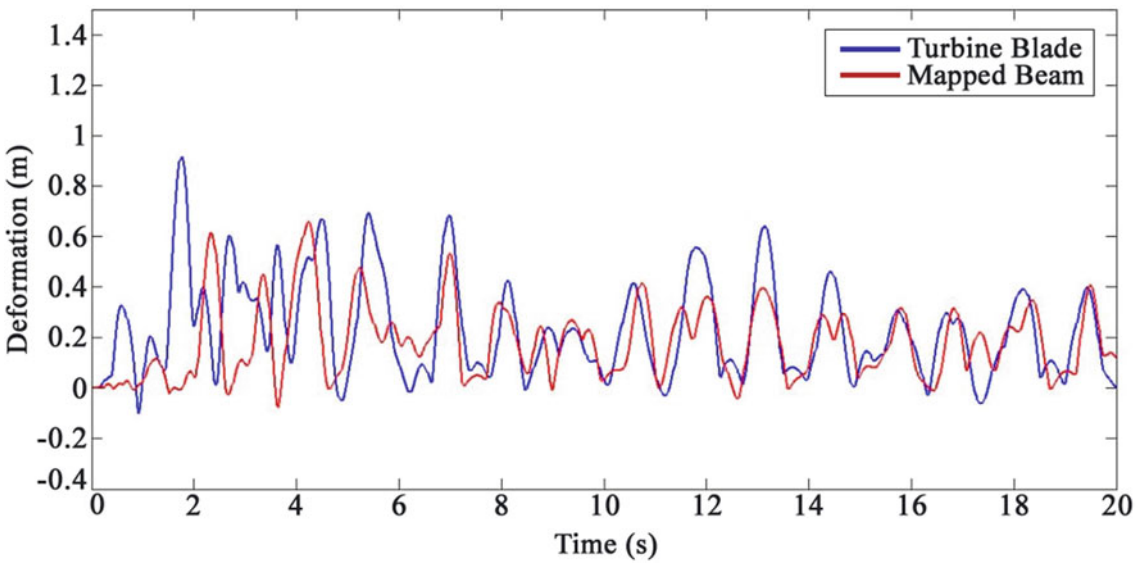

Fig. 1.5 The outcomes of the analytical results and FEM results for the 35th sensor under loading number 2 (30-degree attack angle)

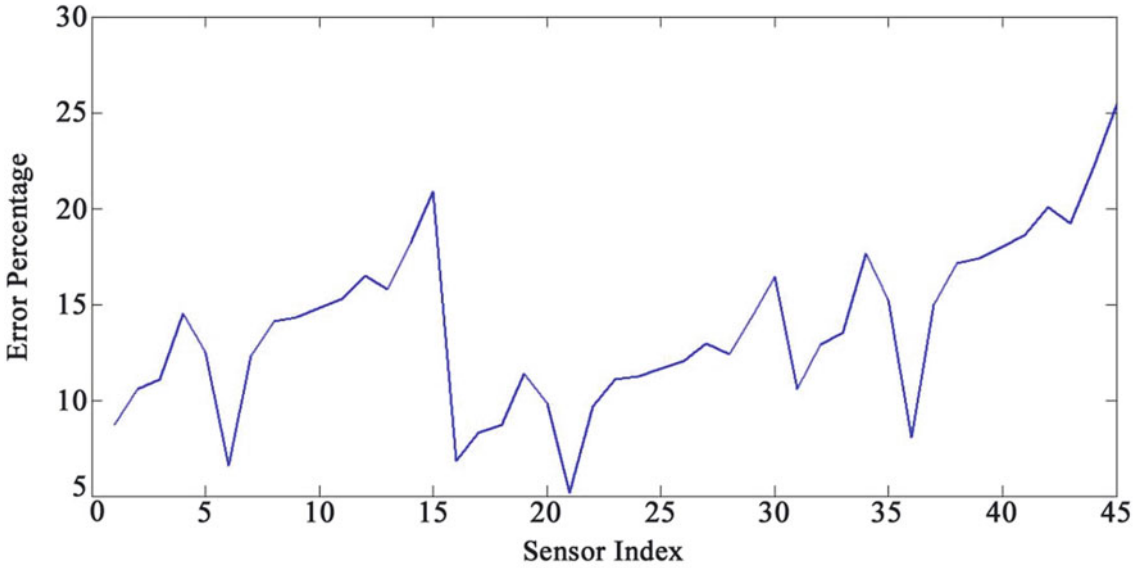

Fig. 1.6 Error percentage for each sensor under loading number 2 (30-degree attack angle)

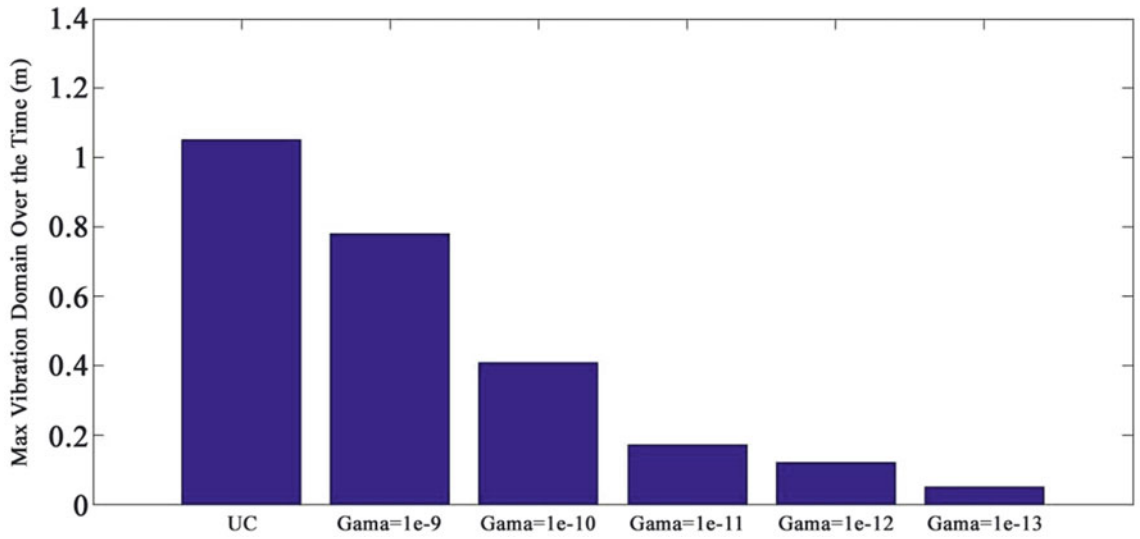

Fig. 1.7 The outcomes of applying controlling rule for the 45th sensor under loading number 2 (30-degree attack angle)

1.4 Conclusion

In this paper, a smart active vibration control system including LQR control method and piezoelectric actuator is proposed to damp the transverse deflection of a wind turbine blade. In the first part, an effective semi-analytical solution based on a unique transfer function matrix for a wind turbine blade is presented. The energy technique was used to drive the governing equations of the Euler-Bernoulli beam with the attached piezoelectric actuator and sensor. The impact of changing mass, stiffness, and electromechanical coupling between the beam and the piezoelectric actuator and sensor is considered by integrating the characteristic vibration equations of the piezoelectric patches into the characteristic equations of the Euler-Bernoulli beam. The obtained governing equations are then solved using the assumed mode method. Rayleigh damping factors are used to develop the FE model of the wind turbine blade and piezoelectric patches. A pulse signal is applied to every actuator's location in both systems to derive initial transfer function matrices and obtain the responses for the Euler-Bernoulli beam with PZT patches and the wind turbine blade with PZT patches. Concerning the linear feature of the whole system, the final transfer function matrix is derived by applying same external dynamic force to both systems. The Euler-Bernoulli beam and

the FE model of a wind turbine blade are loaded independently with three distinct loads to verify the mapping performance of the final transfer function matrix. The results demonstrate that the deflections derived directly from the FE model of the wind turbine blade and the movements obtained using the proposed method have a good correlation. Furthermore, the accuracy of the method diminished by increasing the distance of the sensors from the base of the wind turbine blade due to the natural expansion of the structure's vibration domain in longer distance from the support. To damp the lateral vibration of the wind turbine blade, an active vibration control system was proposed including the designed LQR control system and PZT patches as actuator. Since using finite element modeling commercial software could not be feasible due to the heavy cost of computation, the semi-analytical solution is used for the implementation of controlling rules. Achieved results demonstrate satisfying performance of the proposed active vibration control of the wind turbine blade under external loadings.

Declaration of Conflicting Interests The authors declared no potential conflicts of interest with respect to the research, authorship, and/or publication of this article.

References

1. Huang, C.-L., Lin, W., Hsiao, K.M.: Free vibration analysis of rotating Euler beams at high angular velocity. Comput. Struct. **88**, 991–1001 (2010). https://doi.org/10.1016/j.compstruc.2010.06.001
2. Arvin, H., Bakhtiari-Nejad, F.: Non-linear modal analysis of a rotating beam. Int. J. Non Linear Mech. **46**, 877–897 (2011). https://doi.org/10.1016/j.ijnonlinmec.2011.03.017
3. Crespo Da Silva, M.R.M.: A comprehensive analysis of the dynamics of a helicopter rotor blade. Int. J. Solids Struct. **35**, 619–635 (1998). https://doi.org/10.1016/S0020-7683(97)00065-6
4. Yigit, A., Scott, R.A., Galip Ulsoy, A.: Flexural motion of a radially rotating beam attached to a rigid body. J. Sound Vib. **121**, 201–210 (1988). https://doi.org/10.1016/S0022-460X(88)80024-5
5. Hanagud, S., Sarkar, S.: Problem of the dynamics of a cantilevered beam attached to a moving base. J. Guid. Control. Dyn. **12**, 438–441 (1989). https://doi.org/10.2514/3.20429
6. Baruh, H., Tadikonda, S.S.K.: Issues in the dynamics and control of flexible robot manipulators. J. Guid. Control. Dyn. **12**, 659–671 (1989). https://doi.org/10.2514/3.20460
7. Choura, S., Jayasuriya, S., Medick, M.A.: On the modeling, and open-loop control of a rotating thin flexible beam. J. Dyn. Sys. Meas. Control. **113**, 26–33 (1991). https://doi.org/10.1115/1.2896354
8. Song, B., Jiang, Y., Huang, S., He, W.-S.: Study on the wind-induced dynamic response of wind power tower in consideration of fluid-structure interaction. Atlantis Press (2014). https://doi.org/10.2991/icmce-14.2014.57
9. Wang, Q., Zhou, H., Wan, D.: Numerical simulation of wind turbine blade-tower interaction. J. Marine. Sci. Appl. **11**, 321–327 (2012). https://doi.org/10.1007/s11804-012-1139-9
10. Lee, S.H., Shin, S.H., Yoo, H.H.: Flapwise bending vibration analysis of rotating composite cantilever beams. KSME Int. J. **18**, 240–245 (2004). https://doi.org/10.1007/BF03184733
11. Asr, M.T., Masoumi, M.M., Mustapha, F.: Modal behaviour of vertical axis wind turbine comprising prestressed rotor blades: a finite element analysis, Pertanika. J. Sci. Technol. **25**, 977–982 (2017). http://www.pertanika.upm.edu.my/Pertanika%20PAPERS/JST%20Vol.%2025%20(3)%20Jul.%202017/27%20JST%20Vol%2025%20(3)%20July%202017_JST(S)-0275-2017_pg977-982.pdf. Accessed 21 March 2020
12. Jokar, H., Mahzoon, M., Vatankhah, R.: Dynamic modeling and free vibration analysis of horizontal axis wind turbine blades in the flap-wise direction. Renew. Energy. **146**, 1818–1832 (2020). https://doi.org/10.1016/j.renene.2019.07.131
13. Farsadi, T., Şener, Ö., Kayran, A.: Free Vibration Analysis of Uniform and Asymmetric Composite Pretwisted Rotating Thin Walled Beam. American Society of Mechanical Engineers Digital Collection (2018). https://doi.org/10.1115/IMECE2017-70531
14. Afzali, F., Kapucu, O., Feeny, B.F.: Vibration Analysis of Vertical-Axis Wind-Turbine Blades. American Society of Mechanical Engineers Digital Collection (2016). https://doi.org/10.1115/DETC2016-60374
15. Acar, G.D., Feeny, B.F.: Bend-bend-twist vibrations of a wind turbine blade. Wind Energy. **21**, 15–28 (2018). https://doi.org/10.1002/we.2141
16. Wait, I., Yang, Z.J., Chen, G., Still, B.: Wind-induced instabilities and monitoring of wind turbine. Earthq. Eng. Eng. Vib. **18**, 475–485 (2019). https://doi.org/10.1007/s11803-019-0515-8
17. Lagrangian formulation for the rapid estimation of helicopter rotor blade vibration characteristics | The Aeronautical Journal | Cambridge Core, (n.d.). https://www.cambridge.org/core/journals/aeronautical-journal/article/abs/lagrangian-formulation-for-the-rapid-estimation-of-helicopter-rotor-blade-vibration-characteristics/B10B369138A33EB3D2D46B9DB16605B8. Accessed 4 December 2020
18. Pardo, A.C., Goulos, I., Pachidis, V.: Modelling and analysis of coupled flap-lag-torsion vibration characteristics helicopter rotor blades. Proc. Instit. Mech. Eng. G J. Aerosp. Eng. (2016). https://doi.org/10.1177/0954410016675891
19. Navabi, M., Ghaffari, H.: Modeling and simulation of nonlinear dynamics of helicopter rotor flapping considering offset, blade weight moment and frequency of flapping, Modares. Mech. Eng. **19**, 2523–2534 (2019). http://mme.modares.ac.ir/article-15-19245-en.html. Accessed 4 December 2020
20. Meksi, R., Benyoucef, S., Mahmoudi, A., Tounsi, A., Adda Bedia, E.A., Mahmoud, S.: An analytical solution for bending, buckling and vibration responses of FGM sandwich plates. J. Sandw. Struct. Mater. **21**, 727–757 (2019). https://doi.org/10.1177/1099636217698443
21. Alsabagh, A.S.Y., Fayyad, S.M., Darweesh, N., Alfaqs, F.: Fundamental natural frequencies investigation for a typical 5-MW wind turbine blade. Noise Vib.World. **51**, 77–84 (2020). https://doi.org/10.1177/0957456520901355

22. Chen, Y., Zhang, D., Li, L.: Dynamic analysis of rotating curved beams by using Absolute Nodal Coordinate Formulation based on radial point interpolation method. J. Sound Vib. **441**, 63–83 (2019). https://doi.org/10.1016/j.jsv.2018.10.011
23. Chen, Y., Zhang, J., Zhang, H.: Free vibration analysis of rotating tapered Timoshenko beams via variational iteration method. J. Vib. Control. **23**, 220–234 (2017). https://doi.org/10.1177/1077546315576431
24. Mokhtar, M.A., Kamalakar Darpe, A., Gupta, K.: Investigations on bending-torsional vibrations of rotor during rotor-stator rub using Lagrange multiplier method. J. Sound Vib. **401**, 94–113 (2017). https://doi.org/10.1016/j.jsv.2017.03.026
25. Tang, N., Zhang, B., Lord, C., Marshall, M.: Identification of blade operational mode shapes during wear of abradable coating. J. Sound Vib. **472**, 115204 (2020). https://doi.org/10.1016/j.jsv.2020.115204
26. Structural vibrations and acoustic radiation of blade–shafting–shell coupled system. J. Sound Vib. **463**, 114961 (2019). https://doi.org/10.1016/j.jsv.2019.114961
27. Zeng, J., Ma, H., Yu, K., Xu, Z., Wen, B.: Coupled flapwise-chordwise-axial-torsional dynamic responses of rotating pre-twisted and inclined cantilever beams subject to the base excitation. Appl. Math. Mech. Engl. Ed. **40**, 1053–1082 (2019). https://doi.org/10.1007/s10483-019-2506-6
28. Warminski, J., Kloda, L., Lenci, S.: Nonlinear vibrations of an extensional beam with tip mass in slewing motion. Meccanica. **55**, 2311–2335 (2020). https://doi.org/10.1007/s11012-020-01236-9
29. Rafiee, M., Nitzsche, F., Labrosse, M.: Dynamics, vibration and control of rotating composite beams and blades: a critical review. Thin-Walled Struct. **119**, 795–819 (2017). https://doi.org/10.1016/j.tws.2017.06.018
30. Wang, Q., Quek, S.T.: Flexural vibration analysis of sandwich beam coupled with piezoelectric actuator. Smart Mater. Struct. **9**, 103–109 (2000). https://doi.org/10.1088/0964-1726/9/1/311
31. Investigation on semi-analytical solution of dynamic characteristics of an anti-pitching generating WEC (AG-WEC) | SpringerLink, (n.d.). https://link.springer.com/article/10.1007/s00773-020-00705-w. Accessed 26 November 2020
32. Huang, Y., Deng, Z., Xiong, Y.: High-order model and slide mode control for rotating flexible smart structure. Mech. Mach. Theory. **43**, 1038–1054 (2008). https://doi.org/10.1016/j.mechmachtheory.2007.07.005
33. Lin, S.-M.: PD control of a rotating smart beam with an elastic root. J. Sound Vib. **312**, 109–124 (2008). https://doi.org/10.1016/j.jsv.2007.10.027
34. Active vibration control of composite plate with optimal placement of piezoelectric patches: Mechanics of Advanced Materials and Structures, Vol 26, No 4, (n.d.). https://www.tandfonline.com/doi/full/10.1080/15376494.2017.1387324. Accessed 21 March 2021
35. Larbi, W., Deü, J.-F.: Reduced order finite element formulations for vibration reduction using piezoelectric shunt damping. Appl. Acoust. **147**, 111–120 (2019). https://doi.org/10.1016/j.apacoust.2018.04.016
36. Ma, G., Xu, M., Zhang, S., Zhang, Y., Liu, X.: Active vibration control of an axially moving cantilever structure using PZT actuator. J. Aerosp. Eng. **31**, 04018049 (2018). https://doi.org/10.1061/(ASCE)AS.1943-5525.0000853
37. Sharma, S., Kumar, A., Kumar, R., Talha, M., Vaish, R.: Active vibration control of smart structure using poling tuned piezoelectric material. J. Intell. Mater. Syst. Struct. **31**, 1298–1313 (2020). https://doi.org/10.1177/1045389X20917456
38. Cui, M., Tang, W., Han, Y., Li, Z.: Smart active vibration control system using piezoelectric materials. In: 2020 Chinese Control And Decision Conference (CCDC), pp. 2611–2615 (2020). https://doi.org/10.1109/CCDC49329.2020.9164082
39. Adaptive active vibration control for piezoelectric smart structure with online hysteresis identification and compensation - Yuxue Pu, Cheng Yao, Xiaobao Li, Zhaotao Liu, 2020, (n.d.). https://journals.sagepub.com/doi/abs/10.1177/1077546320980574. Accessed 21 March 2021
40. Brahem, M., Chouchane, M., Amamou, A.: Active vibration control of a rotor bearing system using flexible piezoelectric patch actuators. J. Intell.Mater. Syst. Struct. (2020). https://doi.org/10.1177/1045389X20916804
41. Shakir, A.B., Saber, A.M.: Active vibration control analysis in smart composite structures using ANSYS. Revista Internacional de Métodos Numéricos Para Cálculo y Diseño En Ingeniería. **36** (2020). https://doi.org/10.23967/j.rimni.2020.04.001
42. Sliding mode predictive vibration control of a piezoelectric flexible plate - Zhi-cheng Qiu, Tao-xian Wang, Xian-min Zhang, 2021, (n.d.). https://journals.sagepub.com/doi/10.1177/1045389X20948597. Accessed 21 March 2021
43. Smart vibration control of structures with unknown structural parameters using integrated virtual synchronization method/linear-quadratic regulator approach - Ghaderi - 2020 - Advanced Control for Applications - Wiley Online Library, (n.d.). https://onlinelibrary.wiley.com/doi/full/10.1002/adc2.48. Accessed 21 March 2021
44. Hodel, S.: Linear-quadratic control: an introduction [book review]. IEEE Trans. Autom. Control. **43**, 1191–1192 (1998). https://doi.org/10.1109/TAC.1998.705000

Chapter 2
You Put *How Many* Tuned Mass Dampers in ONE Building?

Michael J. Wesolowsky, Melissa Wong, Hannah H. Kim, and Rabih Alkhatib

Abstract Tuned mass dampers (TMDs) are devices that oppose the motion of a floor which has been excited by occupant footfalls. They have been demonstrated to be effective when considered during the design process or in mitigation situations. If designed and implemented properly, they achieve three goals: (1) maintain structural motion levels below commonly accepted criteria, (2) optimize the size and configuration of the structural system in order to provide more useable space in a building, and (3) reduce the cost of construction due to fewer and/or smaller structural elements. Traditionally, TMDs have only been used to control perceptible and excessive motions from wind loading and crowd movement. As such, they have not been used in laboratory and other sensitive spaces due to equipment criteria which specify vibration levels far below perceptibility.

This paper presents the case study of a 45,000 sm steel-framed structure originally designed as a core and shell office building with 3 levels of below-grade parking, 12 above-grade levels of tenant space, and 2 mechanical penthouse levels. As construction was beginning, a single pharmaceutical firm chose to lease the entire building and required that more than half of the floor plate of each floor meet the strict VC-A criterion (with some areas requiring VC-C). As the building had been designed for typical office occupancy vibration criterion, major last-minute modifications would be required to stiffen the structure to meet the new criterion. Several options were explored, with the final solution incorporating a combination of stiffening of primary structural members, tying floor masses together using interstitial posts, and installing 166 tuned mass dampers (TMDs) within the depth of the floor framing to counteract floor footfall vibrations. Dynamic characterization tests were completed on every area of each floor during construction in order to tune the TMDs in situ as construction was progressing. Final testing conducted once the structure was complete and the TMDs were tuned indicated that the VC-A criterion was achieved in all relevant areas.

Keywords Tuned mass dampers · Footfall vibration · Vibration measurements · Sensitive floors · Vibration serviceability

2.1 Introduction

This paper presents the case study of a project where a newly designed office building was unexpectedly going to be fully occupied by a pharmaceutical firm, which intended to use a major portion of each of the 12 floors as a laboratory space, with the remainder of each being office occupancy. Given that laboratory equipment is often sensitive to vibrations, there was concern that the structure would not satisfy the laboratory vibration requirements due to footfall-induced vibration. We studied and implemented a number of vibration control solutions including beam stiffening, additional posts, and 166 tuned mass dampers (TMDs) to ensure that the final structure would be acceptable for laboratory spaces. These TMDs were installed on levels 2 through 12 of the building. This paper summarizes each of these measures and then demonstrates that the TMDs have been ultimately able to control footfall-induced vibration levels to the intended performance level. It is the authors' understanding that this is the largest such TMD installation in the world to this point.

M. J. Wesolowsky (✉) · M. Wong · H. H. Kim · R. Alkhatib
Thornton Tomasetti, Mississauga, ON, Canada
e-mail: mwesolowsky@thorntontomasetti.com

H. Y. Noh (eds.), *Dynamics of Civil Structures, Volume 2*, Conference Proceedings of the Society for Experimental Mechanics Series, https://doi.org/10.1007/978-3-031-05449-5_2

2.2 Performance Target

Target vibration limits have been established based on the vibration criterion (VC) curves. These curves are intended to provide frequency-dependent sensitivities for wide classes of equipment and are used extensively in lab design for healthcare and research facilities. The VC curves have become internationally accepted as a basis for designing and evaluating the performance of structural systems that support vibration-sensitive equipment and general human occupancies.

The performance target was to meet VC-A in all lab spaces with a possibility of meeting VC-C wherever possible. Note that VC-A is equivalent to 50 μm/s for frequencies between 8 and 80 Hz and rises for frequencies below 8 Hz. VC-C is equivalent to 12.5 μm/s for frequencies between 1 and 80 Hz.

2.3 Vibration Control Solutions

2.3.1 Predictive Modeling

To predict the vibration performance of the structure, finite element method (FEM) models were developed in SAP2000. The structural parameters from the FEM models, including modal frequencies, modal masses, and displacements, were input into our proprietary footfall prediction software. Typical walking speeds ranging from 75 to 126 steps per minute as per the American Institute of Steel Construction's Design Guide 11 (AISC DG11) [1] were used to conduct the analyses. In addition, the analyses assume a typical walker weight of 168 pounds as per AISC DG11. "Heat maps" showing predictive vibration levels throughout the floor were produced to identify which areas were predicted to meet the laboratory vibration criteria. A typical output of such predictive modeling is seen in Fig. 2.1.

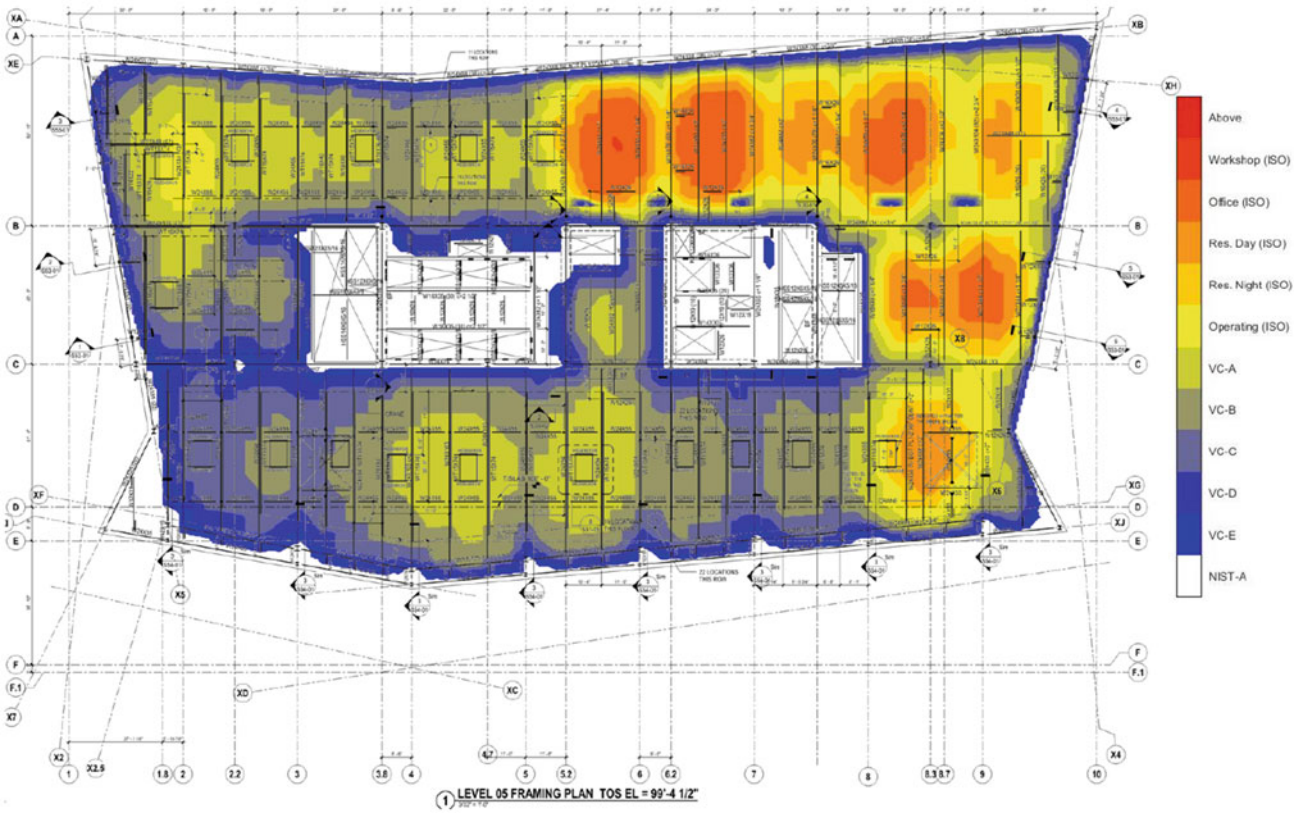

Fig. 2.1 Typical "heat map" of the predicted vibration on a floor

As the original structure was intended for office spaces only, the vibration analyses predicted that the original structure would not be adequate in meeting the laboratory vibration criteria. As such, a number of different vibration control strategies were assessed, including:

- Beam stiffening
- Adding of interstitial posts
- Tuned mass dampers

Through an iterative design process involving different combinations of the vibration control strategies, numerous footfall vibration analyses, and the development of many heat maps, the final combination of vibration control strategies was selected.

2.3.2 Structural Modifications

The following structural elements were added in the base building framing of the lab areas to stiffen the floor:

- WT15 $\times$ 54 sections to the bottom of base building beams
- Interstitial (non-load-bearing) HSS3 $\times$ 3 $\times$ 3/16 posts tying groups of three (3) or four (4) floors together:
  - Structural framing plan levels 2 through 5
  - Structural framing plan levels 6 through 9
  - Structural framing plan levels 10 through 12
- W24 $\times$ 55 infill beams running perpendicular between the base building beams that both stiffen the floor and in some areas connected to the posts that are located between beams

2.3.3 Tuned Mass Dampers (TMDs)

A TMD is a large mass which is connected to the structure using springs, designed to achieve a resonant frequency near to that of the floor, and is generally located on the floor as close as possible to where the expected motion is at its maximum. The result is that the TMD mass resonates with the floor, transferring the vibrational energy from the floor to the TMD. The energy is then dissipated through the use of damping elements similar to shock absorbers on a car. When properly designed, the end result is TMDs which move five to ten times as much as the floor and a floor which moves at a relatively lower level. The typical impact of installing TMDs is a reduction in floor vibrations from walking activity.

It is important to note that sustained walking activity is required in order to fully engage the TMDs and that there may be a slight delay for the damping from the TMD to engage under impulsive excitation. In other words, the TMDs are expected to provide significant damping under steady-state conditions, but there may be briefly higher vibration levels upon initial excitation.

A total of 166 TMDs were designed to be installed in this building. The initial design of the TMD parameters was based on the FEM models that were developed. However, given that theoretical FEM models will always differ from the actual construction, site testing was required to ensure that the TMDs will function as intended.

2.4 Tuned Mass Damper Design and Testing

2.4.1 Initial Site Testing

As the TMDs ranged from 2000 to 4000 kg, the TMD frames and mass plates were installed concurrently with the building's steel framing. The damping and spring components were not installed at that time as the building's natural frequencies had not yet been confirmed. Once the slabs for each set of post-connected floors (e.g., levels 2 through 5) were cured, we conducted vibration testing to determine the required damping and spring components for the TMDs.

All testing was conducted after construction had ended for the day to ensure that there would not be any data contamination due to construction activities.

2.4.2 Testing Methodology

To determine the natural frequency to which the TMDs would need to be tuned, the natural frequency of the structural bays on each floor needed to be determined. The natural frequency was determined through the use of a modal shaker. The modal shaker was placed at the center of the structural bay where the most motion was anticipated. Accelerometers were placed on the modal shaker as well as at various locations in the structural bay. Through a series of frequency sweeps, the frequency of vibrations which induced the most motion of the floor was identified. Once the natural frequency of the floor bay was identified, a free decay test was conducted to identify the existing damping of the structure. This free decay test was conducted by shaking the floor at its identified natural frequency and then stopping the shaker. This methodology was repeated for every structural bay where lab space was anticipated to be located.

2.4.3 Testing Equipment

The following equipment was used to conduct the initial vibration testing:

- LMS SCADAS Mobile or CoCo-80 data acquisition system
- PCB 393B04 or 393A03 1 V/g accelerometers
- PCB 394C06 accelerometer calibrator
- APS 400 modal shaker
- APS 144 amplifier
- BK Precision 4070A 21.5 MHz multifunction arbitrary waveform generator

2.4.4 Testing Results

The purpose of the initial vibration testing was to identify the natural frequency to which each TMD needed to be tuned. Based on the determined natural frequency of each structural bay, the spring components were able to be selected. Note that given the time sensitivity of the project, and the long lead time for spring delivery from the fabricator, a conservative selection of springs was ordered prior to the start of construction. From this initial selection of springs, the final required springs were determined.

2.4.5 Shop Testing

Shop testing of the final spring configurations was required to be conducted prior to their installation onsite due to the expected variance in the spring stiffness parameters. This testing was conducted at the TMD manufacturer (Fig. 2.2). To efficiently test all springs, two TMD test frames were manufactured and stationed at the fabricator's shop. These mass plates in the test frames were repeatedly modified to match those of the number of mass plates already installed onsite. The selected springs were installed in each test frame to verify that the overall TMD achieved the required natural frequency. Adjustments to the tuning bars and mass plates were also made to achieve the correct natural frequencies.

2.4.6 Testing Methodology

To ensure that the TMDs had the correct natural frequency, each test frame was initially set up with the selected spring combinations as well as the predicted required number of mass plates. A modal hammer was then used to strike the center of each TMD test frame. Accelerometers were attached to the TMD to measure the TMD's motion due to the hammer strike. From there, the natural frequency of the TMD was able to be determined. If the measured natural frequency of the TMD was in close proximity to the required frequency, only adjustments of the tuning bars on the sides of the TMD were required. The tuning bars were rotated, and the TMD would be struck again to identify the proper tuning bar rotation required to meet

Fig. 2.2 TMD test frame for shop testing

the correct natural frequency. However, if the difference in the measured natural frequency from the required frequency was too large, adjustments to the mass plates were then conducted. Mass plates were either added or removed depending on the frequency difference. This methodology was repeated for every TMD until all required springs had been tested.

Onsite, the TMD frames and mass plates were originally installed based on conservative assumptions to ensure that should the tested structure differ significantly from the FEM models, the original spring selections would still be able to be tuned to the accurate frequencies. As such, a large number of mass plates were required to be moved from one TMD to another across all floors to match that of the required mass plates as per the shop testing findings.

2.5 Commissioning Testing

2.5.1 Testing Methodology

After the spring and damping component installations for each TMD on each floor were completed, we conducted commissioning testing of a representative sample of the TMDs. The testing methodology for each commissioning location included:

1. Heel drops
2. Slow in-room walking scenarios
3. Fast corridor walking scenarios

Table 2.1 Vibration results summary

Vibration criteria	% of locations meeting vibration criteria
VC-A	100%
VC-B	53%
VC-C	5%

The heel drops were conducted to verify the natural frequency of each slab. Based on the natural frequency of the slab, the walking scenario speeds were determined to induce the worst-case response. For example, if the heel drop showed an 8 Hz natural frequency, then a walker would walk at 2 Hz or 120 steps/minute to induce the worst-case response. This represents the fourth sub-harmonic of the natural frequency (e.g., 8 Hz $\div$ 4 = 2 Hz).

For walking scenarios simulating in-room walking, slower walking speeds ranging between 75 and 111 steps/minute were conducted as typically occupants will not walk as fast due to furniture and other obstacles.

For walking scenarios simulating corridor walking, where there are expected to be fewer obstacles, faster walking speeds between 111 and 126 steps/minute were conducted.

2.5.2 Equipment

To conduct the vibration measurements, the following equipment was used:

- LMS SCADAS Mobile or CoCo-80 data acquisition system
- PCB 393B04 or 393A03 1 V/g accelerometers
- PCB 394C06 accelerometer calibrator

2.5.3 Measurement Results

Over 200 walking tests were conducted and compiled. The percentages of measurement locations meeting the different VC levels under consideration are shown in Table 2.1. As can be seen from the results in Table 2.1, all measurement locations were found to meet VC-A or better during all walking scenarios.

Note that the percentages shown in Table 2.1 are only based on the measurement locations which were selected based on the locations that are expected to have the most floor motion. Other areas which were not measured, such as those located closer to columns or column lines, are expected to have less floor motion and a better vibration performance than those that were measured. For example, it is not uncommon for bays which measured VC-A in the center of the bay to measure VC-C near the columns.

2.6 Conclusions

A combination of vibration control strategies was employed to ensure that the structure under consideration would satisfy the laboratory vibration requirements for a new pharmaceutical facility subjected to footfall-induced vibrations. Based on the results during the commissioning testing to verify the performance of the installed TMDs, all measured locations were found to at least meet the performance target of VC-A when subjected to walking scenarios described.

Reference

1. American Institute of Steel Construction: Steel Design Guide 11: Vibrations of Steel-Framed Structural Systems Due to Human Activity, 2nd edn. USA (May 2016)

Chapter 3
Temperature Variation Modelling of an Assembled Three-Storey Structure

Matthew S. Bonney and David Wagg

Abstract In the utilisation of a digital twin, one of the most critical aspects is the pairing between the physical and digital systems (or twins). This involves the accurate modelling of the physical twin under realistic loading conditions. A lesser considered loading condition is the environmental conditions on the system, particularly the environmental temperature. This effect of temperature variation is of particular importance when there is a material mismatch, such as reinforced concrete or various metals joined together. This work investigates and compares selected methods for modelling these temperature effects for both high- and low-fidelity finite element models and is validated against experimental tests that were performed in an environmental chamber at the Laboratory for Verification and Validation at the University of Sheffield.

Keywords Digital twin · Joint modelling · Model updating

3.1 Introduction

Throughout the life cycle of a system, it will typically experience a wide variety of environmental conditions and excitations. These environmental conditions introduce various thermal strains and cycling that can greatly affect the sensitive nature of the mechanical joint. The ability to monitor and predict these effects is particularly important for digital twins that have a life-long accuracy requirement [1–5]. One of the issues with this requirement is the difficulties associated with modelling the non-rigid connection between materials. This difficulty is exacerbated when there are mismatched materials used.

There has been a large amount of recent research performed by the TriboMechaDynamics (TMD) community in defining accurate models of the nonlinear dynamics associated with the friction used in the mechanical joint [6–9]. This topic is difficult to model in even ideal conditions, and very little research has been focused on addressing the thermal properties of the mechanical joints. However, as a preliminary study, this work approaches the thermal properties from a pragmatic perspective of using simple methods to incorporate the thermal strain introduced by the temperature variations and material mismatched.

This work is comprised of several components. Section 3.2 describes the tested scaled three-storey structure, the test bed and the Digital Twin Operational Platform (DTOP) used to facilitate in the testing, analysis and post-processing of both the experimental and numerical data. The results from the experimental testing and its post-processing are described in Sect. 3.3. To test various modelling techniques, two fidelities of models are compared with a simplified beam model, as described in Sect. 3.5, and a high-fidelity model is described in Sect. 3.6. A discussion of the various techniques and conclusions are presented in Sect. 3.7.

3.2 Three-Storey Structure and the Digital Twin Operational Platform

One of the major components of this research is the thermal properties of the system of interest. For this work, the system is a scaled three-storey structure that is pictured in Fig. 3.1. This system is comprised of extruded T-slot aluminium that constructs the main floors with rolled steel structural supports at the corners of the system with a total height of nearly 2.5 metres tall.

M. S. Bonney (✉) · D. Wagg
Dynamics Research Group, Department of Mechanical Engineering, University of Sheffield, Sheffield, UK
e-mail: m.bonney@sheffield.ac.uk; david.wagg@sheffield.ac.uk

H. Y. Noh (eds.), *Dynamics of Civil Structures, Volume 2*, Conference Proceedings of the Society for Experimental Mechanics Series, https://doi.org/10.1007/978-3-031-05449-5_3

Fig. 3.1 Experimental system of interest

This system is mounted to a ground-based excitation table housed within an environmental chamber at The Structural Dynamics Laboratory for Verification and Validation (LVV) in the University of Sheffield. It is because of this facility's ability to perform vibrational excitations with varied environmental conditions that this work is possible. For the tests performed in this work, the environment of northern Japan was taken for the range of environmental conditions. This location was chosen because Japan is known to have earthquakes at any time of the year with a wide range of environmental conditions. Japan experiences very hot summers with high humidity and cold winters with snow build-up on the buildings. In order to mimic these conditions, the environment was varied between −15 and 35 °C, and a swept sine is performed exciting the range enclosed by the first three bending frequencies in a single direction (3–30 Hz).

To unify the data from the experimental sensors, metadata related to the testing and the finite element simulations, a Digital Twin Operational Platform (DTOP) was created and used to facilitate this research. While there is a discussion to be had about what constitutes a digital twin, this work mainly focuses on the user interface used in the DTOP for data management and simulation scheduling. This DTOP is unique due to the open-source nature and browser-based interface that utilises Python Flask. An earlier version of this DTOP is demonstrated in [10] focusing on the connection between the experimental system and the digital twin. This work expands on the work shown in [10] by utilising finite element analysis (FEA) and scheduling. The DTOP was used to navigate selected components through links via a browser. The main page of this DTOP is shown in Fig. 3.2. This page consists of links to the specific components of the digital twin (FEA simulations, post-processing the experimental data and post-processing the FEA simulations for example) and a visualisation of the system with manufacturer provided drawings.

The DTOP for this system is able to provide a centralised location that contains experimental data, run novel numerical simulations and analyse the data produced from the numerical simulations. This is one of the main advantages of using the DTOP for this type of research. In order to perform these simulations purely locally, one main issue is the data recorded from the experiments and the size requirements/transfer speeds. Within the DTOP, post-processing requests query the PostgreSQL database that houses the data and keeps the information stored in fast memory. Otherwise, the data would have to be transferred from the database to the local hard drive and then loaded into the simulations. For the experiments performed, the

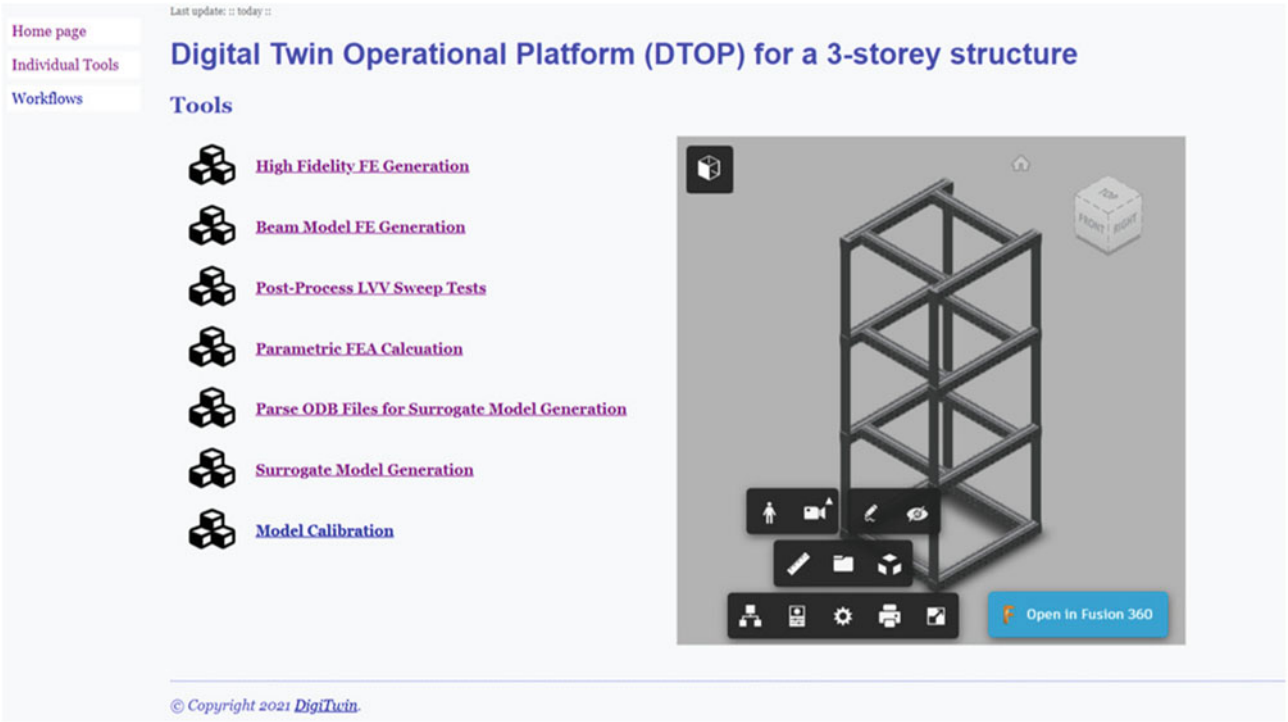

Fig. 3.2 Loading page of DTOP

raw data resulted in about 10 GB worth of data. Performing the simulation locally would require twice the transfer, which will result in the transfer of 20 GB worth of data.

3.3 Experimental Results

The Structural Dynamics Laboratory for Verification and Validation in the University of Sheffield provides advanced capabilities to perform vibration shake table excitation testing within a controlled environment. This in particular is able to test larger systems, compared to traditional academic size systems, to evaluate industrially relevant systems. Because of these capabilities, this large, almost 3 metre tall, system is able to experience vibrational loading at a large variety of temperatures.

For these particular tests, an earthquake-rich environment with a wide range of temperatures is evaluated. Specifically, the area around northern Japan is taken as the inspiration for the environmental conditions. To quantify this, the three-storey structure is subjected to temperatures ranging from $-15\,^{\circ}$ to $35\,^{\circ}$C and vibrations that categorise the first three bending frequencies of the system, from 3 to 30 Hz in a swept sine with a linear increase of 0.1 Hz/sec.

For illustrative purposes, the auto power spectral density (PSD) of the experimental results is shown in Fig. 3.3 for the fundamental frequency near 5.5 Hz. While only the fundamental frequency is shown, the trends are identical for the other bending frequencies tested. There is one major trend found in the experimental results; this trend is that when the environmental temperature increases, the damped natural frequency decreases. This decrease is comprised of both a decrease in the stiffness of the connected joints and an increase in the associated damping.

This trend in the natural frequency and damping is thought to be caused by one main factor, the thermal mismatch of the steel structural supports and the aluminium floors. The difference in the thermal expansion coefficient introduces a thermal strain in the area of the mechanical joint. While this topic of research is well known in the static or quasi-static domain, particularly for welded joints [11, 12], this area is sparsely/non-existent in dynamic characterisation research.

As a preliminary step in defining this dynamic characteristic for a full system (compared to single-joint test systems), a few methods of modelling these temperature-dependent dynamic characteristics are explored in this work. These methods include the effects due to the different fidelity modelling for these types of structures. This work focuses on two main modelling fidelities, a beam element and a high-fidelity 3D continuum element-based FEA model. Each one introduces

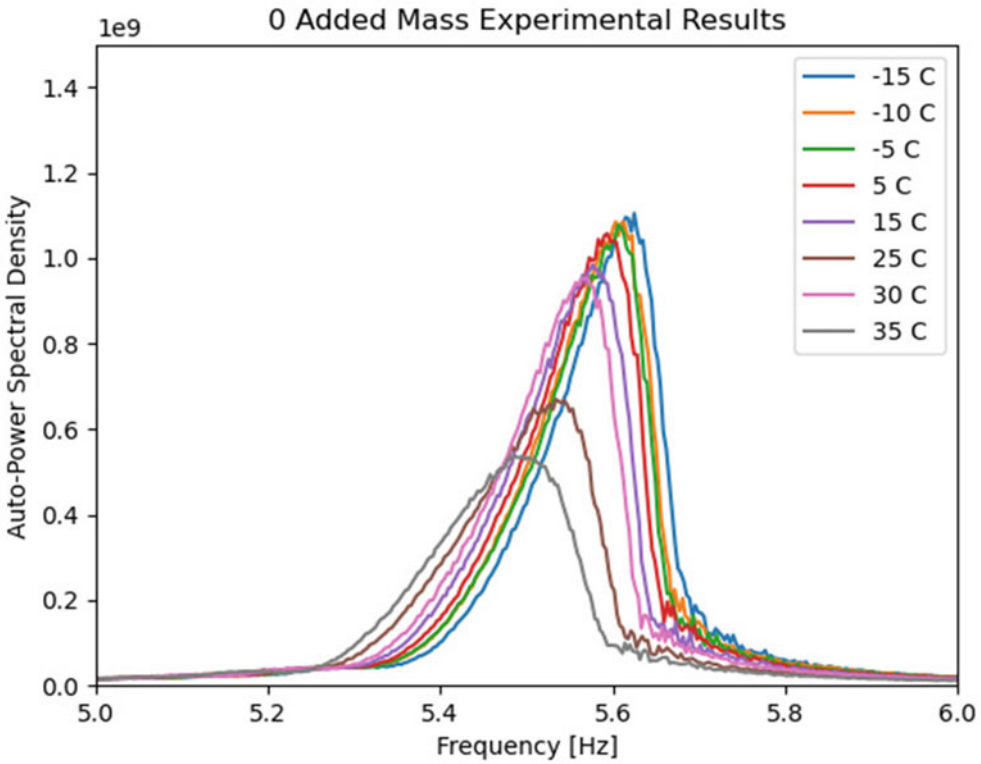

Fig. 3.3 Experimental results for the fundamental frequency

unique difficulties in the modelling procedure. In addition to the modelling fidelities, two general methodologies are used to model the thermal properties of each joint. These methods include using the built-in thermal expansion coefficients used in ABAQUS, and the second is a temperature-dependent stiffness of the joint connection. This calibrated stiffness is reasonable due to the nature of the digital twin correlation. Since a large amount of data is collected during the operation of a physical system, this calibration can utilise these real data to produce an accurate model. While this is not predictive, this can still give insight to a large range of environmental conditions that the physical system experiences. One aspect to note is that this modelling only accounts for the change in stiffness that produces the change in natural frequency. The future work will incorporate the temperature-dependent damping as well, and however, the accurate modelling of damping is also a current area of modern research.

3.4 Model Updating of FEA Models

This system is comprised of two main metals, a stock rolled steel used for the structural supports and 6105-T5 extruded T-slot aluminium. These have nominal properties of $E_{st} = 210$ GPa, $\rho_{st} = 7.89$ g/cm^3 and $\alpha_{st} = 1.17e^{-5}$ C^{-1} for the steel and $E_{al} = 71.3$ GPa, $\rho_{al} = 2.7$ g/cm^3 and $\alpha_{al} = 2.36e^{-5}$ C^{-1} for the aluminium. Since a rigid tie connection is typically used (and is used for the thermal coefficient method), an elastic contact can only produce a less stiff connection, thus lowering the natural frequencies. Because of this property, the nominal models are calibrated to the most stiff testing configuration, the test results for the lowest temperature tested of $-15\,^{\circ}$C.

For the beam model, after doing a sensitivity study, it was found that the material property of the steel is orders of magnitude more significant than the aluminium. In hindsight, this makes sense since the frequencies of interest are the first three global bending modes. These consist of flexure in the steel supports and very slight flexure in the aluminium. Despite this, two attempts at model updated were performed. The first attempt was based on a non-informed decision to modify Young's modulus for both materials. However, this resulted in more than doubling the strength of the aluminium and maintaining nearly nominal strength for the steel. This produced a maximum error of less than 1%. While this produced accurate natural frequencies, the change in the aluminium is deemed to be too excessive and not realistic. Because of this, the

second updating kept the aluminium at its nominal value while varying the steel's Young's modulus. This updating resulted in Young's modulus of the steel to be 210.24 GPa, nearly identical to the nominal value. Despite only varying the steel properties, this updated value produced errors less than 1.25%.

For the high-fidelity model, there appeared to be more dependency on the aluminium properties. Because of this, both materials were calibrated based on the first three bending frequencies. This resulted in the steel's Young's modulus to become 177.27 GPa and the aluminium to be 47.58 GPa. Both of the stiffness decreased compared to the nominal value. This is partially believed to be an inherent feature of the stiffness for the continuum elements compared to the beam elements due to reduced integration and hourglass adjustment.

3.5 Beam FEA Modelling

Once the nominal material properties are defined, then two approaches of temperature modelling were applied to the FEA model. The first approach is the industrialist's methodology; this applies a tie connection between the parts and sets the thermal expansion coefficient to account for the temperature dependency. To accurately account for the variations, the coefficient of thermal expansion was then calibrated to the change in natural frequencies with respect to temperature. To quantify this change, a linear regression is made on the mean values found experimentally. Figure 3.4 shows the experimentally found mean and 95% in blue and the linear regression shown in red. The main quantity used in calibrating the thermal expansion coefficient is the slope found from the regression ($-1.967e-3$ Hz/C for the fundamental frequency).

To calibrate the thermal expansion coefficient, the slope found from the linear regression for the first three frequencies was taken in an ordinary least squares (similar to Young's modulus calibration). This calibration results in the steel coefficient being $6.859e^{-5}C^{-1}$ and the aluminium coefficient of $7.338e^{-5}$ C^{-1}. This resulted in six times the nominal value for the steel and three times for the aluminium. While this multitude of difference is large, the dynamic modelling of thermal strain is difficult to express via a tied interface. This tied connection enforces the displacement but not the strain. Since the material mismatch is expressed via a strain, the connection is not fully adequate to express thermal dynamic characteristic.

Because of this inadequacy for the connection between the materials, the second approach replaces with tied connection with a temperature-dependent elastic connection. For the beam FEA, this reduces down to a temperature-dependent spring between the steel and aluminium. These springs were calibrated to the experimental data collected. This is believed to be reasonable since the system is designed to be a twin, so a large amount of data is collected. In a full deployment, there is a large amount of training data to ensure that the springs are able to account for any of the environmental conditions that the system experiences. In order to calibrate the temperature-dependent spring, the natural frequencies given from the sensors were used in a least-squares sense to determine the stiffness for that given result. The calibration used a gradient decent optimisation within Python, and one example of this for the 35C case is shown in Fig. 3.5.

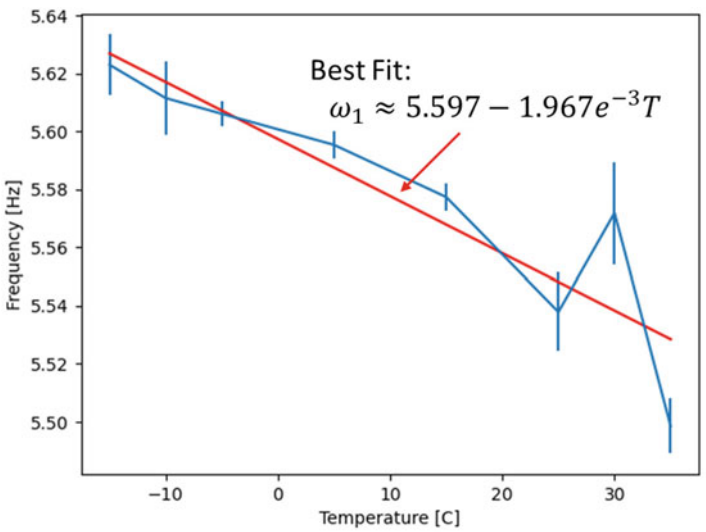

Fig. 3.4 Fundamental frequency temperature variations with linear regression

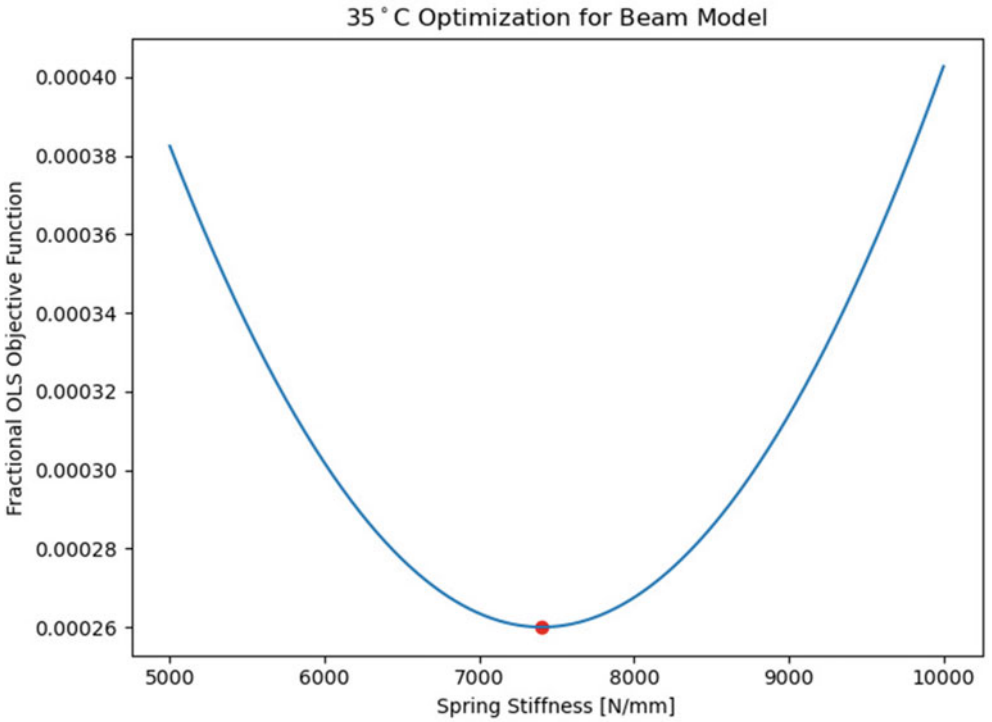

Fig. 3.5 Example spring calibration

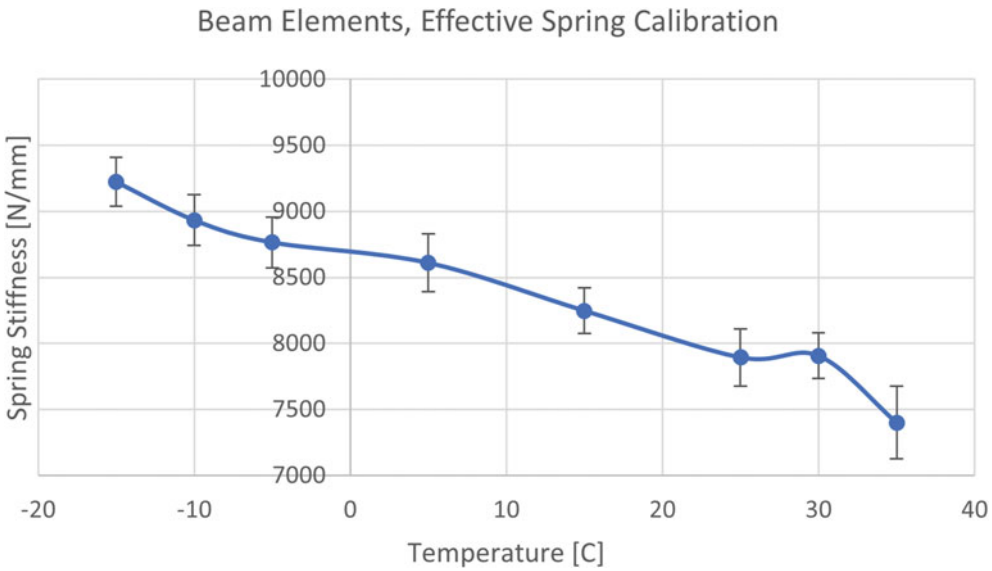

Fig. 3.6 Calibrated temperature-dependent spring stiffness for beam FEA

This procedure for generating an optimal stiffness was applied to all 12 sensors in the excitation direction and the 3 tests per temperature in order to get a mean and standard deviation. The standard deviation can be used as an estimate of the experimental uncertainty that arises from test-to-test variability and sensor location uncertainty. This procedure was applied to each of the temperatures tested and plotted in Fig. 3.6. There are a few aspects to note about the results. The first is that the variability is consistent between tested temperatures. This suggests that the calibration procedure for the beam FEA is a fairly linear process. The second aspect to note is the nearly linear relationship between stiffness and temperature. This suggests that even for temperatures that are not tested, the estimated spring stiffness can produce an accurate estimate with a simple linear fit.

3.6 High-Fidelity FEA Modelling

The high-fidelity FEA was comprised of three types of elements, eight-node bricks (C3D8), six-node triangular prism (C3D6) and four-node tetrahedral (C3D4) elements. For this system, the steel portions were constructed using the tetrahedral elements, while the aluminium was comprised of the eight- and six-node elements. The reason for this is due to the mesh refinement of the contact area. During the initial model updating, it was found that using brick elements for the steel would result in different natural frequencies compared to using tetrahedral elements. This was found to be due to the stress propagation across the joint. To demonstrate this, Fig. 3.7 shows results from identical loadings and mesh seed but different element types. Figure 3.7a shows the case with brick elements, and Fig. 3.7b shows the tetrahedral elements. The tetrahedral elements produced natural frequencies near the experimentally found values. The main aspect to note from Fig. 3.7 is the difference in stress locations, mainly near the centre of the contact patch. In the physical system, there is no contact there since the aluminium has a T-slotted geometry. It was found that refining the brick element mesh by a factor of 4 eliminated this difference but added a large amount of computational time since the system is already large.

After the initial model was created and calibrated, both temperature approaches were applied to the high-fidelity model. First, the coefficient of thermal expansion was modelled. However, this produced some anomalous results. These issues arise in the thermal trends in the natural frequencies. As mentioned in Sect. 3.3, the first three bending modes all decrease in frequency with an increase in environmental temperature. For the high-fidelity model, this trend only occurs for the fundamental frequency and is opposite for the second and third bending modes. Both of these modes increase in natural frequency with an increase in environmental temperature.

There are three possible reasons for this discrepancy, with the first being that the combination of thermal elements and the tied contact make it impossible to model. This would be based on the physics associated with the mass and stiffness matrices for an element. The second possibility is that there is a trade-off between the stiffness and damping for the damped natural frequency found experimentally. It was observed in Sect. 3.3 that there is a noticeable increase in damping that is not taken into account in the modelling. If there is a large increase in the damping and a slight increase in stiffness, then it is still possible for the damped natural frequency to decrease. The third possible reason is due to the tied connection used. This constraint is predominately an enforcement of displacement of the connected nodes on the surfaces. This thermal effect

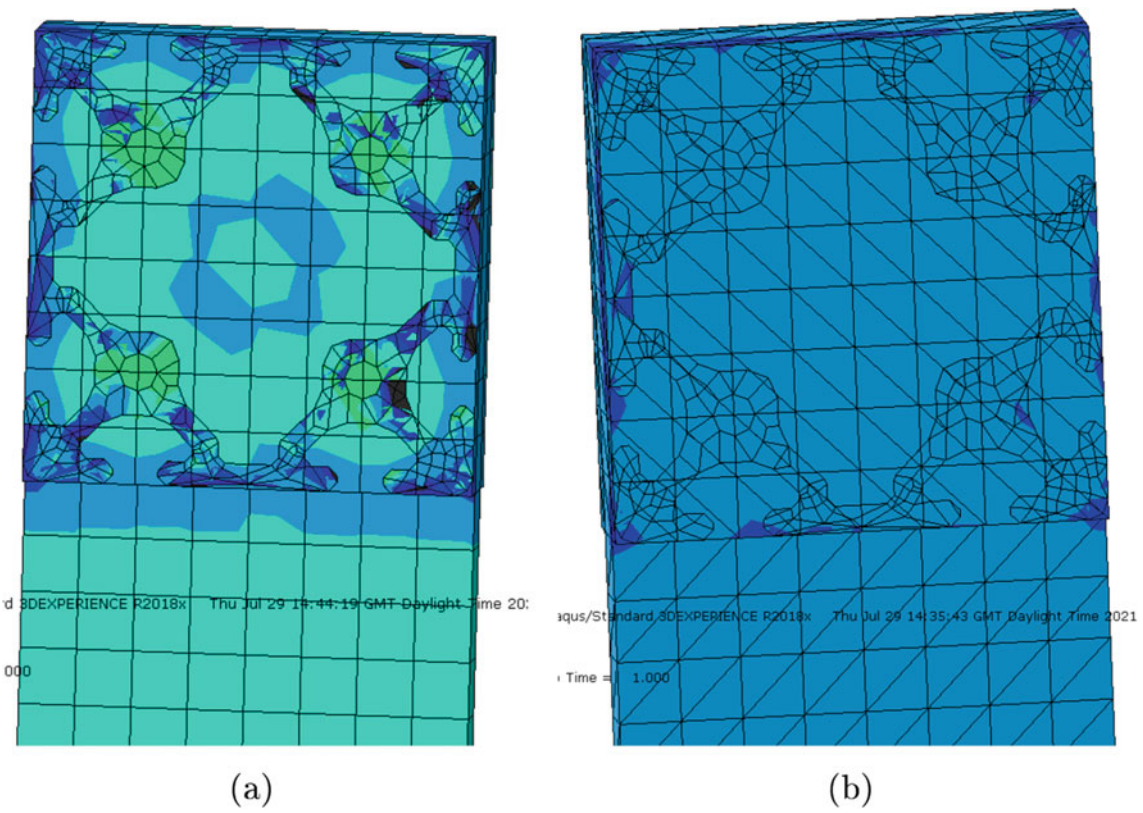

Fig. 3.7 Cross-sectional stress with different steel elements. (**a**) Eight-node brick elements. (**b**) Four-node tetrahedral elements

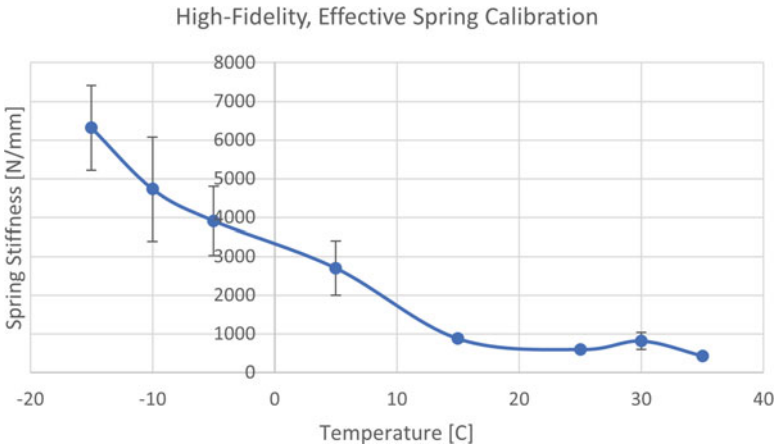

Fig. 3.8 Calibrated temperature-dependent elastic stiffness for high-fidelity FEA

is predominately based on the strain and not the displacement, so this type of connection might not accurately account for these thermal strains. While this third possibility is initially tested by the second thermal approach, the first two are planned future work to get a better understanding of this phenomenon.

The second thermal approach involves replacing this rigid connection with an elastic contact that has a temperature-dependent stiffness. Similarly to the beam model, the stiffness was calibrated for each accelerometer in the excitation direction and repeat tests. The mean and confidence interval found for each test are shown in Fig. 3.8. One aspect to note is that the same experimental data are used, but the temperature trend is very different to the beam model.

There are two main takeaways from this approach. The first takeaway is the trend with increasing temperature. For the beam model, this trend was mostly linear, while the high-fidelity is nearly exponential decay. The cause of this is uncertain but might be related to trends that were seen in the first thermal approach. The second takeaway relates to the variability that was found during the calibration process. For the beam model, the variability is fairly constant, while Fig. 3.8 shows that there is much larger variability for lower temperatures compared to higher temperatures. This is interesting since the same experimental data are used for both models. However, this large variability makes it difficult to identify a representative trend. This can be bilinear, exponential or some other fit depending on the true value within the confidence intervals.

3.7 Conclusions

For digital twin systems, one of the most important aspects is to ensure the accurate pairing between the physical system and the collection of models within the digital twin. This includes the accurate modelling of the environmental loading. The most common loading that is often overlooked is the temperature effect. This work takes experimental data taken at the Laboratory for Verification and Validation and tested various methods to account for the thermal changes on two fidelity of models. The first thermal approach was to use a tied connection between the metals and use the coefficient of thermal expansion, and the second approach replaces the tied connection with an elastic contact with temperature-dependent stiffness.

For the low-fidelity beam model, calibrating the coefficient of thermal expansion resulted in three to six times larger than the nominal value. This is thought of as accounting for the inaccuracy with the rigid connection accounting for the thermal strains. The second approach of using a temperature-dependent spring produced nearly linear correlation between the stiffness and temperature. This also showed nearly constant variability suggesting that the second approach is a near-linear process. For the high-fidelity model, the coefficient of thermal expansion was unable to accurately trend in the same manner as the experimental data. While the experiments showed consistent decrease in natural frequency with an increase in temperature, this model only showed that trend for the fundamental frequency and not for the second and third bending modes. The second approach showed a nearly exponential temperature dependence compared to the linear trend for the beam model. In addition, this approach has a large temperature-dependent variability in the calibration, where lower temperatures have larger variability than the higher temperatures.

This work demonstrates two types of industrialist's approaches to introducing temperature-dependent modelling in a digital twin. To better demonstrate the robustness of both of these approaches, two fidelity of models were used with one being a beam element representation and the second being a high-fidelity continuum element representation of the system.

This work shows that the utilisation of a temperature-dependent elastic contact was able to reproduce the experimental trends in a more robust manner. However, this approach is not predictive since it requires the experimental data to calibrate the temperature-dependent stiffness. The future work could be done in order to characterise this stiffness using contact mechanics to make it predictive.

Acknowledgments The authors would like to acknowledge the support of EPSRC via grant number EP/R006768/1.

References

1. Schwer, L.E.: An overview of the ASME V&C-10 guide for verification and validation in computational solid mechanics. In: 20th International Conference on Structural Mechanics in Reactor Technology (2009), pp. 1–10
2. Wagg, D.J., Worden, K., Barthorpe, R.J., Gardner, P.: Digital twins: State-of-the-art and future directions for modeling and simulation in engineering dynamics applications. ASCE-ASME J. Risk Uncert. Eng. Syst. Part. B Mech. Eng. **6**(3), 030901 (2020)
3. Worden, K., Cross, E.J., Barthorpe, R.J., Wagg, D.J., Gardner, P.: On digital twins, mirrors, and virtualizations: frameworks for model verification and validation. ASCE-ASME J. Risk Uncert Eng. Syst. Part. B Mech. Eng. **6**(3), 030902 (2020)
4. Tuegel, E.J., Ingraffea, A.R., Eason, T.G., Spottswood, S.M.: Reengineering aircraft structural life prediction using a digital twin. Int. J. Aerospace Eng. **2011** (2011). Article ID 154798
5. Grieves, M., Vickers, J.: Digital Twin: Mitigating Unpredictable, Undesirable Emergent Behavior in Complex Systems, pp. 85–113. Springer International Publishing, Cham (2017)
6. Brake, M.R.W.: The Mechanics of Jointed Structures: Recent Research and Open Challenges for Developing Predictive Models for Structural Dynamics. Springer, New York (2017)
7. Brake, M.R.W., Reuss, P., Segalman, D.J., Gaul, L.: Variability and repeatability of jointed structures with frictional interfaces. In: Dynamics of Coupled Structures, vol. 1, pp. 245–252. Springer, New York (2014)
8. Bonney, M.S., Robertson, B.A., Mignolet, M., Schempp, F., Brake, M.R.W.: Experimental determination of frictional interface models. In: Dynamics of Coupled Structures, vol. 4, pp. 473–490. Springer, New York (2016)
9. Lacayo, R., Pesaresi, L., Groß, J., Fochler, D., Armand, J., Salles, L., Schwingshackl, C., Allen, M., Brake, M.R.W.: Nonlinear modeling of structures with bolted joints: a comparison of two approaches based on a time-domain and frequency-domain solver. Mech. Syst. Signal Process. **114**, 413–438 (2019)
10. Bonney, M.S., Gardner, P., Wagg, D., Mills, R.: Case study of connectivity of digital twins and experimental systems. In: Proceedings of the 8th International Conference on Computational Methods in Structural Dynamics and Earthquake Engineering. Streamed from Athens, Greece, June 2021, pp. 1416–1425
11. Tu, S.-T., Yoon, K.-B.: The influence of material mismatch on the evaluation of time-dependent fracture mechanics parameters. Eng. Fract. Mech. **64**(6), 765–780 (1999)
12. Coleman, M.C., Parker, J.D., Walters, D.J.: The behaviour of ferritic weldments in thick section 12cr12mo14v pipe at elevated temperature. Int. J. Press. Vess. Pip. **18**(4), 277–310 (1985)

Chapter 4
Modal Identification of a Railway Bridge Under Train Crossings: A Comparative Study

Semih Gonen, Kultigin Demirlioglu, and Emrah Erduran

Abstract The existing railway bridge infrastructure of Europe is aging rapidly. Yet, rapid increases in technology and consumption bring about higher demands on railway bridges in the form of higher train speeds and axle loads. In order to ensure the safety of railway infrastructure, their dynamic response must be studied in detail and health be monitored. Vibration signatures of railway bridges are commonly used to fulfill these tasks. In particular, ambient or free vibration signals measured on railway bridges are utilized to determine their dynamic characteristics and, subsequently, to update the finite element models. However, the effects of train crossings on the dynamic behavior of bridges have not been investigated thoroughly via experimental testing. This study investigates the modal identification results of a five-span reinforced concrete railway bridge under different vibration sources. Specifically, it focuses on the variations in the dynamic behavior of the bridge observed under train crossings and those obtained from ambient vibrations. The bridge, whose dynamic response is under scrutiny, presents peculiarities in terms of its boundary conditions. They significantly differ from the original design and affect the dominant dynamic response. Fifty train crossing cases are examined, and their results are compared to those obtained using ambient and free vibrations. The results highlight the importance of bridge-train interaction and the influence of the structure's higher vibration modes. The implications of this interaction for model updating and damage detection are also addressed.

Keywords Ambient vibration · Free decay · Dynamic identification · Train loading · Non-destructive testing

4.1 Introduction

Railway bridges play a significant role in the transportation system of European countries. Unfortunately, the existing railway bridge infrastructure is aging rapidly. A significant portion of railway bridges is above or close to the end of their design life. As of 2017, more than 35% of half a million railway bridges in Europe are over 100 years old, with many more on the wrong side of their 50-year design life [1]. Ever-increasing demands for higher speeds, greater axle loads, and extended train sets [2, 3] necessitate a more reliable assessment of the dynamic behavior of railway bridges for their safeguard. Several analytical studies have been conducted to understand the dynamic behavior of bridges [4–8], and the effects of parameters such as train speed, track irregularity, and bridge properties were investigated. Other numerical studies focusing on the frequency characteristics of the train loading [9] also exist. Vibration signatures of railway bridges are commonly used to monitor the health of railway bridges and determine their dynamic properties. Operational modal analysis (OMA) [10–13] is a popular method that is used to identify the vibration characteristics of structures. Generally, in OMA applications, either free vibration or ambient vibration data are used. However, the train loading on railway bridges has a specific frequency spectrum that can significantly impact the bridge's behavior. The effects of train crossings on the dynamic properties of structures have not been investigated thoroughly. More specifically, vibration characteristics identified from train crossing data are scarce.

Recently, acceleration measurements were collected from a railway bridge in Norway to evaluate and understand the effects of the train crossings on the dynamic properties of the bridge. This paper investigates the modal identification results of this five-span reinforced concrete railway bridge under different sources of vibration. It focuses on the vibration modes that are predominantly excited by the train loading and the variability of the dynamic characteristics of the bridge-train system. Fifty train crossing cases that comprise three different types of trains are examined. Dynamic identification results

S. Gonen (✉) · K. Demirlioglu · E. Erduran
Department of Civil Engineering and Energy Technology, Oslo Metropolitan University, Oslo, Norway
e-mail: semihgon@oslomet.no

H. Y. Noh (eds.), *Dynamics of Civil Structures, Volume 2*, Conference Proceedings of the Society for Experimental Mechanics Series, https://doi.org/10.1007/978-3-031-05449-5_4

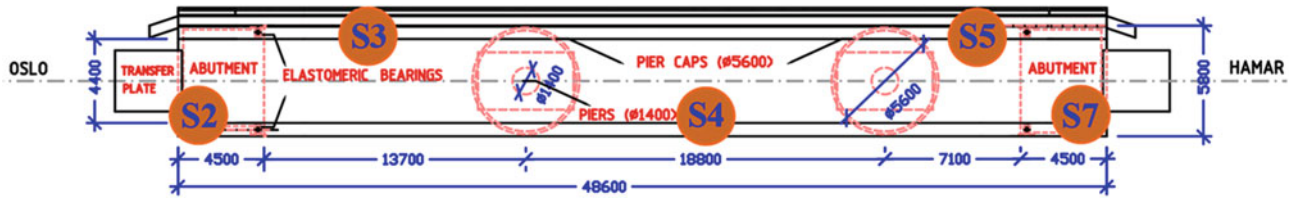

Fig. 4.1 Layout of the Bridge and the sensor setup for OMA (dimensions in mm)

from train crossing data are compared to those obtained using ambient and free vibrations. The results call attention to the importance of bridge-train interaction and the practical aspects of using different data types. Further, the importance of the structure's higher modes of vibration on its dynamic response is highlighted.

4.2 The Railway Bridge

The railway bridge investigated in this study, referred to as "the Bridge" hereafter, is a set of twin bridges that house one track each. It has a unique structural system as the extensions of the bridge from the abutments were designed as cantilevers without any contact between the bridge deck and the abutment. The bridge under scrutiny has five spans and a total length of 48.6 m. Outer spans of the bridge rest on elastic bearings 4.5 m away from the bridge's ends, and two reinforced concrete piers support the mid-spans of the bridge. The piers are located at the 18.2 m and 37.0 m of the bridge. They have a 1.4 m diameter and a pier cap directly connected to the reinforced concrete bridge deck, which is 0.5 m thick. The layout of the Bridge is presented in Fig. 4.1.

4.3 Instrumentation and Measurements

The instrumentation deployed on the bridge consists of a 20-bit low noise low-power data acquisition system and five triaxial MEMS digital accelerometers. The accelerometers were placed at each bridge span, as shown in Fig. 4.1, for a 24-hour period. Data were collected continuously from the five accelerometers during this 24-hour period at a sampling frequency of 250 Hz. During the measurements, both ambient and train-induced vibrations from 50 train crossings were recorded.

Several factors influence the dynamic response of railway bridges. Among those related directly to the loading are the speed and axle load of the train, axle spacing, and stiffness and damping properties of the axles. These affect the dynamic amplification of the bridge response and maximum vertical accelerations of the bridge, thus influencing the bridge's safety and serviceability. However, in this study, there is limited information about the train properties. Among the three types of trains, the express trains are 106 m long and weigh 218 tons. They cross the bridge at higher speeds than the other trains. Passenger trains come in various lengths and weights, ranging from 108 m and 218 tons to 201 m and 411 tons. Similarly, the freight trains' length and weight vary between 359 and 527 m and 549 and 2412 tons. They cross the bridge with the lowest speed. An example of train crossing data for each type of train crossing is presented in Fig. 4.2 by concatenating data obtained from Sensor number 7.

As mentioned earlier, the information about the train properties and speeds is limited. Thus, it is not possible to infer the forcing frequencies of the train loading using the well-known formula of $f = nV/L$, where n is a positive integer, V is the train speed, and L is the distance between the centers of two consecutive carriages.

The distribution of the maximum accelerations recorded at each sensor in the instrumentation setup is depicted in Fig. 4.3. In the figure, each type of train is distinguished by a different marker. While there is no clear trend associated with the train type, freight trains seem to cause higher maximum accelerations at each of the sensors. Figure 4.3 shows that most of the sensors are very well within the limit of 0.35 g set forth by [14]. However, for some train crossings, the maximum recorded maximum accelerations approach the limit of 0.35 g, even exceeding this limit for one case at the ends of the bridge (Sensor 7). This observation suggests that the dynamic behavior of the Bridge is very close to the limits, and a long-term measurement campaign will provide invaluable information that can be further used for approval of the bridge for the current and new train loads.

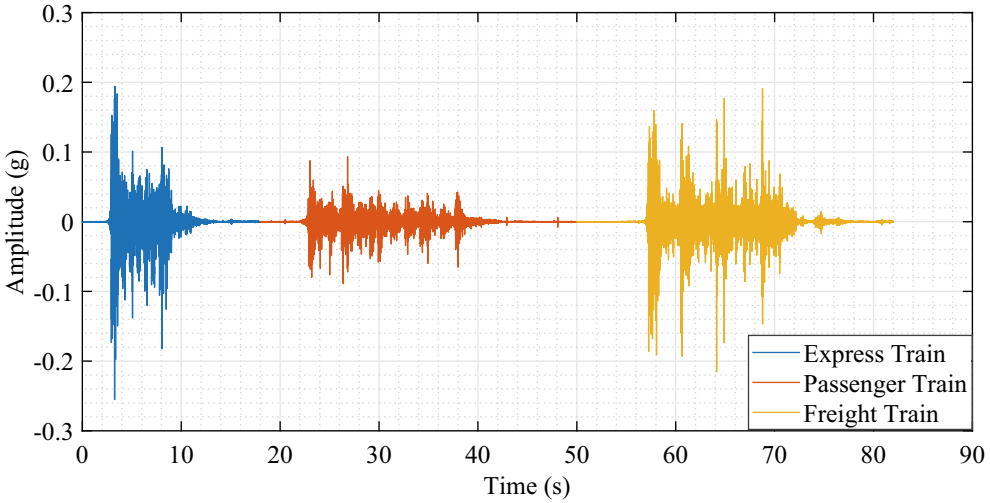

Fig. 4.2 Edited figure showing acceleration data for each type of train crossing (from Sensor 7)

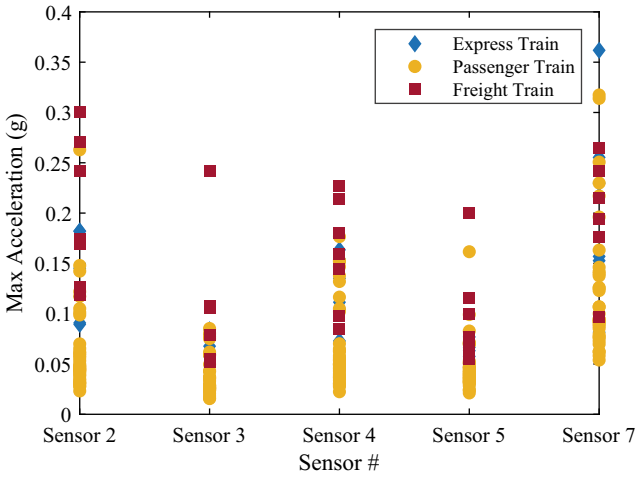

Fig. 4.3 Recorded maximum accelerations (Sensor 4 is on mid-span and Sensors 2 and 7 are on cantilever spans)

4.4 System Identification

4.4.1 Data Processing

The system identification of the Bridge is carried out using vibrations created by three different sources: (1) ambient vibration, (2) free decay after the crossing of the train, and (3) train crossing data in the vertical direction. In this study, we refer to free decay as the vibrations occurring between two distinct points in time: the first of these points in time is the moment the train leaves the bridge and the second point is when the vibrations induced by the train are entirely damped out.

Measured data is processed to obtain series of 60 minutes of ambient vibration data by removing the train crossings and detrending. For the identification from train crossing data, the duration of the time series data used is 60 seconds for all types of trains. The free decay part of the train crossing data is determined manually by visually inspecting the acceleration records, and 30-second-long data is used in all cases even though, for most of the cases, the vibrations are damped out within 5 seconds. It should be noted that an automatic methodology for free vibration detection of railway bridges was proposed recently [15].

In order to process the measured data and find the modal properties of the Bridge, the frequency domain decomposition technique [16] is used. The frequency domain decomposition (FDD) is a non-parametric and output-only modal identification technique that operates in the frequency domain. As the first step in FDD, the power spectral density (PSD) matrix is

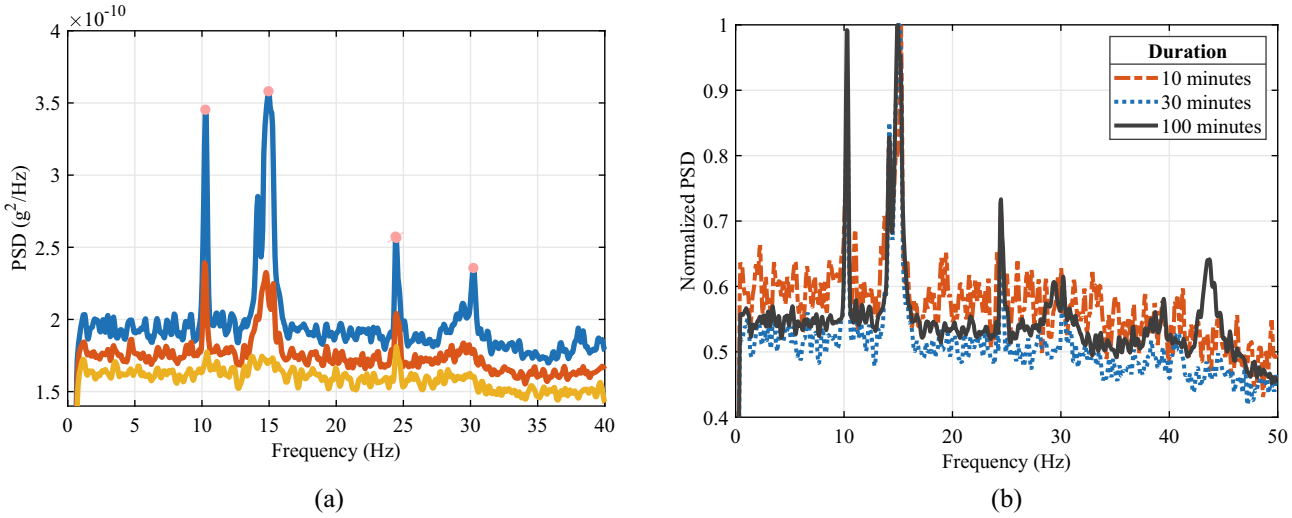

Fig. 4.4 (**a**) PSD of the ambient vibration data and modal frequency peaks. (**b**) Comparison of the PSDs from 10, 30, and 100 minutes of ambient vibration data

estimated. In this study, the Welch method, a Hanning window, and a 50% overlapping are used to estimate the PSD matrix, G_{yy}. The PSD matrix is then decomposed using singular value decomposition (SVD), as in Eq. 4.1.

$$G_{yy}\left(\omega_j\right) = U_j S_j U_j^H \tag{4.1}$$

In the SVD of the PSD matrix, U_j is an orthonormal matrix ($U_j U_j^H = I$) that contains the singular vectors of $G_{yy}(\omega_j)$, and S_j is a diagonal matrix containing the scalar singular values. The decomposition of the spectral matrix into a set of auto-spectral density functions enables obtaining the modal properties of a single degree of freedom system. The system's modal frequencies can be obtained by plotting the first singular values for each frequency and using simple peak-picking, whereas the mode shapes are obtained using the first singular vectors at the corresponding frequency. The damping ratio of the bridge is not investigated in this study.

4.4.2 Results and Discussion

Using ambient vibration and free vibration signals is common for identifying the modal parameters of railway bridges. Therefore, the ambient vibration data is used first to obtain the benchmark dynamic properties of the Bridge. Figure 4.4a shows the auto-spectrum plot where the first three singular values are plotted together and the first four modal frequencies are marked. It should be noted that system identification methods, especially frequency domain methods, are affected by the amount and quality of the data. As there are no guidelines to determine the amount of data to be used, a comparative study in Fig. 4.4b showing the normalized PSDs obtained from 10, 30, and 100 minutes of ambient vibration data highlights the differences in the outcome. Using 10-minute-long ambient vibration data, only the first two vibration modes could be identified. Increasing the length of vibration data to 30 minutes led to the identification of one more vibration mode in addition to the two identified using 10 minutes of data. A total of five vibration modes could be identified using 100 minutes of ambient vibration data. Although not depicted in Fig. 4.4b, 60 minutes of data is also used for modal identification, which enabled us to identify four vibration modes. This discrepancy highlights the effect of the length of the data used in the modal identification using ambient vibration data.

The first four vertical mode shapes obtained from ambient vibration are presented in Fig. 4.5. In the first two mode shapes, the modal displacements are maximum at the middle spans. In contrast, in the third and fourth mode shapes, the maximum modal displacements are observed at the cantilever spans at both ends of the bridge. Recalling that the maximum accelerations are observed at the two ends of the bridge (Fig. 4.3), it can be argued that the dynamic behavior of the bridge is significantly influenced by the third and fourth modes. Here, it should also be noted that neither of these two modes could be

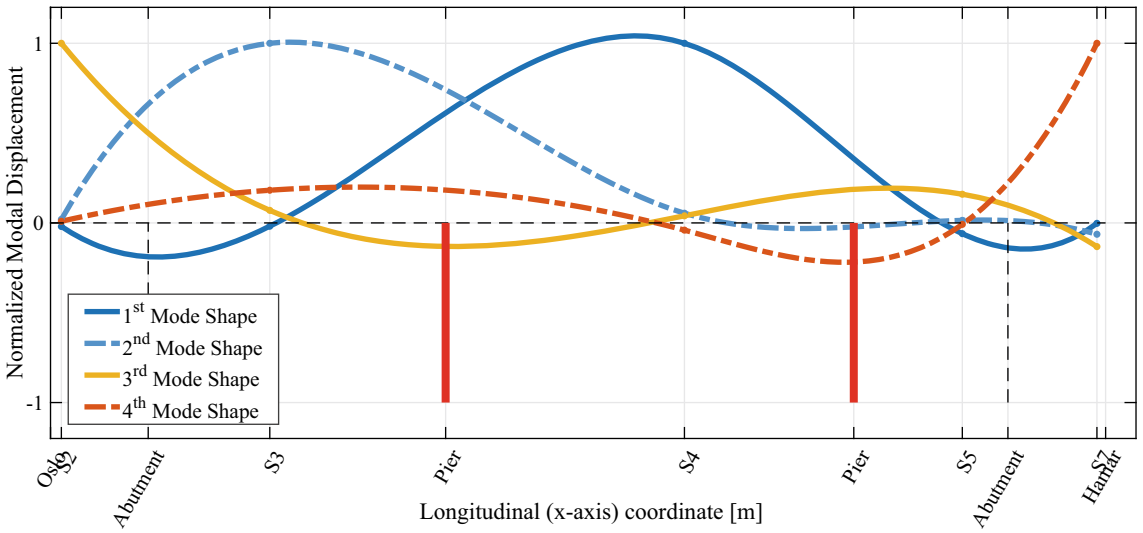

Fig. 4.5 Normalized vertical mode shapes – side view

Table 4.1 Average of the structural frequencies obtained from different data types

	Identified structural frequencies (Hz)			
Data used	f_1	f_2	f_3	f_4
Ambient vibration	10.31	15.05	24.82	30.28
Free vibration	10.23	14.85	25.38	30.48
Train crossing	10.03	14.84	25.11	29.84

Table 4.2 Percentage of the cases in which frequencies identified

	Structural frequencies			
Free vibration	f_1	f_2	f_3	f_4
Identified (%)	93	77	58	51
Not identified (%)	7	23	42	49
Train crossing				
Identified (%)	47	65	65	95
Not identified (%)	53	35	35	5

identified using 10-minute-long ambient vibration data, while only the third mode could be identified when 30-minute-long ambient vibration data was used.

The dynamic identification results from free decay and train crossing data are obtained and compared to those obtained using ambient vibration data. The mean values of the identified vibration frequencies for the first four modes using three different vibration sources are presented in Table 4.1. The mean vibration frequencies obtained using the free decay data are close to those obtained from ambient vibration data. The first two frequencies obtained from free decay data are slightly lower, and the latter two frequencies are slightly higher compared to those obtained from ambient vibration data. The reason for this is the poor frequency resolution in the PSD spectrum due to the limited amount of data, which is only 30 seconds long. Such drawback of using free decay records is also noted in another study [12]. The mode shapes obtained from free decay data are very similar to the ambient vibration data results; therefore, they are not presented for brevity. However, one crucial aspect of using free decay data is the limited information one might get. The amount of energy in the loading excitation differs depending on the train type. Due to the small amount of data, it might not be possible to observe peaks related to the higher modes of the structure. Table 4.2 presents the percentage of the cases in which the specific modal frequencies could be identified. As can be seen, the first two modal frequencies could be identified easily, whereas the third and fourth modal frequencies could not be determined using free decay data in almost half of the 50 cases that are investigated.

When the data from the train crossings is used in modal identification, Table 4.1 shows that the mean values of structural frequencies are slightly lower than their counterparts identified using ambient vibrations or free decay. This stems from the increase in the mass of the system due to additional train mass. What is more interesting is the obtained PSD spectra and the mode shapes. Figure 4.6a presents an example of the PSD spectrum obtained using passenger train crossing data. It shows accumulating energy around the fourth modal frequency (30 Hz) and no clear modal peaks at other frequencies. In

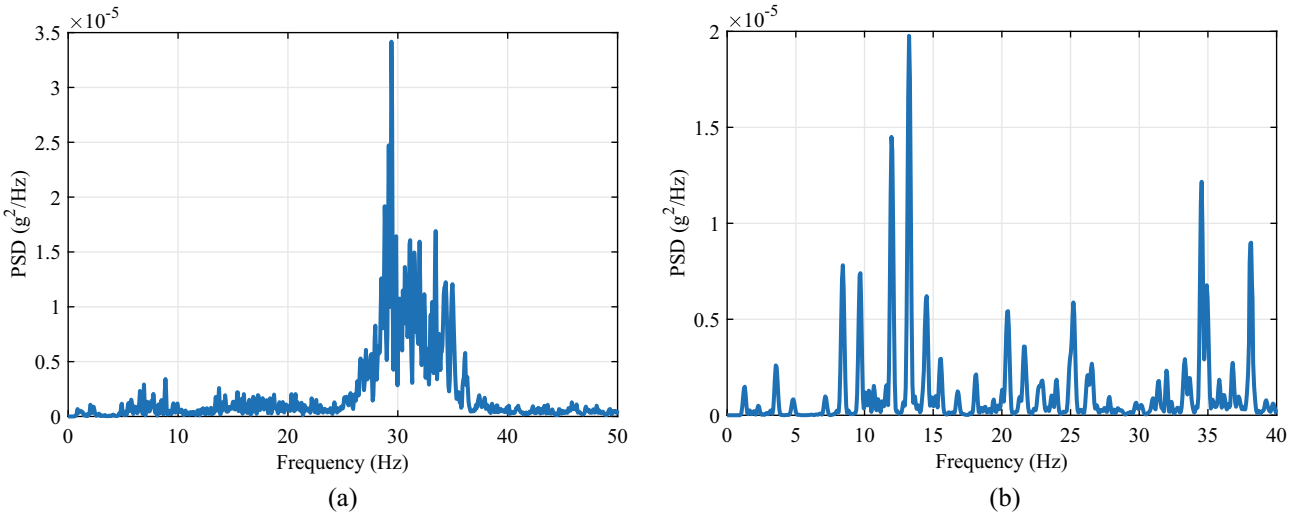

Fig. 4.6 PSD obtained from (**a**) passenger train crossing data and (**b**) express train crossing data

this case, only the fourth mode shape could be identified. Further, in most of the 50 train crossings investigated, the fourth modal frequency is the only one that could be determined; see Table 4.2. In contrast to the free decay, the first and second modes could not be identified for almost half of the cases when train crossing data is used in the modal identification. While Fig. 4.6a is a common type of PSD observed for passenger trains in this study, the PSDs for express and freight trains might significantly differ. For example, in Fig. 4.6b, the loading frequency of the express train dominates the response, and repeating harmonic peaks are visible in the whole frequency range. In some rare cases for freight trains in this study, it is observed that the resonance of the excitation frequencies and the natural frequencies of the bridge enabled obtaining several modal frequencies from a single set of data.

The mode shapes obtained from various train crossings are grouped according to the train type and the direction in which the trains are traveling. Only the passenger trains produced statistically meaningful results; thus, the mode shapes obtained from this group are presented in Fig. 4.7. It is observed that the first mode shape remained unchanged, but all the other mode shapes resemble the fourth mode shape identified from the ambient vibrations. This modal behavior of the bridge-train system combined with the higher maximum accelerations of Sensor 7 in Fig. 4.3 highlights the peculiar dynamic behavior of the ends of the bridge. The fourth mode shape, which has the highest frequency among the structural modes investigated in this study, seems to dominate the dynamic behavior of the bridge. This indicates that the vibrations induced by the trains predominantly excite the fourth mode of the bridge. It should also be noted that this mode, which dominates the behavior of the bridge under train loads, cannot be identified from the ambient vibrations lasting shorter than 60 minutes. Here, it must be acknowledged that the train-bridge system is a coupled time-varying system and the train loads generate non-stationary vibrations [15]. Further, the boundary conditions of the bridge and the loading properties of the trains must be investigated in detail in order to explore and thoroughly understand the dynamic behavior of the bridge. However, the preliminary results presented in this study call attention to the importance of the interaction between the train-induced vibrations and one particular mode that cannot be easily identified using ambient vibrations. The higher modes of vibration are often neglected or given less attention in system identification, model updating, or damage detection studies, and the results presented in this article clearly show that such choices may have severe implications as far as modeling of the behavior of a railway bridge under train loads is concerned.

4.5 Conclusions

Dynamic characteristics and behavior of a railway bridge, whose boundary conditions are rare and peculiar, are investigated in this study. In situ acceleration measurements under several train crossings revealed that the acceleration levels at the end spans of the bridge are high and at the limit provided by the standards. The modal characteristics of the bridge are determined using ambient vibrations first. Then, they are compared to the ones found using free decay and vibrations under

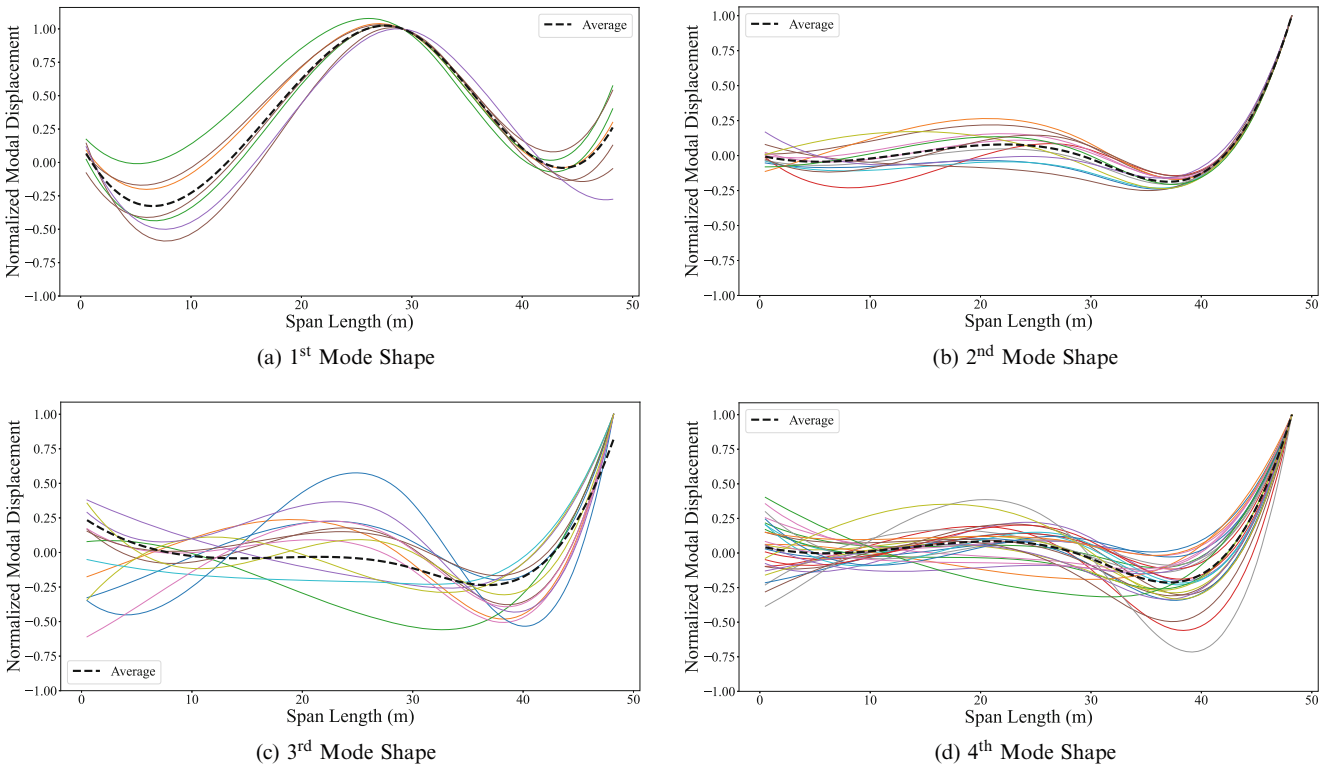

(a) 1st Mode Shape (b) 2nd Mode Shape

(c) 3rd Mode Shape (d) 4th Mode Shape

Fig. 4.7 First four vertical mode shapes obtained from train crossing data. (a) 1st Mode Shape. (b) 2nd Mode Shape. (c) 3rd Mode Shape. (d) 4th Mode Shape

train crossings. Dynamic identification from free decay data matched the ambient vibration results but showed drawbacks such as the poor frequency resolution and inability to detect higher modes in some cases.

A total of 50 train crossings were investigated. All types of trains, the express, passenger, and freight trains, showed different loading characteristics. Thus, the data from train crossings resulted in very broad PSD spectra. In many cases, it was not possible to detect the modal frequencies with high accuracy, except the fourth vibration mode of the structure. The identified modal frequencies were slightly smaller due to the bridge-train interaction. In terms of the mode shapes, only the passenger trains produced statistically meaningful results. The modal identification using the train-induced vibrations clearly showed that the fourth mode dominates the dynamic behavior of the bridge during train crossings. On the other hand, this dominant mode was difficult to identify from free decay and ambient vibration data. Further, in general, higher modes, even though they can be identified using ambient vibration data, are generally not prioritized in applications such as damage detection and finite element model calibration. However, the study presented herein depicts that, due to the train-bridge interaction, the behavior of the railway bridges can be dominated by one of these higher modes and the success of any application, arguably, depends on the successful detection and implementation of this dominant mode.

Acknowledgments This work is supported by the Norwegian Railway Infrastructure Management Directorate (Bane NOR).

References

1. Casas, J.R., Moughty, J.J.: Bridge damage detection based on vibration data: past and new developments. Front. Built Environ. **3**, 1–12 (2017). https://doi.org/10.3389/fbuil.2017.00004
2. Arvidsson, T., Karoumi, R.: Train–bridge interaction – a review and discussion of key model parameters. Int. J. Rail Transp. **2**, 147–186 (2014). https://doi.org/10.1080/23248378.2014.897790
3. Gonzalez, I., Karoumi, R.: Analysis of the annual variations in the dynamic behavior of a ballasted railway bridge using Hilbert transform. Eng. Struct. **60**, 126–132 (2014). https://doi.org/10.1016/j.engstruct.2013.12.026
4. Garinei, A., Risitano, G.: Vibrations of railway bridges for high speed trains under moving loads varying in time. Eng. Struct. **30**, 724–732 (2008). https://doi.org/10.1016/j.engstruct.2007.05.009

5. Zhu, Z., Wang, L., Yu, Z., Gong, W., Bai, Y.: Non-stationary random vibration analysis of railway bridges under moving heavy-haul trains. Int. J. Struct. Stab. Dyn. **18**, 1–21 (2018). https://doi.org/10.1142/S0219455418500359
6. Cheng, Y.S., Au, F.T.K., Cheung, Y.K.: Vibration of railway bridges under a moving train by using bridge-track-vehicle element. Eng. Struct. **23**, 1597–1606 (2001). https://doi.org/10.1016/S0141-0296(01)00058-X
7. Yang, Y.B., Lin, C.L., Yau, J.D., Chang, D.W.: Mechanism of resonance and cancellation for train-induced vibrations on bridges with elastic bearings. J. Sound Vib. **269**, 345–360 (2004). https://doi.org/10.1016/S0022-460X(03)00123-8
8. Ju, S.H., Lin, H.T.: Resonance characteristics of high-speed trains passing simply supported bridges. J. Sound Vib. **267**, 1127–1141 (2003). https://doi.org/10.1016/S0022-460X(02)01463-3
9. Lu, Y., Mao, L., Woodward, P.: Frequency characteristics of railway bridge response to moving trains with consideration of train mass. Eng. Struct. **42**, 9–22 (2012). https://doi.org/10.1016/j.engstruct.2012.04.007
10. Gönen, S., Soyöz, S.: Seismic analysis of a masonry arch bridge using multiple methodologies. Eng. Struct. **226**, 111354 (2021). https://doi.org/10.1016/j.engstruct.2020.111354
11. Gonen, S., Soyoz, S.: Dynamic identification of masonry arch bridges using multiple methodologies. In: Conf. Proc. Soc. Exp. Mech. Ser, pp. 37–47. Springer (2021). https://doi.org/10.1007/978-3-030-47709-7_4
12. Kim, B.H., Lee, J., Lee, D.H.: Extracting modal parameters of high-speed railway bridge using the TDD technique. Mech. Syst. Signal Process. **24**, 707–720 (2010). https://doi.org/10.1016/j.ymssp.2009.11.010
13. Rebelo, C., Simões da Silva, L., Rigueiro, C., Pircher, M.: Dynamic behaviour of twin single-span ballasted railway viaducts – field measurements and modal identification. Eng. Struct. **30**, 2460–2469 (2008). https://doi.org/10.1016/j.engstruct.2008.01.023
14. EN 1991-2: Eurocode 1: Actions on Structures – Part 2: Traffic Loads on Bridges. Brussels (n.d.)
15. Yang, X.-M., Yi, T.-H., Qu, C.-X., Li, H.-N., Liu, H.: Modal identification of high-speed railway bridges through free-vibration detection. J. Eng. Mech. **146**, 04020107 (2020). https://doi.org/10.1061/(asce)em.1943-7889.0001847
16. Brincker, R., Zhang, L., Andersen, P.: Modal identification of output-only systems using frequency domain decomposition. Smart Mater. Struct. **10**, 441–445 (2001). https://doi.org/10.1088/0964-1726/10/3/303

Chapter 5
Real-Time and Web-Based Structural Damage Detection Network for Multiple Structures

Onur Avci, Mustafa Gül, F. Necati Catbas, Ozan Celik, Turker Ince, and Serkan Kiranyaz

Abstract A structural damage detection system specifically designed to monitor multiple structures at a network level is introduced in this paper. Such a monitoring system improves resiliency and helps manage the operation and maintenance of structures in an optimum way. The authors have focused on stadia-type laboratory structures for this network. Health monitoring of stadia has been conducted at multiple places in the world; however, a network of stadia monitored simultaneously with comprehensive monitoring purposes is not known to authors. For structural monitoring of multiple structures at a network level, the work presented in this paper explains and characterizes the major steps to reach this goal by focusing on three laboratory structures with a collaborative research effort among contributors from multiple universities across the globe.

Keywords Vibration-based damage detection · Structural health monitoring · Web-based monitoring · Real-time damage detection

5.1 Introduction

The developments in computational capability and sensor technology have facilitated the real-time structural monitoring of civil infrastructure [1–8] and paved the way for a web-enabled framework for vibration serviceability [9, 10], condition monitoring [11–14], and structural damage detection [15, 16]. Simultaneous monitoring of multiple structures requires an automated system for identifying, locating, and quantifying the damage. The authors used vibration-based methods in conjunction with supervised multi-layer feed-forward artificial neural networks. The study presented in this paper is a product of multiple institutions' joint efforts to develop a network-level monitoring framework by executing analytical and experimental tasks on stadia-like laboratory structures [17–23]. Once structural damage starts to form on engineering structures, it is known to propagate on engineering structures [24, 25], shortening the design lives [26–32], and stadia-like structures are no exception [33–42].

O. Avci (✉)
Department of Civil and Environmental Engineering, West Virginia University, Morgantown, West Virginia, USA
e-mail: oavci@vt.edu

M. Gül
Department of Civil and Environmental Engineering, University of Alberta, Edmonton, Canada

F. N. Catbas · O. Celik
Department of Civil, Environmental and Construction Engineering, University of Central Florida, Orlando, FL, USA

T. Ince
Department of Electrical and Electronics Engineering, Izmir University of Economics, Izmir, Turkey

S. Kiranyaz
Department of Electrical Engineering, Qatar University, Doha, Qatar

H. Y. Noh (eds.), *Dynamics of Civil Structures, Volume 2*, Conference Proceedings of the Society for Experimental Mechanics Series, https://doi.org/10.1007/978-3-031-05449-5_5

5.2 Laboratory Structures and Monitoring System

The laboratory structures used in this monitoring framework development were intentionally designed with the flexibility and geometry to represent a part of a stadium grandstand so that the authors can also focus on the vibration serviceability. Vibration serviceability is an essential concern for various types of civil infrastructure, and it governs the structural designs, especially during the era of slender architectural concepts [43–52]. As a result of experimental and analytical work performed on three laboratory structures, a monitoring framework was developed to be used on a network level at multiple stadia. The developed system is designed to collect online vibration data from the laboratory structures and then store and share it for visualization tasks needed for the framework. The structure built at Qatar University (QU Grandstand) has been the largest instrumented grandstand type structure constructed in a controlled laboratory environment. The structure is a 20° inclined steel-grid structure with footprint dimensions of 4.2 m × 4.2 m and consisting of 25 filler beams, 4 columns, 8 girders, and several brace elements. The authors have run damage detection studies by loosening the bolts at one of the beam-to-girder connections and then detecting and quantifying the minor change of rotational stiffness (bolt loosening) at various joints (Fig. 5.1). This structure and the laboratory structures built at the University of Central Florida and the University of Alberta are shown in Fig. 5.2.

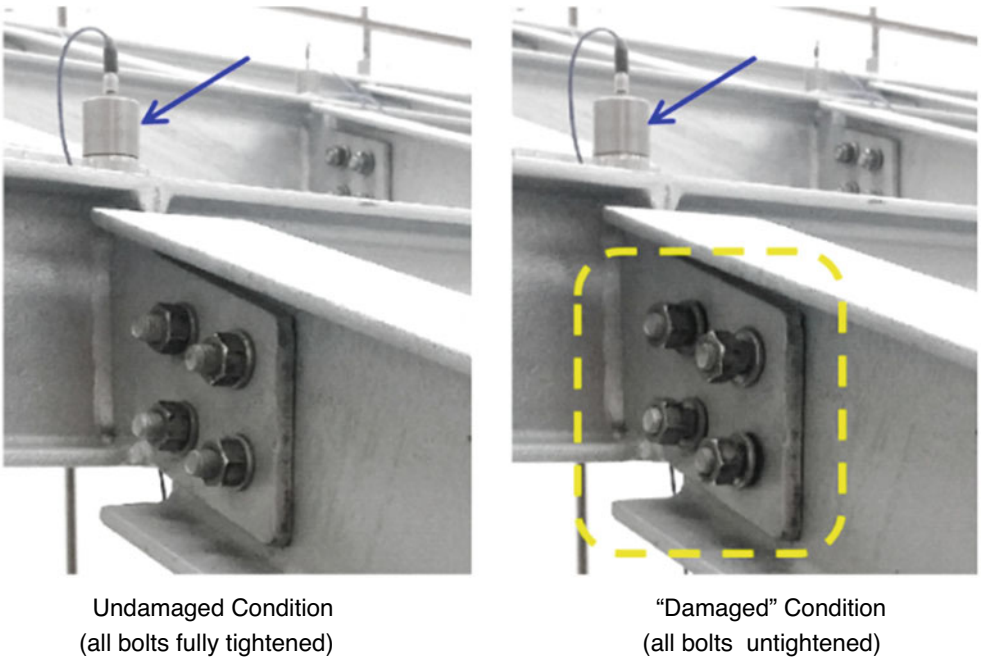

Fig. 5.1 Bolt loosening at beam-to-girder connections

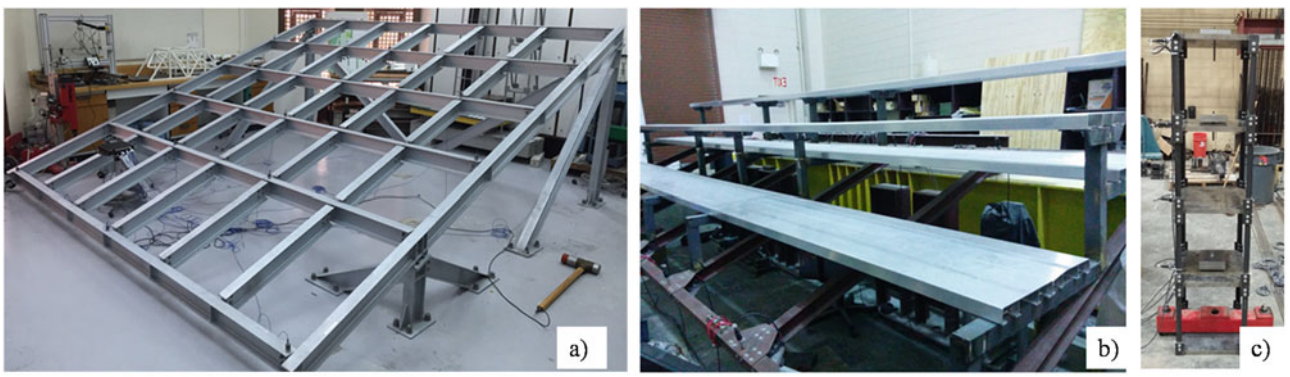

Fig. 5.2 The laboratory structures at (**a**) Qatar University, (**b**) the University of Central Florida, and (**c**) the University of Alberta

5.3 Data Collection and Visualization on the Network

A pertinent feature of the monitoring system is to have easy access to data on the framework. The developed framework is an integrated system consisting of a data collection network with storage and visualization capabilities. The system enables the users to collect, store, and conduct analysis through a user interface with a graphical display of real-time and archived data (suitable for permanent monitoring). For the monitoring framework, the system is built to be compatible with MATLAB Data Acquisition Toolbox [53], making it a good fit for a wide range of data acquisition devices. The system is then able to perform the following:

- Collect acceleration data from multiple laboratory structures under ambient conditions.
- Analyze the raw acceleration data in real time for structural damage detection and provide information on the location and level of damage. Store the information and publish it on a database.
- Enable monitoring of the structural condition of multiple structures in real time on the internet.

5.4 System Components, Database, and Web-Based Application

For the real-time web-based system, the major components of the MATLAB-based application are hardware for data collection and processing, signal processing algorithms, online database, and web application (Fig. 5.3). First, the sensor network is deployed on each structure which is operated by multiple data acquisition systems connected to a computer. A high-speed internet connection is required to process and share data on the framework. MATLAB Database Toolbox is also needed to be installed to enable communication with the online MySQL database [54, 55].

In the framework, the network for each structure is responsible for processing the collected acceleration data locally to extract the damage indices, assess vibration levels, and then publish them to the online database in real time. Various damage detection algorithms were used to extract damage indices in real time, working directly on the measured acceleration signals from monitored structures [56]. The damage index represents the probability of damage at various locations on the structures through which the existing structural condition can be assessed. The authors implemented the one-dimensional convolutional neural network (1D-CNN) algorithm [57–61], which processes the raw acceleration signal collected from the laboratory

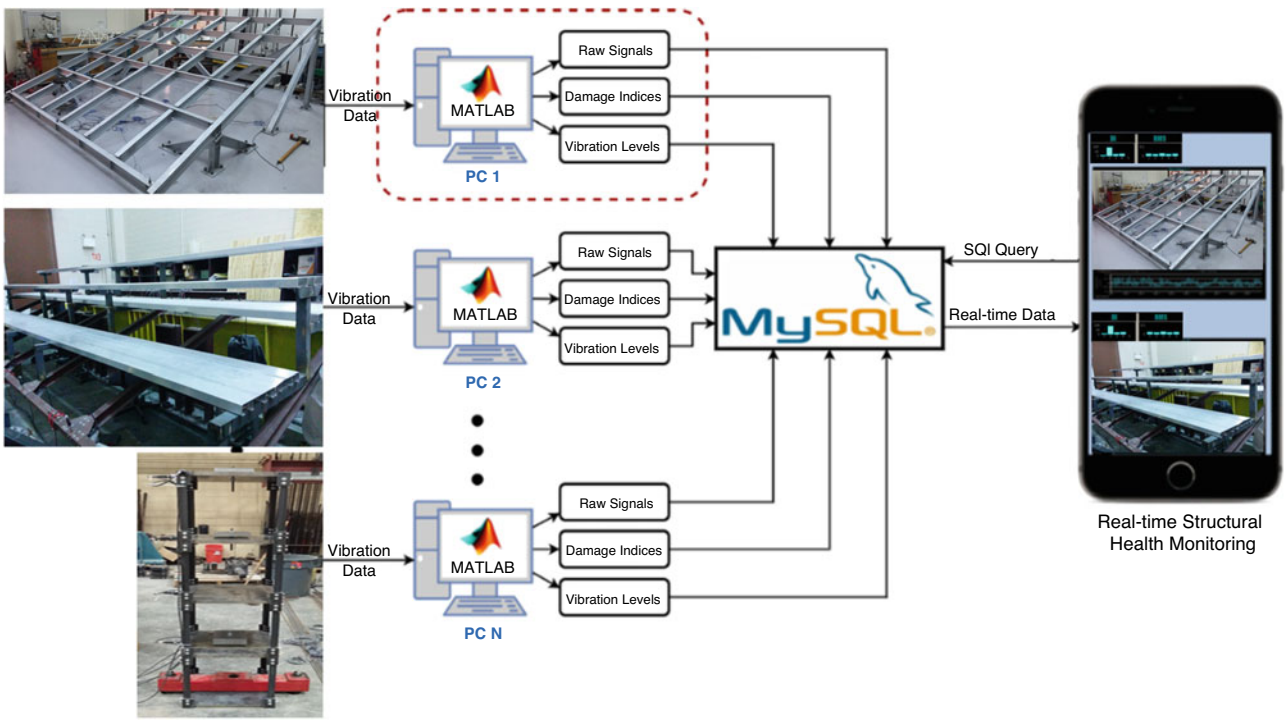

Fig. 5.3 Real-time web-based damage detection system

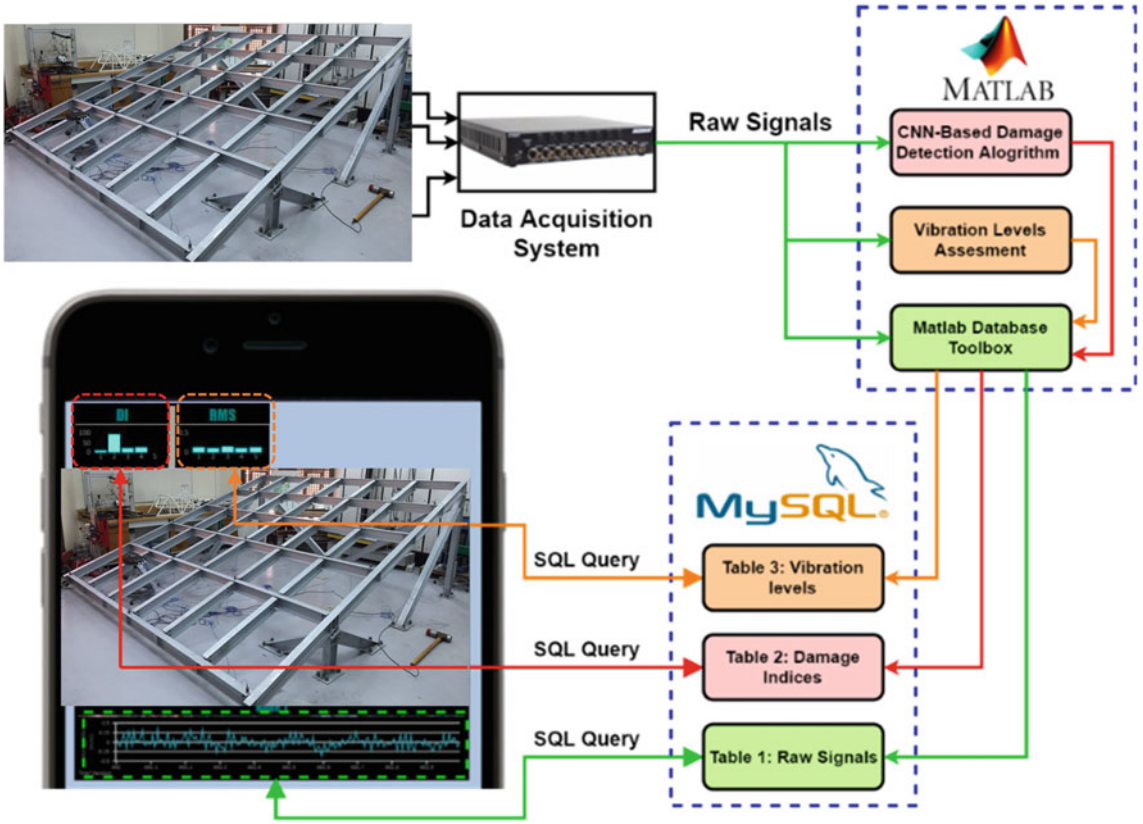

Fig. 5.4 Illustration of the real-time web-based damage detection system

structures to compute the probability of damage values that display the existing structural condition. The system is also capable of evaluating vibration serviceability levels for human comfort. As a result, the raw vibration signals, the extracted damage indices, and vibration levels at each accelerometer location are published to an online MySQL database through the MATLAB Database Toolbox. In the setup used by the authors, the raw acceleration signals are updated every 2 seconds, and the damage indices and acceleration vibration levels are updated every 30 seconds.

MySQL database is used to test the developed damage detection system. MySQL is an open-source database used for the development of scalable web applications. Through PHP scripting, a web application can connect, interact, and manipulate a MySQL database [62–64]. A connection can be formed between MATLAB and MySQL databases using the Database Toolbox along with a suitable JDBC driver. MySQL database presented in this paper includes three tables per structure, as shown in Fig. 5.4. In the figure, the first table is for storing the raw vibration signals, while the second and third tables are for storing the extracted damage indices and vibration levels, respectively. The stored data can be viewed and downloaded via phpMyAdmin, a software used for MySQL Databases.

The authors also developed a web application enabling the user to monitor the structural condition and vibration levels of multiple structures. This web application efficiently works on personal computers and smartphones. Based on the application interface shown in Fig. 5.4, for each monitored structure, the existing damage indices (shown as DI) and vibration levels (shown as RMS) are placed on the top left corner of each frame dedicated to the monitored structure. The real-time raw acceleration time-history signal at a selected location is shown under the frame of the monitored structure. The users can choose from the various accelerometer locations on the structure to see raw acceleration signals in real time. The web application communicates with the MySQL Database through PHP scripts which conduct the required SQL queries. JavaScript and JSON are utilized to update the interface every second to get the latest information from the database. These updates enable the live display of live raw accelerations, vibration levels, and real-time damage indices.

5.5 System Testing and Validation

Two laboratory structures at Qatar University (QU) and the University of Central Florida (UCF) were connected to the framework and monitored to run and test the proposed web-based system. Each laboratory structure was instrumented with five accelerometers for this exercise. Figure 5.5 shows the web application interface where the damage indices, vibration levels, and raw signals of monitored structures are displayed in real time. For demonstration purposes, the RMS value was shown to report the current acceleration levels for human comfort; yet other assessment methods can be integrated into the system. For the test runs, a negligible amount of rotational stiffness change (bolt loosening) was introduced at the second node of the QU structure. Based on this, one can notice that the system has detected and located the "structural damage" in real time by indicating an increased value for the damage indices (DI) assigned to the second node of the QU laboratory structure, as shown in Fig. 5.5. It is noted that the DI values for the other nodes remained very low, indicating that they are unaffected (undamaged) by the stiffness change on the second node. In other words, the bolt loosening was applied on the second node of the QU structure, and the system recognized this as an increased DI value for this node.

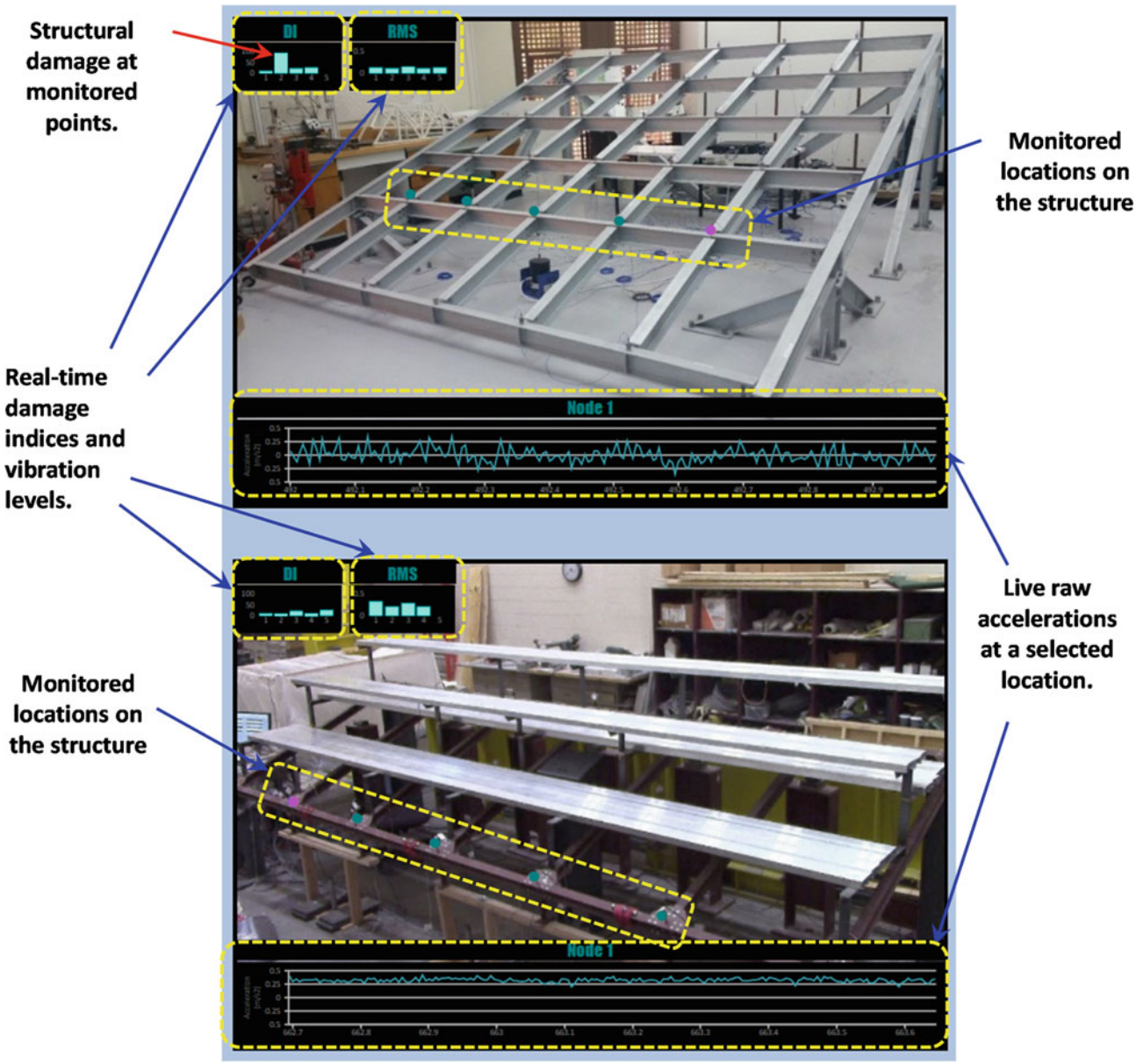

Fig. 5.5 Real-time monitoring of Qatar University and the University of Central Florida laboratory structures

5.6 Conclusions

The trend toward slender architectural designs has increased the importance of structural monitoring systems not only for vibration serviceability assessment but also for damage detection purposes. The elevated vibration levels caused by human-induced excitations, in addition to detection of structural damage under various conditions, are more critical than ever. Therefore, there is great value to the public and stakeholders in monitoring multiple structures for resiliency and integrity. In a collaborative effort through Qatar University, the University of Central Florida, the University of Alberta, and contributors from other universities, experimental and analytical studies were conducted on stadium-like laboratory structures to develop a network-level web-based damage detection framework using sensing suites and specialized signal processing algorithms. This paper summarized the steps to develop the final product, the real-time monitoring system operating at a network level that can be accessed online for decision-making. The developed methodologies are demonstrated in the laboratory environment so that the framework can later be showcased on real-scale structures for both vibration serviceability assessment and structural damage detection purposes.

Acknowledgments The financial support for the research presented in this paper was provided by Qatar National Research Fund (QNRF, a member of the Qatar Foundation) via the National Priorities Research Program (NPRP), Project Number NPRP 6-526-2-218. The statements made herein are solely the responsibility of the authors.

References

1. Krishnan, M., Bhowmik, B., Hazra, B., Pakrashi, V.: Real time damage detection using recursive principal components and time varying auto-regressive modeling. Mech. Syst. Signal Process. (2018). https://doi.org/10.1016/j.ymssp.2017.08.037
2. Bhowmik, B., Tripura, T., Hazra, B., Pakrashi, V.: Real time structural modal identification using recursive canonical correlation analysis and application towards online structural damage detection. J. Sound Vib. (2020). https://doi.org/10.1016/j.jsv.2019.115101
3. de Oliveira Dias Prudente dos Santos, J.P., Crémona, C., da Silveira, A.P.C., de Oliveira Martins, L.C.: Real-time damage detection based on pattern recognition. Struct. Concr. (2016). https://doi.org/10.1002/suco.201500092
4. Tripura, T., Bhowmik, B., Pakrashi, V., Hazra, B.: Real-time damage detection of degrading systems. Struct. Heal. Monit. (2020). https://doi.org/10.1177/1475921719861801
5. An, Y., Spencer, B.F., Ou, J.: Real-time fast damage detection of shear structures with random base excitation. Meas. J. Int. Meas. Confed. (2015). https://doi.org/10.1016/j.measurement.2015.07.006
6. Brownjohn, J.M.W., Carden, P.: Real-time operation modal analysis of Tamar bridge. In: Conf. Proc. Soc. Exp. Mech. Ser (2008)
7. Brownjohn, J.M.W., Carden, E.P., Goddard, C.R., Oudin, G.: Real-time performance monitoring of tuned mass damper system for a 183 m reinforced concrete chimney. J. Wind Eng. Ind. Aerodyn. (2010). https://doi.org/10.1016/j.jweia.2009.10.013
8. Vafaei, M., Bin Adnan, A., Rahman, A.B.A.: Real-time seismic damage detection of concrete shearwalls using artificial neural networks. J. Earthq. Eng. (2013). https://doi.org/10.1080/13632469.2012.713559
9. Abdeljaber, O., Hussein, M.F.M., Avci, O.: In-service video-vibration monitoring for identification of walking patterns in an office floor. In: 25th Int. Congr. Sound Vib. Hiroshima, Japan, 2018
10. Abdeljaber, O., Hussein, M.F.M., Avci, O., Davis, B., Reynolds, P.: A novel video-vibration monitoring system for walking pattern identification on floors. Adv. Eng. Softw. **139**, p. 102710 (2020)
11. Chen, B., Liu, W.: A web-based structural health monitoring sensor network. Int. J. Comput. Appl. Technol. (2012). https://doi.org/10.1504/IJCAT.2012.049082
12. Hsu, T.-Y., Huang, S.-K., Lu, K.-C., Loh, C.-H., Wang, Y., Lynch, J.P.: On-line structural damage localization and quantification using wireless sensors. Smart Mater. Struct. **20**, 105025 (2011). https://doi.org/10.1088/0964-1726/20/10/105025
13. Abdeljaber, O., Sassi, S., Avci, O., Kiranyaz, S., Ibrahim, A.A., Gabbouj, M.: Fault detection and severity identification of ball bearings by online condition monitoring. IEEE Trans. Ind. Electron. (2019). https://doi.org/10.1109/TIE.2018.2886789
14. Avci, O., Abdeljaber, O., Kiranyaz, S., Sassi, S., Ibrahim, A., Gabbouj, M.: One dimensional convolutional neural networks for real-time damage detection of rotating machinery. In: Conf. Proc. Soc. Exp. Mech. Ser. (2021)
15. Kosnik, D.E., Dowding, C.H.: Autonomous monitoring of dynamic response of in-service structures for decision support. J. Struct. Eng. (2015). https://doi.org/10.1061/(asce)st.1943-541x.0001044
16. Guo, Y., Kwon, D.K., Kareem, A.: Near-real-time hybrid system identification framework for civil structures with application to Burj Khalifa. J. Struct. Eng. (2016). https://doi.org/10.1061/(asce)st.1943-541x.0001402
17. Avci, O., Abdeljaber, O., Kiranyaz, S., Hussein, M., Inman, D.J.: Wireless and real-time structural damage detection: a novel decentralized method for wireless sensor networks. J. Sound Vib. **24**, 158–172 (2018)
18. Avci, O., Abdeljaber, O., Kiranyaz, S., Inman, D.: Structural damage detection in real time: implementation of 1D convolutional neural networks for SHM applications. In: Niezrecki, C. (ed.) Struct. Heal. Monit. Damage Detect. Proc. 35th IMAC, A Conf. Expo. Struct. Dyn, vol. 7, pp. 49–54. Springer International Publishing, Cham (2017). https://doi.org/10.1007/978-3-319-54109-9_6
19. Avci, O., Abdeljaber, O., Kiranyaz, S., Inman, D.: Convolutional neural networks for real-time and wireless damage detection. In: Conf. Proc. Soc. Exp. Mech. Ser. (2020). https://doi.org/10.1007/978-3-030-12115-0_17
20. Avci, O., Abdeljaber, O., Kiranyaz, S., Hussein, M., Gabbouj, M., Inman, D.J.: A new benchmark problem for structural damage detection: bolt loosening tests on a large-scale laboratory structure. In: Conf. Proc. Soc. Exp. Mech. Ser. (2021)

21. Abdeljaber, O., Younis, A., Avci, O., Catbas, N., Gul, M., Celik, O., Zhang, H.: Dynamic testing of a laboratory stadium structure. In: Geotech. Struct. Eng. Congr. 2016 – Proc. Jt. Geotech. Struct. Eng. Congr (2016). https://doi.org/10.1061/9780784479742.147
22. Abdeljaber, O., Avci, O., Kiranyaz, S., Gabbouj, M., Inman, D.J.: Real-time vibration-based structural damage detection using one-dimensional convolutional neural networks. J. Sound Vib. **388**, 154–170 (2017). https://doi.org/10.1016/j.jsv.2016.10.043
23. Kiranyaz, S., Avci, O., Jaber, O.A.Q.A.: Real-Time Structural Damage Detection by Convolutional Neural Networks, US16031519. (2019). https://patents.google.com/patent/US20190017911A1/en
24. Avci, O., Abdeljaber, O., Kiranyaz, S., Hussein, M., Gabbouj, M., Inman, D.J.: A review of vibration-based damage detection in civil structures: from traditional methods to machine learning and deep learning applications. Mech. Syst. Signal Process. (2021). https://doi.org/10.1016/j.ymssp.2020.107077
25. Avci, O., Abdeljaber, O., Kiranyaz, S.: Structural damage detection in civil engineering with machine-learning: current state of the art. In: Conf. Proc. Soc. Exp. Mech. Ser. (2021)
26. Ahmad, S.: Reinforcement corrosion in concrete structures, its monitoring and service life prediction – a review. Cem. Concr. Compos. (2003). https://doi.org/10.1016/S0958-9465(02)00086-0
27. Kwon, S.J., Na, U.J., Park, S.S., Jung, S.H.: Service life prediction of concrete wharves with early-aged crack: probabilistic approach for chloride diffusion. Struct. Saf. (2009). https://doi.org/10.1016/j.strusafe.2008.03.004
28. Alghamdi, S.A., Ahmad, S.: Service life prediction of RC structures based on correlation between electrochemical and gravimetric reinforcement corrosion rates. Cem. Concr. Compos. (2014). https://doi.org/10.1016/j.cemconcomp.2013.06.003
29. Segura, I., Cavalaro, S., de la Fuente, A., Aguado, A., Alegre, V.: Service-life assessment of existing precast concrete structure exposed to severe marine conditions. J. Perform. Constr. Facil. (2016). https://doi.org/10.1061/(asce)cf.1943-5509.0000765
30. Pang, L., Li, Q.: Service life prediction of RC structures in marine environment using long term chloride ingress data: comparison between exposure trials and real structure surveys. Constr. Build. Mater. (2016). https://doi.org/10.1016/j.conbuildmat.2016.03.156
31. Dhawan, S.K., Bindal, A., Bhalla, S., Bhattacharjee, B.: Expected residual service life of reinforced concrete structures from current strength considerations. Adv. Struct. Eng. (2019). https://doi.org/10.1177/1369433218818001
32. Prakash, G., Narasimhan, S., Al-Hammoud, R.: A two-phase model to predict the remaining useful life of corroded reinforced concrete beams. J. Civ. Struct. Heal. Monit. (2019). https://doi.org/10.1007/s13349-019-00327-w
33. Celik, O., Catbas, F.N., Do, N.T., Gul, M., Abdeljaber, O., Younis, A., Avci, O.: Issues, codes and basic studies for stadium dynamics. In: Proc. Second Int. Conf. Infrastruct. Manag. Assess. Rehabil. Tech., Sharjah, UAE, 2016
34. Catbas, F.N., Celik, O., Avci, O., Abdeljaber, O., Gul, M., Do, N.T.: Sensing and monitoring for stadium structures: a review of recent advances and a forward look. Front. Built Environ. **3**, 38 (2017). https://doi.org/10.3389/fbuil.2017.00038
35. Celik, O., Do, N.T., Abdeljaber, O., Gul, M., Avci, O., Catbas, F.N.: Recent issues on stadium monitoring and serviceability: a review. In: Conf. Proc. Soc. Exp. Mech. Ser (2016). https://doi.org/10.1007/978-3-319-29763-7_41
36. Almutairi, M., Avci, O., Nikitas, N.: A review of experimental studies on laboratory grandstands. In: Exp. Vib. Anal. Civ. Struct (2020). https://doi.org/10.1201/9781003090564-36
37. Ngoan, D.T., Mustafa, G., Osama, A., Onur, A.: Stadium vibration assessment for serviceability considering the vibration duration. In: Proceedings, Annu. Conf. – Can. Soc. Civ. Eng (2017)
38. Do, N.T., Gul, M., Abdeljaber, O., Avci, O.: Novel framework for vibration serviceability assessment of stadium grandstands considering durations of vibrations. J. Struct. Eng. (United States). **144** (2018). https://doi.org/10.1061/(ASCE)ST.1943-541X.0001941
39. Hoath, R.M., Blakeborough, A., Williams, M.S.: Using video tracking to estimate the loads applied to grandstands by large crowds. In: Conf. Proc. Soc. Exp. Mech. Ser. (2007)
40. Jones, C.A., Reynolds, P., Pavic, A.: Vibration serviceability of stadia structures subjected to dynamic crowd loads: a literature review. J. Sound Vib. (2011). https://doi.org/10.1016/j.jsv.2010.10.032
41. Shen, Y., Yang, P., Zhang, P., Luo, Y., Mei, Y., Cheng, H., Jin, L., Liang, C., Wang, Q., Zhong, Z.: Development of a multitype wireless sensor network for the large-scale structure of the National Stadium in China. Int. J. Distrib. Sens. Netw. (2013). https://doi.org/10.1155/2013/709724
42. Letchford, C.W., Denoon, R.O., Johnson, G., Mallam, A.: Dynamic characteristics of cantilever grandstand roofs. Eng. Struct. (2002). https://doi.org/10.1016/S0141-0296(02)00035-4
43. Avci, O.: Modal parameter variations due to joist bottom chord extension installations on laboratory footbridges. J. Perform. Constr. Facil. **29** (2015). https://doi.org/10.1061/(ASCE)CF.1943-5509.0000635
44. Avci, O.: Effects of Bottom Chord Extensions on the Static and Dynamic Performance of Steel Joist Supported Floors. Virginia Polytechnic Institute and State University (2005)
45. Younis, A., Avci, O., Hussein, M., Davis, B., Reynolds, P.: Dynamic forces induced by a single pedestrian: a literature review. Appl. Mech. Rev. **69** (2017). https://doi.org/10.1115/1.4036327
46. Royvaran, M., Avci, O., Davis, B.: Analysis of floor vibration evaluation methods using a large database of floors framed with W-shaped members subjected to walking excitation. J. Constr. Steel Res. **164**, p. 105764 (2020)
47. Royvaran, M., Avci, O., Davis, B.: An overview on floor vibration serviceability evaluation methods with a large database of recorded floor data. In: Conf. Proc. Soc. Exp. Mech. Ser (2021). https://doi.org/10.1007/978-3-030-47634-2_10
48. Muhammad, Z., Reynolds, P., Avci, O., Hussein, M.: Review of pedestrian load models for vibration serviceability assessment of floor structures. Vibration. (2018). https://doi.org/10.3390/vibration2010001
49. Bhargava, A., Isenberg, J., Feenstra, P.H., Al-Smadi, Y., Avci, O.: Vibrations assessment of a hospital floor for a magnetic resonance imaging unit (MRI) replacement. In: Struct. Congr. 2013 Bridg. Your Passion with Your Prof. – Proc. 2013 Struct. Congr. (2013)
50. Avci, O., Bhargava, A., Al-Smadi, Y., Isenberg, J.: Vibrations serviceability of a medical facility floor for sensitive equipment replacement: evaluation with sparse in-situ data. Pract. Period. Struct. Des. Constr. **24**(1), p. 05018006 (2019)
51. Barrett, A.R., Avci, O., Setareh, M., Murray, T.M.: Observations from vibration testing of in-situ structures. In: Struct. Congr. 2006 (2006). https://doi.org/10.1061/40889(201)65
52. Devin, A., Fanning, P.J., Pavic, A.: Nonstructural partitions and floor vibration serviceability. J. Archit. Eng. (2016). https://doi.org/10.1061/(asce)ae.1943-5568.0000171
53. The Mathworks Inc., MATLAB – MathWorks (2016). https://doi.org/2016-11-26

54. Welling, L., Thomson, L.: PHP and MySQL Web Development. SAMS Publishing, England (2005)
55. R. Yohanes, S.E. Antonius, Web Server Development System with Php, Mysql, and Jsp Configuration, Proxies: Jurnal Informatika, 1(1), pp.15–21 (2017)
56. Avci, O., Abdeljaber, O., Kiranyaz, S.: An overview of deep learning methods used in vibration-based damage detection in civil engineering. In: Conf. Proc. Soc. Exp. Mech. Ser (2021)
57. Abdeljaber, O., Avci, O., Kiranyaz, M.S., Boashash, B., Sodano, H., Inman, D.J.: 1-D CNNs for structural damage detection: verification on a structural health monitoring benchmark data. Neurocomputing. (2017). https://doi.org/10.1016/j.neucom.2017.09.069
58. Kiranyaz, S., Avci, O., Abdeljaber, O., Ince, T., Gabbouj, M., Inman, D.J.: 1D convolutional neural networks and applications: a survey. Mech. Syst. Signal Process. **151** (2021). https://doi.org/10.1016/j.ymssp.2020.107398
59. Kiranyaz, S., Ince, T., Abdeljaber, O., Avci, O., Gabbouj, M.: 1-D Convolutional neural networks for signal processing applications. In: ICASSP, IEEE Int. Conf. Acoust. Speech Signal Process. – Proc (2019). https://doi.org/10.1109/ICASSP.2019.8682194
60. Almutairi, M., Avci, O., Nikitas, N.: Efficiency of 1d cnns in finite element model parameter estimation using synthetic dynamic responses. In: Proc. Int. Conf. Struct. Dyn. EURODYN (2020). https://doi.org/10.47964/1120.9009.19640
61. Avci, O., Abdeljaber, O., Kiranyaz, S., Boashash, B., Sodano, H., Inman, D.J.: Efficiency validation of one dimensional convolutional neural networks for structural damage detection using a SHM benchmark data. In: 25th Int. Congr. Sound Vib (2018)
62. Olsson, M.: PHP Quick Scripting Reference (2013). https://doi.org/10.1007/978-1-4302-6284-8
63. Andress, J., Linn, R.: Introduction to web scripting with PHP. In: Coding for Penetration Testers (2017). https://doi.org/10.1016/b978-0-12-805472-7.00005-x
64. Kromann, F.M.: Beginning PHP and MySQL From Novice to Professional. Springer, New York (2018)

Chapter 6
Identification of Damage in Composite Beams Involving Both Flexural and Shear Link Damages

Yu Gu and Yong Lu

Abstract Composite structures are widely used in bridge and building construction. In fact, the majority of bridge structures, which are arguably the main subject of structural monitoring and damage identification, involve some form of composite components. The structural performance of a composite structure is dependent upon the conditions of the basic flexure-pertinent constituents, e.g., the material degradation (reduced Young's modulus) or cracking in the concrete slab of a slab-beam system, as well as the constituents that enable the composite effect, i.e., the shear connectors. It is therefore imperative that damages in a composite structure need be distinguished between "flexural" and "composite" nature. However, in the existing damage identification literature, especially when vibration-based techniques are employed, composite structures such as bridge decks are often treated as monolithic structures, and accordingly, structural parameters are identified in terms of gross flexural parameters without differentiating between flexure and shear link properties. This could lead not only to incorrect identification of the actual flexural properties but also potentially to misleading results in case serious damage to shear links occurs. In this paper, we will provide an overall discussion on the distinctive effects of flexural and shear link damages on the global structural stiffness in a composite beam. On this basis, the possibility and rationale to identify the mixed presence of flexural and shear link damage parameters using modal data from typical vibration tests are discussed. A genetic algorithm-based finite element model updating procedure is then implemented. The results show that separation of the flexural and shear link parameters is possible and satisfactory accuracy can be achieved with the FE model updating the proposed scheme.

Keywords Damage identification · Composite beams · Flexural parameters · Shear link parameters · Finite element model updating · Genetic algorithms

6.1 Introduction

Composite structures are widely used in bridge and building construction. Most bridge structures, which are actually the main subject of structural monitoring and damage identification at present, involve some form of composite members. The structural performance of a composite structure is determined by the conditions of the basic flexure-relevant constituents, such as material degradation (lower Young's modulus) or cracking in a slab-beam system's concrete slab, as well as the constituents that enable the composite effect, such as shear connectors. To date, although some studies have been reported on the condition assessment of composite beams [1, 2], composite structures are often treated as equivalent monolithic structures, and accordingly, structural parameters are identified in terms of gross flexural parameters without differentiating between flexure and shear link properties. In some studies, both flexural and shear connector properties are updated in a routine updating procedure; there often lack proofs that the updated results for both sets of parameters are good enough or physically meaningful. There has not been a systematic study in terms of how the flexural and shear connector properties correlate with the change of the gross flexural stiffness and thereby the vibration data that may be acquired through the conventional transverse vibration measurements.

In this paper, an overall discussion on the distinctive effects of flexural and shear link damages on the global structural stiffness in a composite beam is provided. On this basis, the possibility and rationale to identify the mixed presence of flexural and shear link damage parameters using modal data from typical vibration tests are discussed. A genetic algorithm-based

Y. Gu · Y. Lu (✉)
Institute for Infrastructure and Environment, School of Engineering, University of Edinburgh, Edinburgh, UK
e-mail: yong.lu@ed.ac.uk

H. Y. Noh (eds.), *Dynamics of Civil Structures, Volume 2*, Conference Proceedings of the Society for Experimental Mechanics Series, https://doi.org/10.1007/978-3-031-05449-5_6

finite element model updating procedure is then implemented. The results show that separation of the flexural and shear link parameters is possible and satisfactory accuracy can be achieved with the FE model updating the proposed scheme.

6.2 Background Theory-Governing Differential Equations for Free Vibration of Simply Supported Composite

In a real situation, the composite effect of a composite beam is determined by the shear stiffness of the connectors and the "stiffness" (modulus) of the surrounded material. Hence, even for a designed full composite beam, the interface slip inevitably exists between two component beams, which leads to an extra deflection [3] or in other words a reduction in the stiffness. In the case of a partial composite design, more slip between the two component beams could occur. Furthermore, the distribution of the stiffness reduction caused by localized weakening of the composite effect is distinctively different from localized flexural stiffness reduction. Therefore, it is not suitable to use a monolithic structure, e.g., the Euler beams, to represent a composite beam for the purpose of damage assessment.

To have a clear demonstration, the dynamic behavior of the governing differential equations for free vibration of a simply supported composite beam is presented in this section under the following assumptions:

1. All constitutive materials are linear, with small deformation.
2. The shear connectors between the two sub-elements are continuous and evenly distributed longitudinally.
3. There is no lateral separation at the contact interface, which means that two sub-elements have the same curvatures in any cross-section.
4. The governing differential equations are based on the Euler-Bernoulli beam theory without considering the influences of rotary inertia and shear deformations [4].

The governing differential equations of flexural deflection y for the free vibration of a composite beam can be expressed by:

$$\frac{\partial^4 y}{\partial x^4} - \gamma_1 \beta \frac{\partial^4 y}{\partial x^2 \partial t^2} - \alpha^2 \left(\frac{\partial^4 y}{\partial x^4} + \gamma_1 \frac{\partial^2 y}{\partial t^2} \right) = 0 \tag{6.1}$$

where x is coordinate, t is time, and α, β, and γ_1 are defined below:

$$\alpha^2 = k_s \left(\frac{1}{E_2 A_2} + \frac{1}{E_1 A_1} + \frac{h^2}{EI_1 + EI_2} \right) \tag{6.2}$$

$$\beta^2 = \frac{EI_{full}}{EI_1 + EI_2} \tag{6.3}$$

$$\gamma_1 = \frac{\rho_1 A_1 + \rho_2 A_2}{EI_{full}} \tag{6.4}$$

where k_s is the distributed shear rigidity of the shear connector. E_i, A_i, I_i, and ρ_i denote Young's modulus, the cross-sectional area, the second moment of area, and the density of the two sub-elements; h is half of the distance between the centroids of two sub-elements under the non-composite conditions. EI_{full} is flexural stiffness of the full composite beam. For a simply supported beam, it can be assumed the time and shape function of flexure deflection y are:

$$y = Y_0 \sin\left(\frac{n\pi x}{L}\right) e^{iwt} \tag{6.5}$$

where L is the length of the beam and ω is the frequency.

Substituting Eq. (6.4) into Eq. (6.1) gives:

$$\xi^6 - \alpha^2 \xi^4 - \gamma_1 \left(\alpha^2 + \beta^2 \xi^2 \right) \omega^2 = 0 \tag{6.6}$$

in which $\xi = n\pi/L$, and then, the natural frequency of the partial interaction beam can be solved as:

$$\omega^2 = \left(1 - f_{\text{slip}}\right)\omega_0^2 \tag{6.7}$$

where $\omega_0 = \left(\frac{n\pi}{L}\right)^2 \cdot \left(\frac{\text{EI}_{\text{full}}}{\rho_1 \cdot A_1 + \rho_2 \cdot A_2}\right)^{0.5}$ is the n-th frequency of a full composite beam and factor f_{slip} denotes the effect of the interlayer slip, which is:

$$f_{\text{slip}} = \frac{\beta^2 - 1}{\beta^2 + \frac{\alpha^2}{\xi^2}} \tag{6.8}$$

In this study, we define the equivalent gross cross-section rigidity of a composite beam as:

$$\text{EI}_{\text{composite}} = \omega^2 \left(\frac{L}{n\pi}\right)^4 (\rho_1 \cdot A_1 + \rho_2 \cdot A_2) \tag{6.9}$$

And substituting Eq. (6.7) into Eq. (6.9) gives:

$$\text{EI}_{\text{composite}} = \left(1 - f_{\text{slip}}\right) \cdot \text{EI}_{\text{full}} \tag{6.10}$$

From Eqs. (6.8) and (6.10), it can be established that with an increase of the mode number n, the slip factor f_{slip} increases as well, and this leads to a decrease of the equivalent cross-section rigidity $\text{EI}_{\text{composite}}$. To demonstrate this, a theoretical simply supported composite beam is analyzed. The beam consists of two rectangular beam sections of the equal depth of 0.05 m and width of 0.3 m. The length of the composite beam is 2 m. The cross-section rigidities for the top beam and bottom beam are equally 8.125×10^4 N $\cdot$ m^2. The density of the beams is set as 2300 kg/m^3. The k_s is set as 4×10^8 N/m^2.

Figure 6.1 presents the ratio (in %) between the equivalent gross cross-section rigidity $\text{EI}_{\text{composite}}$ and the gross cross-section rigidity of the full composite section under the different number of the mode. It can be observed that with an increase

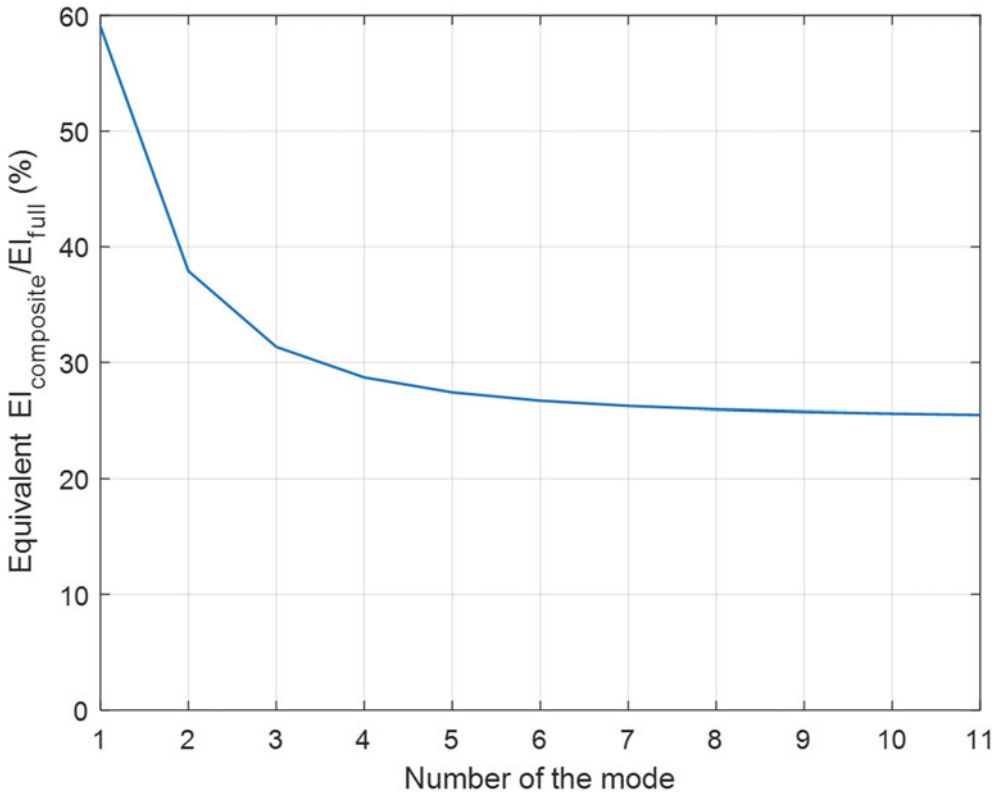

Fig. 6.1 Percentage of theory equivalent gross cross-section rigidity $\text{EI}_{\text{composite}}$ to the gross cross-section rigidity of full composite under the different number of the mode

of the mode order, the equivalent gross cross-section rigidity $EI_{composite}$ decreases from about 60% of full composite gross cross-section rigidity for the first mode to about 32% for the third mode and then more gradually decreases to eventually approach the non-composite EI (25% of EI_{full}). This can be explained by the fact that with the increase of the mode order, the distance between the contra flexure points along the beam length decreases, which means the effective length within which the composite effect develops also decreases, resulting in a decrease of the equivalent flexural rigidity. In comparison, the gross flexural rigidities of an Euler beam do not vary under different modes. Hence, it is not suitable to treat a composite beam as an equivalent monolithic beam without differentiating the flexure and shear link properties.

6.3 General Effects of Flexural and Shear Link Damage on Stiffness Distribution, Modal Frequencies, and Mode Shapes

Vibration-based structural damage identification commonly uses transverse vibration properties, which are effectively governed by the gross flexural rigidity of individual members and its distribution along the member length. In the case of assessing a composite beam, both the typical "flexural" damage, such as a crack, and the condition of the shear connectors, which influences the degree of the composite effect, can influence the gross bending stiffness of a composite beam. However, the degradation of the composite effect caused by damage in the shear connectors depends not only on the degree of damage in the shear studs itself but also on the position of the shear studs. Furthermore, the involvement of a shear connector at a particular location is effectively dependent on the shear slip tendency at the interface between two beams; therefore, the composite effect and the equivalent flexural rigidity at a particular location depend also upon the adjacent shear connectors. Combined with the phenomenon mentioned previously that the composite effect decreases with increase of the mode number, the correlation between damage in shear connectors and the vibration properties, including modal frequencies and mode shapes, becomes very complicated.

In this section, a finite element model of a simple composite beam is established in Abaqus according to the description of the last section. A total of 20 discrete shear connectors with the stiffness of 40 kN/mm are arranged along the beam length uniformly and numbered 1–20 in sequence from the left to right, as shown in Fig. 6.2. For damage identification, the upper part of the composite beam, assuming to be made of concrete, is grouped into ten segments along the length direction. In this way, the direct flexural damage can be simulated by reducing the stiffness (Young's modulus) at any one or more of these segments.

As a verification of the above FE model, the natural frequencies computed from the FE model are compared with the theoretical values in Fig. 6.3. It can be observed that the results from the FE model are very close to the theoretical values, indicating that the FE model is sufficiently accurate and can be used for further investigations.

To demonstrate the significant differences in the effects between the flexural and shear connector damage on the modal information, two beam section (flexural) damage and two shear damage scenarios are selected to be presented. For the first scenario, the shear connectors No.5 and No.6 are removed. For the second scenario, the shear connectors No.10 and No.11 are removed. For the third scenario, the beam stiffness of segment 5 is reduced to 40% of the intact stiffness. For the fourth scenario, the beam stiffness of segment 2 is reduced to 40% of the intact stiffness. The first mode shape curvatures of these four damage scenarios are compared with that of the intact composite beam in Fig. 6.4.

From Fig. 6.4a, which compares the mode shape curvatures of two shear connector damage scenarios, it can be observed that when the shear connectors No.5 and No.6 are removed, the mode shape curvature has a significant variation almost on the whole left beam, which indicates the effect extends beyond the position where the two damage shear links are located. On the contrary, the removal of shear links No.10 and No.11 has little influence on the mode shape curvature, which is almost the same as the mode shape curvature under the intact situation. This is because that the shear slip at the midsection of the composite beam in the first mode is limited, so these shear connectors contribute little toward the composite effect under this vibration mode. In comparison, a direct damage to the beam section causes an immediate effect on the mode shape curvature at the location where the flexural damage occurs, as can be clearly observed in Fig. 6.4b. This is significantly different from the effect of damage in shear connectors at the same part of the composite beam.

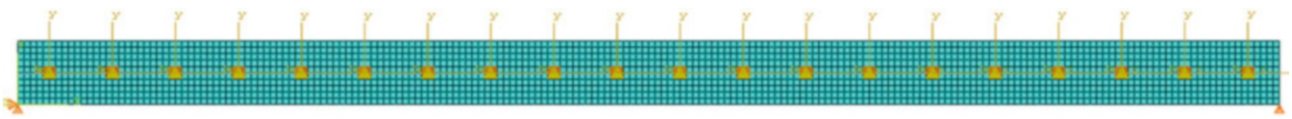

Fig. 6.2 FE model of a representative composite beam

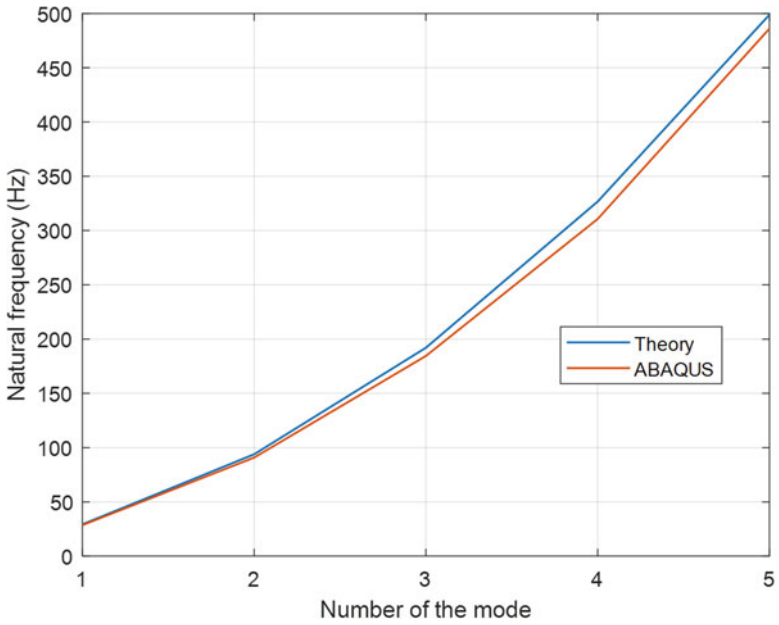

Fig. 6.3 Comparison of natural frequency (left graph) and equivalent gross cross-section rigidity (right graph) between theoretical value and finite element model's value under different modes

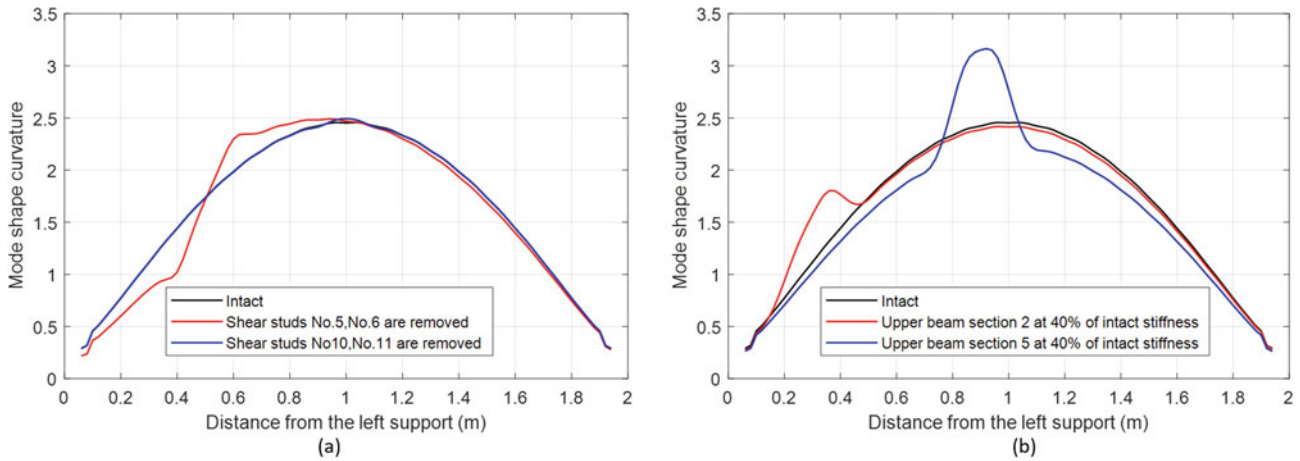

Fig. 6.4 Comparison of the first mode shape curvature of four scenarios: Left graph (**a**) compares the shear connectors' damages. Right graph (**b**) compares the component beam section damages

Table 6.1 further presents the first four modal frequencies of these four damage cases with comparison to the frequencies of the intact composite beam. It can be seen that for the damage scenario of removing shear links No.5 and No.6, although it has a significant impact on the first mode, for the second mode, the impact of this damage is quite limited. This can be explained by the fact that the shear connectors No.5 and No.6 are located around the quarter point of the beam from the left end, which is almost the peak displacement location in Mode 2, where there are limited tendency of slip and subsequently limited involvement of the shear links No.5 and No.6 under this particular mode. In comparison, No.10 and No.11 shear connectors are located at the middle of the beam, which is around the peak displacement location of modes 1 and 3, but is at the inflection points of modes 2 and 4. For the same reason mentioned above, the percentage difference of the natural frequency between this damage scenario and the intact beam is relatively more significant under mode 2 and mode 4, but almost negligible under mode 1 and mode 3. On the other hand, in the case of beam section (flexural) damage, segment No.5 is closer to the peak displacement compared to segment No.2 in the first mode; hence, the percentage variation of the first mode frequency to the intact situation brought by flexural damage in segment No.5 is more significant than the variation caused by damage in section No.2. For the same reason, under the second mode, the damage in segment No.2 has a more significant effect on the second mode frequency than the damage in segment No.5.

Table 6.1 Mode frequency comparison between selected damage scenario and intact situation

–	Intact (Hz)	S5, S6 = 0 (Hz)	Percentage difference to the intact situation (%)	S10, S11 = 0 (Hz)	Percentage difference to the intact situation (%)	Section 2 at 40% of intact stiffness (Hz)	Percentage difference to the intact situation (%)	Section 5 at 40% of intact stiffness (Hz)	Percentage difference to the intact situation (%)
Mode 1	28.59	27.62	−2.10%	28.59	0.00%	28.33	−0.91%	27.6	−3.46%
Mode 2	90.83	89.70	−0.07%	87.77	−3.37%	88.88	−2.15%	90.34	−0.54%
Mode 3	184.5	184.3	−1.14%	184.3	−0.11%	179	−2.98%	179.9	−2.49%
Mode 4	310.7	310.0	−1.29%	306.6	−1.32%	302.9	−2.51%	306.3	−1.42%

The above numerical simulation results indicate that the effect of damage to the shear connectors on the overall structural performance is complicated, on the one hand, and, on the other hand, the effect on the modal frequencies and mode shapes is distinctively different from flexural damage. This suggests that using transverse vibration data should contain pertinent information that could allow the separation of the two groups of parameters in a composite beam. In the next section, we will demonstrate the identification of the two groups of damage parameters using the framework of finite element model updating with genetic algorithms.

6.4 Identification of Damage in Composite Beams Using Genetic Algorithm-Based Finite Element Model Updating

In the FE model updating-based structural damage assessment, the main idea is to establish a residual (objective) function that represents the discrepancy of dynamic properties between the damaged structure and the finite element model and then by means of a global optimization algorithm to update the parameters of the finite element model until the dynamic properties computed from the FE model minimizes the residual function [5].

In this section, the objective function is established with the residuals of the mode frequency and mode shape information, shown by Eq. (6.11). In order to minimize the influence of the basic model error, the measured and theoretical modal information of the damaged beam is normalized with respect to its undamaged counterpart, and the objective function of the residual error is formulated by the normalized values:

$$R = \frac{1}{N_{\mathrm{f}}} \sum_{i=1}^{N_{\mathrm{f}}} abs\left(\frac{f_{dNmi}^2}{f_{0Nmi}^2} - \frac{f_{dNci}^2}{f_{0Nci}^2} \right) + \frac{1}{N_{\mathrm{ms}} N_{\mathrm{n}}} \sum_{j=1}^{N_{\mathrm{ms}}} \sum_{i=1}^{N_{\mathrm{n}}} abs\left(\left(\frac{\phi_{dm_i}^j}{\phi_{0m_i}^j} \right)^2 - \left(\frac{\phi_{dc_i}^j}{\phi_{0c_i}^j} \right)^2 \right) \tag{6.11}$$

where f_{Ni} represents i-th natural frequency and subscripts "c" and "m" stand for the FE calculated and the measured data, respectively. Subscripts "d" and "0" stand for the damaged and intact states of the beam, respectively. $\phi_{m_i}^j$ is the j-th element in the i-th displacement normalized mode shape vector. Subscripts "c" and "m" stand for the FE calculated and measured data. N_{f}, N_{ms}, and N_{n} represent the number of the natural frequency, number of the mode shape, and number of the measured node, respectively.

The stiffness parameter of each segment is used to update the model, and the genetic algorithm (GA) is employed to guide the updating process [5]. Generally speaking, GA-based model updating has several advantages. For example, the GA searching results do not depend on the initial setting of the updating parameters; thus, a global optimal result rather than a local one is generally guaranteed. Furthermore, there is no need to calculate the sensitivity matrix of the structure during the updating process, and this makes the updating more robust. In the present study, the standard GA function in MATLAB has been used to update the FE model. A random distribution of the section stiffness on each segment of the beam is assigned firstly in MATLAB. Then these stiffness parameters are imported into Abaqus to calculate the modal information. Subsequently, the calculated modal information is exported to MATLAB from Abaqus to calculate the R function. If the value of the fitness function does not meet a pre-set requirement, the GA will carry out an iteration to find a more suitable distribution of segment stiffness parameters. If the fitness meets the requirement, the iteration process stops, and the optimized distribution of segment stiffness parameters is exported.

The previously introduced FE model (Sect. 6.3) is used here to demonstrate the damage identification procedure. To extract the mode shape information, 19 measurement points are uniformly arranged along the bottom of the composite beam, staring at the position of 0.1 m from the left end to the right end with an interval of 0.1 m. As previously stated, the top portion of the composite beam is separated into 10 segments, and the 20 shear connectors are similarly divided into 10 groups, each

having 2 adjacent shear connectors in the same condition. Therefore, there is a total of 20 stiffness parameters involved in the updating process.

For demonstration purpose, two scenarios both involving a single beam flexural damage and a single shear connector damage in combination are investigated herein. For the first damage scenario, the stiffness of the top part of the No.3 beam segment reduces to 60% of the intact situation, and the stiffness of the No.3 shear connector group reduces to 10% of the intact situation (simulating a near-total damage in these shear connectors). For the second damage scenario, the stiffness of the top part of the No.5 beam segment reduces to 60% of the intact situation, and the stiffness of the No.2 shear connector group reduce to 10% of the intact situation.

For both of the above damage scenarios, the "measured" modal data are acquired from the analysis of the finite element model with these specific two damage scenarios. For the intact states, both the "measured" and FE model data are from the numerical calculations and so they are identical, which means $f_{0Nmi} = f_{0Nci}$ and $\phi^j_{0m_i} = \phi^j_{0c_i}$.

In this study, the first five mode frequencies and the first three mode shapes are used to form the objective function. Regarding the settings of the GA parameters, a population size of 100 is selected, and the crossover fraction and mutation rate are set as 0.8 and 0.02. The fitness limit is set as 0.01, which means the threshold of the sum value of the percentage of mean square error of mode frequencies and mode shapes between measured data and calculated data is set as 1%. Once the value of the residual function is lower than 0.01, the updating process stops, and the updated stiffness parameters are presented. For speeding up the converging process, the search range of the shear connector stiffness starts from 5% to 100% of the intact stiffness; for the concrete section, the search range starts from 30% to 100% of the intact stiffness. The stiffness intervals to be searched are both set as 1% of corresponding intact stiffness.

The updating results of the two damage scenarios are presented in Fig. 6.5 in comparison with the objective stiffness parameters. It can be observed that for both damage scenarios, all the stiffness parameters can be updated correctly. In the first damage scenario, even though the shear damage and concrete damage are located at the same part of the composite beam, the damage of the shear connectors and the beam section can be assessed accurately. Furthermore, in the second

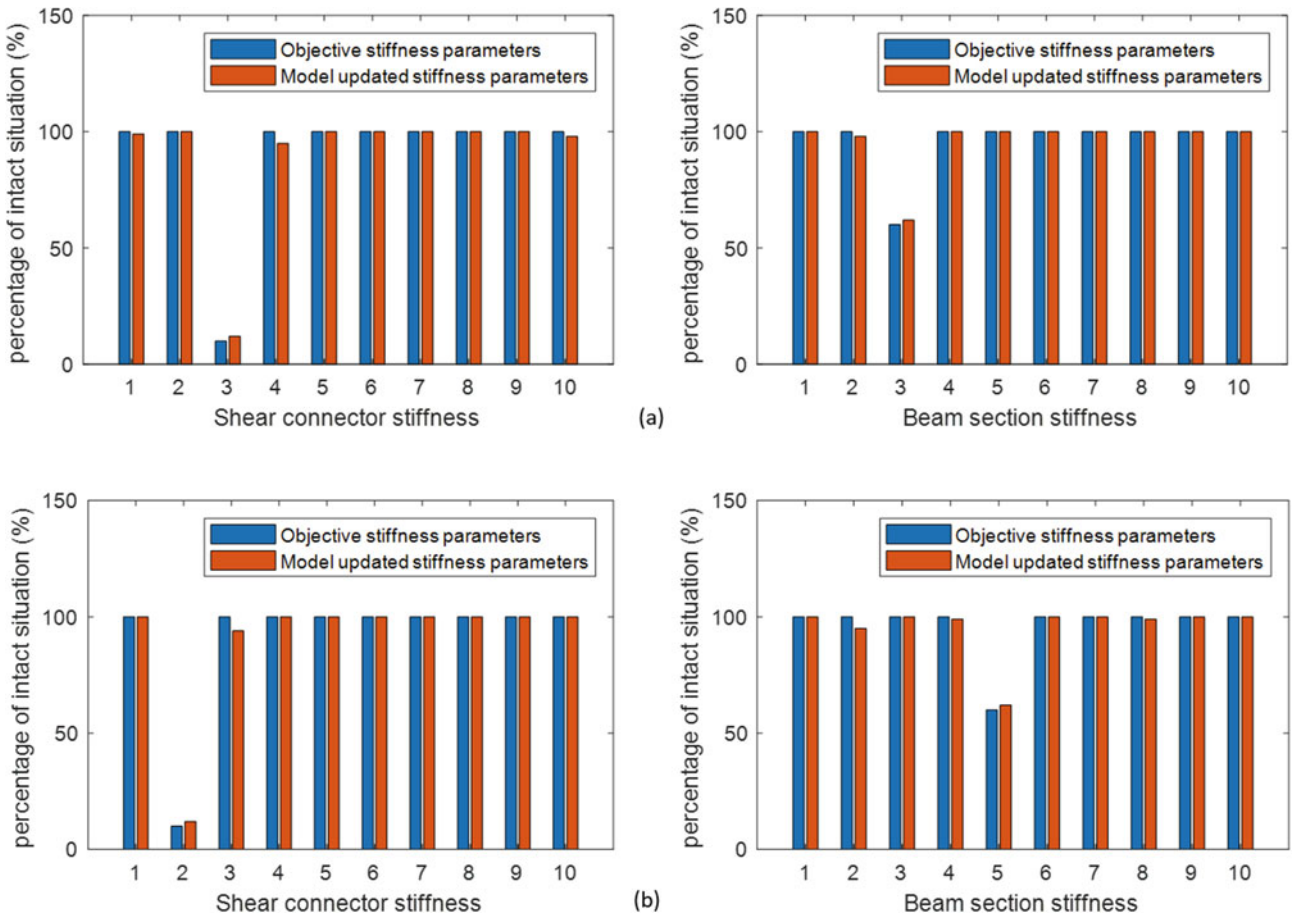

Fig. 6.5 Comparison between updated stiffness parameter and objective stiffness parameters: (**a**) damage scenario 1; (**b**) damage scenario 2

damage scenario, the shear damage near the end of the composite beam and the beam section near the middle part of the beam can be assessed accurately as well.

These results indicate that it is possible to use the proposed genetic algorithm-based model updating framework to differentiate and identify flexural and shear connector damages in a composite beam.

It should be noted that the above investigation and observations are aimed at demonstrating the separation of the flexural and shear connector parameters from a principle point of view. The actual effectiveness of the approach still requires continued study in a more realistic structural and measurement conditions, and it is anticipated that more sophisticated use of the measurement features and dedicated algorithms may be needed.

6.5 Concluding Remarks

In this paper, the characteristic effects of the "flexural" damages and shear connector damages on the rigidity and its distribution in a composite beam are presented, and the influences of such effects on the transverse vibration properties are discussed in the context of damage identification. It is found that, firstly, the equivalent cross-section rigidity of the composite beam decreases with an increase of the mode number, and this is attributed to the decrease of the effective length of the composite beam with increase of the mode number. This suggests that treating composite beams as a monolithic structure could lead not only to incorrect identification of the structural (stiffness) properties but also potentially to misleading results in case serious damage occurred to shear connectors. Secondly, a shear connector damage is found to affect the gross bending stiffness and therefore the mode shape over an extended area. Thus, the shear connector damage tends to induce a distinctive difference from the flexural damage in terms of the vibration properties in a composite beam, and this paves a way for possible separation of these two groups of parameters in an identification process using transverse vibration data. Finally, a genetic algorithm-based model updating is used to actually identify mixed flexural and shear connector damages in the composite beam. Results show that the damages in shear connectors and beam section can be identified with good accuracy. Further investigation into the robustness of the proposed method against noise and using real measurement data for the identification of damages in composite beams will be conducted in further study.

References

1. Xia, Y., Hao, H., Deeks, A.J., Zhu, X.: Condition assessment of shear connectors in slab-girder bridges via vibration measurements. J. Bridge Eng. **13**(1), 43–54 (2008)
2. Malveiro, J., Ribeiro, D., Sousa, C., Calçada, R.: Model updating of a dynamic model of a composite steel-concrete railway viaduct based on experimental tests. Eng. Struct. **164**(2018), 40–52 (2018)
3. Nie, J., Cai, C.S.: Steel–concrete composite beams considering shear slip effects. J. Struct. Eng. **129**(4), 495–506 (2003)
4. Wu, Y.-F., Xu, R., Chen, W.: Free vibrations of the partial-interaction composite members with axial force. J. Sound Vib. **299**(4–5), 1074–1093 (2007)
5. Tu, Z., Yong, L.: FE model updating using artificial boundary conditions with genetic algorithms. Comput. Struct. **86**(7–8), 714–727 (2008)

Chapter 7
Anomaly Detection Through Long-Term SHM: Some Interesting Cases on Bridges

D. La Mazza, F. Basone, M. Longo, P. Darò, and A. Cigada

Abstract The growing demand for health assessment of civil infrastructure has allowed for a dense control, among others, of many bridges. The new industrial design of monitoring systems, based on cheaper hardware, at the same time granting satisfactory performances, is making available huge data flows, allowing researchers not just to create a wide database but also to create logbooks of possible anomalies and defects, which can be both related to the infrastructure and the monitoring system. When prompt alarms are to be sent to the bridge manager, to avoid failures, there is the risk to produce false positives, due to specific data features or ambiguous recorded structural behaviors that may appear as damage, therefore requiring a deeper knowledge level of the expected structural response, to be fully understood and classified as not dangerous in terms of risk for the human life (structural reliability).

Only the combination of a continuous monitoring with the availability of an updated digital twin and a meticulous data interpretation of an expert engineer in the monitoring field can lead to a thorough understanding of the structural behavior and a proper asset management. In the present paper, an apparent damage identified by monitoring the dynamic response of a reinforced concrete bridge, under operational conditions, has proven to be a change of the static scheme of the structure, with a consequent bi-stable periodic variation of the structural behavior, explained, thanks to a fit-to-the-purpose numerical modeling.

Keywords Structural health monitoring · MEMS sensors · Operational modal analysis · Numerical modeling · Damage detection

7.1 Introduction

Since the early stages of SHM, a discussion started about the "sensing density": how many sensors or sensor nodes should be deployed on a structure and for how much time do we need to get data? These choices can have a dramatic impact on the system efficiency, as well as on the costs related to the initial installation, the periodic controls, and maintenance in general.

When managing a complex infrastructure, like a highway, a proper asset monitoring and decision-making process to optimize maintenance should be planned, to guarantee safety and resilience of transport infrastructure. The strategies may vary according to the outcome of a value-of-information analysis, based on a cost-benefit evaluation and resource optimization. Timed short-term monitoring or experimental testing (discrete in time) can help in saving money, as, given a certain budget, a higher number of sensors can be temporarily installed on the structure, providing a better spatial density, and then removed after the test completion, to be moved to another bridge. As a drawback, in this case, a higher personnel cost related to the team in charge of the monitoring system is to be accounted for. The opposite solution consists in designing a monitoring system to be permanently deployed on the structure: this solution offers many pros and cons, as the system has to be lighter, meaning a lower sensor density, though allowing for a continuous stream of information regarding the structural behavior. Therefore, it is possible to detect an immediate response to extreme events, like an earthquake or a flood in the case of bridges over rivers, or to get the seasonal trends due to temperature. This latter solution can help in reducing the

D. La Mazza · F. Basone · M. Longo · P. Darò
Sacertis Ingegneria S.r.l, Torino, Italy

A. Cigada (✉)
Department of Mechanical Engineering, Politecnico di Milano, Milan, Italy
e-mail: alfredo.cigada@polimi.it

H. Y. Noh (eds.), *Dynamics of Civil Structures, Volume 2*, Conference Proceedings of the Society for Experimental Mechanics Series, https://doi.org/10.1007/978-3-031-05449-5_7

number of false positives, alarms generated without a real structural problem, and which can anyway imply important social and economic costs and impact if not properly managed.

The problem of SHM in an industrial and robust perspective has already been the object of a series of references. After the milestone by Worden and Farrar [1] concerning the adoption of statistical and then machine learning approaches to structural health monitoring, other references, like [2, 3], have considered into details the challenges of dense sensing, when a higher volume of data needs to be managed for a prompt and quick evaluation.

Other papers have addressed the issues and the advantages in using systems based on MEMS and microcontrollers which constitute the basic step for extensive and dense monitoring both in space and in time [4, 5]: even a recent literature survey has shown how most of these devices [6, 7] are still confined to the world of research and they hardly comply with the robustness and the reliability issues which are to be considered a pre-requisite in the development of wide and industrial monitoring systems [5]. A second step aimed at providing value to long-term data is the capability to filter out environmental effects, at the same time avoiding to delete also those useful to detect damage [8]; in the end, once solved these aspects, the sensing capabilities are to be completed and supported by a proper data analysis, able to timely identify any eventual ongoing damage. Machine learning can be of great help, as simple events can be autonomously managed by a software; conversely, it has to be considered that any clustering cannot rely on a wide sample of damaged structures for proper supervised learning, and in addition, there is the risk of losing control on the more complex situations never managed by an automated damage recognition procedure. If prompt decisions are to be taken, an approach similar to that proposed in ISO 10816-1 [9] can be adopted, even if this standard has been developed for the condition monitoring of machines: in fact, the standard provides alerts and alarms based on zones whose boundaries are given by vibration magnitude criteria, evaluated as RMS amplitudes, an easy task to be evaluated; any further and more complex action depends upon the reached RMS vibration level.

The present paper is inserted into the described SHM trend: a bridge has been monitored using an industrial system developed with MEMS sensors, equipped with microcontrollers; then the network has been designed through a series of gateways and a connection to a cloud. The considered bridge is part of a more complex network made of more than 50 different structures being monitored by Sacertis Ingegneria: the proposed monitoring solutions have been optimized not for the single structure, but rather on the need to deploy standard devices which can be easily adapted to various structural kinds. Continuous monitoring has helped in a thorough understanding of an apparently odd structural behavior of one among the monitored bridges: any other choice would have hardly offered the chance to properly interpret the observed behavior. It is to be highlighted that the case presented in this paper is not unique: in the authors' experience, other quite similar cases are being carefully observed.

The paper sections will be organized as follows: first a description of the bridge will be given, together with some basic information about the specific measurement system, as part of the mentioned industrial design of the SHM process. Then the description of an observed anomaly will be provided together with an in-depth discussion on the supporting data analytics as well as the phenomenon structural explanation offered by the FEM digital twin numerical modeling.

7.2 The Monitored Structure

The viaduct under analysis is a reinforced concrete structure, built in the late 1950s and located in Northern Italy. It presents an overall length of approximately 118 m, divided by two structural joints into three parts, assumed as independent, with lengths, respectively, equal to 18 m (2 spans), 92 m (5 continuous spans, of which the maximum span is equal to at 32 m), and 8 m (1 span). The deck girder consists of five beams of variable height (2.9 m ÷ 3.7 m) and a slab with a thickness of 27 cm. The pier frames have two H-shaped concrete cross sections, connected to each other by transverse beams, as shown in Fig. 7.1.

7.3 The Monitoring System

The structure has been subject to continuous monitoring, as part of a wider testing, aimed at providing a structural diagnosis of existing and aging structures within a highway network. The monitoring system, installed on the structure during August 2019, consists of a wired network of 67 biaxial MEMS clinometers, 38 triaxial MEMS accelerometers, and 1 IoT gateway installed on one of the abutments. Two networks managed by the same gateway allow to get both slow varying data and dynamic data: the former is a power line-based architecture and the latter a CAN bus network. The acquired data are therefore

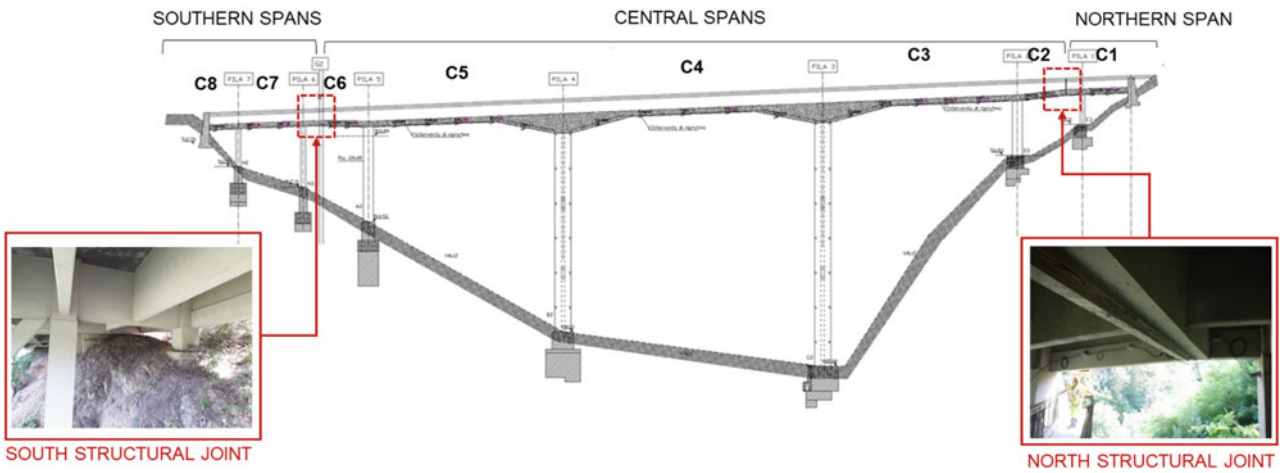

Fig. 7.1 Bridge elevation view with identification of the structural joint position

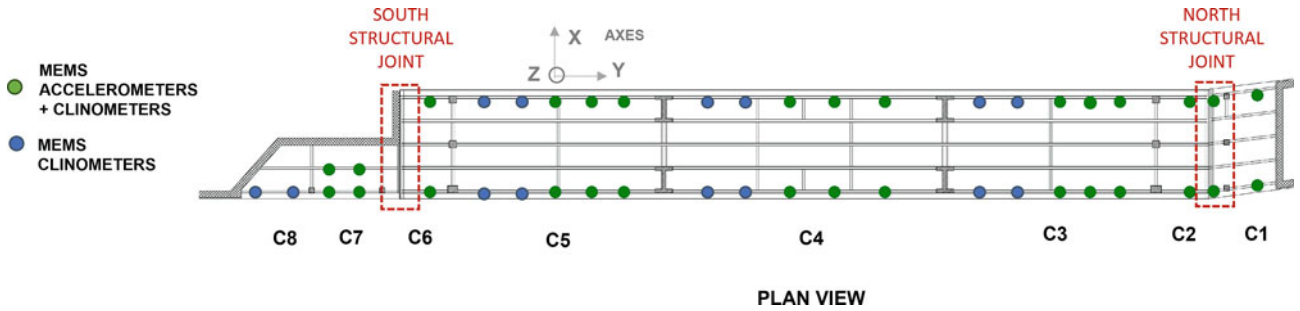

Fig. 7.2 Plan view of the bridge: Cn identifies the n^{th} span, blue dots are two-axis clinometers, and green dots identify a node made of a two-axis clinometer and a three-axis accelerometer

collected, pre-preprocessed, and filtered at the gateway level, to send a selection of significant information to the cloud for further analyses and long-term storage.

The biaxial MEMS clinometers installed on the viaduct have two measuring axes x and y, aligned to the transversal and longitudinal directions of the bridge, respectively, while the triaxial MEMS accelerometers have the additional z-axis oriented along the vertical direction as shown in Fig. 7.2. Both clinometers and accelerometers are equipped with a 32-bit microcontroller for data processing at the sensor level.

The clinometer data acquisition is executed by the gateway following a "polling cycle," a predetermined time interval interrogation under a sequential node order, adaptable with remote control. Each clinometer records a window of 1 second length with a sampling frequency of 208 Hz, providing synthetic statistical parameters like the mean value, standard deviation, maximum and minimum rotation, internal temperature, and relative humidity. The chosen sequential approach allows to spare network resources, missing the chance to have contemporary sampling: this just provides the bridge average behavior over a certain time lag in the order of minutes. To optimize the cloud resources and to guarantee some redundancy, the gateway stores the data received locally in a buffer memory and forwards it via a mobile network to the cloud database. The accelerometers perform a continuous data stream, with a sampling frequency of 100 Hz on the three measurement axes: as anti-aliasing filters are not provided, the real sampling frequency is 56 kHz, then followed by proper filtering and downsampling at the microcontroller level to get to the mentioned 100 Hz sampling frequency, without aliasing. The data are pre-selected and filtered at the gateway level to record and send to the cloud only those data selected from continuous acquisitions that have the most relevant energy content in terms of vibrational response. In addition, the gateway can further perform some pre-analysis based on defined threshold levels and on relevant groups of sensors, presenting the opportunity to have a prompt alerting system in case of anomalies. Anomaly conditions detected by different sensors correlated in space and time and the possibility to perform multi-parameter cross-checks help increase the reliability offered by the SHM system, avoiding false positives as much as possible. In the case of threshold exceedance, alerts are propagated to the cloud with attached an estimated severity metadata, to be handled with the appropriate urgency.

As such, the data collection, filtering, and pre-processing should be supported by a detailed and comprehensive analysis process of experts in assessing the structural state of health and conservation. FE numerical model updating procedures based on the monitoring data, detailed modal analysis, and reliability evaluation are needed to explore critical scenarios, identify threshold limits, and develop algorithms to perform long-term data interpretation, to efficiently support the asset management process.

7.4 Anomaly Detection and Data Analytics

The bridge has been subject to monitoring since August 2019, and at present, it's still under continuous control, with over 2 years of recorded data available, as a base to support the structural diagnostics and response interpretation. After the monitoring system installation, a diagnostic load test has been performed on the instrumented bridge to identify the static and dynamic structural response under given load conditions, with the aim to calibrate the preliminary finite element (FE) model, based on the available design information and the results of the periodic inspections. The measured responses have been compared with those derived from the theoretical model under the same loading condition and used as the basis for validating the FE model. The so-called model-updating procedure consists of an ad hoc optimization multi-step deterministic algorithm, developed by Sacertis, that aims to minimize an objective function expressing the residuals between numerical and experimental data. The updated FE model has been used to define thresholds for the key performance indicators (frequency shifts, STD, instantaneous or residual rotations, etc.) as a result of the simulation of relevant damage scenarios for the viaduct. Additional statistical thresholds have been defined, based on the initially recorded behavior, considered as the standard baseline, to perform a near-real-time anomaly detection at the gateway level.

Anomalies arose early, just after the initial baseline behavior characterization and threshold settings, as the monitoring systems identified a sudden change in the natural frequencies and longitudinal mode shapes, as well as a threshold exceedance of the average vibrational levels (STD) of the sensor group near the north joint. The anomaly persisted, showing an unstable dynamic response of the bridge, until it reached a new steady condition from the end of November up to May, when a second process of anomaly detection was followed by the return to the baseline behavior already observed in spring. There was clear evidence of a seasonal dependence of the bridge behavior from the environmental conditions; thermal actions were considered as the main actor playing a role in determining the anomaly, causing a variable joint behavior. This assumption was confirmed during summertime, when a third static scheme became apparent, characterized by a significant frequency shift (increase) of the lateral in-plane modal shape. Prompt analysis of the acquired data as well as of the FE models was performed to understand and justify the measured structural response (Fig. 7.3).

The first simplified analyses were carried out at the sensor level to offer the bridge management prompt and reliable surveys, on all the accelerometers belonging to the network, processing data in both the time and the frequency domains. In the frequency domain, operational modal analysis (OMA) algorithms were implemented, since under operational conditions the structure excitation, mainly given by traffic and ambient vibrations, has been reasonably assumed as white noise. The structure natural frequencies were derived analyzing the power spectral densities (PSDs) calculated on accelerations recorded by each sensor and each measurement axis, identifying the spectral peaks and later connecting information coming from the

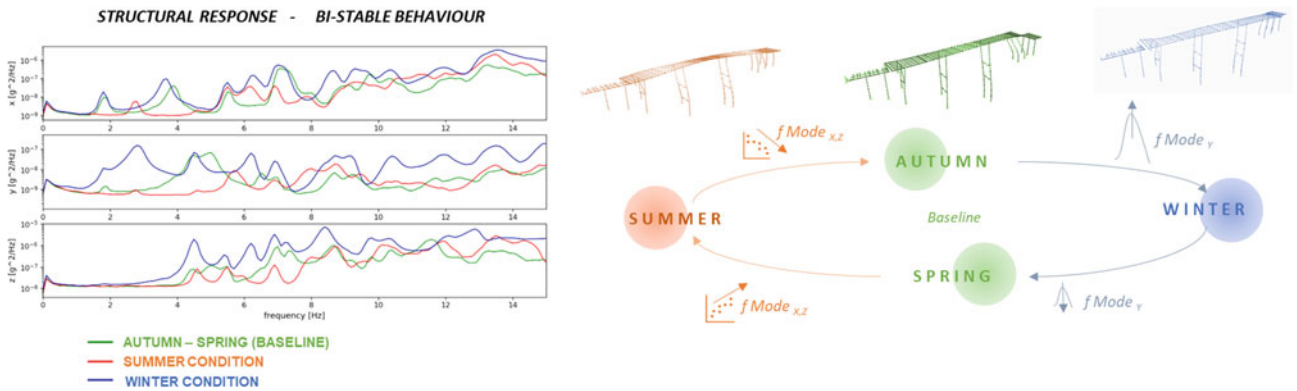

Fig. 7.3 Comparison of the three different bridge dynamic behaviors: green is autumn (this is the baseline), blue is winter, and red is summer; power spectral densities from one accelerometer are given of the left (each of them represents a stable and repeatable condition), and the first mode shapes are represented on the right

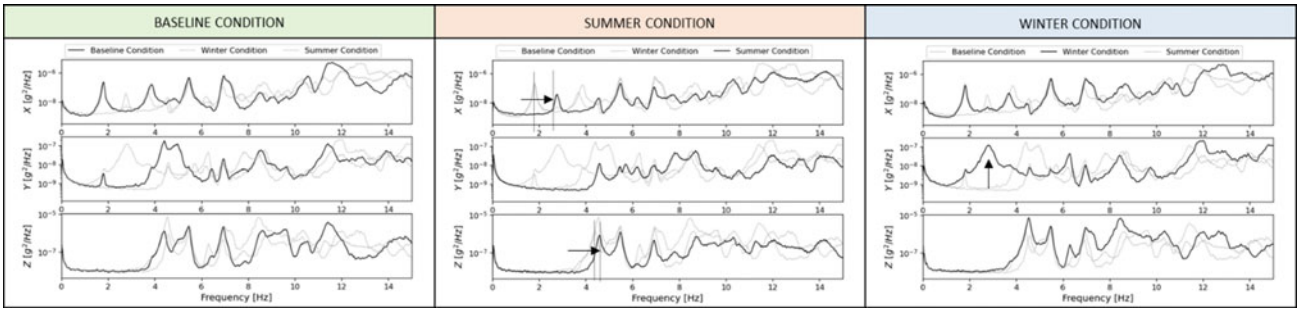

Fig. 7.4 PSDs evaluated based on one accelerometer recording in the three different conditions: (**a**) baseline, (**b**) winter, and (**c**) summer

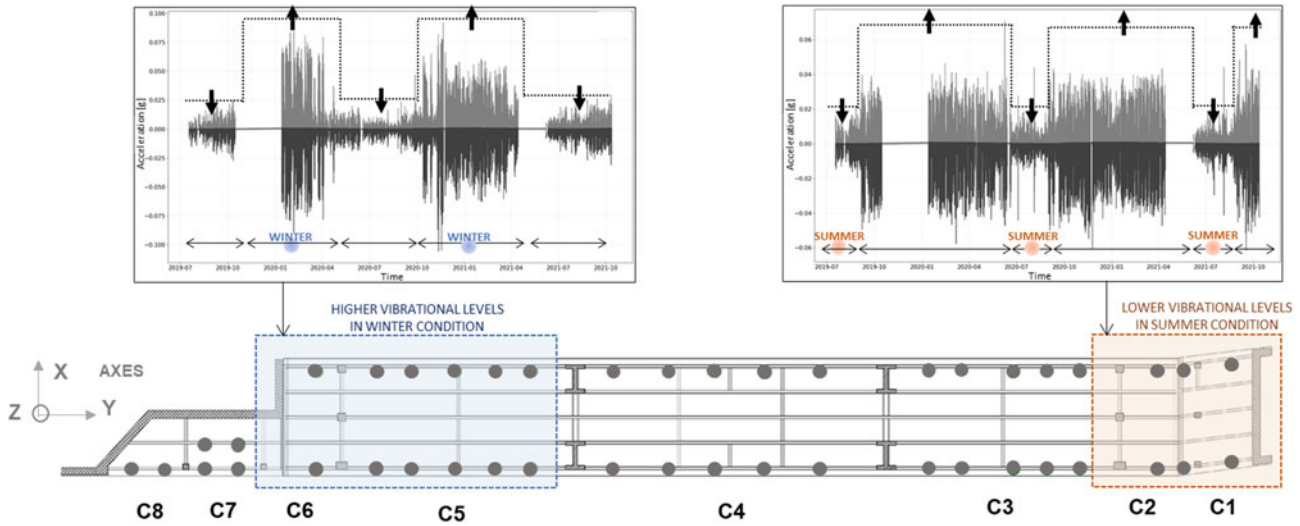

Fig. 7.5 Localization on the groups of sensors recording exceedance of vibrational thresholds in winter and summer time

entire network. Conversely, in time domain, the bridge vibrational behavior was characterized evaluating the trend of simple statistical parameters (STD, peak-to-peak, etc.), directly calculated on the collected raw accelerations.

Time-frequency domain analyses highlighted the dynamic behavior of the monitored bridge, exhibiting periodical changes in terms of both frequencies (Fig. 7.4) and vibrational response amplitudes (Fig. 7.5). In particular, three different dynamic responses were observed and characterized during the 2 years of monitoring.

The first response, hereinafter referred to as "baseline condition," was observed during early spring and early autumn. The structure showed the following principal modes of vibration: two lateral modes at 1.83 Hz and 3.9 Hz, respectively, the first flexural one at 4.4 Hz, a mixed flexural and torsional mode at 5.5 Hz, and a second flexural mode at 8.6 Hz. This situation was identified only from sensors installed in the central portion of the bridge (C2–C6) comprised within the two joints, confirming the assumed independent behavior of the deck parts between the two structural joints. In Fig. 7.4a, PSDs evaluated from baseline signals are shown, with regard to a sensor installed at mid-span of a central span (C4) and all its measuring axes (x, y, z). PSDs referred to in-plane directions (x and y), i.e., those mainly interested by a lateral mode, clearly show the presence of a prominent peak around 1.83 Hz, while visible peaks along the z-axis PSD are around frequencies associated with the already mentioned flexural vibration modes. This configuration corresponds to the structural response characterized at the beginning of the monitoring activities, as a base for the FE model updating process.

The second dynamic configuration has been identified periodically during the warmest season, hereby referred to as "summer condition." When in this state, the viaduct shows a global increase of the frequencies of the corresponding lateral and flexural modes. The increase is particularly evident in the lateral mode, where a positive variation of 1 Hz is experimented, while lower variations can be observed on the flexural modes (Fig. 7.4b). The out-of-plane mode is well recognizable in almost all the sensors, including those installed on the left and right sides of the structural joints (C1 and C7–C8 spans), as the three parts of the deck behave monolithically now. The change in the structure dynamic behavior affects the vibrational response, too. Indeed, sensors in proximity of the northern joint, in summer condition, showed a decrease in the

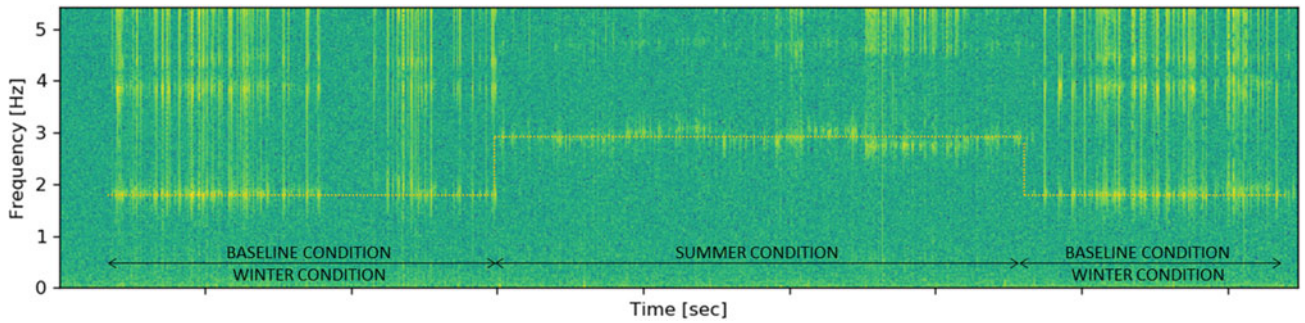

Fig. 7.6 Spectrogram of the frequencies registered by one of the sensors installed on the central spans

average vibration levels, highlighted through an exceedance of thresholds preliminarily fixed on vibration control parameters (STD and peak-to-peak – Fig. 7.5).

In the end, the third dynamic condition, hereinafter defined as "winter condition," was observed in cold weather. When temperature decreases, the bridge natural frequencies change again, showing a new longitudinal mode of vibration (3 Hz), highlighted in Fig. 7.4c, with prominent peaks in the PSDs calculated on acceleration data recorded along the y-axis, i.e., the direction parallel to the deck longitudinal axis. If the first lateral mode is considered, this remains the same as that of the baseline condition, while the first flexural mode frequency now lies between baseline and summer condition. The bridge vibrational response globally increases during winter condition for all the spans close to the southern joint, with respect to what was observed in the previous two dynamic configurations: in this state, the monitoring system detected an exceedance of the threshold levels on the group of sensors close to the joint.

In Fig. 7.6, it is shown a spectrogram of the frequencies registered by one of the sensors installed on the central spans, where it is evident the seasonal frequency shift of the lateral mode described above.

7.5 FE Numerical Digital Twin

The purpose of the FE modeling is to create a digital twin of the structure to support the monitoring system and simulate what, at a first glance, could have been considered as damage. Numerical models have been developed to compare and validate the data from the sensors. In fact, without a numerical simulation, it would be difficult to characterize the expected structural behavior in "standard" conditions and consequently to identify the onset of any anomalies.

The first step in the development of the digital twin is to model the structure, considering the available historical information; the second step involves the static and dynamic updating of the model to simulate the structural behavior at the time the monitoring started; this constitutes the initial state to which refer any future changes in behavior recorded by the sensors. Model updating is an essential activity since, especially in the case of existing structures, the response can differ significantly from the behavior that the viaduct had at the time of construction or was originally designed for.

Once the updated model has been defined, this can be used as a support tool to simulate the behavior recorded by the sensors (e.g., by simulating local damage to structural elements, by modifying the behavior of joints and supports, etc.) and to investigate the reasons that have produced the change in the structural response. This is the procedure followed also in the case of the viaduct in question, schematically represented in the following figure.

The model was developed in SAP2000, by means of "beam" elements (1D) spatially connected to each other and having non-linear behavior based on a formulation of concentrated plasticity; each element is associated with a fiber hinge to which the corresponding cross section, discretized into fibers, is assigned so that each fiber has a reference material (i.e., concrete or steel); once the strain of each fiber is obtained, the software is able to calculate the corresponding stress level and, by means of numerical integration, can define the behavior of each beam element and then of the entire structure. In this case, considering the static scheme of the viaduct and the anomalies recorded, it is necessary to give particular emphasis to the modeling of the structural joints: in fact, analyzing the seasonality of the measured changes, it was assumed that the response variations could be determined by a particular behavior of the joints rather than by a damage to structural elements (Fig. 7.7).

Starting from the updated model defined "baseline," sensitivity studies have been undertaken to justify the summer and winter conditions identified with the data analytics, in which the behavior of the structural joints has been investigated. For this purpose, NL-Links able to simulate the behavior at the interface between the initially assumed independent deck portions

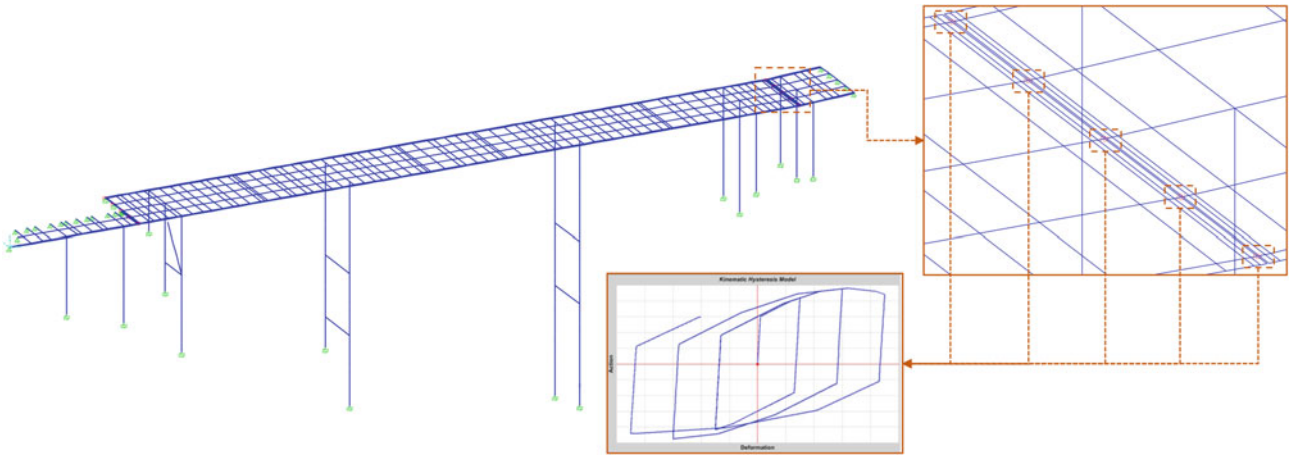

Fig. 7.7 3D view of the FE model with a detail of the southern structural joint and the related force-deformation law of each link

were introduced into the model, at the floor level. Each link allows to set six different stiffness values (three for rotational d.o.f. and three for rotational d.o.f.) with linear or non-linear law.

Based on the structural registered behavior, it was hypothesized that the variation in the response could be attributed to phenomena of a frictional nature, especially in the hottest periods in which, due to the thermal expansion of the deck and the presence of debris inside the joints, the end faces of the decks could come in direct contact, by modifying the dynamic response of the structure. Considering the nature of the phenomena to be simulated, each link has been associated with non-linear laws, different for the translational degrees of freedom in the horizontal and vertical plane, whose stiffness has been individually calibrated to reproduce the dynamic behavior over the year (cold periods-open joint vs warm periods-closed joint). The following figure illustrates a comparison of the out-of-plane modal shape simulated in two different structural joints conditions: "baseline" and "summer condition" (Fig. 7.8).

The following table shows a comparison between the results obtained by FE modeling and the frequencies measured by the sensors (Table 7.1).

The comparison in Table 7.1 shows that the modeling of the different joint conditions has allowed to reach a good approximation of the main structural modes in the different periods of the year; in fact, the differences between the frequencies measured by the accelerometers and those simulated by FE models are rather limited, in the range -8.9% $\div$ $+9.3\%$, and could be further refined by a more detailed updating: but the aim here was to explain the apparently odd bridge behavior.

7.6 Conclusion

Through the analysis of a real case, the paper aims at demonstrating some crucial aspects of a correct approach to SHM. A recurrent question arises about the choice to have periodic dynamic checks rather than a continuous monitoring. The road operator in charge of the bridge management had these checks taken randomly, getting results which could be hardly properly interpreted: the continuous monitoring and controls allowed to both identify the anomalies and interpret the recorded response using the reference updated FE non-linear model, also providing a structural diagnostics service as a support to the decision-making asset management process. Continuous monitoring provided accurate and in-time information concerning the structural health condition and performance. The continuous data stream and the automatic data processing controls at both the gateway and cloud level have allowed to rely on a wide database defining the different behaviors, and this, in turn, has required industrial and robust systems, in which the density of sensing, the quality of measurements, and self-diagnostics have played a crucial role.

A second key aspect to highlight is that the mentioned correct interpretation of the bridge behavior relies on a numerical model, properly tuned through measurements; this digital twin is an invaluable tool to interpret situations which data-driven approaches can detect but not interpret what is happening: the presence of a skilled engineer, together with the proper interpretation tools, becomes an unavoidable aspect preventing from false damage detection, with the associated huge money loss, in case an odd, perfectly understandable behavior is wrongly interpreted as damage.

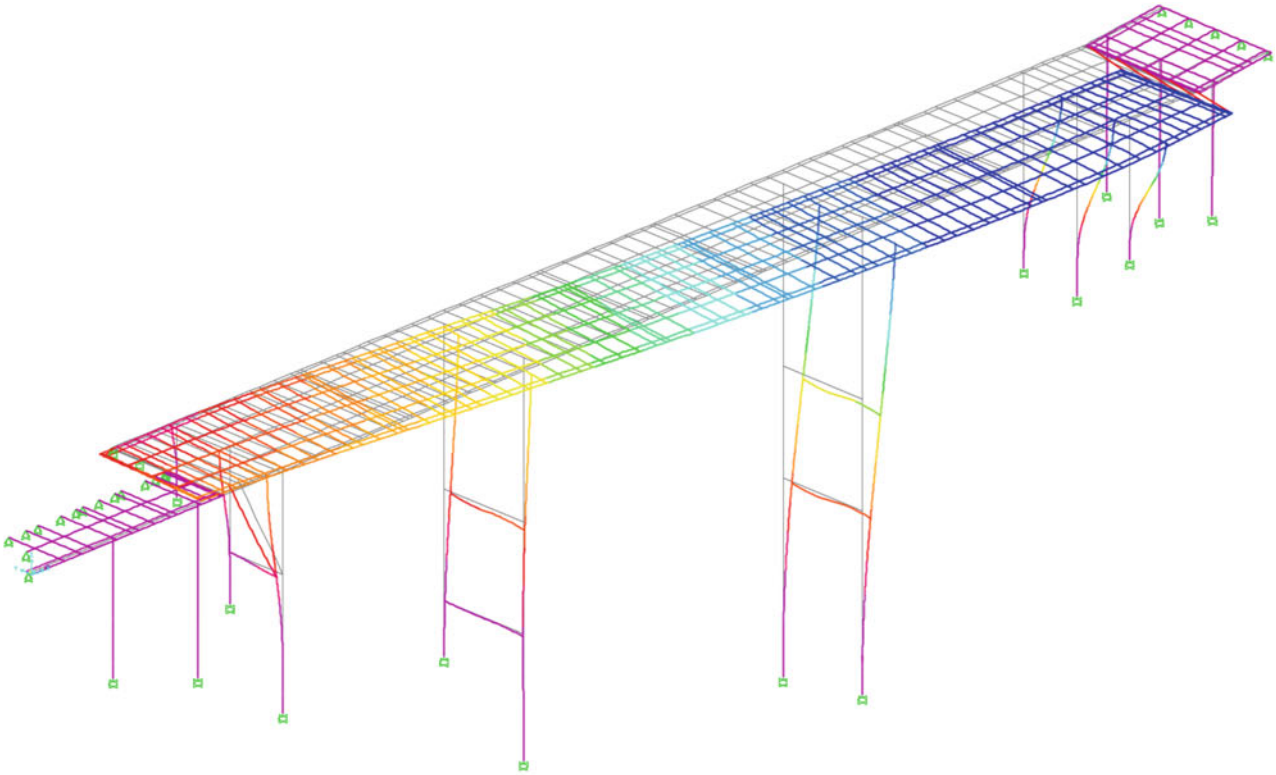

a) Baseline condition – out of plane mode – Freq. 1.79Hz

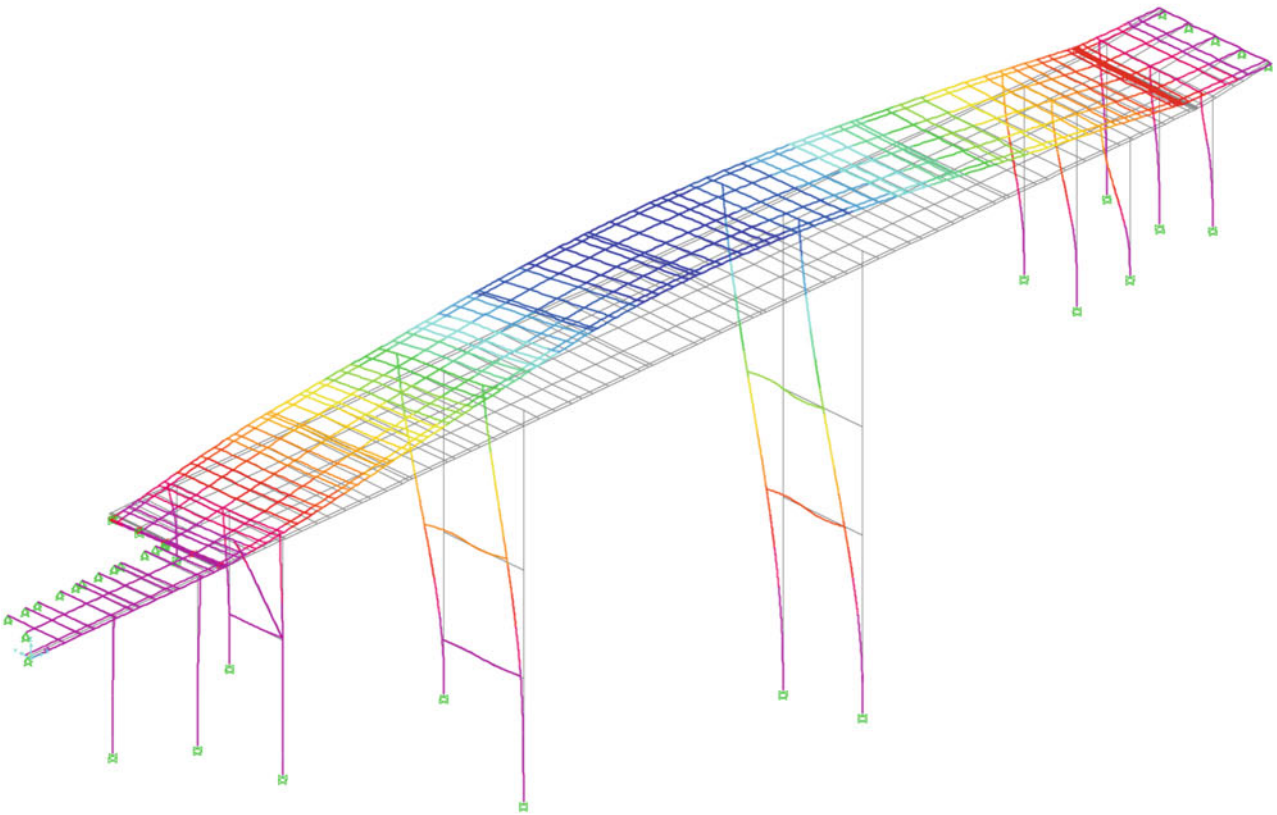

b) Summer condition – out of plane mode – Freq. 2.55Hz

Fig. 7.8 Comparison between out-of-plane modal shapes in distinct structural joints conditions: (**a**) "baseline" and (**b**) "summer"

Table 7.1 Comparison between experimental data and those provided by the FE model

Mode	Type	Baseline frequencies [Hz]			Summer frequencies [Hz]			Winter frequencies [Hz]		
		Sensors	FEM	Δ [%]	Sensors	FEM	Δ [%]	Sensors	FEM	Δ [%]
a	Lateral	1.83	1.79	−2.2	2.80	2.55	−8.9	1.80	1.85	+2.8
b	Flexural	4.40	4.26	−3.2	4.77	4.98	+4.4	4.60	5.03	+9.3
c	Flexural	8.60	8.77	+2.0	9.40	8.74	−7.0	8.45	8.74	+3.4

References

1. Farrar, C.R., Worden, K.: Structural Health Monitoring: A Machine Learning Perspective. Wiley (2012)., ISBN: 978-1-119-99433-6
2. Cury, A., Ribeiro, D., Ubertini, F., Todd, M.: Structural Health Monitoring Based on Data Science Techniques. Springer (2022)., ISBN 978-3-030-81715-2
3. Lynch, J.P., Sohn, H., Wang, M.L.: Sensor Technologies for Civil Infrastructures, Volume 2: Applications in Structural Health Monitoring. Woodhead Publishing Series in Civil and Structural Engineering (2014)., ISBN 9781782422426
4. Cigada, A., Lucà, F., Malavisi, M., Mancini, G.: Structural health monitoring of a damaged operating bridge: a supervised learning case study. In: Dynamics of Civil Structures, Volume 2, Proceedings of the 38th IMAC, A Conference and Exposition on Structural Dynamics. Springer (2020)., ISBN: 978-3-030-47633-5
5. Cawley, P.: Structural health monitoring: closing the gap between research and industrial deployment. Struct. Health Monit. **17**(5), 1225–1244 (2018). https://doi.org/10.1177/1475921717750047
6. Kavitha, S., Daniel, R.J., Sumangala, K.: High performance MEMS accelerometers for concrete SHM applications and comparison with COTS accelerometers. Mech. Syst. Signal Process. **66–67**, 410–424 (2016)
7. Ribeiro, R.R., de Melo Lameiras, R.: Evaluation of low-cost MEMS accelerometers for SHM: frequency and damping identification of civil structures. In: CILAMCE 2018: Ibero-Latin American Congress on Computational Methods in Engineering
8. Concepcion, R.S., Cruz, F.R.G., Uy, F.A.A., Baltazar, J.M.E., Carpio, J.N., Tolentino, K.G.: Triaxial MEMS digital accelerometer and temperature sensor calibration techniques for structural health monitoring of reinforced concrete bridge laboratory test platform. In: 2017 IEEE 9th International Conference on Humanoid, Nanotechnology, Information Technology, Communication and Control, Environment and Management (HNICEM), pp. 1–6 (2017). https://doi.org/10.1109/HNICEM.2017.8269422
9. ISO 20816-1:2016 Mechanical vibration — Measurement and evaluation of machine vibration — Part 1: General guidelines

Chapter 8
A Framework for Developing Efficient Vehicle-Bridge Interaction Models Within a Commercial Finite Element Software

Omar R. Abuodeh and Laura Redmond

Abstract The development of vehicle-bridge interaction (VBI) models is a popular technique to characterize the dynamic properties of vehicles and bridges. However, there is inherent complexity in the development of VBI models which must account for multibody dynamics of vehicles, structural dynamics of bridges, and vehicle-bridge contact relationships. Within the literature, three distinct frameworks exist for handling the model complexity of VBI: (1) hard coding the equations of motion of the vehicles and bridges while numerically coupling them in an arbitrary programming language; (2) developing a co-simulation that leverages a commercial finite element (FE) software to model the bridge and separately solve for the equations of motion of a vehicle; or (3) develop high-fidelity representations of both the bridge and vehicle through a commercial FE environment alone. While these unique frameworks offer accurate and reliable results, there exists a trade-off between frameworks that require sophisticated coding of the user but result in high computational speed (1 and 2) and frameworks with simple implementation but longer computation times (3). The present study attempts to bridge this gap and formulate a computationally efficient framework for implementing VBI modeling into a commercial FE software (Abaqus). This requires minimal coding by the user and could then be used by both the industrial and the research community. A VBI model of a passenger vehicle traveling across a bridge is modeled using the bicycle model concept and Euler beam element formulations within Abaqus. Robust node-to-surface contact algorithms within Abaqus are implemented to couple the vehicle to the bridge during the analysis. The dynamic responses of both the vehicle and bridge are verified with data from the literature. The study primarily follows a 2D scheme but concludes with a discussion of how these methods can be extended to a 3D scheme.

Keywords Vehicle-bridge interaction · Commercial finite element · Model verification · Abaqus

8.1 Introduction

Traditional techniques for inspecting damage in bridges rely on subjective assessments that lack resolution and often lead to inconsistent observations [1]. This motivated the research community to migrate toward other methods of quantifying structural damage such as examining changes in its modal/dynamic properties [2]. One recent health monitoring method, known as drive-by health monitoring (DBHM), involves using vehicle-mounted accelerometers to monitor bridge vibration through the acceleration readings taken from the vehicle [3, 4]. Afterward, the measured signals can be analyzed via physics-based [2, 5] or data-driven machine learning techniques [6]. In physics-based approaches, measured signals are often compared to the signals produced by a program-automated finite element (FE) model of the bridge-vehicle system that iteratively simulates different damage scenarios on a bridge, and then a machine learning (ML) algorithm is used to quantify the most likely location and severity of the damage in the bridge [1, 2, 5]. The FE models often consist of a moving sprung mass (i.e., vehicle body) on multiple 1D beam elements where a vehicle-bridge interaction (VBI) system is required to couple the vibration of these two bodies. Within the literature, three distinct frameworks exist for handling the model complexity of VBI: (1) hard coding the equations of motion of the vehicles and bridges while numerically coupling them in an arbitrary programming language [1, 2, 6–9]; (2) developing a co-simulation that leverages a commercial finite element (FE) software to model the bridge and separately solve for the equations of motion of a vehicle [10–12]; or (3) develop high-

O. R. Abuodeh (✉) · L. Redmond
Glenn Department of Civil Engineering, College of Engineering, Clemson University, Clemson, SC, USA
e-mail: oabuode@g.clemson.edu

H. Y. Noh (eds.), *Dynamics of Civil Structures, Volume 2*, Conference Proceedings of the Society for Experimental Mechanics Series, https://doi.org/10.1007/978-3-031-05449-5_8

fidelity representations of both the bridge and vehicle while employing a built-in contact formulation through a commercial FE environment alone [12–15].

While these unique frameworks offer accurate and reliable results, there exists a trade-off between frameworks that require sophisticated coding of the user but result in high computational speed (1 and 2) and frameworks with simple implementation but longer computation times (3). For instance, Yang et al. [7] manually coded in the VBI system for a sprung mass traveling across Euler beam elements to study the feasibility of extracting the bridge's natural frequency from the acceleration data measured from the sprung mass. However, the VBI system used does not account for nonlinear geometry or inelastic material definitions. In particular, Yu et al. [10] sought to overcome these shortcomings by linking MATLAB to Ansys, a commercial FE software with a suite of material definitions, and independently solving the equations of motion of the vehicle to obtain time histories of the tire locations and their respective contact forces. The time histories of these contact forces are applied to the bridge in a separate transient analysis using Ansys. Once the analysis is completed, the resulting time histories of the bridge nodal displacements are applied back to the vehicle model in MATLAB to solve the equations of motion of the vehicle and recompute the new tire forces that begin the analysis cycle again. This process continues until the difference between the tire forces computed in MATLAB and Ansys are minimal. The previous framework is limited to a specialized audience who is proficient in automating FE models with separate programming languages. In addition, it requires multiple iterations for the model to converge for a single vehicular trip, which makes it undesirable for applications like FE model updating in DBHM with ML algorithms.

Developing a VBI system entirely within a user-friendly commercial FE software would simplify the procedure and can be useful to a broader audience. However, to the authors' knowledge, the available published articles that analyze VBI systems completely in a commercial FE software are too computationally expensive for use in physics-based ML algorithms for DBHM [12–15]. For instance, Kwasniewski et al. [15] carried out an extensive 3D FE model of a VBI system involving a heavy truck and a selected highway bridge in Florida within LS-DYNA. The bridge deck, girders, steel reinforcement, and prestressed strands were all included in the model using elastic material definitions. The truck was completely replicated within the FE environment such that the tire was modelled using shell elements with two layers, an elastic rubber material and a fabric material for tire cord, while also employing an airbag option that simulates internal pressure in all tires. As a result, approximately 420,000 elements were generated for this study, including multiple point constraints and contact algorithms used during the dynamic analysis. The researchers reported a good correlation between field measurements and FE analysis. However, fully replicating a field test can prove to be time-consuming and difficult since appropriate modeling strategies must be followed to prevent instabilities that result from nodal misalignment.

The present study attempts to bridge the aforementioned gaps by completely proposing a framework to construct an efficient VBI entirely within a commercial FE software (Abaqus). A quarter-car and half-car models are completely modeled in Abaqus where the VBI is defined using a robust node-to-surface interaction command. Bridge/vehicle data reported in published articles [1, 7] are used to verify the proposed modeling framework.

8.2 Model Development

The most common method for developing a VBI model is to model the vehicle as a sprung mass, hereafter referred to as a quarter-car model, with two degrees of freedom; vertical motion of the center of mass and tire point of the vehicle model. An extension of the quarter-car model that accounts for additional modes is the half-car model, which uses the bicycle concept and has six degrees of freedom, two of which are vertical bounce and pitching motion of the half-car body and the remaining four are vertical motions of the front wheel, rear wheel, front tire, and rear tire. Both of these models are summarized in Fig. 8.1, where the subscripts "q," "v," "t," "R," "F," "S," and "R" are the quarter-car, half-car, tire, rear, front, rear, sprung, and un-sprung, respectively, and u and θ are vertical and pitch degrees of freedom, respectively. M and I are the mass and mass moment of inertia of the vehicles, respectively. K, C, and N are the stiffness, damping, and contact node of the vehicles, respectively. For the bridge model, E_b is the elastic modulus of the beam element, I_b is the moment of inertia of the beam element, A_b is the area of the beam element, μ_b is the mass per length of the beam element, and V is the constant velocity the vehicle drives.

In Abaqus, the vehicle and bridge bodies are modelled independently, and contact is represented using one of Abaqus's interaction definitions. Finally, the vehicle body is pushed with a user-given displacement across the bridge within a time period that is equal to the user-given velocity, while gravity is being applied to the mass of the vehicle.

The bridge elements are discretized with 2-node B23 Euler beam elements which use cubic interpolation functions with consistent mass matrix formulations. The quarter-car body is discretized with 4-node CPS4R plane stress elements and prescribed a rigid body definition. The half-car body is discretized using 2-node B21 linear Timoshenko elements which

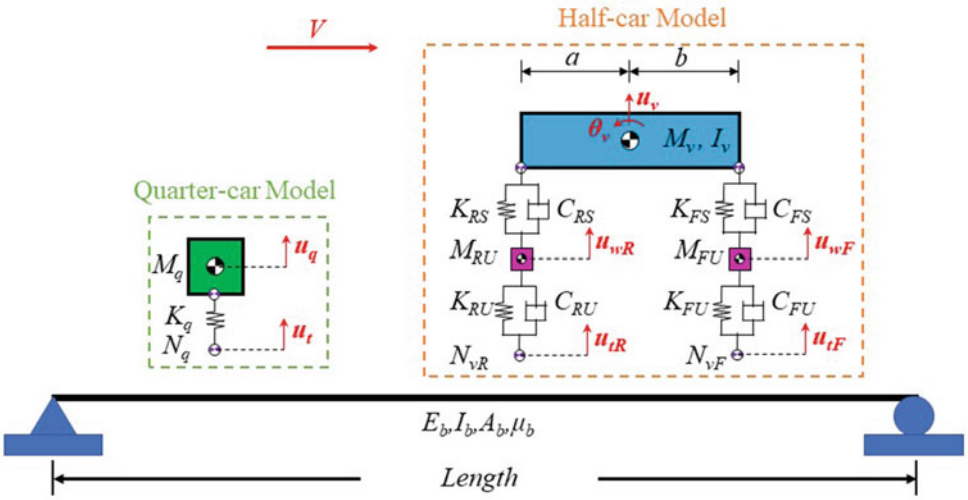

Fig. 8.1 A schematic of a Quarter-car model on a simply supported beam

use lumped mass formulations and are also prescribed a rigid body definition. The stiffness of the quarter-car and half-car models are modelled using SPRING2 elements, and the damping of the half-car model are modelled using DASHPOT2 elements [16]. Essentially, the bridge and vehicle elements are assigned density values to obtain desired inertial properties for the dynamic analysis. For defining density in a vehicle body, if the user desires the vehicle's center of mass to be located away from its midpoint, uniform density cannot be prescribed. Instead, the beam elements should be partitioned into multiple segments each with a user-defined density that would cumulatively yield the desired total mass, mass moment of inertia, and center of mass location. For a half-car model with its center of gravity at the midpoint between the wheels, it is important to note that more than one element should be used, since the mass moment of inertia calculated from the user-given density can deviate from the theoretical one for courser meshes [16]. In addition, depending on the vehicle configuration employed, the nodes that connect to the spring elements should be defined as either *pin* or *tie* nodes, where the pin nodes have only translational degrees of freedom associated with the rigid body (quarter-car model) and the tie nodes have translational and rotational degrees of freedom associated with the rigid body (half-car model) [16].

Furthermore, the vehicle and bridge bodies are coupled together using the *contact pair* formulation. In this study, node-to-surface contact pairs are employed where the tire node is the slave node and the beam surface is the master surface. The "hard" contact pressure-overclosure relationship is used to minimize penetration and avoid excessive contact chatter during the analysis. Similar contact formulations were used in a previous work [17], where Yao et al. constructed a framework for including surface roughness in a commercial FE software and verified it only against a quarter-car model.

Prior to analyzing the problem, the type and number of numerical methods, hereafter referred to as *steps*, should be defined. The vehicle needs to be in vertical static equilibrium before traveling across the beam elements. This requires the user to define gravity for the vehicle throughout all the steps. However, placing a *DASHPOT element within the initial static step results in long convergence times to reach static equilibrium. Therefore, the "`*Model change`" command [16] is used to temporarily remove the dampers during this step followed by adding them back in the next step. The model consists of three steps: two static steps and one implicit dynamic step. The first static step is defined to settle the vehicle body to its static equilibrium position vertically using gravity while removing DASHPOT2 elements. Afterward, the next static step is defined to add back the DASHPOT2 elements while maintaining static equilibrium. Finally, the last implicit dynamic step is defined to push the vehicle with a user-given velocity. During all the steps, the gravity load is only applied to the vehicle body of interest using the "`*Dload`" [16]. Figure 8.2 shows the "`*Dload`" and "`*Model change`" commands that are used in this study where their description can be found in [16]. It is worth noting that the first two steps are not required for a vehicle body without any dampers, similar to the work described in [17].

The Hilber-Hughes-Taylor time integration scheme is used during the implicit dynamic step where the integration parameters α, β, and γ are used for the direct integration of the equations of motion [16]. The β and γ integration parameters are part of the Newmark family where values of 1/4 and 1/2 follow the trapezoidal rule, which is numerically non-dissipative

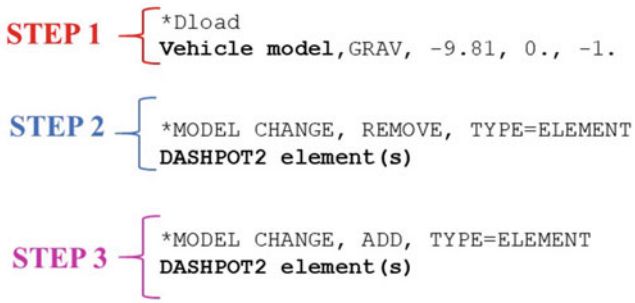

Fig. 8.2 Input file commands for adding gravity and changing element presence

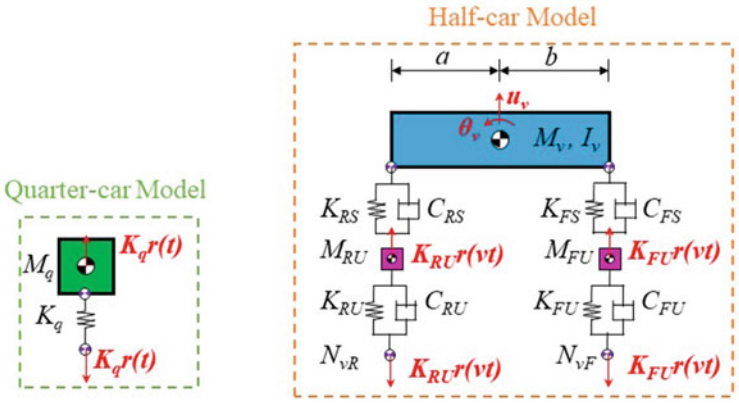

Fig. 8.3 Surface profile idealization for commercial FE software

in the presence of high-frequency vibration problems like contact penetrations/chatter [18]. Therefore, the α integrator parameter was introduced to provide numerical damping where the new relationships are described in Eqs. (8.1) and (8.2).

$$\beta = \frac{1}{4}(1-\alpha)^2 \tag{8.1}$$

$$\gamma = \frac{1}{2} - \alpha \tag{8.2}$$

Including surface roughness into VBI models is necessary to reflect noise present in physical tests of coupled bridge-vehicle systems. In a typical hard-coded FE model, a surface roughness profile is generated where the velocity and acceleration values are derived from the generated surface profile. The displacement, velocity, and acceleration are then used to calculate the contact force between the vehicle and the bridge within the equation of motion in a time-dependent scheme. Yao et al. [17] developed a simpler framework that mimics this dynamic response where it can be easily employed in a commercial FE software like Abaqus. An equivalent force with the magnitude equal to the product of the spring stiffness by the surface elevation is applied on both the contact point and the vehicle body to simulate the dynamic response that is observed when the vehicle drives on a rough surface. Further information regarding the development of this framework can be found in [17]. Figure 8.3 summarizes the framework in which the stiffness notation is similar to that of Fig. 8.1, whereas $r(vt)$ is the surface elevation at the position of the tire during its travel.

Material damping is incorporated into the model to represent realistic material behavior. To incorporate material damping in beam elements, Abaqus contains a material definition for applying the Rayleigh damping method in which two factors must be defined: α_R for mass proportional damping and β_R for stiffness proportional damping [16]. Equations (8.3) and (8.4) are used to compute these factors, where ξ is the damping ratio, ω_1 is the first mode's natural frequency, and ω_2 is the second mode's natura l frequency. The natural frequencies of beam elements can be computed using one of Abaqus's

built-in eigenvalue extraction methods: Lanczos, automated multi-level substructuring (AMS), and subspace iteration [11]. The Lanczos solver is used in this study.

$$\alpha_R = \xi \frac{2\omega_1\omega_2}{\omega_1 + \omega_2} \tag{8.3}$$

$$\beta_R = \xi \frac{2}{\omega_1 + \omega_2} \tag{8.4}$$

8.3 VBI Verification Study

In this study, two VBI models, a quarter-car model and a half-car model, are created using the proposed approach in Abaqus, and their results are compared to the dynamic response of hard-coded VBI models taken from the literature [1, 7]. For the quarter-car model, the following properties taken from Yang et al. [7] are used to model the beam: length $L = 25$ m, $E_b = 2.75 \times 10^{10}$ N/m^2, $\mu_b = 4800$ kg/m, $I_b = 0.12$ m^4, and no damping. The vehicle properties are $M_q = 1200$ kg, $K_q = 500{,}000$ N/m, $V = 10$ m/s, and zero damping. The natural frequencies of the bridge (ω_b) and vehicle (ω_v) can be computed individually using the built-in frequency step in Abaqus and are $\omega_b = 2.08$ Hz (first mode's natural frequency) and $\omega_v = 3.25$ Hz. A surface profile was not defined during the quarter-car simulation.

For the half-car model, the following properties are used from Locke [1] to model the beam: $L = 21.3$ m, $E_b = 200 \times 10^9$ N/m^2, $\mu_b = 5600$ kg/m, $\xi = 3\%$, and $I_b = 0.0842$ m^4. The properties of the vehicle are $M_v = 12{,}404$ kg, $I_v = 172{,}160$ kg/m^2, $M_{FU} = 725.4$ kg, $M_{RU} = 725.4$ kg, $K_{FS} = 727{,}812$ N/m, $K_{RS} = 1{,}969{,}034$ N/m, $K_{FU} = 1{,}972{,}900$ N/m, $K_{RU} = 4{,}735{,}000$ N/m, $V = 10$ m/s, $a = 3$ m, and $b = 3$ m. Similar to the quarter-car model, the natural frequencies are computed using the frequency step and are $\omega_b = 6.00$ Hz (first mode's natural frequency), $\omega_{v1} = 1.27$ Hz (pitch with front unsprung bounce), $\omega_{v2} = 2.17$ Hz (pitch mode with rear unsprung mass bounce), $\omega_{v3} = 9.75$ Hz (front unsprung masses bounce), and $\omega_{v4} = 15.4$ Hz (mode rear unsprung bounce). In both models, the beams are discretized into 50 elements following a trial-and-error Scheme. A road profile is generated using the power spectral density (PSD) method defined by ISO-8608 standards [19] where Road Class A was used with a displacement PSD (G_d) of 32×10^{-6} m^{-1} with a spatial frequency (n_0) of 0.1 cycles/m. The spatial frequency band spans from 0.001 to 10 cycles/m at an increment of $1/L$. During the implicit dynamic step, a common issue that users face when employing contact algorithms in Abaqus is contact chatter, which is when a slave node falls off a master surface [16]. To overcome this issue, the *moderate dissipation* application is used to stabilize the model and reduce contact chatter [16] where $\alpha = -0.41421$, $\beta = 0.5$, and $\gamma = 0.91421$, while the time step used was 0.001 seconds. A sensitivity analysis was carried out to test different numerical damping values and found the recommended use of the moderate dissipation application removed contact chatter with and resulted in negligible change in vehicle response and change in bridge response.

Figure 8.4 shows the results that were extracted from the quarter-car simulation for both the proposed FE model and Yang's FE model [2], where Fig. 8.4a, b are the acceleration signals extracted at midspan of the bridge and center of mass

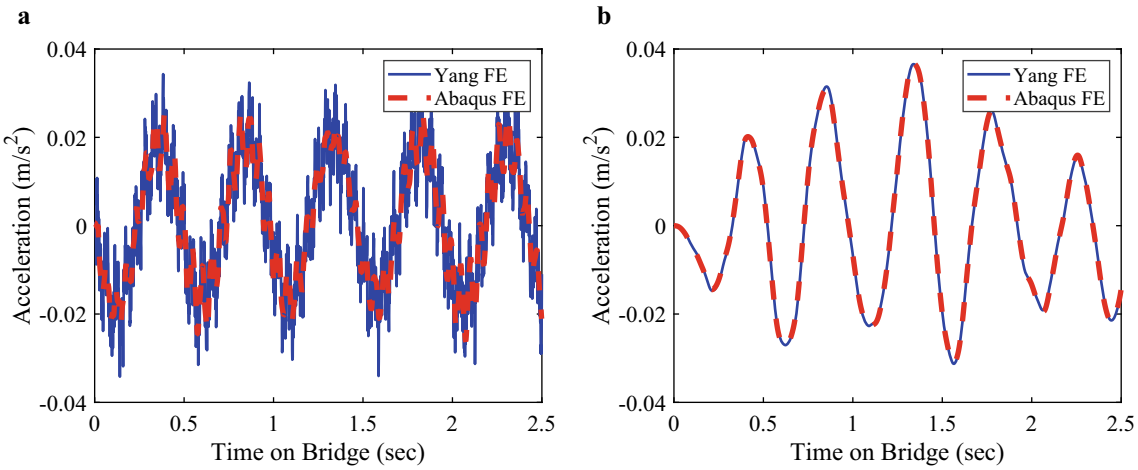

Fig. 8.4 Quarter-Car dynamic response curves. (**a**) Acceleration signal of bridge midspan. (**b**) Acceleration signal of sprung mass

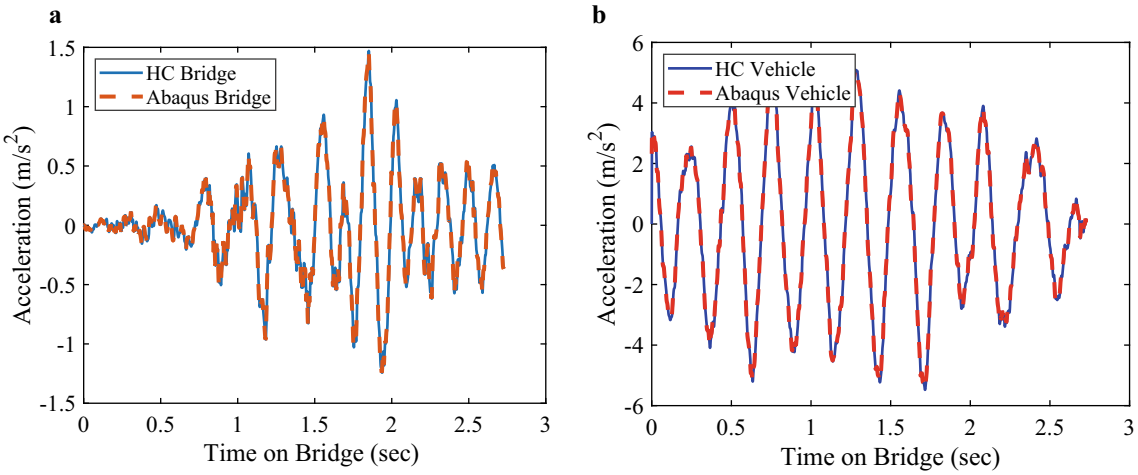

Fig. 8.5 Half-Car dynamic response curves. (**a**) Acceleration signal of bridge at midspan. (**b**) Acceleration signal of vehicle

of the vehicle, respectively. It can be observed that the acceleration at midspan of the bridge for both models are not fully in line with each other. This is attributed to the method employed when distributing the contact force of the tire to the adjacent nodes of a beam element. Yang et al. [2] used the cubic Hermitian interpolation function for the transverse displacement of the element to compute the displacement, velocity, and acceleration of two nodes based on the position of the vehicle within contacted element. However, the proposed Abaqus FE model uses a node-to-surface contact formulation in which the contact force is resolved using a hard contact pressure-overclosure relationship and is based on the tire's contact force as a function of its penetration [11]. This means that Abaqus internally generates a stiffness matrix for the contact area during the analysis in which the equivalent contact force is computed relative to the node of that contacted element, thus causing a smoothing effect on the acceleration response, as shown in Fig. 8.5a. Furthermore, discrete Fourier transform (DFT) is carried out to map acceleration signals into their respective frequency domains for further verification. The computed peak spectrum amplitudes and their corresponding frequencies are 0.0113 m/s^2 and 2.20 Hz in both models, respectively, for the vehicle acceleration signals and 0.00880 m/s^2 and 1.99 Hz, respectively, for the bridge acceleration signals in both models.

Figure 8.5 shows the results that were extracted from the half-car simulation for both the proposed FE model and the hard-coded (HC) FE model [1], where Fig. 8.5a, b are the acceleration signals recorded at midspan of the bridge and center of mass of the vehicle, respectively. As opposed to the quarter-car simulations, the half-car simulation demonstrates bridge acceleration curves that are more in line, as shown in Figs. 8.4a and 8.5a. This is attributed to the effects that material damping and surface roughness have on the dynamic response of the bridge where the sharp amplitudes that are supposed to occur in the HC FE model are smoothened. Similar to the quarter-car simulation, the DFT of the signals are computed where the peak spectral amplitudes and frequencies are 13.7 m/s^2 and 3.66 Hz, respectively, for the vehicle signals in both models, respectively, and 0.0947 m/s^2 and 6.22 Hz, respectively, for the bridge signals in both models.

8.4 Conclusion

This study proposes an efficient framework to construct a VBI model entirely within Abaqus using minimum coding from the user. The implementation of such a framework can be advantageous to users who are interested in exploring the realm of VBI to include nonlinear effects while maximizing computation efficiency. In addition, this study can be expanded to a three-dimensional outlook to increase the user's parameter space by including more modal shapes when processing the data using physics-based or ML-driven approaches. The presented framework is composed of representing the vehicle and bridge bodies using Abaqus's built-in element definitions; defining appropriate material definitions that reflect the physical aspects of the problem; employing a node-to-surface contact formulation that is responsible for coupling the vehicle and bridge; and defining the numerical methods used to solve a typical VBI problem. As a result, the proposed approach was successful in producing FE models that agree with the VBI models employed in published literature. The following can be concluded from the present work:

- Abaqus consists of element and material libraries that can be used to capture the dynamic response of VBI models.
- The use of node-to-surface contact formulations in Abaqus is successful in coupling the vehicle to the bridge.
- The proposed three-step methodology of deleting and adding dashpot elements allows the vehicle to reach static equilibrium quickly before traveling across the bridge.
- Representing surface profiles using equivalent forces is an accurate and simple technique for recreating the effects of surface roughness on the dynamic response of a vehicle body within commercial FE software packages.
- Moderate dissipation in the dynamic analysis step was sufficient to remove contact chatter without significantly influencing coupled vehicle-bridge dynamics.

Acknowledgments Omar Abuodeh was supported by Clemson's NRT RIES program and the National Science Foundation under grant #1633608. Such financial aid is greatly acknowledged.

References

1. Mokalled, S., Locke, W., Abuodeh, O.R., Redmond, L., McMahan, C.: Drive-by health monitoring of highway bridges using Bayesian estimation technique for damage classification. Struct. Control Health Monit. **29**, e2944 (2021)
2. Locke, W., Mokalled, S., Abuodeh, O.R., Redmond, L., Mcmahan, C.S.: An intelligently designed AI for structural health monitoring of a reinforced concrete bridge. Proceedings of The Concrete Industry in the Era of AI, 1–9 (2021)
3. Lin, C.W., Yang, Y.B.: Use of a passing vehicle to scan the fundamental bridge frequencies: an experimental verification. Eng. Struct. **27**(13), 1865–1878 (2005)
4. Miyamoto, A., Yabe, A.: Bridge condition assessment based on vibration responses of passenger vehicle. J. Phys. Conf. Ser. **305**, 1–10 (2011)
5. Lam, H.-F., Yang, J.-H., Au, S.-K.: Markov chain Monte Carlo-based bayesian method for structural model updating and damage detection. Struct. Control. Health Monit. **25**(4), 1–22 (2018)
6. Locke, W., Sybrandt, J., Redmond, L., Safro, I., Atamturktur, S.: Using drive-by health monitoring to detect bridge damage considering environmental and operational effects. J. Sound Vib. **468**(3), 1–17 (2020)
7. Yang, Y.B., Lin, C.W., Yau, J.D.: Extracting bridge frequencies from the dynamic response of a passing vehicle. J. Sound Vib. **272**(3–5), 471–493 (2004)
8. Siringoringo, D.M., Fujino, Y.: Estimating bridge fundamental frequency from vibration response of instrumented passing vehicle: analytical and experimental study. Adv. Struct. Eng. **15**(3), 417–433 (2012)
9. Kim, C.W., Kawatani, M., Kim, K.B.: Three-dimensional dynamic analysis for bridge-vehicle interaction with roadway roughness. Comput. Struct. **83**(18–19), 1627–1645 (2005)
10. Yu, H., Wang, B., Li, Y., Zhang, Y., Zhang, W.: Road vehicle-bridge interaction considering varied vehicle speed based on convenient combination of Simulink and ANSYS. Shock. Vib., 1–14 (2018)
11. Wang, L., Kang, X., Jiang, P.: Vibration analysis of a multi-span continuous bridge subject to complex traffic loading and vehicle dynamic interaction. KSCE J. Civ. Eng., 1–10 (2015)
12. Li, Y., Xu, X., Zhou, Y., Cai, C.S., Qin, J.: An interactive method for the analysis of the simulation of vehicle-bridge coupling vibration using ANSYS and SIMPACK. Proc. Inst. Mech. Eng. F J. Rail Rapid Transit. **232**(3), 663–679 (2018)
13. Lu, X., Kim, C., Chang, K.: Finite element analysis framework for dynamic vehicle-bridge interaction system based on ABAQUS. Int. J. Struct. Stab. Dyn., 1–36 (2020)
14. Shui-rong, G., Lu, L., Shui-sheng, C., Hui, Z.: Research on models of a highway bridge subjected to a moving vehicle based on the LS-DYNA simulator. J. Highw. Transp. Res. Dev. **8**(3), 76–82 (2014)
15. Kwasniewski, L., Li, H., Wekezer, J., Malachowsk, J.: Finite element analysis of vehicle-bridge interaction. Finite Elem. Anal. Des. **42**, 950–959 (2006)
16. Smith, M.: ABAQUS/Standard User's Manual. Dassault Systems Simulia Corp (2020)
17. Yao, Z., Sheng, Z., Tjhen, L.S.: A simple approach for simulating the road surface roughness involved in vehicle-bridge interaction systems. Int. J. Struct. Stab. Dyn. **18**(7), 1–10 (2018)
18. Hilber, H.M., Hughes, T.J.R., Taylor, R.L.: Improved numerical dissipation for time integration algorithms in structural dynamics. Earthq. Eng. Struct. Dyn. **5**, 283–292 (1977)
19. ISO-8608, Mechanical vibration — road surface profiles — reporting of measured data

Chapter 9
Damaged Metamaterials: Structural Health Monitoring and Damage Tolerance

Daniel Kiracofe, Utkarsh Wani, and Y. F. Xu

Abstract Locally resonant metamaterials have been gaining intense interest recently for their ability to greatly attenuate shock and vibration. All existing studies of metamaterials assume that the structure is intact and undamaged. However, all real-world structures will eventually experience some damage (e.g., due to manufacturing defects, material inclusions, handling damage, corrosion, etc.). For metamaterials to be placed in service in real applications, an understanding of their behavior in the presence of damage is necessary. This chapter explores two related concepts: structural health monitoring (i.e., damage detection) and damage tolerance (i.e., robust performance in the presence of failures). Central to both concepts is the fact that metamaterial damage creates highly localized modes near the damaged location, which may cause undesirable high local stresses. Damage can be detected by observing the presence of these modes, and damage tolerance can be improved by designing the metamaterial in such a way as to tailor these local modes to mitigate the stress increases.

Keywords Elastic metamaterials · Band gaps · Bloch's theorem · Damage detection · Damage index · Structural health monitoring · Damage tolerance · Vibration isolation

9.1 Introduction

Metamaterials are structures designed in such a way that wave propagation/transmission through the material is modified from that of a naturally occurring material. Application areas include cloaking, isolation, and lensing [1–6]. Classes of metamaterials include optical, acoustic, and elastic, depending on the type of wave propagation being considered. A unique feature of a metamaterial is a bandgap, a frequency range over which waves will not propagate. For elastic metamaterials, bandgaps can be created via two mechanisms: phononic crystals (PCs), which rely on periodic modulation of properties, and local resonators (LRs), which include a periodic arrangement of resonant mass/spring system [7]. A sample LR metamaterial and the corresponding bandgap are illustrated in Fig. 9.1.

Locally resonant elastic metamaterials have intensely studied recently due to their unique abilities to achieve extremely high vibration and shock attenuation [8–13]. However, virtually all existing works on the subject assume that the material is completely intact and undamaged.

Various researchers have considered optimizing width of the bandgap [14], the location (frequency) of the bandgap [15], the maximum attenuation inside the bandgap (for a finite structure) [16], or increasing performance while minimizing resonator mass [17]. No attention has been paid to damage tolerance or robustness in the presence of failure or to reducing the probability of failures in the first place.

D. Kiracofe · U. Wani · Y. F. Xu (✉)
Mechanical & Materials Engineering, University of Cincinnati, Cincinnati, OH, USA
e-mail: kiracodl@ucmail.uc.edu; wanius@mail.uc.edu; xu2yf@uc.edu

H. Y. Noh (eds.), *Dynamics of Civil Structures, Volume 2*, Conference Proceedings of the Society for Experimental Mechanics Series, https://doi.org/10.1007/978-3-031-05449-5_9

9.2 Behavior of Damaged Metamaterials

Arrays of equally spaced identical resonators appear in many contexts, for example, MEMS [18], and turbomachinery [19], as well as the sound and vibration literature prior to the widespread use of the term "metamaterials" [20]. In all these contexts, it is known that normal vibration modes have energy that is spread out among the different resonators, but if one resonator is significantly different from the others, then there will be vibration modes that are very localized at the unique resonator.

A good example of this concept is given by Gao et al. [21], who demonstrated the effect of point damage on an acoustic metamaterial. This is also the only work the authors are aware of that specifically investigated the effect of damage on metamaterials. They studied the distributions of acoustic intensity and phase for various oscillation modes of a 1D metastructure made up of Helmholtz resonators. Local modes were observed at specific frequencies resulting in trapped oscillations near the location of point defect. At the frequency of the defect mode, acoustic energy is highly localized at the defect location along with its surrounding and decreases away from it exponentially.

In this chapter, three metastructures referred to as intact, heavily damaged, and slightly damaged are studied. In the next section, we will show that wide bandgaps are observed in the FRFs associated with the intact metastructure, while the FRFs of the two damaged metastructures show large peaks in the bandgaps due to their respective damages. Local modes are observed in the vicinity of the bandgaps due to the damage. In Sect. 9.3, the occurrence and locality of the damage in the two damaged metastructures is detected using a driving-point damage index. Furthermore, in Sect. 9.4, we show that the presence of highly localized modes near the damaged locations causes undesirable high local stresses at those locations. The damage tolerance of the metamaterial can be enhanced by designing it to tailor these local modes to attenuate increase in stresses.

9.2.1 Example Using Finite Element Models

In this section, we show the local modes that can arise in the typical finite length metastructure shown in Fig. 9.1a. The basic geometry of a host beam with beam-like resonators is similar to that used by Qureshi et al.[22] although the geometry is different. The material is assumed to be steel (E = 200 GPa, $\mu = 0.3$, and $\rho = 7850$ kg/m^3). For convenience, a numbering scheme is illustrated: the clamp is location 1, the locations where the resonators are attached are denoted with odd numbers, and the locations in between resonators are denoted with even numbers.

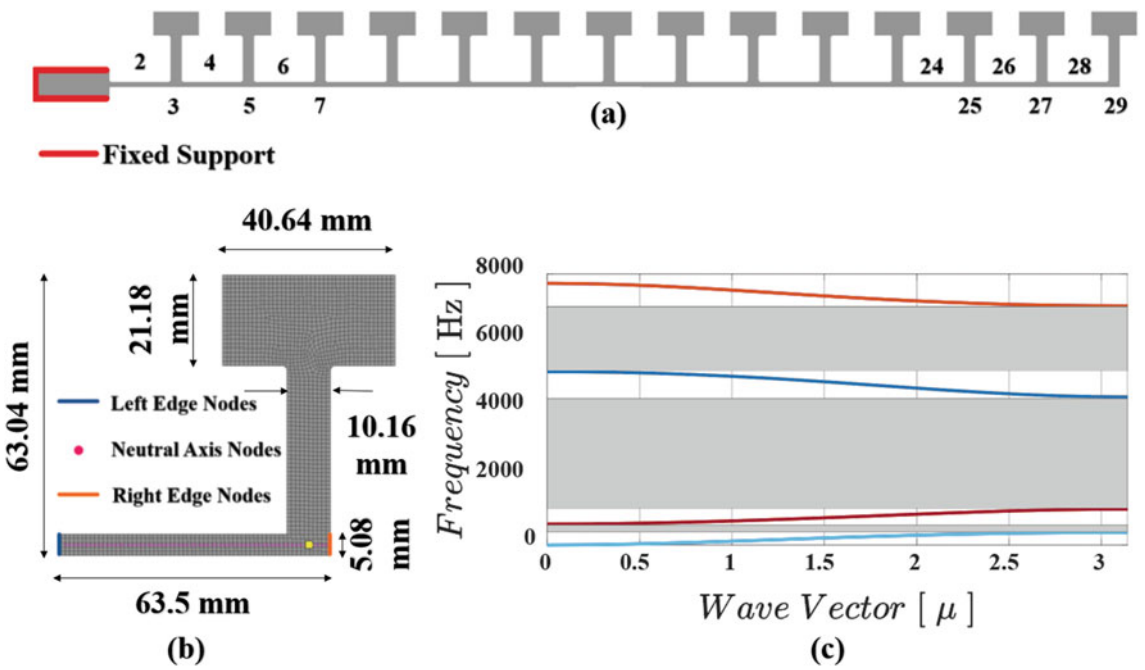

Fig. 9.1 (**a**) Typical metastructure consisting of a host beam with 14 resonators attached periodically, (**b**) meshed finite element model of a single unit cell of the metastructure, and (**c**) flexural dispersion curve of the unit cell from part (**b**). The bandgaps are shaded gray

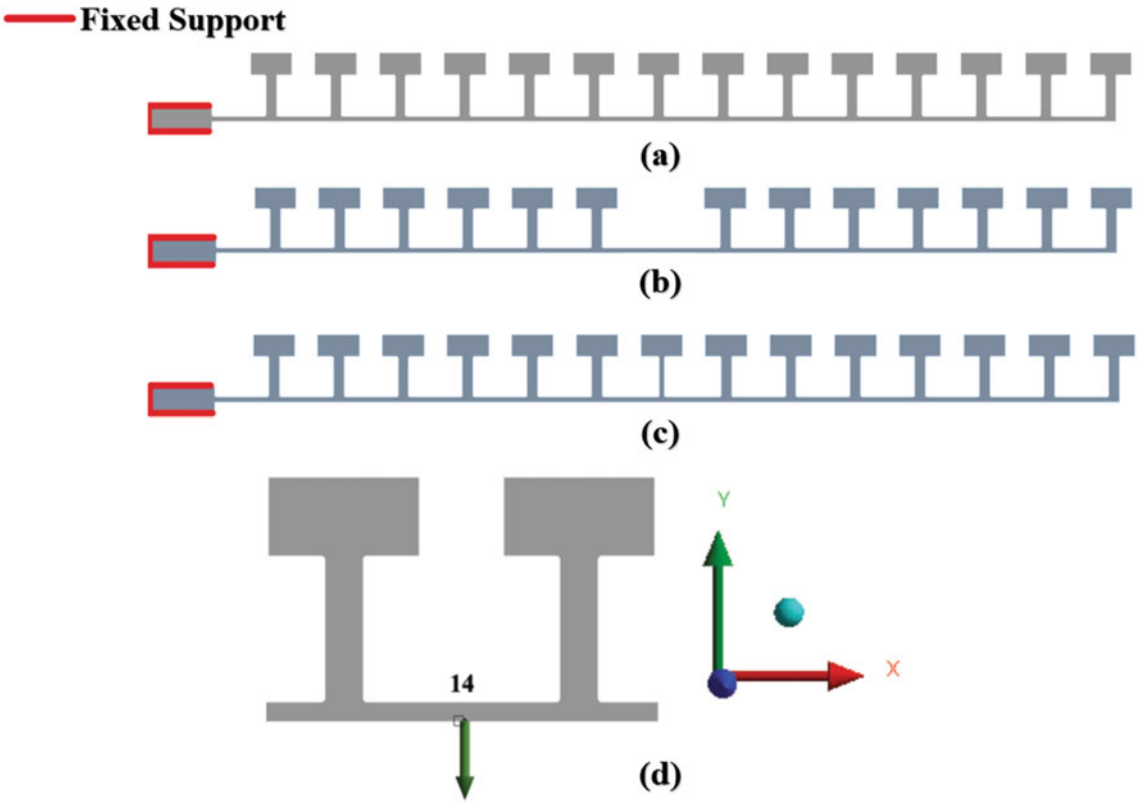

Fig. 9.2 Illustration of three different finite length metastructures. (**a**) Baseline fully intact, (**b**) heavily damaged metastructure, the seventh resonator is entirely removed, (**c**) slightly damaged metastructure, the connection between the host beam and the seventh resonator mass is thinned to decrease the stiffness, and (**d**) forced response simulations for all three were conducted using the excitation and response locations shown: between the sixth and seventh resonators

To obtain the infinite structure dispersion curve for this structure, a typical unit cell shown in Fig. 9.1b is meshed using plane stress elements in ANSYS Mechanical. In order to show only the flexural modes on the dispersion curve, motion in the axial direction is constrained on the neutral axis. The resulting stiffness and mass matrices are then exported, with the left edge nodes and right edge nodes identified as shown, and the dispersion curve is computed using the method of Bloch theorem, which governs the displacement of the element nodes. Floquet boundary conditions are used, which simulate an infinite tessellation of the unit cell [23]. The resulting dispersion curve is shown in Fig. 9.1c. As is typical for this type of structure, there are multiple frequency ranges, bandgaps, in which flexural waves cannot propagate, and these are shaded in gray.

To understand the behavior of a damaged structure, we now simulate a finite length metastructure with and without damage. Figure 9.2 shows (a) the intact structure, (b) a heavily damaged structure with one of the resonators removed, (c) a slightly damaged metastructure with one of the resonators damaged, and (d) location of excitation and response for one of the metastructures. The results of a forced response analysis are shown in Fig. 9.3a. Considering the FRF (frequency response function), the intact metastructure has a very high attenuation in the bandgap regions. As the structure is finite length and not infinite, flexural waves can propagate in the bandgap region, but they are strongly attenuated. However, for the damaged metastructure, there are multiple strong peaks in the bandgap region. These correspond to highly localized modes, the modeshapes of which are illustrated in Fig. 9.3b–g. A flexural wave can propagate in the damaged region with no resonator, but it cannot propagate beyond that into the region with resonators. Therefore, the mode becomes "trapped" in the narrow region around the damaged resonator.

The above is an extreme example of damage, and the entire resonator is completely removed. A less extreme example might be a small crack forming in the resonator connection, which would reduce stiffness. This is simulated for the metastructure in Fig. 9.2c, in which the thickness of the connector is reduced in order to reduce the stiffness. The results of an analysis on this structure are shown in Fig. 9.4. Similar to the heavily damaged case, local modes are visible in this case too. However, the peaks in the FRF are not quite as high, and the modes are not quite as localized near the damaged location.

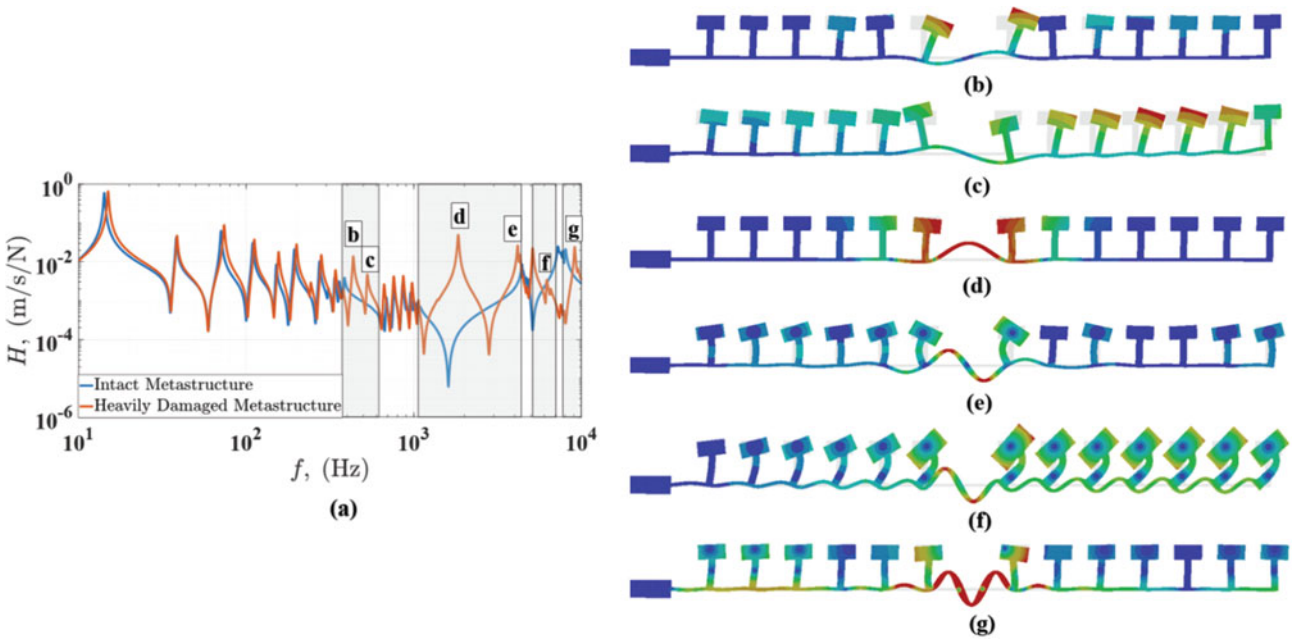

Fig. 9.3 Results of a forced response simulation comparison between an intact metastructure (Fig. 9.2a) and a heavily damaged metastructure (Fig. 9.2b). (**a**) Shows the FRF comparison. Notably, there are multiple prominent peaks in the bandgaps for the damaged structure that do not appear for the intact structure. (**b**)–(**g**) Show the local modeshapes corresponding to the labeled peaks in (**a**)

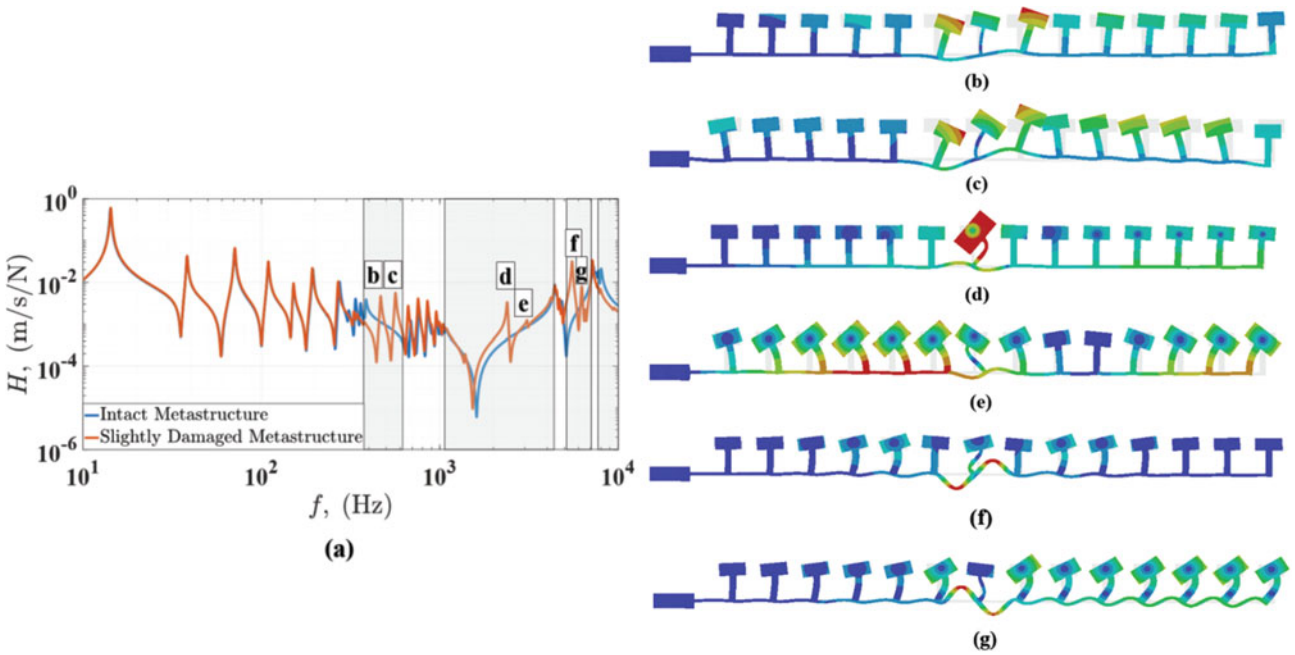

Fig. 9.4 Results of a forced response simulation comparison between an intact metastructure (Fig. 9.2a) and a slightly damaged metastructure (Fig. 9.2c). (**a**) Shows the FRF comparison. As in the heavily damaged structure, Fig. 9.3, there are multiple peaks in the bandgaps that do not appear for the intact structure. However, the peaks are less prominent. (**b**)–(**g**) Show the local modeshapes corresponding to the labeled peaks in (**a**). These are localized near the damaged location, but less so than in Fig. 9.3

9.3 Damage Detection

Vibration-based damage detection is a major research topic of structural dynamics. It aims to identify the existence of damage and its quantitative information, such as locations and extent, based on changes of vibration characteristics of a structure before and after occurrence of damage. A vibration-based damage detection method can be categorized as a model-based (e.g., [24]) or non-model-based method (e.g., [25]), depending on whether it requires an accurate physics-based model or not. A major advantage of model-based methods is that minimum amounts of vibration measurements are needed, while its immediate drawback is that accurate models are difficult to develop, especially for structures with complex geometries and material properties. Though non-model-based methods usually require extensive vibration measurements, they are more likely to yield accurate damage identification results with robustness against measurement noise. Uses of modal parameters of linear elastic structure, including natural frequencies, mode shapes, and damping ratios [26, 27], have been studied for detecting damage. However, its application to elastic metamaterials has not been studied to date.

In Sect. 9.2.1, it is observed that the existence of the damage can introduce anomalies to its frequency response functions, and high-magnitude peaks are introduced to the bandgaps that belong to the undamaged metastructure. Those magnitudes correspond to local modes that exist within the bandgaps, whose mode shapes are shown in Figs. 9.3 and 9.4. These local modes do not exist in the intact metastructure. In experimental modal analysis, modal parameters are estimated based on frequency response functions; a frequency response function of a structure with P_i and P_j being response and excitation points, respectively, can be expressed by

$$h_{i,j}(\omega) = \sum_{k=1}^{N} \frac{\phi_{k,i}\phi_{k,j}}{\mathrm{j}\omega_k - \mathrm{j}\omega} + \frac{\left(\phi_{k,i}\phi_{k,j}\right)^*}{-\mathrm{j}\omega_k - \mathrm{j}\omega} \tag{9.1}$$

where ω is the circular frequency, ω_k is the kth natural frequency, $\mathrm{j} = \sqrt{-1}$, $\phi_{k,i}$ and $\phi_{k,j}$ are the ith and jth entries of the kth mass-normalized mode shape vector, and N is the total number of modes of the structure. In practice, when measuring frequency response functions for experimental modal analysis, either the roving-hammer or roving-sensor technique is used, where certain excitation or response points are selected, and either a row or a column of the frequency response function matrix

$$\mathbf{H}(\omega) = \begin{bmatrix} h_{1,1}(\omega) & \dots & h_{1,j}(\omega) & \dots & h_{M,j}(\omega) \\ \vdots & \ddots & \vdots & \ddots & \vdots \\ h_{i,1}(\omega) & \dots & h_{i,j}(\omega) & \dots & h_{i,M}(\omega) \\ \vdots & \ddots & \vdots & \ddots & \vdots \\ h_{M,1}(\omega) & \dots & h_{M,j} & (\omega) \dots & h_{M,M}(\omega) \end{bmatrix}_{M\times M} \tag{9.2}$$

is measured, where M is the total number of measurement points, assuming that each measurement point can be used as an excitation point and a response point. If the jth measurement point is selected as the response point in a roving-hammer technique, the jth row of $\mathbf{H}$ in Eq. (9.2) is measured and used to estimate the modal parameters, i.e., ω_k and $\phi_{k,i}$. However, $\phi_{k,i}$ associated with some local modes may not be estimated using the measured $h_{i,j}$, when $\phi_{k,j}$ is equal or close to zero. In other words, the selected response point is at or close to a node of the local modes or it locates at a nodal line of a local mode. Furthermore, it is tedious and time-consuming to capture all modes, including local ones, by measuring every entry of $\mathbf{H}$ in experimental modal analysis using the roving-hammer or roving-sensor technique. Based on these observations and considerations, an efficient damage detection method is proposed by inspecting driving-point frequency response functions of a metastructure. A driving-point frequency response function is a special case of frequency response functions, whose excitation and response points are the same. A driving-point frequency response function associated with the jth measurement point can be expressed by

$$h_j(\omega) = \sum_{k=1}^{N} \frac{\phi_{k,j}^2}{\mathrm{j}\omega_k - \mathrm{j}\omega} + \frac{\left(\phi_{k,j}^2\right)^*}{-\mathrm{j}\omega_k - \mathrm{j}\omega} \tag{9.3}$$

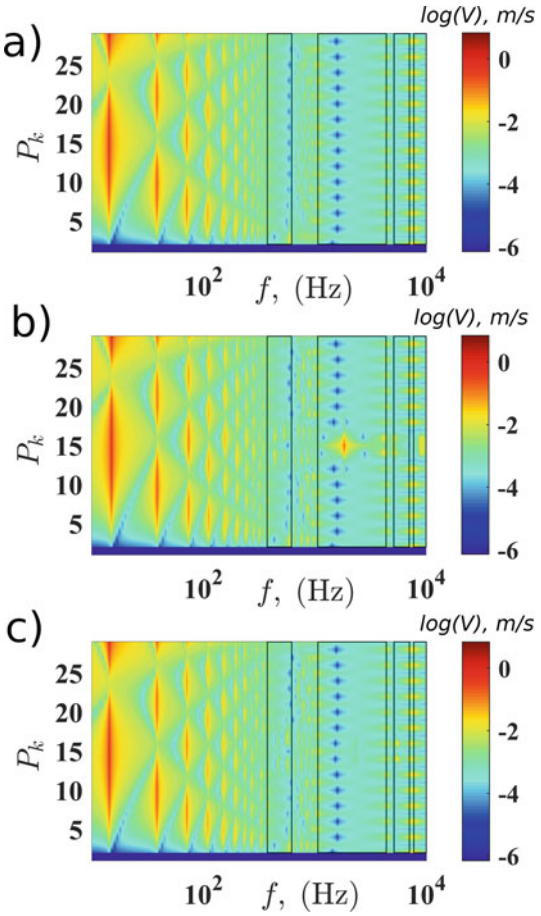

Fig. 9.5 Results of Driving-point velocity FRF comparison between an intact metastructure (Fig. 9.2a), slightly damaged metastructure (Fig. 9.2b), and heavily damaged metastructure (Fig. 9.2c). Bandgaps are boxed

Unlike $h_{i,j}$ measured by the roving-hammer or roving-sensor technique, h_j corresponds to a diagonal entry of **H** in Eq. (9.2). Though $\phi_{k,j}$ can be equal or close to zero, h_j can be used to identify all natural frequencies that can be identified using **H**. Driving-point frequency response functions h_j corresponding to the intact, slightly damaged, and heavily damaged metastructures are shown in Fig. 9.5a, b and c, respectively. It can be seen that the extra frequency response function magnitudes exist in the neighborhood of the damage, i.e., P_{15}, in the bandgaps, and such peaks can indicate the location of the damage.

Based on the unique advantage of driving-point frequency response functions, a damage index (DI) is formulated; the DI associated with a bandgap of h_j ranging between ω_1 and ω_2 is expressed by

$$\delta_j = \int_{\omega_1}^{\omega_2} h_j^2(\omega)\,\mathrm{d}\omega \tag{9.4}$$

The location of damage can be identified at neighborhoods with high δ_j values. The DI δ_j corresponding to the intact, slightly damaged, and heavily damaged metastructures is shown in Fig. 9.6, with ω_1 and ω_2 corresponding to the first bandgap. With δ_j corresponding to the intact metastructure, one can identify the anomaly of δ_j corresponding to the two damaged metastructures that indicates the location of the damage. The DI δ_j corresponding to the heavily damaged metastructure has higher values at the neighborhood of the damage, i.e., P_{15}, than δ_j corresponding to the slightly damaged metastructure. Effectiveness of δ_j for identifying the anomaly caused by damage can be further visualized by comparing δ_j corresponding to the three metastructures, which is shown in Fig. 9.7, and it is verified that more severe damage leads to a higher level of anomaly in h_j and a higher δ_j value. These observations can be further verified by DI results associated with the second bandgap shown in Figs. 9.8 and 9.9, where local anomalies can be observed in the neighborhood of the damage. As compared to a DI for the first bandgap, the DI for the second bandgap shows a much high sensitivity for the heavily damaged structure.

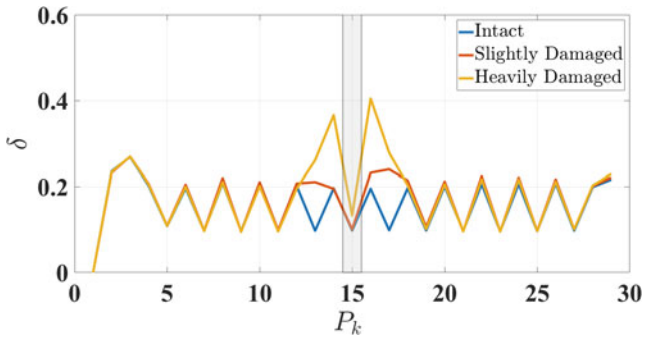

Fig. 9.6 Damage index δ_j corresponding to the intact, slightly damaged, and heavily damaged metastructures, when using ω_1 and ω_2 corresponding to the first bandgap. The slight damage and heavy damage exist at P_{15}

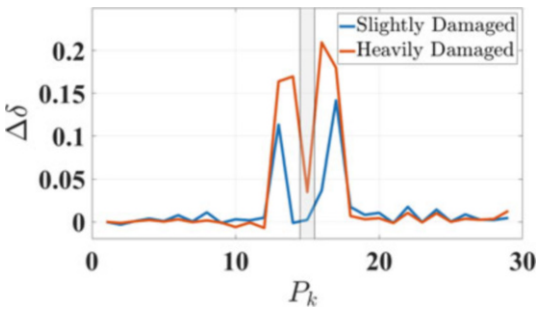

Fig. 9.7 Difference between δ_j corresponding to the intact metastructure and that corresponding to the slightly damaged and heavily damaged metastructures, when using ω_1 and ω_2 corresponding to the first bandgap. The slight damage and heavy damage exist at P_{15}

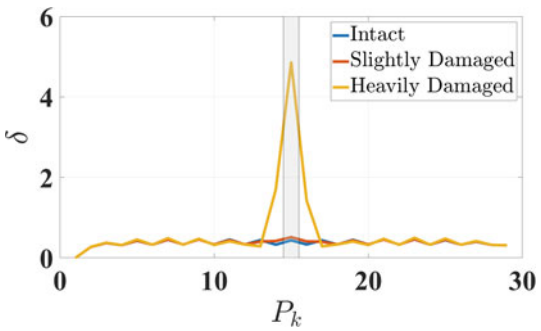

Fig. 9.8 Damage index δ_j corresponding to the intact, slightly damaged, and heavily damaged metastructures, when using ω_1 and ω_2 corresponding to the second bandgap. The slight damage and heavy damage exist at P_{15}

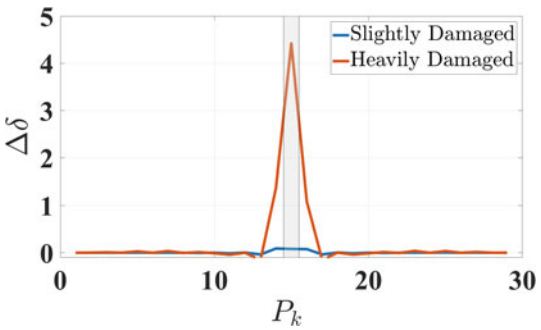

Fig. 9.9 Difference between δ_j corresponding to the intact metastructure and that corresponding to the slightly damaged and heavily damaged metastructures, when using ω_1 and ω_2 corresponding to the second bandgap. The slight damage and heavy damage exist at P_{15}

Furthermore, this method could potentially be modified to be a reference-free method. Observe that the damage index corresponding to the intact structure is very periodic, with nearly every resonator having the same pattern. Therefore, if the DI δ_j of the intact structure was not available, it could be approximately reconstructed based on observing the repeating pattern for the non-damaged resonators in the DI corresponding to a damaged metastructure.

9.4 Damage Tolerance

We call a metamaterial robust or damage-tolerant if a localized failure has a small effect on the overall performance (i.e., attenuation in the bandgap) and such localized failure does not propagate to a larger failure. Most well-designed metamaterials meet the first part of the definition. For example, the LR metamaterial illustrated in Fig. 9.1 and discussed in Sect. 9.3 has a sufficiently large number of local resonators such that the failure of any single resonator has virtually no effect on the ability of the overall structure to meaningfully attenuate vibration in the bandgaps (i.e., for an excitation at one end of the structure, the vibration response on the far end is minimally impacted by the failure of any single resonator in between). However, many metamaterials are susceptible to a cascading failure mode, illustrated in Fig. 9.10. If a resonator close to the excitation source fails (e.g., due to manufacturing defect, handling damage, corrosion, or high cycle fatigue), a localized mode is created. This mode may have very high stresses in resonators adjacent to the failure. Failure of these resonators can then create high stress in the next resonators, and so on.

In this section, we present two examples on how to improve metamaterial robustness. Note: for computational efficiency, these results were generated using 1D beam elements (i.e., BEAM188 in ANSYS), instead of the plane stress elements in the prior section. The results are qualitatively similar, but with slight quantitative differences.

9.4.1 Damped Resonators

For beam-like structures with beam-like resonators considered in this work so far, if the host and resonators are made out of the same material (i.e., cut out of the same piece of metal, or additively manufactured with the same material), then it would be reasonable to expect a similar damping ratio between the host and resonators. But consider what happens if the resonators (including the connection with the host beam) have a significantly higher damping ratio than the host structure (e.g., made out of a different material, or having an applied damping treatment such as constrained layer damping).

The first observation is that this damping treatment has very little effect on the overall vibration attenuation of an intact structure, as shown in Fig. 9.11. However, for the failed structure, there is a considerable difference in the stresses in the local modes, as shown in Fig. 9.12. With damped resonators, the local modes are still present, but the peak stress is reduced by approximately half.

9.4.2 Geometry Optimization

The damage tolerance can also be improved with modifications to the geometry. The local modes that are created with damage can vary depending on the construction of the metastructure, and some configurations will be more favorable than others. To give one example, consider the basic structure introduced in Fig. 9.1, but consider the thickness of the host beam to be variable, all other parameters kept constant.

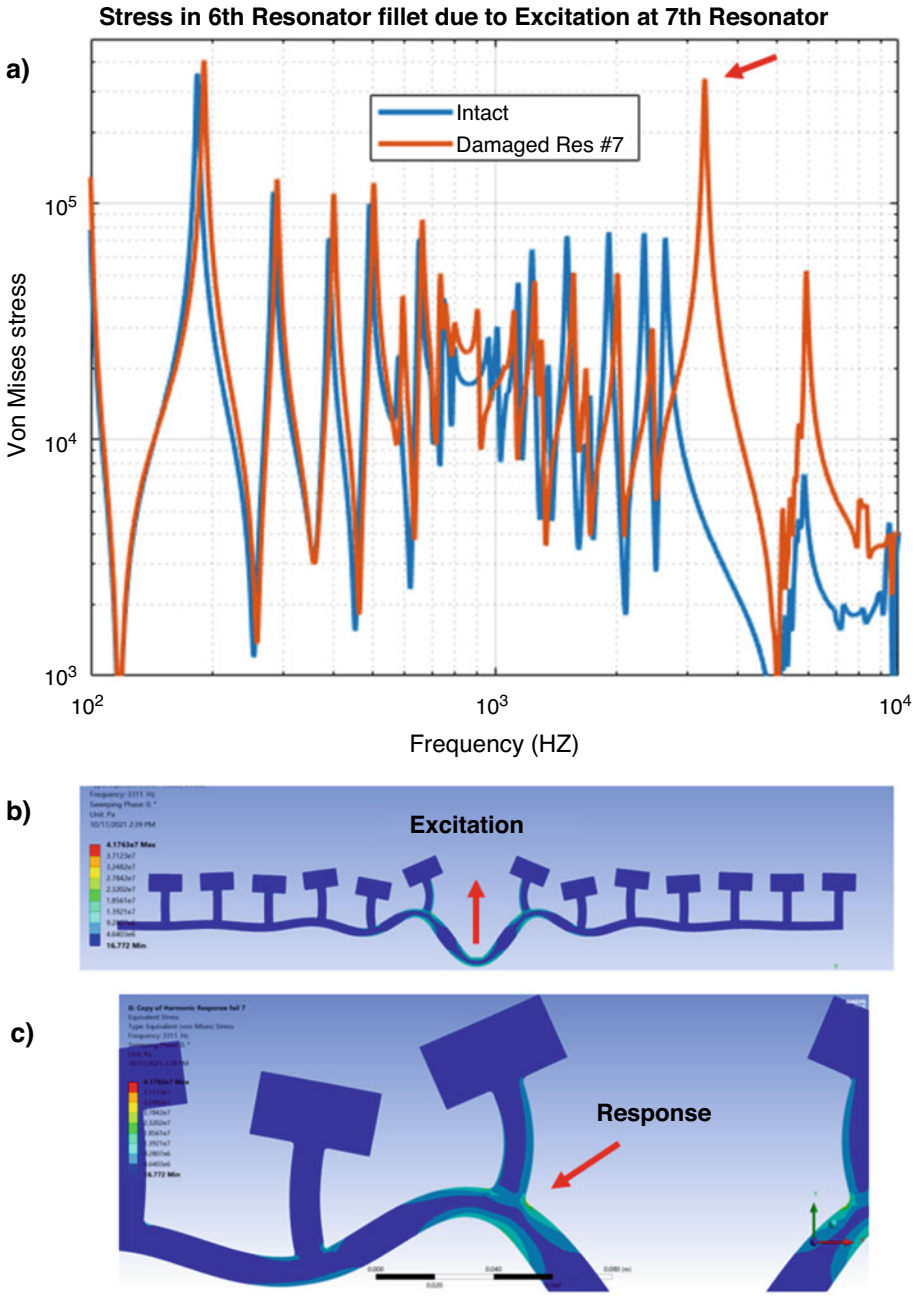

Fig. 9.10 Illustration of cascading failure mode. Geometry is the same as Fig. 9.1 except that host beam thickness is 10.16 mm. (**a**) FRF of stress at 6th resonator (i.e., P_{13}) due to excitation at 7th resonator (P_{15}). If the 7th resonator is damaged, local modes get created with large stress in the adjacent resonators. (**b**) ODS at the mode marked in (**a**). (**c**) Zoom in on 6th resonator location

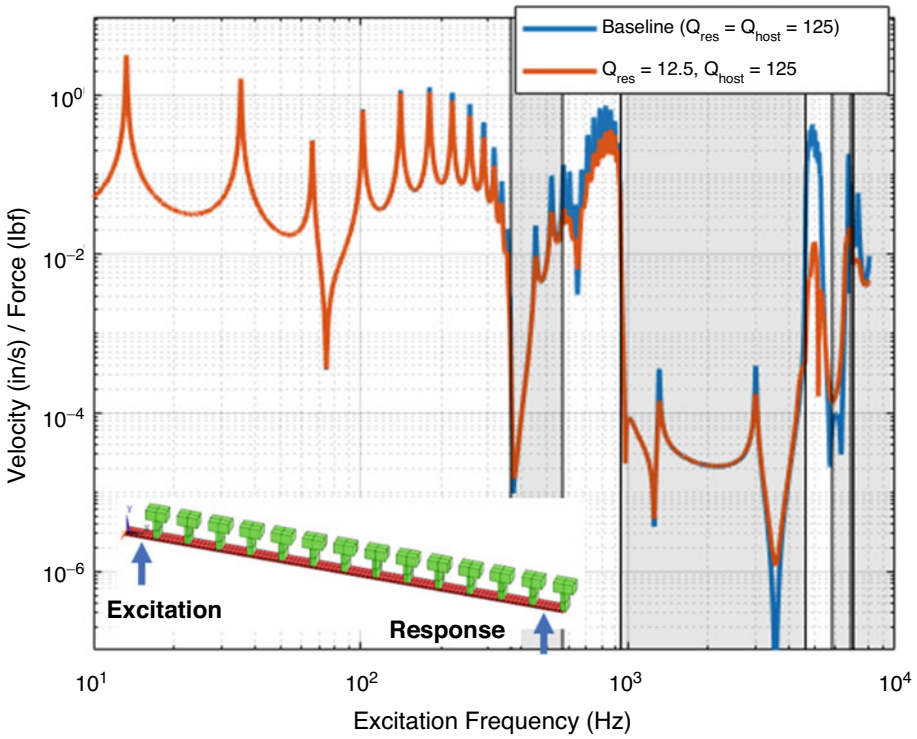

Fig. 9.11 Effect of resonator damping on the overall vibration attenuation across the beam. There is very little effect on the response. The bandgaps are shaded based on the infinite structure dispersion curve. Several small peaks within the bandgaps are due to edge modes [28]. The inset shows the excitation and response locations, and the color indicates the different material properties

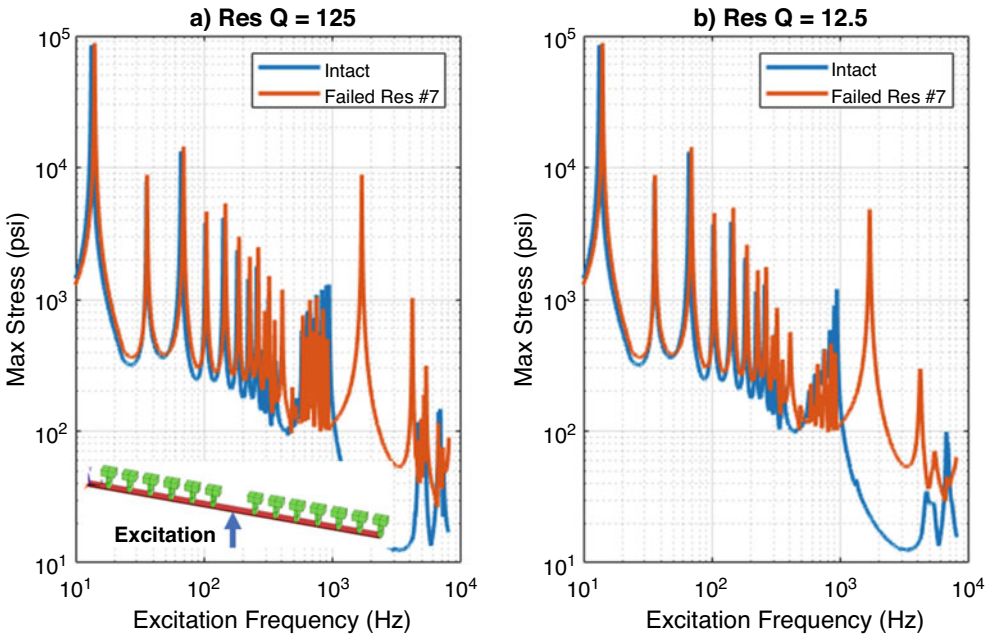

Fig. 9.12 Effect of resonator damping on local modes stress. Each line shows the maximum stress across all 14 resonator units for an excitation at resonator#7. (**a**) In the baseline condition (both resonator and host beam have Q = 125), failure of resonator #7 causes a significant stress increase in adjacent resonators (which may themselves fail next). (**b**) For damped resonators (Q = 12.5), the peak stress is reduced by nearly half if a resonator fails

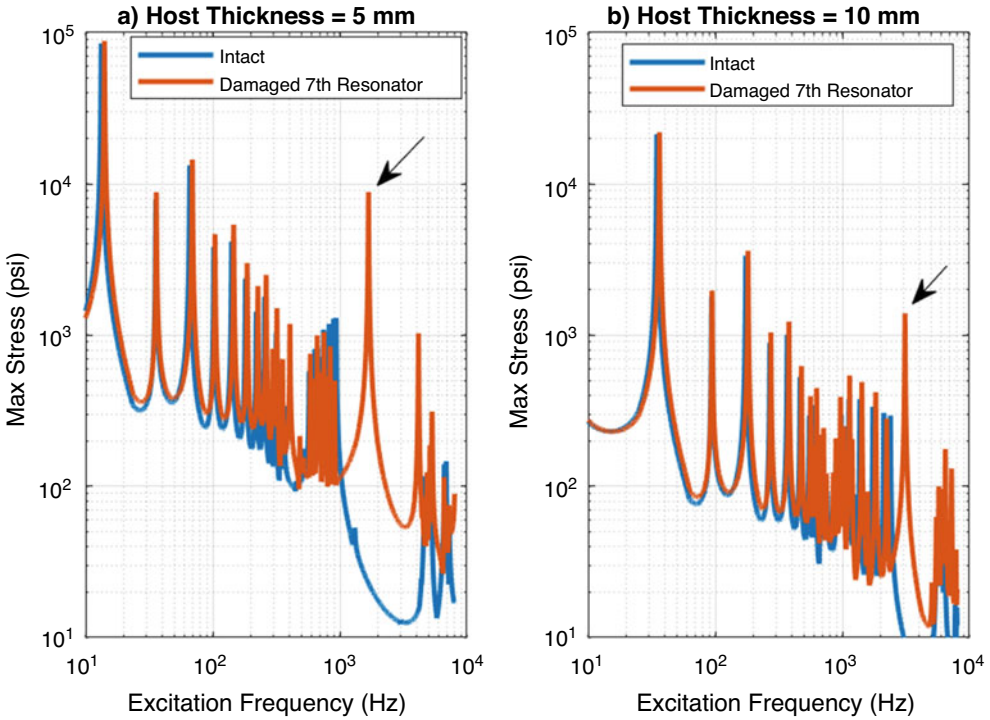

Fig. 9.13 Comparison of local modes for two different geometries. The maximum stress across the entire structure is plotted. (**a**) In the baseline structure (similar to that considered in Sect. 9.3), the local mode generates a very high stress. (**b**) With a thicker host structure, the local mode still exists, but the peak stress is reduced (note that the bandgap is also shifted in frequency). Mode shapes corresponding to the marked peaks are shown in Fig. 9.14

Figure 9.13 compares two beams with different thicknesses in terms of the overall stress throughout the beam. In the baseline condition, 5.08 mm thick beam, a local mode with high stresses is created when one resonator fails. When the host beam is made thicker, to 10.16 mm, now there is still a local mode, but the overall stress increase is much less. The reason for this decrease can be seen by examining the mode shapes shown in Fig. 9.14. With the thicker beam, the mode is less localized near the damaged resonator. In other words, for the thinner beam, the resonators are very effective at trapping the wave, so the energy is very localized near the damage. As the host structure becomes stiffer, the resonators become less effective at trapping the wave, and therefore the energy in the local mode is more spread out. Spreading the energy out over a large section of the beam results in less strain energy in any given segment of the beam, therefore a lower stress.

To quantify the effectiveness of the wave trapping, we compute the complex dispersion curves, using the method of Ref. [29]. With the normal boundary conditions, a series of wave vectors k are specified, and the frequencies ω are computed at each k by solving an eigenvalue problem. In this method instead, a series of frequencies ω are specified, and the wave vectors k are computed at each ω. This allows complex wave vectors to be computed. Inside the bandgaps, the wave vectors are purely imaginary representing decaying waves rather than propagating waves. Thus, $Im(k)$ gives information on how much the amplitude decays when passing through one unit cell, rather than how much the phase changes when passing through one cell. The complex dispersion curves for these two structures are computed and shown in Fig. 9.15. In the region of the second bandgap, the imaginary part of the wave vector is approximately double for the thin beam (location marked with an arrow) versus the thick beam. In other words, a wave would decay to approximately $e^{-0.85}$ of the initial amplitude across one unit cell of the thick beam, but $e^{-1.9}$ for the thin beam, which is nearly a factor of 3 difference. Considering vibration attenuation over a large number of resonators, the thick beam is still very capable (i.e., $e^{-14(0.85)}$ is still quite a small number, even if it is not as small as $e^{-14(-1.9)}$).

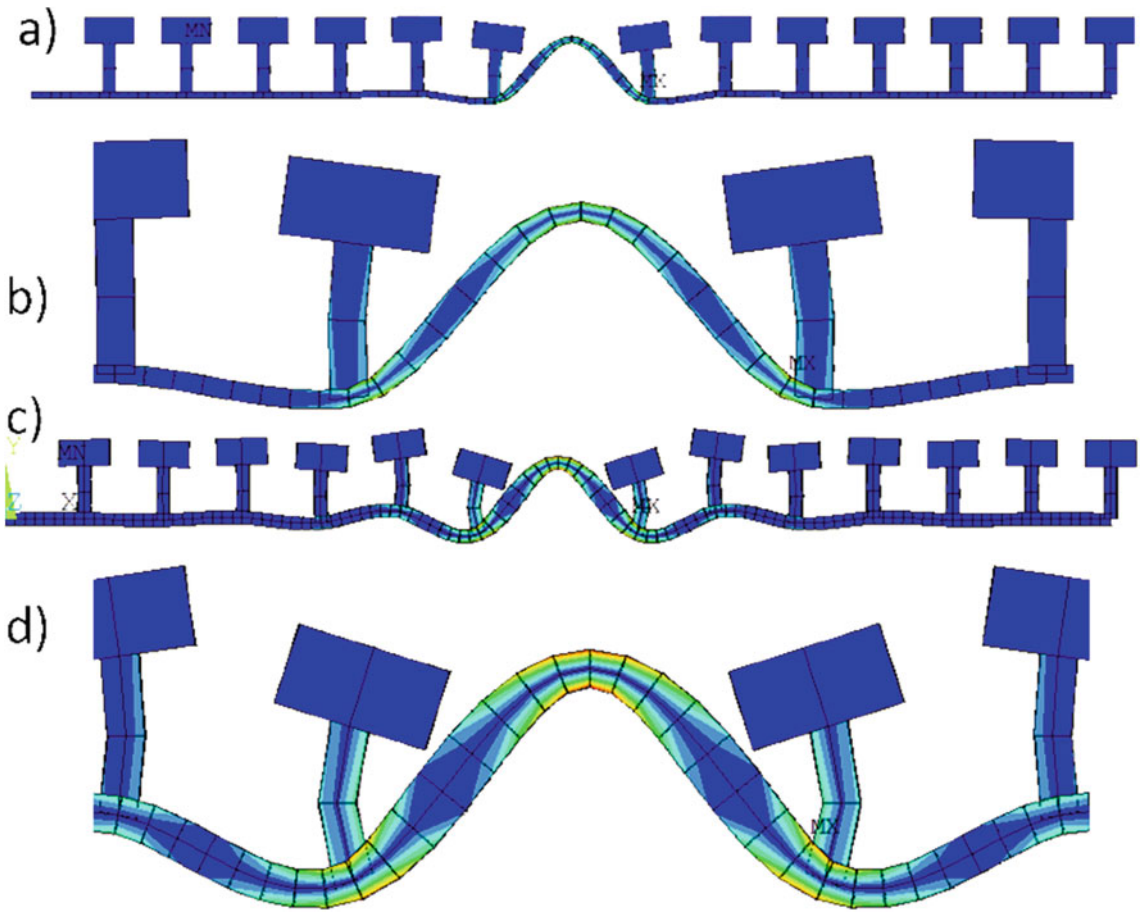

Fig. 9.14 Mode shapes for the marked local modes from Fig. 9.13. The color shows von Mises stress. (**a**) 5 mm thick beam, (**b**) zoom -in near damaged location, and (**c**) 10 mm thick beam. The mode is much less localized. (**d**) Zoom in near damaged location

9.5 Conclusions and Future Work

This work has demonstrated for the first time a damage detection method for metastructures. A simple damage index based on driving-point FRFs in the bandgap region is used. The damage index is able to detect small damages in the local resonators due to the presence of highly localized modes near the damage.

To this point, the damage detection method has been demonstrated only on a single metastructure design. It is expected that this method should be generalizable to most if not all other types of metastructures (e.g., gyroid lattices as in Ref. [23]), as all metastructures should exhibit similar types of highly localized modes. However, this has not yet been conducted. An experimental program is also in progress to confirm the simulation predictions. Development of a reference-free method looks to be possible and should be explored as this will improve the practical application of the method.

This work has also introduced the concept of robust/damage tolerant metastructures and given some example of how this can be improved. This concept too has only been demonstrated by simulation on a single design. The concept needs to be generalized to other types of metastructures and confirmed by experiment.

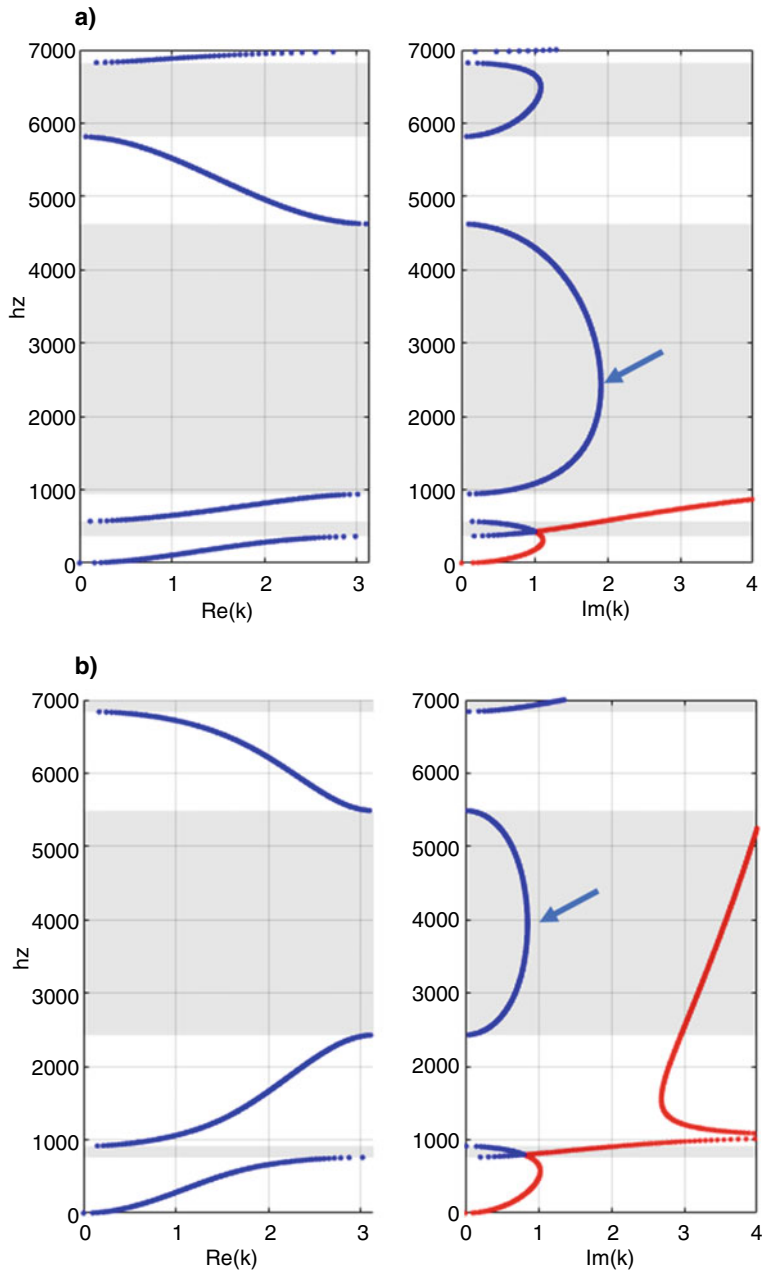

Fig. 9.15 Complex dispersion curves for the intact beams compared in Figs. 9.13 and 9.14, illustrating that the wave is more trapped in the thin beam, due to the higher Im(k). For clarity, the components of k are not plotted when they are zero. (**a**) Host thickness 5 mm. (**b**) Host thickness 10 mm

Appendix

See Fig. 9.16.

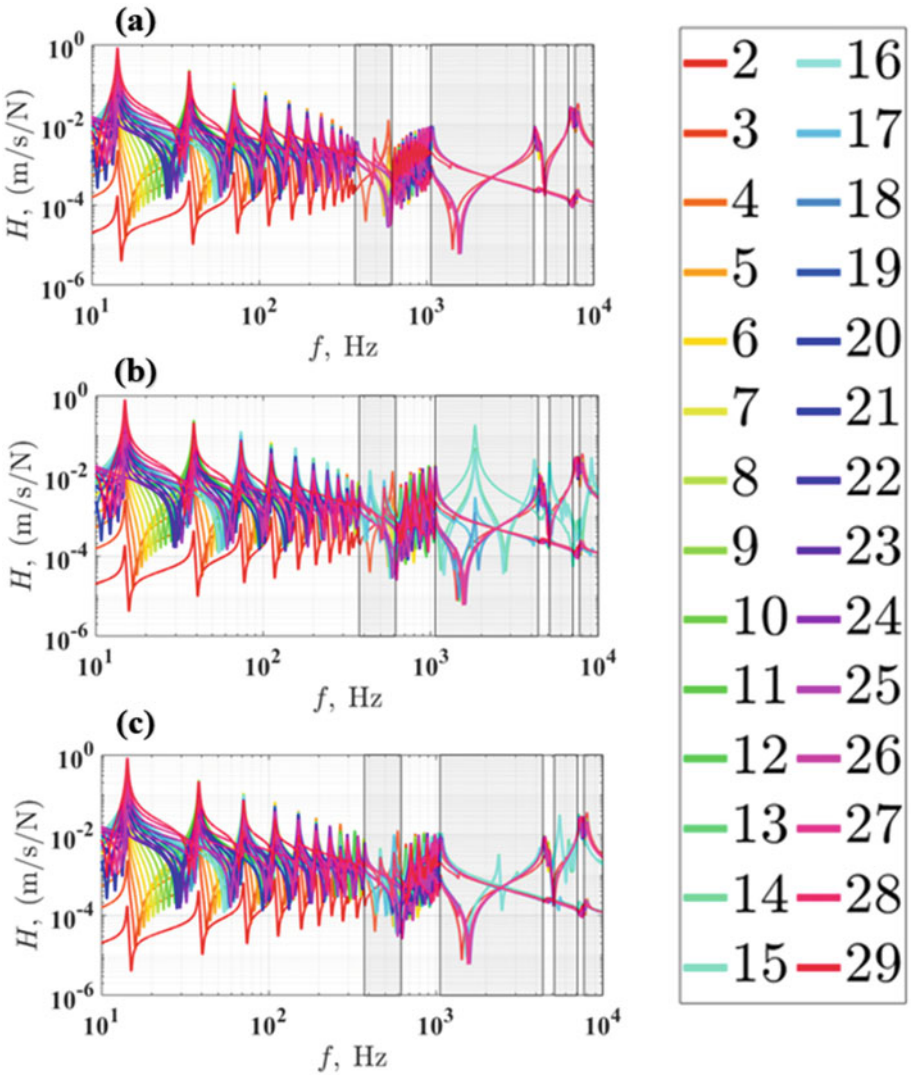

Fig. 9.16 Results of Driving-point velocity FRF comparison between an intact metastructure (Fig. 9.2a), heavily damaged metastructure (Fig. 9.2b), and slightly damaged metastructure (Fig. 9.2c). The same data as of Fig. 9.5 but plotted as stacked lines

References

1. Anand, M.: Applications of metamaterial negative refractive index lens (MNRI-lens). Int. J. Tech. Res. Appl. **1**, 94–97 (2013)
2. Lee, K.-T., Ji, C., Iizuka, H., Banerjee, D.: Optical cloaking and invisibility: from fiction toward a technological reality. J. Appl. Phys. **129**(23), 231101 (2021)
3. Valipour, A., Kargozarfard, M.H., Rakhshi, M., Yaghootian, A., Sedighi, H.M.: Metamaterials and their applications: an overview. In: Proceedings of the Institution of Mechanical Engineers, Part L: Journal of Materials: Design and Applications (2021). https://doi.org/10.1177/1464420721995858
4. Lv, J., Zhou, M., Gu, Q., Jiang, X., Ying, Y., Si, G.Y.: Metamaterial lensing devices. Molecules **24**, 2460 (2019)
5. Xie, Y., Fu, Y., Jia, Z., Li, J., Shen, C., Xu, Y., Chen, H., Cummer, S.A.: Acoustic imaging with metamaterial Luneburg lenses. Sci. Rep. **8**(1), 1–6 (2018)

6. Reynolds, M., Daley, S.: An active viscoelastic metamaterial for isolation applications. Smart Mater. Struct. **23**(4), 045030 (2014)
7. Phani, A.S., Hussein, M.I.: Elastodynamics of lattice materials. In: Dynamics of Lattice Materials, pp. 53–59 (2017). cited By 55
8. Zhou, X., Liu, X., Hu, G.: Elastic metamaterials with local resonances: an overview. Theor. Appl. Mech. Lett. **2**(4), 041001 (2012)
9. Chang, I.L., Liang, Z.X., Kao, H.W., Chang, S.H., Yang, C.Y.: The wave attenuation mechanism of the periodic local resonant metamaterial. J. Sound Vib. **412**, 349–359 (2018)
10. Bao, H., Wu, C., Zheng, W., Yan, B.: Vibration bandgap of a locally resonant beam considering horizontal springs. JVC/J. Vib. Control (March 2020) (2021)
11. Elmadih, W., Chronopoulos, D., Syam, W.P., Maskery, I., Meng, H., Leach, R.K.: Three-dimensional resonating metamaterials for low-frequency vibration attenuation. Sci. Rep. **9**(1), 1–8 (2019)
12. Matlack, K.H., Bauhofer, A., Krödel, S., Palermo, A., Daraio, C.: Composite 3D-printed metastructures for low frequency and broadband vibration absorption. Proc. Natl. Acad. Sci. U. S. A. **113**(30), 8386–8390 (2016)
13. Raza, I.M.H., Lannucci, L., Curtis, P.T.: Additive manufacturing of locally resonant composite metamaterials. In: ECCM 2016 - Proceeding of the 17th European Conference on Composite Materials, April 2016
14. Yang, X.W., Lee, J.S., Kim, Y.Y.: Effective mass density based topology optimization of locally resonant acoustic metamaterials for bandgap maximization. J. Sound Vib. **383**, 89–107 (2016)
15. Li, L., Cai, A.: Low-frequency band gap mechanism of torsional vibration of lightweight elastic metamaterial shafts. Eur. Phys. J. Appl. Phys. **75**(1), 10501 (2016)
16. Meng, H., Chronopoulos, D., Fabro, A.T., Maskery, I., Chen, Y.: Optimal design of rainbow elastic metamaterials. Int. J. Mech. Sci. **165**, 105185 (2020)
17. Li, Y., Li, H.: Bandgap merging and widening of elastic metamaterial with heterogeneous resonator. J. Phys. D: Appl. Phys. **53**(47), 475302 (2020)
18. Judge, J.A., Houston, B.H., Photiadis, D.M., Herdic, P.C.: Effects of disorder in one-and two-dimensional micromechanical resonator arrays for filtering. J. Sound Vib. **290**(3–5), 1119–1140 (2006)
19. Yuan, J., Scarpa, F., Allegri, G., Titurus, B., Patsias, S., Rajasekaran, R.: Efficient computational techniques for mistuning analysis of bladed discs: a review. Mech. Syst. Signal Process. **87**, 71–90 (2017)
20. Langley, R.S.: Wave transmission through one-dimensional near periodic structures: optimum and to random disorder. J. Sound Vib. **188**(5), 717–743 (1995)
21. Gao, D., Zeng, X., Liu, X., Han, K.: Resonant modes of one-dimensional metamaterial containing Helmholtz resonators with point defect. J. Mod. Phys. **08**(10), 1737–1747 (2017)
22. Qureshi, A., Li, B., Tan, K.T.: Numerical investigation of band gaps in 3d printed cantilever-in-mass metamaterials. Sci. Rep. **6**, 28314 (2016)
23. Elmadih, W., Syam, W.P., Maskery, I., Chronopoulos, D., Leach, R.: Mechanical vibration bandgaps in surface-based lattices. Addit. Manuf. **25**(2018), 421–429 (2019)
24. Bagchi, A., Humar, J., Xu, H., Noman, A.S.: Model-based damage identification in a continuous bridge using vibration data. J. Perform. Constr. Facil. **24**(2), 148–158 (2010)
25. Xu, Y.F., Zhu, W.D., Smith, S.A.: Non-model-based damage identification of plates using principal, mean and gaussian curvature mode shapes. J. Sound Vib. **400**, 626–659 (2017)
26. Farrar, C.R., Doebling, S.W., Nix, D.A.: Vibration–based structural damage identification. Philos. Trans. R. Soc. Lond. Ser. A: Math. Phys. Eng. Sci. **359**(1778), 131–149 (2001)
27. Fan, W., Qiao, P.: Vibration-based damage identification methods: a review and comparative study. Struct. Health Monit. **10**(1), 83–111 (2011)
28. Sangiuliano, L., Claeys, C., Deckers, E., Desmet, W.: Influence of boundary conditions on the stop band effect in finite locally resonant metamaterial beams. J. Sound Vib. **473**, 115225 (2020)
29. Mace, B.R., Duhamel, D., Brennan, M.J., Hinke, L.: Finite element prediction of wave motion in structural waveguides. J. Acoust. Soc. Am. **117**(5), 2835–2843 (2005)

Chapter 10
Indirect Bridge Health Monitoring Using Time-Frequency Analysis: Analytical and Experimental Studies

Premjeet Singh and Ayan Sadhu

Abstract Bridges are among the crucial elements of public infrastructure and are inspected regularly for maintenance purposes. Often, these inspections are conducted visually, which can be particularly limited to detecting hidden and minor damage, for instance, fatigue cracks, delamination, and corrosion of embedded reinforcement. Ideally, the bridge inspectors need to identify any changes in dynamic parameters of the bridge, such as natural frequencies, damping ratio, and stiffness. Recently, there has been a shift from using fixed sensor networks to moving sensor networks that can detect changes in these dynamic parameters. Moving sensor networks rely on indirect measurements taken from within the vehicle while traveling over the bridge. The signal collected from within a passing vehicle contains the bridge's structural response, vehicle suspension input, and surface roughness-induced vibrations. This paper investigated the feasibility of drive-by bridge monitoring using numerical and experimental assessments and addressed their challenges using the time-frequency method. The proposed methodology uses Wavelet Packet Transform (WPT), which extracted modal responses and delineated the bridge frequency components from the driving and vehicle frequencies using the wavelet packet coefficients. The performance of the proposed method was validated using both numerical simulations and a laboratory experiment. The effects of vehicle parameters on vehicle acceleration response were studied using analytical modeling. In the laboratory experiment, a moving cart was used as a vehicle traveling over a scaled bridge model. The results demonstrated that the proposed method could efficiently extract and separate the bridge dynamics from the vehicle response.

Keywords Wavelet packet transform · Vehicle-bridge interaction · Indirect bridge health monitoring · Time-frequency method

10.1 Introduction

Bridge infrastructure is imperative to economic development; however, it is subjected to continuous deterioration due to aging, traffic, and environmental conditions. The extent of deterioration needs to be monitored regularly to ensure the structural integrity of bridges. According to ASCE 2021 Report Card, nearly 231,000 bridges in the USA still need repair and preservation work. The majority of the bridges are assessed periodically using visual inspections, which can be subjective, expensive, and susceptible to errors. Bridge health monitoring (BHM) provides an effective solution to address these challenges of assessing the severity of the aging state of bridge infrastructure. Vibration-based BHM usually involves direct instrumentation with sensors such as accelerometers to extract the modal parameters from the ambient or forced vibrations [1, 2]. However, it involves traffic interruptions, bridge closures, high labor and equipment costs, and a high risk to the equipment being used on site.

As an alternative to direct BHM, researchers [3–5] have focused on indirect BHM (iBHM) in recent years. iBHM leverages the vehicle traveling over the bridge as a data acquisition device as well as a source of excitation. While traversing over the bridge, an instrumented vehicle can excite the bridge and collect the vibration response of the bridge. The majority of iBHM studies have focused on moving mass, moving load, and moving sprung-mass model to capture the dynamic effects of bridges in vehicle measurements. Out of these studies, the moving sprung mass model best represents the moving vehicle over the bridge by considering the inertia effects of the vehicle. However, the vehicle measurements passing over a bridge always contain bridge frequencies along with driving frequency and vehicle frequency. Therefore, it is always a challenge

P. Singh · A. Sadhu (✉)
Department of Civil and Environmental Engineering, University of Western Ontario, London, Canada
e-mail: asadhu@uwo.ca

H. Y. Noh (eds.), *Dynamics of Civil Structures, Volume 2*, Conference Proceedings of the Society for Experimental Mechanics Series, https://doi.org/10.1007/978-3-031-05449-5_10

to delineate the effects of the latter two parameters from the measured data. Moreover, many factors such as road profile, vehicle systems, and vehicle-bridge interactions affect the performance of iBHM [5].

The idea of using a test vehicle to extract the bridge frequencies was initially proposed by [6] and was validated numerically by [7] using a simply supported beam. It was concluded that vehicle response was largely dominated by driving frequency, vehicle frequency, and the associated pairs of shifted frequencies of bridges. It was also observed that the displacement response of the vehicle was influenced by the vehicle speed, while the vehicle acceleration response was affected by the bridge frequencies. In this study, it was assumed the mass of the vehicle was small compared to the bridge. Later, empirical mode decomposition (EMD) was used by [8] to extract the higher modes of the bridge using experimental studies [9], and the importance of the selection of the most appropriate vehicle properties in a bridge was discussed. Unlike identification of bridge frequencies using previous iBHM methods, [10] conducted a study to identify the absolute damping of a bridge from the vehicle response and detect the damage. Theoretical simulations, including a simplified 2 degree-of-freedom (DOF) half-car vehicle-bridge interaction model, were used to validate the method for a range of bridge spans and vehicle speeds.

The relationship between driving velocity, vehicle frequency, and bridge frequency was examined analytically and experimentally by [11]. In their study, the effects of surface roughness, vehicle damping, and expansion joints were ignored. From the results, it was clear that higher vehicle velocities, in this case, larger than 30 km/h, created technical and practical difficulties due to vehicle bouncing impact on expansion joint and shorter response duration. [12] used the vehicle response to identify the vehicle bridge interaction (VBI) forces. The identification process was completed using a coupled 4-DOF half-car model in theoretical simulations. Based on moving force identification (MFI) theory, the proposed method identified the global bending stiffness of a bridge and predicted the pavement roughness, which was insensitive to noise. This was the first-ever approach that used the MFI theory to solve the VBI model and identify unknown vehicle forces. In a recent study, the finer frequency resolution capability of wavelet transform was leveraged by [13] to visualize the bridge damage using the response from a passing vehicle. The study also investigated the use of a subtracted signal from two consecutive axles to remove the effect of road roughness and showed good agreement between the extracted and theoretical bridge frequencies. In another study, [14] introduced the wavelet entropy theory in which the optimal wavelet scale is selected by minimizing wavelet entropy. This approach was a step forward in enhancing the existing wavelet-based damage detection methods.

[15] examined the practical viability of drive-by bridge inspection using numerical and experimental investigations. The authors proposed an index based on vehicle and bridge frequencies to quantify the performance of transmission between the bridge and the vehicle. The results indicated that more information related to bridge dynamics could be collected using a vehicle with a higher sensitivity index. The first few bridge vibration modes were identified using the test vehicle moving at constant and low speed. The study provided a benchmark that can be used to design a bridge inspection system capable of practical drive-by monitoring. [16] proposed an instantaneous frequency identification technique based on modified S-transform reassignment. The resolution was enhanced by introducing a frequency function in the Gaussian window with two parameters determined by the time-frequency (TF) concentration criterion. Numerical studies validated the effect of road profile roughness and vehicle parameters such as weight and speed on the time-varying characteristic identification. However, throughout the literature, little attention has been made to the investigation of VBI using time-frequency domain analysis. The time-varying nature of VBI due to the movement of the vehicle along the bridge gives rise to frequency variations. A powerful TF analysis method can track the frequencies of the VBI system in which vehicle and bridge are coupled at the contact point, and instantaneous frequencies vary in time.

This paper aims at exploring the difference in types of frequencies found in the vehicle response from iBHM using a robust time-frequency method, namely, Wavelet Packet Transform (WPT). In the numerical investigation, a vehicle travels over a bridge model at varying speeds, and its response is collected to be analyzed using the proposed methodology. In the laboratory experiment, a moving vehicle model travels over a scaled bridge model. WPT is used to decompose the signal collected from the vehicle into its individual components, namely, bridge frequencies, vehicle frequencies, and driving frequencies. Direct and indirect monitoring data are compared using the proposed methodology. The arrangement of this paper is provided as follows: the next section is used to provide a background about the VBI and WPT and their respective governing equations, followed by the proposed methodology of this paper. In the next two sections, the numerical and experimental investigations are presented, and lastly, a conclusion is provided for the highlights and contributions of this study.

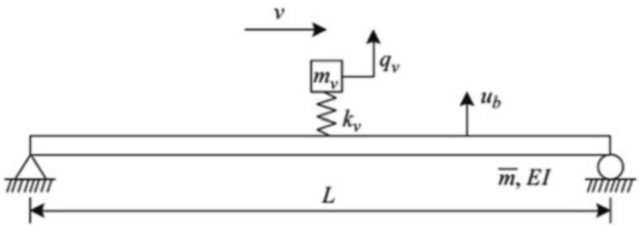

Fig. 10.1 Vehicle model moving across the bridge [8]

10.2 Background

10.2.1 VBI in iBHM

The concept of iBHM uses a vehicle passing over a bridge as an excitation source and as a sensor. Figure 10.1 shows an example of a simplified VBI model that is used for the theoretical formulation. The vehicle is modeled as a quarter car with lumped mass m_v and spring of stiffness k_v. The bridge is modeled as a simply supported Euler-Bernoulli beam with length L and a constant cross-section and smooth profile. The beam is assumed to have a constant flexural rigidity EI and a constant mass density $\overline{m}$ throughout the length. The vertical displacements of the vehicle and the beam are denoted by q_v and u_b, respectively. From the equation of motion of coupled VBI system, the solution in the form of vertical displacement of the beam can be expressed as [7]:

$$u_b(x,t) = \sum_n \frac{\Delta_{stn}}{1-S_n^2}\left\{\sin\frac{n\pi x}{L}\left[\sin\frac{n\pi vt}{L} - S_n \sin\omega_{bn}t\right]\right\} \tag{10.1}$$

Using Duhamel's integral, the vertical displacement of the vehicle can be obtained as [8]:

$$q_v(t) = \sum_n \left\{H_{dl,n}\cos\tfrac{(n-1)\pi v}{L}t - H_{dr,n}\cos\tfrac{(n+1)\pi v}{L}t + H_{v,n}\cos\omega_v t - H_{bl,n}\cos\left(\omega_{b,n} - \tfrac{n\pi v}{L}\right)t + H_{br,n}\cos\left(\omega_{b,n} + \tfrac{n\pi v}{L}\right)t\right\} \tag{10.2}$$

The vertical acceleration response of a vehicle can be obtained by differentiating Eq. 10.2 [8]:

$$\ddot{q}_v(t) = \sum_n \left\{-\tilde{H}_{dl,n}\cos\tfrac{(n-1)\pi v}{L}t + \tilde{H}_{dr,n}\cos\tfrac{(n+1)\pi v}{L}t - \tilde{H}_{v,n}\cos\omega_v t + \tilde{H}_{bl,n}\cos\left(\omega_{b,n} - \tfrac{n\pi v}{L}\right)t - \tilde{H}_{br,n}\cos\left(\omega_{b,n} + \tfrac{n\pi v}{L}\right)t\right\} \tag{10.3}$$

$$H_{dl,n} = \frac{\Delta_{st,n}}{2\left(1-S_n^2\right)\left(1-\mu_{n-1}^2 S_{n-1}^2\right)} \tag{10.4}$$

$$H_{dr,n} = \frac{\Delta_{st,n}}{2\left(1-S_n^2\right)\left(1-\mu_{n+1}^2 S_{n+1}^2\right)} \tag{10.5}$$

$$H_{v,n} = \frac{2\Delta_{st,n}\mu_n^2 S_n^2}{\left(1-S_n^2\right)}\left[\frac{1}{\left(1-\mu_{n-1}^2 S_{n-1}^2\right)\left(1-\mu_{n+1}^2 S_{n+1}^2\right)} - \frac{1}{\left\{1-\mu_n^2\left(1-S_n^2\right)\right\}\left\{1-\mu_n^2(1+S_n)\right\}^2}\right] \tag{10.6}$$

$$H_{bl,n} = \frac{\Delta_{st,n}S_n}{2\left(1-S_n^2\right)\left\{1-\mu_n^2(1-S_n)^2\right\}} \tag{10.7}$$

$$H_{br,n} = \frac{\Delta_{st,n}S_n}{2\left(1-S_n^2\right)\left\{1-\mu_n^2(1+S_n)^2\right\}} \tag{10.8}$$

$$\widetilde{H}_{dl,n} = H_{dl,n}\omega_{b,n-1}^2 S_{n-1}^2 \tag{10.9}$$

$$\widetilde{H}_{dr,n} = H_{dr,n}\omega_{b,n+1}^2 S_{n+1}^2 \tag{10.10}$$

$$\widetilde{H}_{v,n} = H_{v,n}\omega_v^2 \tag{10.11}$$

$$\widetilde{H}_{bl,n} = H_{bl,n}\omega_{b,n}^2 (1 - S_n)^2 \tag{10.12}$$

$$\widetilde{H}_{br,n} = H_{br,n}\omega_{b,n}^2 (1 - S_n)^2 \tag{10.13}$$

The acceleration response of the vehicle traveling over the bridge can be generated using Eq. 10.3. Five terms involved in vehicle response in Eq. 10.3 can be labeled into three groups as driving frequencies, including $\left(\frac{(n-1)\pi v}{L}\right.$ and $\left.\frac{(n+1)\pi v}{L}\right)$; vehicle frequency ω_v; and bridge frequencies, including $\left(\omega_{bn} - \frac{n\pi v}{L}\right.$and $\left.\omega_{bn} + \frac{n\pi v}{L}\right)$. n indicates the index of the vibration modes of the bridge. It may be observed that the bridge frequencies ω_{bn} are shifted by an equal amount to the vehicle speed $\pm\frac{n\pi v}{L}$. The importance of bridge frequency terms $\left(\omega_{bn} - \frac{n\pi v}{L}\right.$ and $\left.\omega_{bn} + \frac{n\pi v}{L}\right)$ is crucial, and it will be verified whether these terms are practically visible in the vehicle response.

10.2.2 WPT

Wavelet packet transform (WPT) is a powerful time-frequency decomposition technique that can be used to decompose a particular signal into its low- and high-frequency components. This method results in both approximated and detailed coefficients [17]. Recently, [18] used a scaled bridge model for the damage detection in the shear connectors. The damage was characterized using changes in wavelet packet energy. Over the recent years, WPT has also been explored for structural damage identification [19–21]. The decomposition process using WPT is a recursive filter-decimation operation. After j levels of decomposition, a signal $f(t)$ can be represented as [18]:

$$f(t) = \sum_{i=1}^{2j} f_j^i(t) \tag{10.14}$$

A linear combination of wavelet packet functions $\psi_{j,k}^i(t)$ can be used to represent the wavelet packet component signal $f_j^i(t)$ [18]:

$$f_j^i(t) = \sum_{k=-\infty}^{\infty} c_{j,k}^i(t)\psi_{j,k}^i(t) \tag{10.15}$$

where a wavelet packet is a function with three indices, i, j, and k, which correspond to modulation, scale, and translation, respectively. Furthermore, wavelet packet coefficients, $c_{j,k}^i(t)$, can be calculated as:

$$c_{j,k}^i(t) = \int_{-\infty}^{\infty} f(t)\psi_{j,k}^i(t)dt \tag{10.16}$$

In another study, wavelet packet energy spectrum was used to create a real-time and early damage alarming system for an operational metro subway line. [22] utilized the signal denoising and wavelet packet energy spectrum to estimate and construct the damage indicators, namely, energy ratio deviation and energy ratio variance. Computational issues and accurate sensor placement were the shortcomings of this study. The application of WPT in the detection of micro-damage initiation

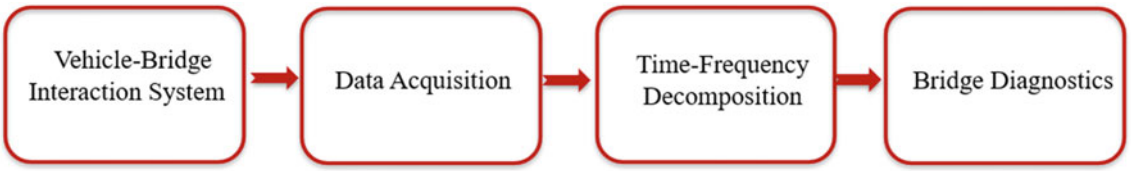

Fig. 10.2 Proposed methodology

was experimentally verified by [23]. To identify the beginning and growth of micro-damage in concrete, the energy change rate of the wavelet packet was calculated and defined as a criterion for micro-damage initiation. The results revealed that a larger wavelet packet energy change rate corresponded to a larger distribution area of micro-damage.

10.3 Methodology

In this section, the proposed methodology and the steps involved in analyzing the data are discussed. The proposed method includes indirect monitoring, acquisition of vehicle measurement, and post-processing of the measured data. In Fig. 10.2, the data is collected from the vehicle containing the contributions of the vehicle and the bridge. After the data acquisition step, WPT is used for signal processing and to decompose the signal into its simpler components. The output of this step includes driving frequencies, bridge frequencies, and vehicle frequencies. In the next two sections, the proposed approach is verified using experimental data.

10.4 Numerical Investigation

A coupled VBI system is simulated using Eq. 10.2 and the model shown in Fig. 10.1. Consider a simply supported beam subjected to a vehicle moving at speed υ. The mass and stiffness of the vehicle are 1200 kg and 500 kN/m, respectively. The simply supported beam has a length of 25 m and a mass density of 4800 kg/m. Young's modulus of elasticity, E, for the beam is 2.75 $\times$ 1010 N/m^2, and moment of inertia, I, for the beam is 0.12 m^4.

Figure 10.3 shows the Fast Fourier Transform (FFT) of the vehicle acceleration response traveling at a speed of 40 km/h. The first frequency peak in this figure corresponds to the driving frequency, and the second and third frequency peaks represent the bridge frequency terms. The fourth frequency peak in Fig. 10.3 represents vehicle frequency, and the last two frequency peaks represent the second pair of bridge frequencies. As the dynamic response of the bridge is measured through the vehicle, the resultant is a pair of bridge frequencies, and the bridge frequency can be calculated by averaging the two values. The signal is processed through the WPT, which decomposes it into wavelet coefficients, shown in Fig. 10.4. It can be seen that the WPT algorithm can efficiently decompose the signal into its components. Driving frequencies, bridge frequencies, and vehicle frequencies are well separated using WPT. Figures 10.5 and 10.6 show the FFT and WPT results, respectively, for a vehicle traveling at a speed of 60 km/h over the bridge. It can be noted that WPT can decompose the frequency peaks from Fig. 10.5 into distinct individual peaks, which can be further classified into bridge frequencies, vehicle frequencies, and driving frequencies.

10.5 Laboratory Experiment

A scaled vehicle bridge interaction model is built to investigate the viability of the indirect bridge monitoring approach. The bridge model used in the experiment is a 2.4 m simply supported wooden beam shown in Fig. 10.7. The bridge is instrumented with accelerometer sensors at the mid-span to collect the bridge response during the vehicle crossings shown in Fig. 10.8. The parameters for the bridge are shown in Table 10.1. A two-axle vehicle, shown in Figs. 10.7 and 10.8, is selected to travel across the bridge at a speed of 2 m/s. The vehicle is remotely controlled using a smartphone during its multiple passages over the bridge. An accelerometer sensor is mounted under the vehicle between the two axles to collect the vibration response of the vehicle shown in Fig. 10.8. A sampling frequency of 200 Hz is used for both sensors used in this

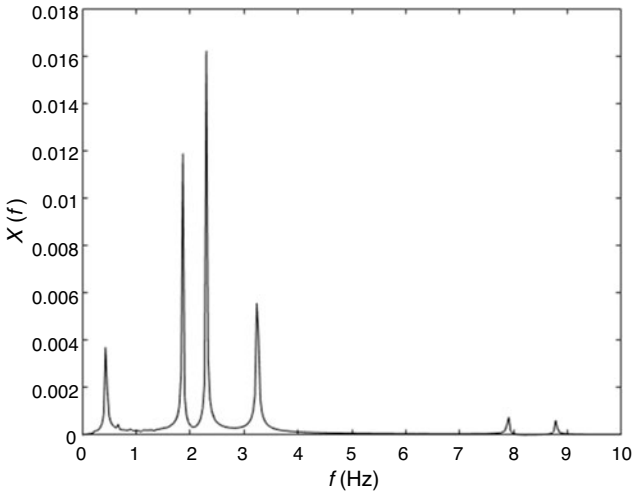

Fig. 10.3 FFT of vehicle acceleration response at a speed of 40 km/h

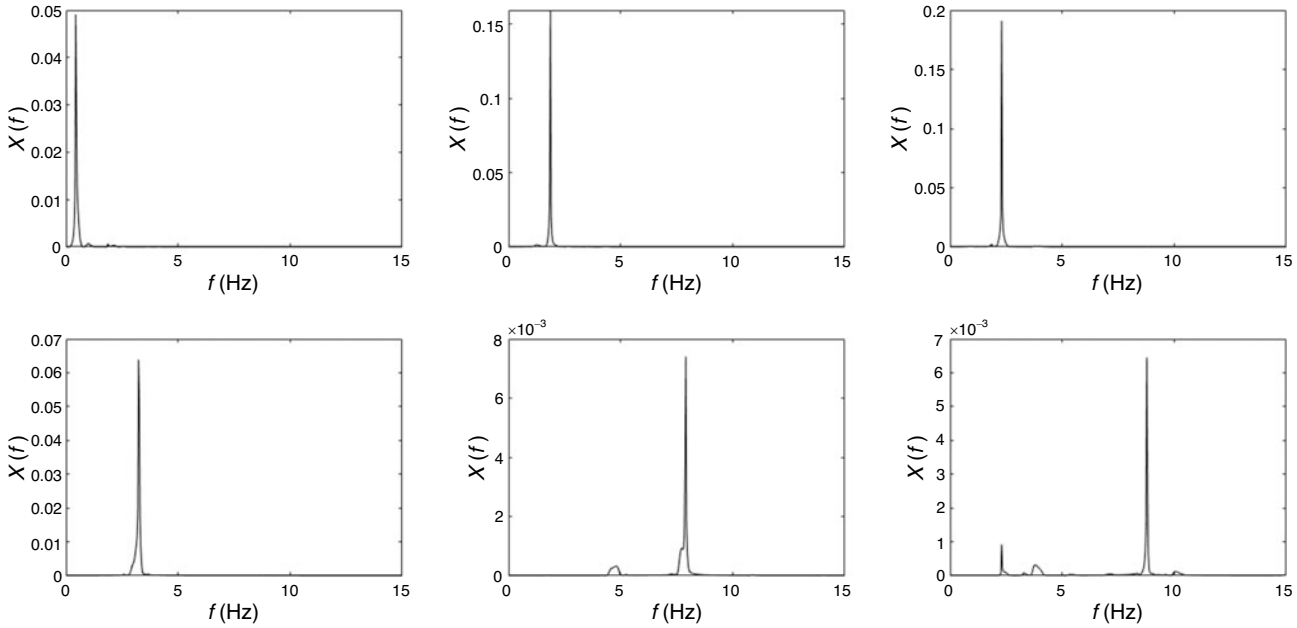

Fig. 10.4 WPT coefficients of vehicle acceleration response at a speed of 40 km/h

experiment. The bridge is subjected to forced vibrations using a shaker table from underneath, shown in Fig. 10.8. Forced vibrations are used to mimic the ambient vibrations of a bridge that may be caused due to wind excitations.

Figure 10.9 shows the FFT results for the bridge and vehicle acceleration response. Two bridge frequencies directly measured from the bridge deck, which can be seen in Fig. 10.9a, are mentioned in the first column (f_{direct}) of Table 10.2. Using the analytical formula to calculate the bridge frequency pair, the frequency pair values are calculated and are shown in the second column ($f_{\text{analytical pair}}$) of Table 10.2. The measured values of the frequency pair are shown in Fig. 10.9b and are tabulated in the third column ($f_{\text{measured pair}}$) of Table 10.2. By averaging the frequency pair values from column 3 of Table 10.2, the bridge frequencies are calculated for the indirect method and are shown in column 4 (f_{indirect}) of Table 10.2. It can be seen that the values from column 1 and column 4 of Table 10.2 are close to each other and indirect monitoring can be used as a reliable way of measuring the natural frequencies of a bridge. Figure 10.10 shows the WPT coefficients for the vehicle acceleration response from Fig. 10.9b. It shows that the various frequency components from Fig. 10.9b can be well separated by the WPT algorithm and can be classified using a TF method. Further studies are undergoing to differentiate between these frequencies separated by the WPT algorithm.

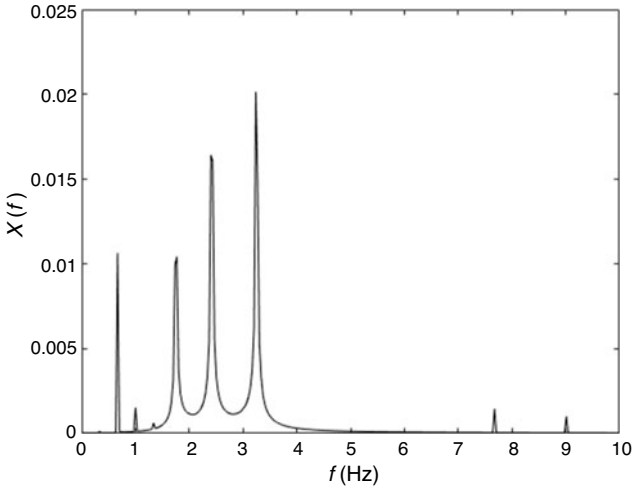

Fig. 10.5 FFT of vehicle acceleration response at a speed of 60 km/h

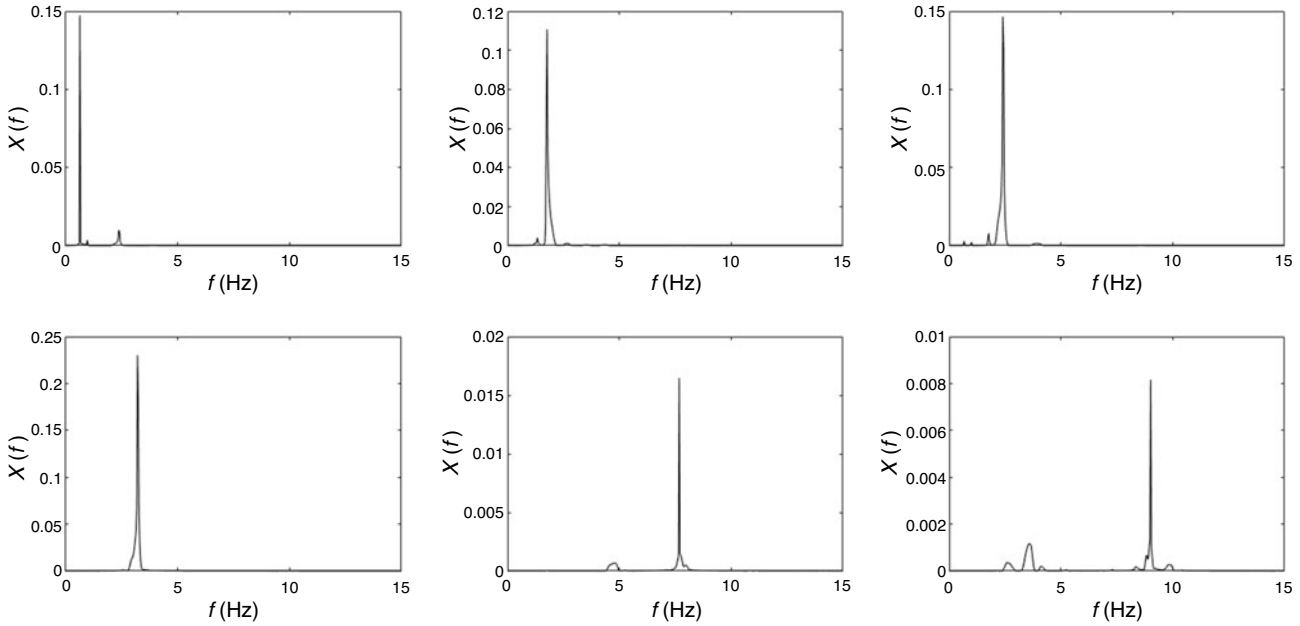

Fig. 10.6 WPT coefficients of vehicle acceleration response at a speed of 60 km/h

Table 10.1 Properties of the bridge model

Width (m)	Length (m)	Thickness (mm)	$\overline{m}$ (kg/m)	ω_1 (Hz)	ω_2 (Hz)
0.6	2.4	12.7	3.34	4.71	9.96

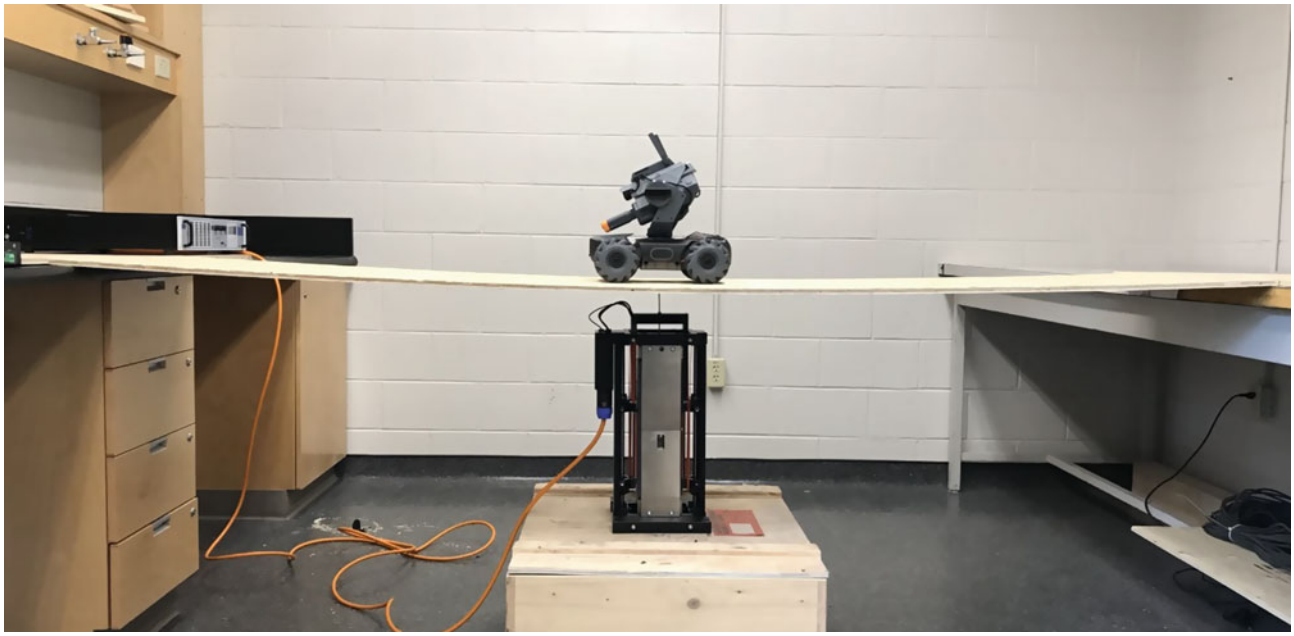

Fig. 10.7 Experimental vehicle model

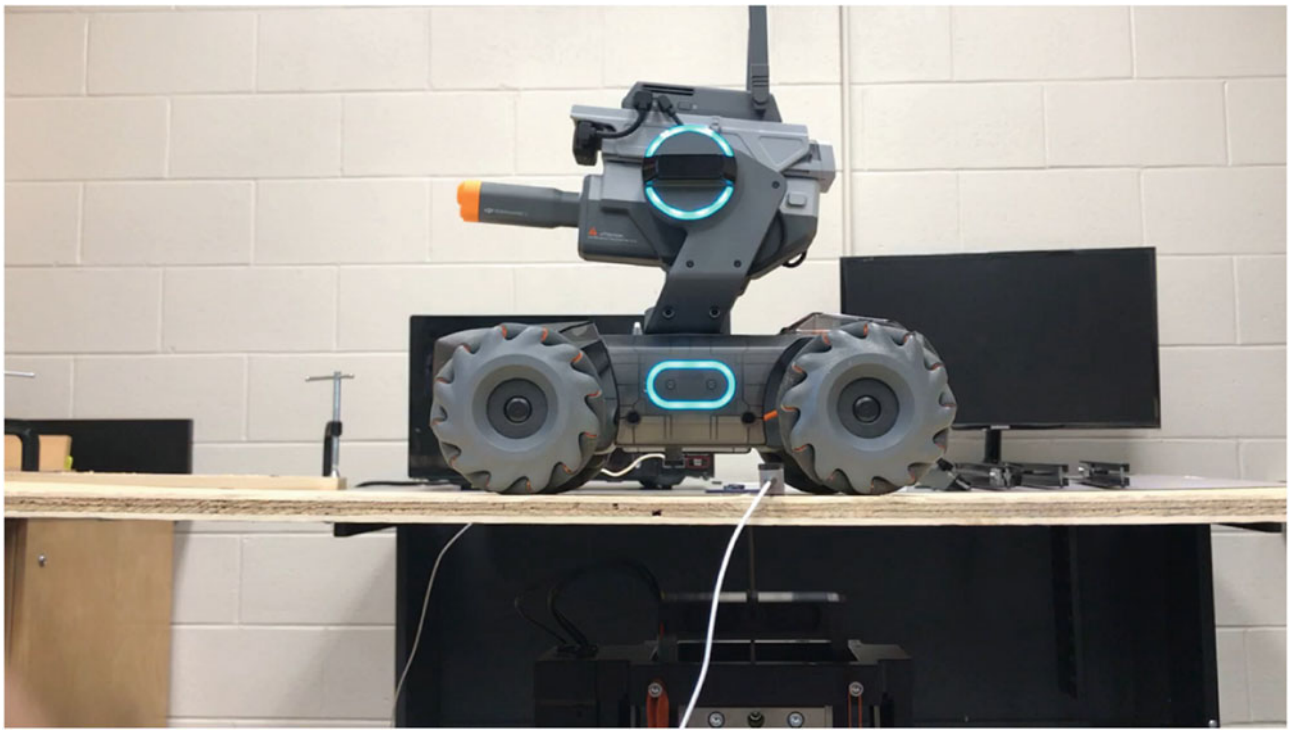

Fig. 10.8 Vehicle and beam instrumented with accelerometer sensors

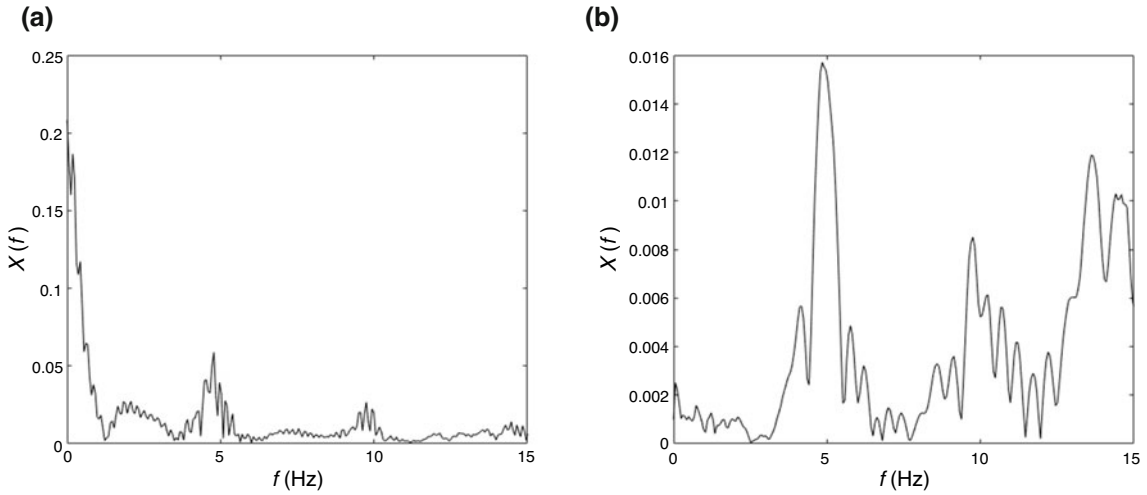

Fig. 10.9 FFT of (**a**) bridge acceleration response and (**b**) vehicle acceleration response

Table 10.2 Frequency values of bridge and vehicle responses

f_{direct}	$f_{\text{analytical pair}}$	$f_{\text{measured pair}}$	f_{indirect}
	4.37	4.17	
4.78			4.57
	5.19	4.96	
	8.93	9.13	
9.74			9.69
	10.57	10.24	

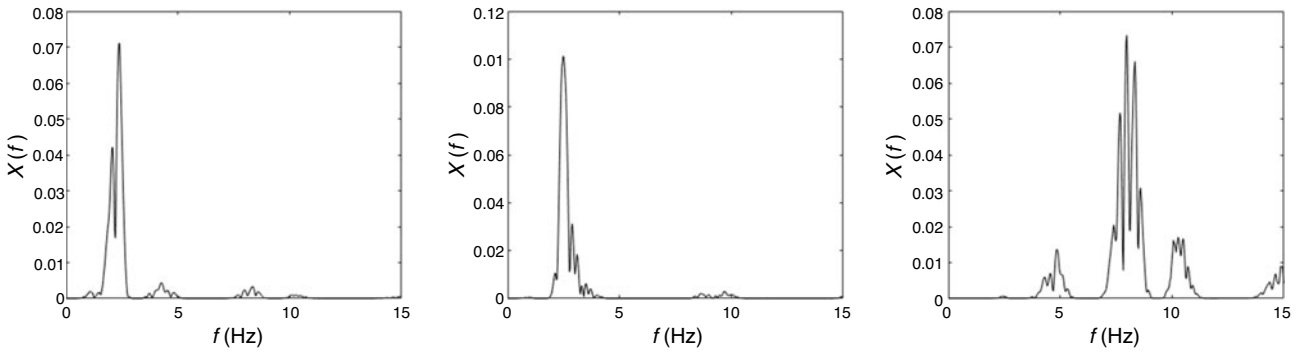

Fig. 10.10 WPT coefficients of vehicle acceleration response

10.6 Conclusion

Bridge infrastructure is an important element of economic development and needs to be maintained regularly. Mobile sensor networks can be leveraged to monitor the bridges at a fractional cost of current monitoring methods. Using the passing vehicles traveling over a bridge as an actuator and a sensor is an active research area. This study investigates the feasibility of drive-by bridge monitoring with numerical and experimental investigations. Responses from the passing vehicle, containing the bridge dynamics data filtered through the suspension of the vehicle itself, are collected and fed into the WPT algorithm. WPT is used to delineate the various frequency contributions from the bridge, vehicle, and vibrations due to the movement of the vehicle. The output of WPT contains bridge frequencies, vehicle frequencies, and driving frequencies, which cannot be differentiated without a TF method. A TF-based modulation can be used as a quantification method to classify the individual components resulting from WPT. Future studies are underway to differentiate between the frequency components using the feature extraction tools.

Acknowledgments The proposed research was funded by the Natural Sciences and Engineering Research Council (NSERC) of Canada through the Discovery Grant and NSERC WSS Accelerator Grant awarded to the last author through Western University.

References

1. Singh, P., Sadhu, A.: Limited sensor-based bridge condition assessment using vehicle-induced nonstationary measurements. Structure. **32**, 1207–1220 (2021)
2. Singh, P., Keyvanlou, M., Sadhu, A.: An improved time-varying empirical mode decomposition for structural condition assessment using limited sensors. Eng. Struct. **232**, 111882 (2021)
3. Malekjafarian, A., McGetrick, P.J., OBrien, E.J.: A review of indirect bridge monitoring using passing vehicles. Shock. Vib. **286139** (2015)
4. Yang, Y.B., Yang, J.P.: State-of-the-art review on modal identification and damage detection of bridges by moving test vehicles. Int. J. Struct. Stab. Dyn. **18**(2), 1850073 (2018)
5. Shokravi, H., Shokravi, H., Bakhary, N., Heidarrazaei, M., Kaloor, S.S.R., Petru, M.: Vehicle-assisted techniques for health monitoring of bridges. Sensors. **20**, 3460 (2020)
6. Yang, Y.B., Lin, C.W., Yan, J.D.: Extracting bridge frequencies from the dynamic response of a passing vehicle. J. Sound Vib. **272**, 471–493 (2004)
7. Yang, Y.B., Lin, C.W.: Use of a passing vehicle to scan the fundamental bridge frequencies: an experimental verification. Eng. Struct. **27**, 1865–1878 (2005)
8. Yang, Y.B., Chang, K.C.: Extraction of bridge frequencies from the dynamic response of a passing vehicle enhanced by the EMD technique. J. Sound Vib. **322**, 718–739 (2009)
9. Yang, Y.B., Lin, C.W.: Vehicle-bridge interaction dynamics and potential applications. J. Sound Vib. **284**, 205–226 (2005)
10. Gonzalez, A., OBrien, E.J., McGetrick, P.J.: Identification of damping in a bridge using a moving instrumented vehicle. J. Sound Vib. **331**, 4115–4131 (2012)
11. Siringoringo, D.M., Fujino, Y.: Estimating bridge fundamental frequency from vibration responses of instrumental passing vehicle: analytical and experimental study. Adv. Struct. Eng. **15**(3), 417–433 (2012)
12. OBrien, E.J., McGetrick, P.J., Gonzalez, A.: A drive-by inspection system via vehicle moving force identification. Smart Struct. Syst. **13**(5), 821–848 (2014)
13. Tan, C., Elhattab, A., Uddin, N.: Drive-by bridge frequency-based monitoring utilizing wavelet transform. J. Civ. Struct. Heal. Monit. **7**, 615–625 (2017)
14. Tan, C., Elhattab, A., Uddin, N.: Wavelet-energy approach for detection of bridge damages using direct and indirect bridge records. J. Infrastruct. Syst. **26**(4), 04020037 (2020)
15. Alamdari, M.M., Chang, K.C., Kim, C.W., Kildashti, K., Kalhori, H.: Transmissibility performance assessment for drive-by bridge inspection. Eng. Struct. **242**, 112485 (2021)
16. Zhang, J., Yang, D., Ren, W.X., Yuan, Y.: Time-varying characteristics analysis of vehicle-bridge interaction system based on modified S-transform reassignment technique. Mech. Syst. Signal Process. **160**, 107807 (2021)
17. Kankanamge, Y., Hu, Y., Shao, X.: Application of wavelet transform in structural health monitoring. Earthq. Eng. Eng. Vib. **19**(2), 515–532 (2020)
18. Ren, W., Sun, Z., Xia, Y., Hao, H., Deeks, A.J.: Damage identification of shear connectors with Wavelet Packet Energy: laboratory test study. J. Struct. Eng. **134**(5), 832–841 (2008)
19. Han, J.G., Ren, W.X., Sun, Z.S.: Wavelet packet-based damage identification of beam structures. Int. J. Solids Struct. **42**, 6610–6627 (2005)
20. Ding, Y., Li, A., Liu, T.: A study on the WPT-based structural damage alarming of the ASCE benchmark experiments. Adv. Struct. Eng. **11**, 121–127 (2008)
21. Sadhu A.: Decentralized ambient system identification of structures, Ph.D. Thesis, Department of Civil and Environmental Engineering, University of Waterloo, Canada (2013)
22. Pan, Y., Zhang, L., Wu, X., Zhang, K., Skibniewski, M.J.: Structural health monitoring and assessment using wavelet packet energy spectrum. Saf. Sci. **120**, 652–665 (2019)
23. Zhou, K., Lei, D., He, J., Zhang, P., Bai, P., Zhu, F.: Single micro-damage identification and evaluation in concrete using digital image correlation technology and wavelet analysis. Constr. Build. Mater. **267**, 120951 (2021)

Chapter 11
Bayesian Uncertainty Assessment for Modulus of Elasticity of Concrete and Mechanical Properties of Steel Reinforcing Bar

Felipe Guerrero, Albert R. Ortiz, and Julian Carrillo

Abstract The variability in the mechanical properties of the concrete and reinforcing steel used in reinforced concrete (RC) in Colombia affects structural systems' design process and performance. It leads to struggling to comply with the requirements of local building codes. This study presents and discusses the uncertainty quantification (UQ) of both the mechanical parameters of the stress–strain curve of steel reinforcing bars and the modulus of elasticity of concrete. The database comes from experimental programs, including monotonic axial tests on steel bars from different manufacturers in the country, and axial compression tests reported in 22 studies on concrete made in 13 different cities of Colombia. Bayesian inference methods were used to update the Raynor model of the monotonic stress–strain curve of the steel and the equations proposed by the Colombian and the ACI 318–19 building codes for E_c as a function of concrete strength and unitary weight. Distributions for both materials are then presented, and predictive check tests are performed for validation. The Bayesian statistical analysis allowed to contrast the mechanical properties obtained experimentally, with nominal properties specified by the manufacturers, in the case of the steel bars. New equations and their associated uncertainties are proposed for representative estimates of the modulus of elasticity of the concrete in Colombia

Keywords Stress-strain curve · Modulus of elasticity of concrete · Bayesian uncertainty quantification · Concrete structures · Steel reinforcing

11.1 Introduction

The nominal mechanical properties of materials are necessary for the design and the structural analysis of reinforced concrete buildings. In the case of concrete material, the variability in the modulus of elasticity is widely used because of its influence in the stiffness of structures. Traditionally, the estimation of this variable is made with a function of other parameters that are known, like the maximum concrete strength, density, and type of the coarse aggregates. In 2010, the current Colombian building code (NSR-10) [1] proposes a group of equations following the structure of the ACI 318-08 [2]. Constants of these equations were updated by a local study by Farias in 1994 [3].

From 1994 to today, there are new studies of the concrete modulus of elasticity proposing different constants. These studies came from different regions and used diverse methodologies to analyze the data. The variability in methods and tests affects a generalization model of the modulus, even when the available data of these studies are a more extensive and more varied sample than that used in the equations currently proposed in the NSR-10. Because of the variability in tests and methodologies, this study presents a general model to calculate the modulus of elasticity of the concrete involving Bayesian statistical analysis methods.

Other cases where uncertainties may lead to design problems are in the reinforcing steel because its mechanical properties must comply with the current regulations for earthquake-resistant construction, such as ductility or yielding ratios. The NSR-10 has requirements that are primarily those prescribed by ACI-318 [2]; however, there is steel coming irregularly from other

F. Guerrero (✉) · A. R. Ortiz
School of Civil Engineering and Geomatics, Universidad del Valle, Cali, Colombia
e-mail: felipe.guerrero@correounivalle.edu.co; albert.ortiz@correounivalle.edu.co

J. Carrillo
Department of Civil Engineering, Universidad Militar de Nueva Granada, Bogotá, Colombia
e-mail: wilmer.carrillo@unimilitar.edu.co

H. Y. Noh (eds.), *Dynamics of Civil Structures, Volume 2*, Conference Proceedings of the Society for Experimental Mechanics Series, https://doi.org/10.1007/978-3-031-05449-5_11

countries [4] that may not meet the requirements of local building codes and material standards, increasing the risk of collapse in earthquake-resistant constructions.

Using the Bayesian statistical analysis, this chapter presents and discusses the quantification of uncertainty of the stress–strain curve of steel bars marketed in Bogotá. This study regards the main mechanical properties of grade steel bars

11.2 Background

11.2.1 Concrete Modulus of Elasticity

The relationship between the modulus of elasticity of concrete (E_c) and the maximum compressive strength of concrete (f'_c) is proportional to the square root of the latter, as shown in Eq. (11.1). Similarly, the modulus of elasticity can also be calculated based on the unit weight of concrete, w_c (kg/m^3), with an additional parameter that corresponds to the cube root of the density squared, as shown in Eq. (11.2). In both equations, the terms k_1 and k_2 correspond to adjustment factors that vary according to the manufacturing conditions and characteristics of the aggregates, so it is common to find differences between regions or countries.

$$E_c = k_1 \cdot \sqrt{f'_c} \tag{11.1}$$

$$E_c = w_c^{1.5} \cdot k_2 \cdot \sqrt{f'_c} \tag{11.2}$$

For the case of Colombia, the NSR-10 proposes the value of k_1 = 3900 in MPa for Eq. (11.1) and k_2 = 0.034 in MPa for Eq. (11.2). When the origin of the coarse aggregate is discriminated, the NSR-10 reports different values of the proportional constants k_1 y k_2. Table 11.1 presents a summary of the values reported in Sect. 8.5 of Title C of the NSR-10.

11.2.2 Stress–Strain Behavior of Steel Bars

The Raynor model for the monotonic envelope curve [5], shown in Fig. 11.1, was used for the quantification of the uncertainty of the mechanical parameters of the stress–strain curve of steel reinforcements. The monotonic envelope curve is defined by a three-piece function as shown by the following equations:

$$\sigma_{env} = \epsilon \cdot E \quad for \ \ \epsilon \ \leq \epsilon_y \tag{11.3}$$

$$\sigma_{env} = \sigma_y + (\epsilon - \epsilon_y) \cdot E_y \quad for \ \ \epsilon_y < \epsilon \ \leq \ \epsilon_{sh} \tag{11.4}$$

$$\sigma_{env} = \sigma_u - (\sigma_u - \sigma_{sh}) \cdot \left(\frac{\epsilon_u - \epsilon}{\epsilon_u - \epsilon_{sh}} \right)^{C_1} \quad for \ \ \epsilon_{sh} < \epsilon \ \leq \ \epsilon_u \tag{11.5}$$

where

$$\epsilon_y = \sigma_y / E \tag{11.6}$$

$$\sigma_{sh} = \sigma_y + (\epsilon_{sh} - \epsilon_y) \cdot E_y \tag{11.7}$$

Table 11.1 Values of the proportional constants reported in NSR-10

Origin of aggregate	k_1	k_2
Igneous	5500	0.047
Metamorphic	4700	0.041
Sedimentary	3600	0.031
Without distinguishing	3900	0.034

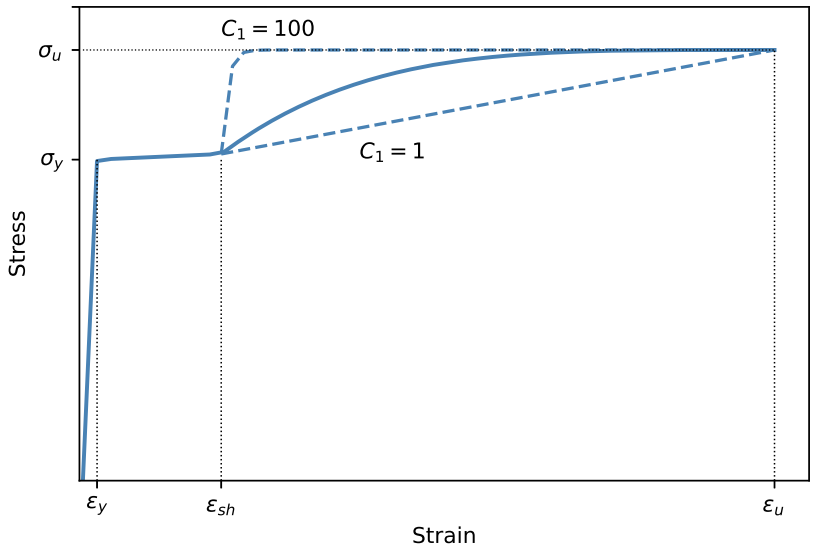

Fig. 11.1 Raynor model for monotonic envelope curve for steel

σ_{env} is the envelope stress, E is the elastic modulus, σ_y and ϵ_y are stress and strain at steel yield, E_y is the slope of the yield plateau, σ_{sh} and ϵ_{sh} are stress and strain at the onset of strain hardening, σ_u and ϵ_u are ultimate peak stress and strain, and C_1 is a parameter that defines the curvature of the strain hardening curve.

11.2.3 Model Updating Using Bayesian Inference

This study uses Bayesian inference to update the models indicated in Eqs. (11.1) to (11.7). The methodology of Bayesian inference is based on Bayes' theorem. It allows to obtain the maximum probability points that minimize the adjustment error and the probability distribution of the parameters and the error associated with the model that is being updated. Bayes' theorem tries to update the terms of the model and estimate the variation of the error. According to Bayes' theorem, the term $p(|M, D)$ is the posterior term that presents the probability density function of the parameters being adjusted according to experimental data D and a model M, and it is calculated with Eq. (11.8).

$$p(\theta|M, D) = \frac{p(\theta|M, D)p(\theta)}{p(D)} \tag{11.8}$$

The term $p(\theta)$ corresponds to the probability associated with the prior knowledge of the parameters, called the prior. The denominator $p(D)$ is a normalization factor also called a Bayes factor. The term $p(D|\theta, M)$ is known as the likelihood function and is the probability of fitting the data D given a set of parameters θ.

11.3 Analysis

11.3.1 Model Updating of the Concrete Modulus of Elasticity

There are 22 documents on the study of the modulus of elasticity of concrete in Colombia that publish the original experimental data. The original data are needed because the inference is made from the original data and not from factors obtained by other authors. The documents used for this analysis are summarized in Table 11.2. Figure 11.2 presents the data of the modulus of elasticity of the concrete as a function of the compressive strength as a function of the region and the origin of the aggregate.

Table 11.2 Documents used as source of information for estimating E_c

Year	Authors	University	City/origin	Data
1987	Cajas and Herneńdez [6]	Universidad Nacional de Colombia	Bogotá/unreported	77
1991	Oscar Ardila Roa [7]	Universidad de los Andes	Bogotá/sedimentary	348
1992	Farias [8]	Pontificia Universidad Javeriana	Bogotá/sedimentary	180
1993	Cano [9]	Universidad del Valle	Cali/sedimentary	47
1993	Barbosa and Castro [10]	Pontificia Universidad Javeriana	Villavicencio/metamorphic	60
1993	Murcia and Valencia [11]	Pontificia Universidad Javeriana	Cali/igneous	100
1993	González y Maldonado [12]	Pontificia Universidad Javeriana	Cartagena /sedimentary	88
1993	Ángulo et al [13]	Pontificia Universidad Javeriana	Bogotá/sedimentary	532
1993	Plano and Campos [14]	Pontificia Universidad Javeriana	Ibagué/sedimentary	139
1993	Cabrales and Salas[15]	Pontificia Universidad Javeriana	Montería/sedimentary	69
1994	Bockelman and Rodríguez [16]	Pontificia Universidad Javeriana	Barranquilla/sedimentary	80
1994	Saraga and Seuscun [17]	Pontificia Universidad Javeriana	Tunja/sedimentary	100
1994	Albán and Serrano [18]	Pontificia Universidad Javeriana	Bucaramanga/sedimentary	240
1994	Silva and Vargas [19]	Pontificia Universidad Javeriana	Neiva/igneous	99
1994	Ortiz and Pimienta [20]	Pontificia Universidad Javeriana	Valledupar/igneous	69
1994	Barreto [21]	Pontificia Universidad Javeriana	Guamo/sedimentary	124
2001	López and Montejo [22]	Universidad del Valle	Cali/igneous	35
2001	Sandino and Orozco [23]	Universidad del Valle	Cali/igneous	34
2006	De la Rosa and Durán [24]	Universidad del Magdalena	Santa Marta/metamorphic	65
2012	Carvajal and González [25]	Universidad Pontificia Bolivariana	Bucaramanga/unreported	30
2015	Brand [26]	Universidad La Gran Colombia	Bogotâ/unreported	60
2016	Orozco [27]	Universidad La Gran Colombia	Bogotâ/sedimentary	42

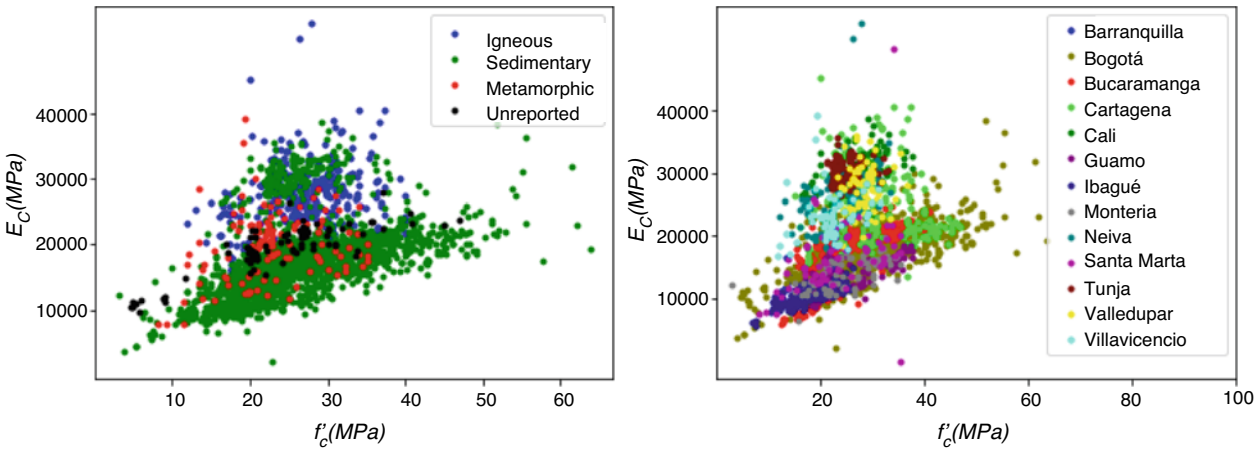

Fig. 11.2 Variation of the modulus of elasticity as a function of the measured compressive strength of the concrete according to the origin of the aggregate or the city of origin

Figure 11.3 presents the posterior distribution of the parameter k_1 and σ after running 10000 samples using a Markov Chain Monte Carlo. The distribution of the parameter k_1 has a mean of 4402 $\sqrt{MPa}$, and it was obtained from all the data as a function of the compressive strength, corresponding to Eq. (11.1) (without distinction of coarse or density). The term σ refers to the standard deviation of the likelihood term, and it is associated with the deviation of the model to the data. The mean value of the standard deviation follows a distribution with mean of 5637 MPa.

When using Eq. (11.2), which includes the density of the concrete, the updating process shows the variation as seen in Fig. 11.4. Analogously to each of the previous results, Table 11.3 summarizes the results of the proposed values for k_1 and k_2 depending on the origin of the aggregate.

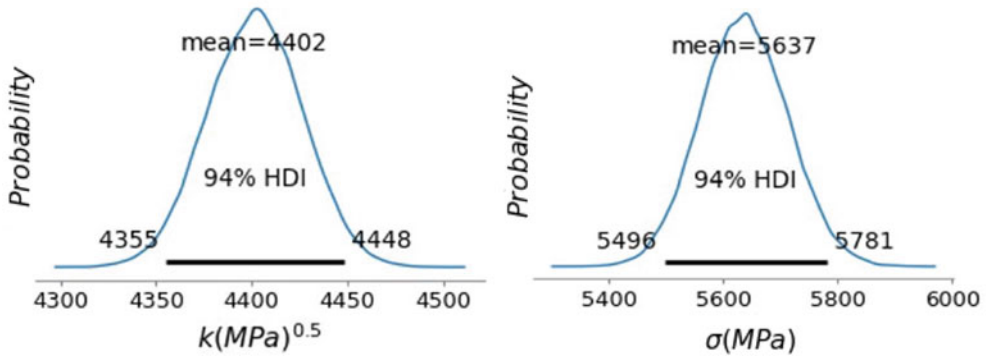

Fig. 11.3 (**a**) Characterization of the parameter k_1 for the general elasticity model as a function of the compressive strength (Eq. (11.1)). (**b**) Standard deviation of the general elasticity model as a function of compressive strength (Eq. (11.1))

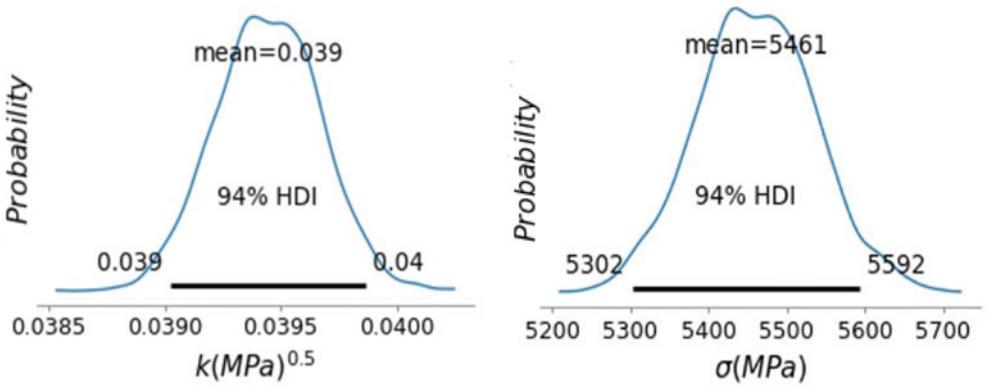

Fig. 11.4 (**a**) Characterization of the parameter k_2 for the general elasticity model as a function of the compressive strength (Eq. (11.2)). (**b**) Standard deviation of the general elasticity model as a function of compressive strength (Eq. (11.2))

Table 11.3 Proposed values of propositional constants k_1 and k_2

	Eq. (11.1)		Eq. (11.2)	
Origin of aggregate	k_1	σ_{E_c} (MPa)	k_2	σ_{E_c} (MPa)
Igneous	6002	5778	0.051	5475
Metamorphic	4995	5572	0.051	4944
Sedimentary	4112	4767	0.037	4636
Without distinguishing	4402	5637	0.039	5462

Table 11.4 Distribution of the number of specimens per diameter and per company

	Diameter of the bar					
Company	#3	#4	#5	#6	#7	#8
A	5	5	5	5	0	5
B	0	5	5	5	5	5
C	4	5	5	5	5	5

11.3.2 Model Updating of the Strain–Stress Curve of Steel Bars

For the analysis of the uncertainty of the stress–strain curve of the reinforcing steel bars, 85 monotonic stress tests were carried out. The data include steel bars of different diameters, with a range between 9.5 mm (3/8”) and 25.4 mm (1”), and from three different companies, named as A, B, and C. Table 11.4 shows the distribution of the considered specimens, where the # indicates the nominal diameter of the bar in one-eighth of an inch as custom in Colombia. Figure 11.5 shows the variability of the data in the stress–strain graph of the reinforcing bars of the same diameter (# 3) from company A.

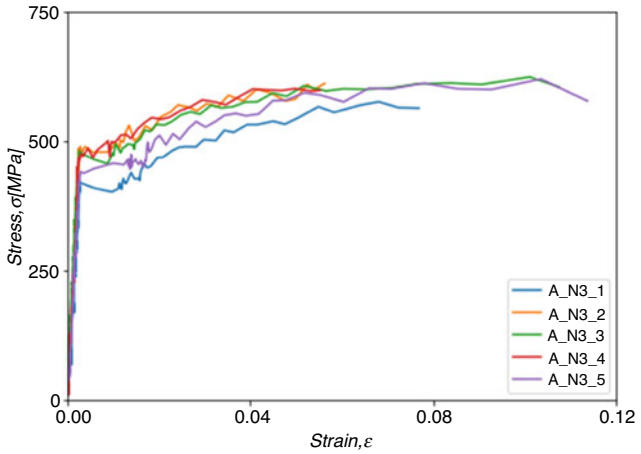

Fig. 11.5 Samples of bars of the same diameter (#3), company A

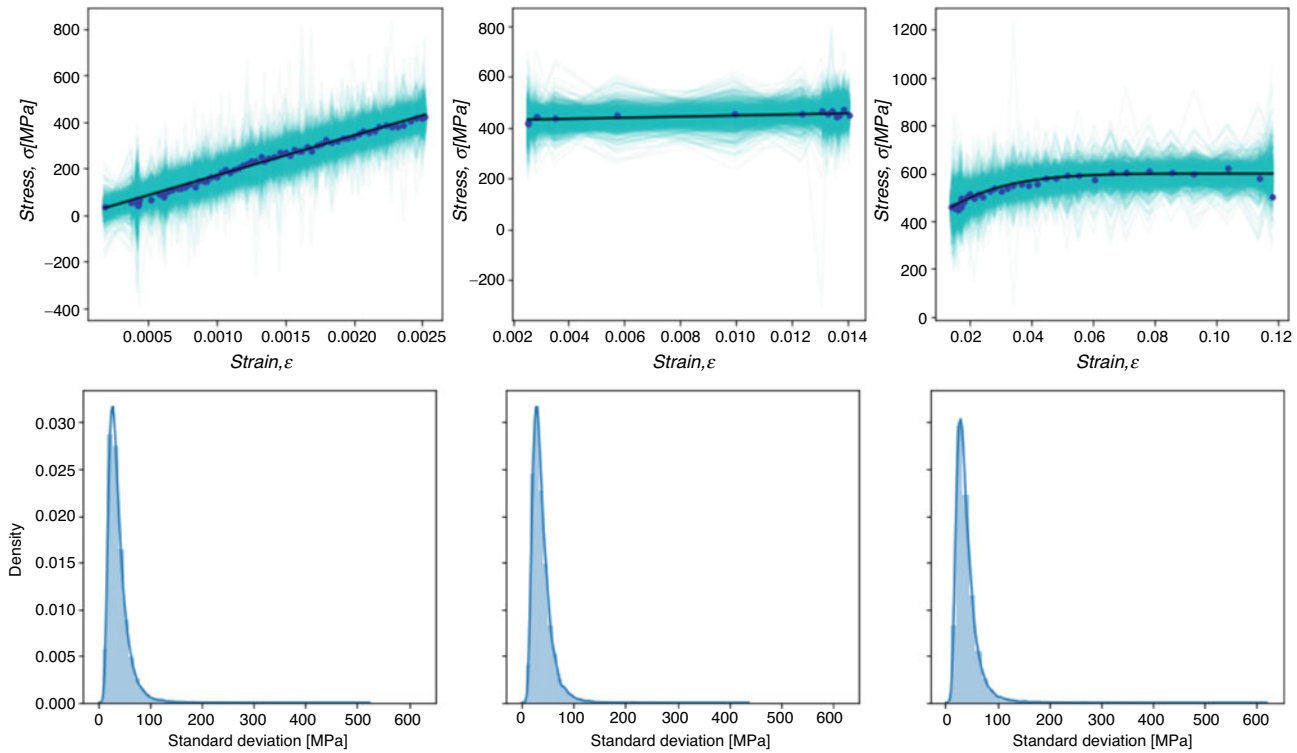

Fig. 11.6 Model fit and uncertainty by sections of the stress–strain curve for the linear part, yield, and strain hardening

Figure 11.6 shows the updated model and the uncertainty associated with each of the pieces of the stress–strain diagram. The curve is divided into the linear elastic part (Eq. (11.4)), yield (Eq. (11.5)), and strain hardening (Eq. (11.6)) with their respective standard deviations. Figure 11.7 shows the convergence of each parameter and the standard deviation of the model. This Bayesian analysis allows to find the correlations between the parameters of the model. Figure 11.8 plots the correlations obtained for the bars # 3 of company A.

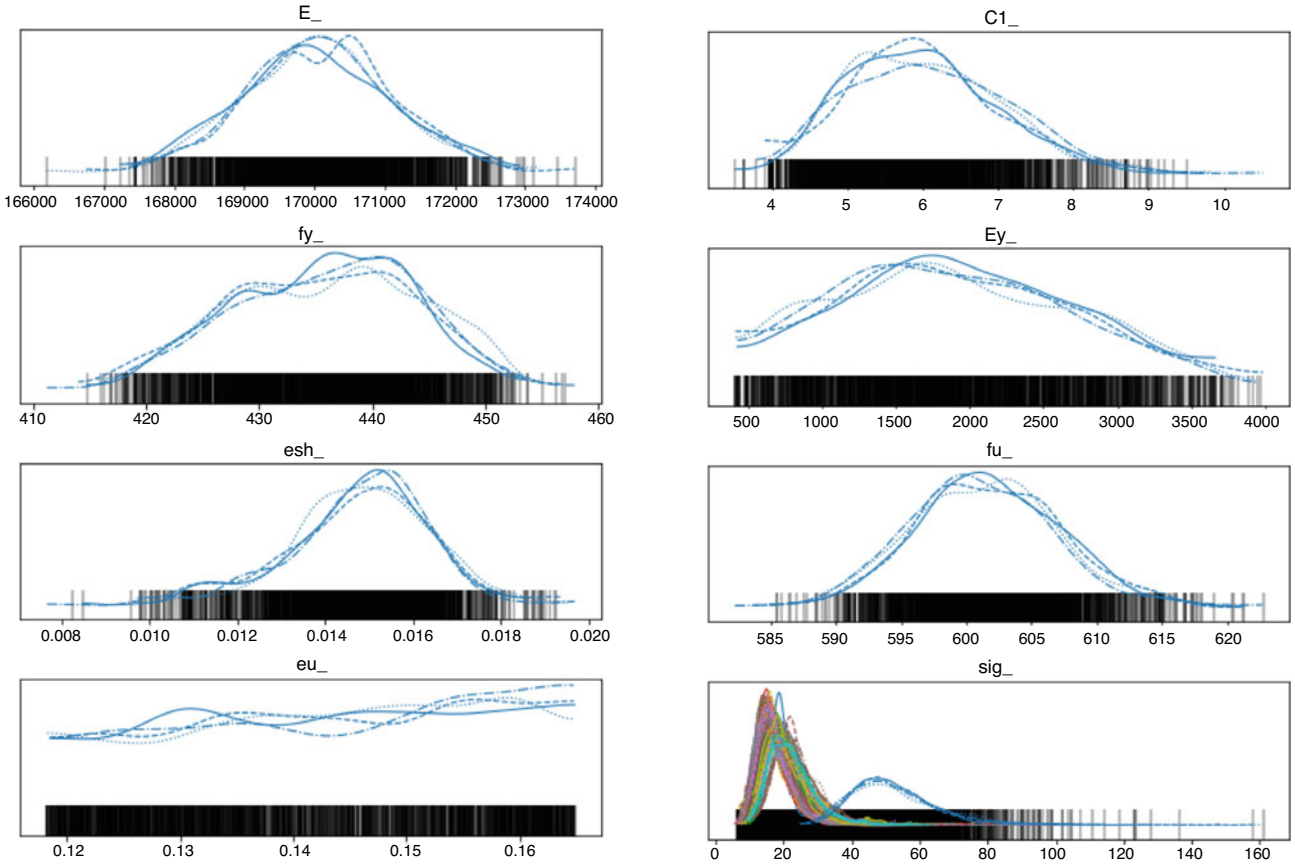

Fig. 11.7 Parameter convergence, specimen of company A

11.4 Conclusion

This work applies Bayesian inference to estimate the uncertainty in the models of the two main construction materials: concrete and steel. The analysis focuses on the modulus of elasticity (concrete) and the parameters that describe the Reynor model for the stress–strain curve (steel). The study of the variation of the modulus of elasticity of concrete was carried out as a function of the concrete compressive strength, concrete's weight, and the coarse aggregate's origin. The analysis included studies from 1987 to 2016, with a total of 2,618 samples taken in several cities of Colombia (Barranquilla, Villavicencio, Cali, Tunja, Cartagena, Bucaramanga, Bogotá, Neiva, Valledupar, Ibagué, Montería, Guamo, and Santa Marta).

In the general expression of the modulus of elasticity as a function of the concrete strength, the constant k_1 yields a distribution with an average of 4402. When the unit weight is included in the equation (as in Eq. (11.2)), k_2), k_2 constant yields to 0.039. Both values are higher than those proposed by the current guidelines. In both cases, the coefficient of variation yields to approximately 25%.

For the stress–strain model of the steel, the characterization of the uncertainty is carried out using the ten parameters of the curve. The model was updated for each slice of the stress–strain curve, obtaining a standard deviation of approximately 20 MPa independently of the piece. In the updated model, a high correlation between the f_y (strain yield) and the E_y (slope of the yield plateau) can be observed. Also, a modulus of elasticity lower than expected was found (170 GPa vs 200 GPa).

The inclusion of the variability of both materials, concrete and steel, allows estimating more realistic scenarios on the mechanical behavior of concrete structures in Colombia. In addition, the information produced in this document could suit an extensive program for reliability analysis of structures, leading to update design factors, and avoiding using imported factors from different latitudes that may not apply to the Colombian materials.

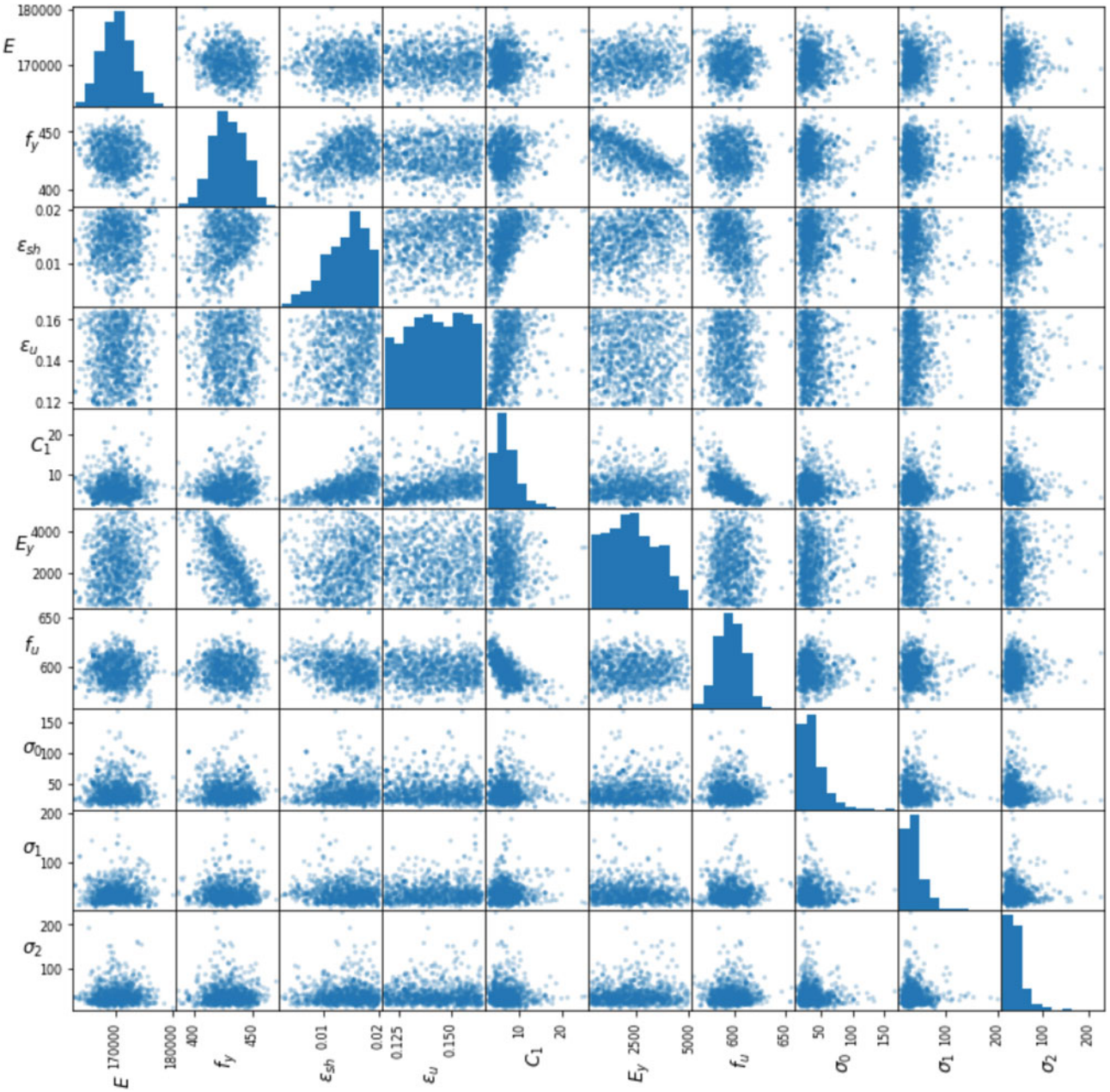

Fig. 11.8 Parameter correlations, bar # 3 of company A

Acknowledgments The authors would like to acknowledge Vicerrectoría de Investigaciones of the UMNG for the financial support through Project EXT-INV-3575, and to university members of the Colombian Earthquake Engineering Research Network – CEER. The views expressed in this paper are solely those of the authors and do not necessarily reflect the views of the sponsors.

References

1. A. AIS: Asociación Colombiana de Ingeniería Sísmica. Reglamento Colombiano de Construcción Sismo Resistente NSR-10 (2010)
2. ACI Committee y International Organization for Standardization, Building code requirements for structural concrete (ACI 318-08) and commentary (2008)
3. Farias, S.: Recopilación de la información de los ensayos sobre el módulo de elasticidad del concreto en diferentes ciudades del país. Ph.D. thesis, Universidad de los Andes (1994)

4. Carrillo, J., Lozano, H., Arteta, C.: Mechanical properties of steel reinforcing bars for concrete structures in central Colombia. J. Build. Eng. **33**, 101858 (2021). https://doi.org/10.1016/j.jobe.2020.101858. https://www.sciencedirect.com/science/article/pii/S2352710220334914
5. Raynor, D.J., Lehman, D.E., Stanton, J.F.: Bond-slip response of reinforcing bars grouted in ducts. Struct. J. **99**(5), 568–576 (2002)
6. Cajas, F.A., Hernández, L.M.: Evaluación del módulo de elasticidad estático secante del hormigón. Ph.D. thesis, Universidad Nacional de Colombia (1987)
7. Roa, O.A., Módulo secante de elasticidad del concreto. Ph.D. thesis, Universidad de los Andes (1991)
8. Farias, S.L.: Aproximación a la obtención del módulo de elasticidad del concreto. Ph.D. thesis, Pontificia Universdidad Javerian (1992)
9. Moya, S.L.C.: Evaluación del módulo de elasticidad del concreto para la ciudad de cali. Ph.D. thesis, Universidad del Valle (1993)
10. Vásquez, C.H.C., Barbosa, I.D.: Ciclo investigativo para la obtención del módulo de elasticidad del concreto en la ciudad de villavicencio, Ph.D. thesis, Pontificia Universidad Javeriana (1993)
11. Valencia, R., Murcia, L.C.: Ciclo investigativo para la obtención del módulo de elasticidad del concreto en la ciudad de cali. Ph.D. thesis, Pontificia Universdidad Javeriana (1993)
12. Padrón, A.M., de Jesús Gonzalez, J.: Ciclo investigativo para la obtención del módulo de elasticidad del concreto en la ciudad de cartagena. Ph.D. thesis, Pontificia Universidad Javeriana (1993)
13. Padilla José Antonio, A.J.F.A.L., Cortés, A., Fernando, C., Polo, Ciclo investigativo para la obtención del módulo de elasticidad del concreto en la ciudad de bogotá (segunda parte). Ph.D. thesis, Pontificia Universidad Javeriana (1993)
14. Campos, A.P.A.: Ciclo investigativo para la obtención del módulo de elasticidad del concreto en la ciudad de ibagué. Ph.D. thesis, Pontificia Universidad Javeriana (1993)
15. Salas, A., Cabrales, E.: Ciclo investigativo para la obtención del módulo de elasticidad del concreto en la ciudad de montería. Ph.D. thesis, Pontificia Universidad Javeriana (1993)
16. Valdez, J.L.R.C.C.E.B.: Ciclo investigativo para la obtención del módulo de elasticidad del concreto en la ciudad de barranquilla. Ph.D. thesis, Pontificia Universidad Javeriana (1994)
17. Cuervo, G.A.S.A.A.S.: Ciclo investigativo para la obtención del módulo de elasticidad del concreto en la ciudad de tunja. Ph.D. thesis, Pontificia Universidad Javeriana (1994)
18. Albán, R.E.: Serrano, Ciclo investigativo para la obtención del módulo de elasticidad del concreto en la ciudad de bucaramanga. Ph.D. thesis, Pontificia Universidad Javeriana (1994)
19. Silva, J.E.V.M.F.: Ciclo investigativo para la obtención del módulo de elasticidad del concreto en la ciudad de neiva. Ph.D. thesis, Pontificia Universidad Javeriana (1994)
20. Pimienta, A.O.M.: Ciclo investigativo para la obtención del módulo de elasticidad del concreto en la ciudad de valledupar. Ph.D. thesis, Pontificia Universidad Javeriana (1994)
21. Barreto, E.D.: Ciclo investigativo para la obtención del módulo de elasticidad del concreto en el guamo. Ph.D. thesis, Pontificia Universidad Javeriana (1994)
22. Montejo, L.A., López, H.: eterminación de las propiedades mecánicas del concreto endurecido usados en el diseño estructural para los concretos elaborados en la ciudad de cali con materiales elaborados de la región. Ph.D. thesis, Universidad del Valle (2001)
23. Luna, D.A.O., Sandino, C.: Determinación de las propiedades mecánicas del concreto endurecido usados en el diseño estructural para los concretos elaborados en la ciudad de cali con materiales elaborados de la región. Ph.D. thesis, Universidad del Valle (2001)
24. la Rosa, H.D., Duran, D.: Determinación del módulo de elasticidad para concretos estructurales utilizados en la ciudad de santa marta. Ph.D. thesis, Universidad del Magdalena (2006)
25. Barragán, E.A.G.B.M.F.C.: Comparación de los módulos de elasticidad de concreto normal, con el ensayo de compresión y el ensayo de flexió, Ph.D. thesis, Pontificia Bolivariana Seccional (2012)
26. Murcia, R.A.B.: Obtención del módulo de elasticidad y la relación de poisson, para concretos de 21 y 28 mpa en seis diferentes obras ubicadas en la zona occidental de bogotá. Ph.D. thesis, Universidad La Gran Colombia (2015)
27. Pineda, J.M.O.: Determinación de la relación de poisson y módulo de elasticidad para concretos de 21 y 28 megapascales en concretos de la ciudad de villavicencio. Ph.D. thesis, Universidad La Gran Colombia (2016)